Revista Brasileira de Ciências Mecânicas

Journal of the Brazilian Society of Mechanical Sciences

1

PUBLICAÇÃO DA ABCM - ASSOCIAÇÃO BRASILEIRA DE CIÊNCIAS MECÂNICAS

VOL. XXI - No.1 - MARCH 1999 ISSN 0100-7386

JOURNAL OF THE BRAZILIAN SOCIETY OF MECHANICAL SCIENCES
REVISTA BRASILEIRA DE CIÊNCIAS MECÂNICAS

REVISTA BRASILEIRA DE CIÊNCIAS MECÂNICAS
JOURNAL OF THE BRAZILIAN SOCIETY OF MECHANICAL SCIENCES
Vol. 1, Nº 1 (1979)-
Rio de Janeiro: Associação Brasileira de Ciências Mecânicas
Trimestral
Inclui referências bibliográficas.
1. Mecânica
ISSN-0100-7386

A REVISTA BRASILEIRA DE CIÊNCIAS MECÂNICAS publica trabalhos que cobrem os vários aspectos da ciência e da tecnologia em Engenharia Mecânica, incluindo interfaces com as Engenharias Civil, Elétrica, Química, Naval, Nuclear, Aeroespacial, Alimentos, Agrícola, Petróleo, Materiais, etc., bem como aplicações da Física e da Matemática à Mecânica.

INDEXED by Applied Mechanics Reviews and Engineering Information, Inc.

Publicação da / Published by
ASSOCIAÇÃO BRASILEIRA DE CIÊNCIAS MECÂNICAS
THE BRAZILIAN SOCIETY OF MECHANICAL SCIENCES

Secretária da ABCM : Ana Lúcia Fróes de Souza
Avenida Rio Branco, 124 18º Andar
20040-001 Rio de Janeiro RJ
Tel.: (021) 221-0438/Fax: (021) 509-7128
www.puc-rio.br/parcerias/abcm
abcm@domain.com.br

Presidente: Carlos Alberto de Almeida
Vice-Presidente: Hans Ingo Weber
Secretário: Paulo Batista Gonçalves
Diretor de Patrimônio: Felipe Bastos de F. Rachid
Secretário Geral: Nestor Alberto Z. Pereira

Secretária da RBCM: Maria de Fátima Alonso de Sousa
UNICAMP - FEM - C.P. 6122
13083-970 Campinas SP
Tel.: (019) 788-3205/Fax: (019) 289-3722
E-Mail: abcm@fem.unicamp.br

REVISTA FINANCIADA COM RECURSOS DO
Programa de Apoio a Publicações Científicas
MCT CNPq FINEP

RBCM - J. of the Braz. Soc. Mechanical Sciences
Vol. XXI - No.1 - 1999 - pp. 1-9
ISSN 0100-7386
Printed in Brazil

Tool Wear of Polycrystalline Cubic Boron Nitride and Ceramic Materials When Hard Turning Bearing Steel

Alexandre Mendes Abrão
Universidade Federal de Minas Gerais
Escola de Engenharia
Departamento de Engenharia Mecânica
31270-901 Belo Horizonte, MG Brazil
abrao@vesper.demec.ufmg.br

David Keith Aspinwall
University of Birmingham
School of Manufacturing and Mechanical Engineering
Edgbaston, Birmingham B152TT U. K.

Abstract

This work aims to investigate the principal wear mechanisms involved when turning AISI E53100 bearing steel hardened to 60-62HRC using two grades of polycrystalline cubic boron nitride (PCBN) and three grades of ceramic tool materials (mixed alumina, whisker reinforced alumina and silicon nitride-based). In addition to the tool life data, scanning electronic micrographs of the cutting edge and the profile of the rake and clearance faces are presented. The results suggest that the mixed alumina tool presented highest flank wear resistance when cutting under finishing conditions, whereas the low content PCBN compact was superior when rough cutting. Diffusion, abrasion and plastic deformation were the main cause of tool failure.
Keywords: *Hard Turning, Bearing Steel, PCBN and Ceramic Tools.*

Introduction

The advent of cubic boron nitride in the 70's and further developments on oxide and non-oxide ceramic tool materials allowed cutting of some difficult to machine materials, particularly hardened steels, hard cast irons and nickel-based alloys. However, due to differences in composition and properties, the performance of these tool materials will obviously vary according to the cutting parameters and workpiece material. This paper compares the performance of five tool materials when turning bearing steel hardened to 62 HRC with regard to tool life and wear resistance.

Gradual wear of advanced ceramic tool materials when machining hardened steels is a complex process which involves several concurrent mechanisms. The relevance of each of these mechanisms to the tool life will vary according to the composition, and consequently the hardness, of the workpiece and tool materials and the operating parameters being used. According to Hooper et al. (1989) three main processes are involved in the wear of polycrystalline cubic boron nitride (PCBN) cutting tools: chemical wear caused by interactions with the environment (including atmospheric oxidation), the formation of a protective layer on the surface of the tool at high temperature and the removal of this layer by the swarf at lower cutting speeds (lower temperature) leading to attrition wear and further chemical wear. When comparing the wear of a high content PCBN compact (Amborite) with a low content tool (DBC50) during finish cutting, Hooper and Brookes (1984) found that higher cutting temperatures were generated when using DBC50 due to its lower thermal conductivity, leading to the formation of the protective layer on the rake face of the tool and consequently, lower wear rates than when using Amborite. Klimenko et al. (1992) also found signs of a liquid phase between the tool-workpiece and the tool-chip interfaces when turning bearing steel (60-62 HRC) using PCBN compacts. However, it was not clear how the presence of this layer affected the wear behaviour of PCBN tool materials. Such layer was not observed when using alumina-based ceramic cutting tools. Other researchers (Chen ,1993 and Xin, 1980) have identified the formation of this protective layer on PCBN tools.

Abrasion caused by hard particles present in the workpiece material, together with dislodged tool material grains, are likely to play a part. Wear of PCBN and both white and mixed alumina tools when turning cold work die steel (JIS SKD11, 60 HRC) is reported by Ohtani and Yokogawa (1988) as the result of abrasion caused by hard alloy carbide particles present in the workpiece.

Diffusion wear is probably of more significance, especially when considering the high temperatures that can be achieved at the tool-chip-workpiece interface. It is believed that the presence of titanium

Manuscript received: March 1998, Technical Editor: Alisson Rocha Machado.

carbide (TiC) in the composition of the cutting tool can lead to the formation of the above mentioned protective layer on PCBN tools under a specific range of cutting temperatures and that this film can act to prevent diffusion wear. Although there is some evidence for such a layer, it has not been explained how it can inhibit tool wear or why it is not observed on Al_2O_3-TiC products. Such tools possess lower thermal conductivity than PCBN compacts containing TiC and therefore are capable of generating similar or even higher temperatures in the cutting zone. Narutaki and Yamane (1979) considered remote the possibility of diffusion wear of PCBN tools when machining hardened steels owing to the low affinity of the CBN grain with iron and to the lower temperatures generated at the cutting zone compared with cemented carbide tool materials.

Static diffusion tests between PCBN tools of different compositions and DIN 100Cr6 bearing steel (60 HRC) have indicated that recrystallisation of the secondary phase occurs at high temperature leading to the weakening of the binder material and hence contributing to the wear of the tool material (König and Neises, 1993). In addition, subsequent abrasion tests carried out by the authors using a diamond indenter showed that the amount of wear increased with temperature rise, the wear scars on the low concentration PCBN tools being slightly deeper than on the high concentration products, although the weight loss caused by abrasion was not significant. Cutting tests, however, showed opposite results. One reason for this could be the massive loss of CBN grains when the binder phase surrounding the grain is eroded. The presence of TiC in the binder phase of DBC50 increased its etching resistance thereby minimising chemical wear. Sliding tests using single CBN and Al_2O_3 grits against hardened M-50 tool steel (62 HRC) indicated that CBN grains presented approximately half of the friction coefficient of the alumina, thereby producing a more uniform track and less ridges and microcracks (Calabrese and Murray, 1989).

With regard to attrition wear, welding of workpiece fragments is reported to protect the cutting edge, however when this material is removed, particles of the cutting tool may also be affected. Takatsu et al. (1983) reported the welding of the workpiece material on the cutting edge after cutting different types of hardened steels using cutting tools with various CBN concentrations. The amount of welding apparently increased with a decrease in the CBN content and protected the cutting edge from wear. Work by Oishi and Nishida (1992) involving PCBN and several conventional ceramic tool materials when machining hardened JIS SUJ2 bearing steel (66 HRC) indicated that under dry finishing conditions, there was a critical cutting speed below which tool fracture did not take place. This critical cutting speed was higher for the PCBN than for a mixed alumina cutting tool. Surprisingly, the use of cutting fluid had a positive effect on the tool life of the mixed alumina tool material. Similar results have been reported when turning hardened low alloy steel (En2), where above 50 m/min cutting speed the zirconia toughened alumina tool was outperformed by the PCBN, failing by chipping of the cutting edge (Nakai et al., 1988).

Gane and Stephens (1983) reported tests involving turning of hardened alloy steel En26 (550HV) using Amborite and mixed alumina (Al_2O_3 + 20% TiC) cutting tools. At low cutting speeds (50 m/min) the flank wear of the PCBN tool was three times greater than that of the mixed alumina, but when the cutting speed was increased to 75 m/min the life of the alumina tool was limited by cracking and chipping of the cutting edge, whereas the PCBN insert showed relatively low wear. It was suggested that the poor performance of the mixed alumina tool at the higher cutting speed was due to its lower thermal conductivity and inferior thermal shock resistance.

When machining hardened cold work die steel AISI D2 using Amborite inserts, it has been reported by Notter and Heath (1988) that wear occurs almost immediately, after which the cutting edge stabilises and further wear takes place at a much reduced rate. Machining the same workpiece material with BZN-6000, Bhattacharyya et al. (1978) asserted that in general, a uniform flank wear occurred as a combination of high cutting speeds and relatively high feed rates. The crater wear depth increased with an increase in the cutting speed. The crater width was dependent only on the feed rate (increasing the feed rate caused a decrease in the crater width). When face milling hardened steels using PCBN tools, the tool can also fail due to flaking/spalling and tearing of the flank face and also flaking of the rake face as a consequence of thermal fatigue in addition to the gradual wear mechanisms, Xiangning and Guangmin (1994).

Enomoto et al. (1988) suggest that the wear of PCBN tool when cutting low alloy steel (JIS SCM435H) of various hardnesses is caused by abrasion and adhesion. Minimum flank wear was obtained using cutting tools with 60% CBN content and small CBN grain size (2 μm). It was suggested that reducing the grain size increased the contact area between the CBN grains and the bonding material leading to a greater bonding force.

Built-up edge is not a critical problem when machining hardened steels owing to the fact that the temperatures generated in the cutting zone are above the recrystallisation temperature. When machining

hardened steels with mixed alumina ceramic tools, the formation of built-up edge was reported by Vander Voort and Lesher (1994) to be dependent only on the hardness of the workpiece. When the hardness exceeded a critical value, the built-up edge disappeared irrespective of the cutting speed used.

Finally, plastic deformation leading to sudden fracture of the cutting edge seems to affect mixed alumina tools to a greater extent than PCBN tools because of the lower hot hardness of the conventional ceramic material. As with cemented carbide tool materials, the occurrence of sliding wear, and consequently notching of the leading and trailing edges of ceramic tools, especially when machining hardened tool steels, is not well understood and requires further investigation.

Experimental Procedure

Bars of AISI E52100 bearing steel approximately 150 mm in diameter and 750 mm long were used as workpiece material. The hardness of the workpiece was monitored with a portable hardness tester and it was found within the range 60-62 HRC. Two grades of PCBN cutting tools (De Beers Amborite and DBC50) were tested in addition to conventional ceramic tooling (Sandvik CC650-mixed alumina, CC670-whisker reinforced alumina and CC690-silicon nitride based ceramic). The PCBN indexable inserts conformed to SNGN 090316 and were employed in a top clamp tool holder which provided the following geometry: cutting edge angle χ_r=45°, normal rake angle γ_n=-6° and cutting edge inclination angle λ_s=-7°. They incorporated a T-land chamfer of 0.2 mm x 20°. The ceramic tools conformed to SNGN 120416 and were similarly located, but the normal rake angle was γ_n =-7° due to differences between the two toolholders used to accommodated different size inserts. In this case the T-land chamfer was 0.25 mm x 20° for CC650 and CC690 and 0.1 mm x 20° for CC670.

Continuous dry turning tests were conducted on a high stiffness turning centre (30 kW, 3000rpm maximum rotational speed) equipped with a CNC unit. Tests were performed in accordance to ISO 3685-1977 using the following cutting parameters: cutting speeds (v_c) of 70, 140 and 200 m/min, feed rates (f) of 0.06 and 0.25 mm/rev and depths of cut (a_p) of 0.5 and 2.0 mm. A full factorial experiment was designed resulting in 12 cutting conditions for each tool material.

Initially, a tool life criterion based on a average flank wear VB=0.3 mm was established. However, tests were stopped after 30 minutes if this value had not been reached. In several instances this was the case and therefore the v-T results are presented using VB=0.2 mm to avoid the use of extrapolated data. Flank wear was measured using a toolmaker's microscope equipped with digital micrometers. Workpiece surface roughness was monitored using a Mitutoyo Surftest 201 unit set with a 0.8 mm cut-off length.

The profile of the rake and flank face were obtained with a Talysurf 5 system after etching sample cutting tools in a 50% HCl solution. Photographs of worn cutting tools were taken using a scanning electron microscope and due to differences in the electrical conductivity of the tool materials used, all inserts were gold coated before examination.

Results

Tool life curves obtained from the flank wear data for a depth of cut of 0.5 mm and feed rate of 0.06 mm/rev are shown in Fig. 1, whereas Fig. 2 shows the results when feed rate was increased to 0.25 mm/rev. The mixed alumina tool (CC650) provided best results at a feed rate of 0.06 mm/rev, but failed when both feed rate and cutting speed were increased, whereas the low content PCBN tool (DBC50) gave good results under both 0.06 and 0.25 mm/rev. At the lower feed rate CC670 produced a negative slope much steeper than the rest of the tool materials, however, without the tool life values at 70 m/min for DBC50, CC650 and CC670 (which did not reach the tool life criterion, and therefore, are not presented) it is difficult to establish precisely the tendencies for these tool materials.

The whisker reinforced alumina (CC670) also failed suddenly when cutting speed increased to 200 m/min. Due to its high hardness and toughness, the high content PCBN tool (Amborite) was expected to perform better at high feed rates, but this was not the case. Finally, the silicon nitride-based cutting tool presented the worst results for all cutting conditions.

Figures 3 and 4 show the v-T curves obtained for feed rates of 0.06 and 0.25 mm/rev, respectively, and a depth of cut of 2.0 mm. In general, it can be seen that for a feed rate of 0.06mm/rev the same trend observed previously was maintained, where CC650 gave longer tool life, however, a slight reduction in tool life was reported in comparison to a_p=0.5 mm. Additionally, only CC670 and CC690 reached VB_B=0.3 mm before 30 minutes of cutting.

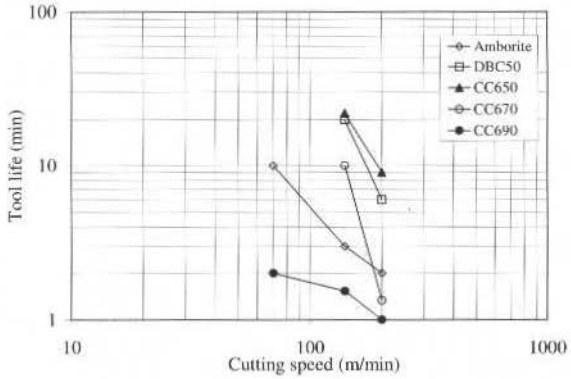

Fig. 1 v-T curves for hardened bearing steel at f=0.06 mm/rev and a_p=0.5 mm.

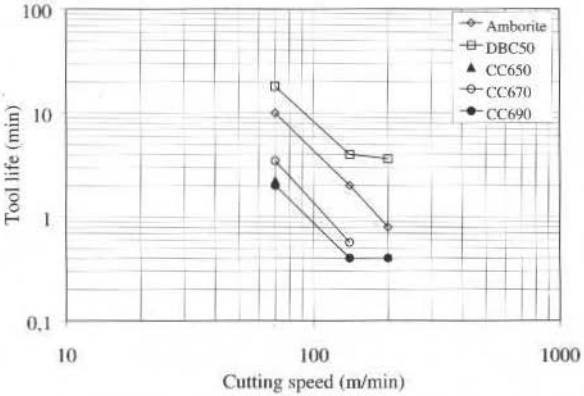

Fig. 2 v-T curves for hardened bearing steel at f=0.25 mm/rev and a a_p=0.5 mm.

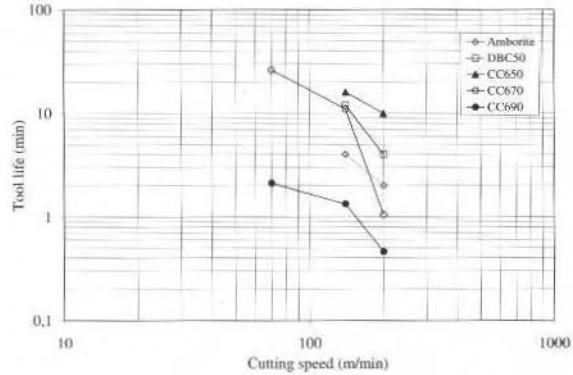

Fig. 3 v-T curves for hardened bearing steel using a f=0.06 mm/rev and a_p=2.0 mm.

A further diminishing in tool life was noticed when the feed rate increased to 0.25 mm/rev. Under this circumstance the mixed alumina material could not withstand cutting even at the lowest cutting speed. For the most severe operating condition Amborite provided the best result, lasting less than one minute.

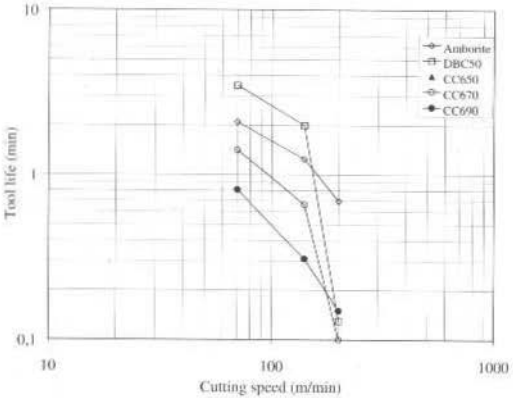

Fig. 4 v-T curves for hardened bearing steel using a f=0.25 mm/rev and a_p=2.0 mm.

Figure 5 shows samples of tool wear generated after reaching the tool life criterion under various cutting conditions for those materials which presented superior performance, i.e., CC650, DBC50 and Amborite.

When finish turning with CC650 an increase in cutting speed from 70 to 200 m/min (Fig. 5a and 5b, respectively) led to chipping of the cutting edge and accelerated flank and crater wear. Rough turning parameters caused the fracture of the cutting edge. The same trend was observed when cutting with DBC50 tools (Figs. 5c and 5d). When cutting with Amborite (Figs. 5e and 5f) the tool wear appeared to be more severe when finishing than when roughing. Increasing the cutting speed and feed rate led to the appearance of grooves on the crater surface near the rake face. The discontinuous film shown in Fig. 5f was due to poor adhesion of the gold coating applied prior to the SEM analysis.

The profile of the clearance and rake faces after reaching the tool life criterion when finishing and roughing can be seen in Figs. 6 and 7, respectively, where the cutting time is shown between brackets.

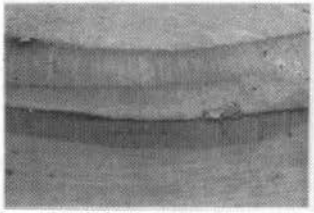

a) CC650 v_c=70 m/min, f=0.06mm/rev and a_p=0.5 mm

b) CC650 v_c=200 m/min, f=0.06 mm/rev and a_p=0.5 mm

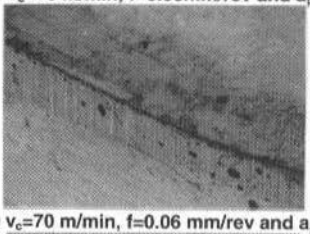

c) DBC50 v_c=70 m/min, f=0.06 mm/rev and a_p=2.0 mm

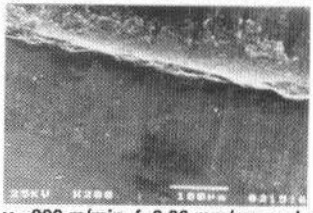

d) DBC50 v_c=200 m/min, f=0.06 mm/rev and a_p=0.5 mm

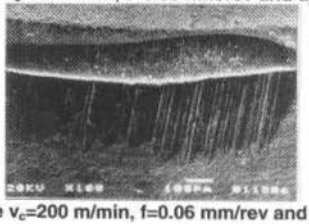

e) Amborite v_c=200 m/min, f=0.06 mm/rev and a_p=0.5 mm

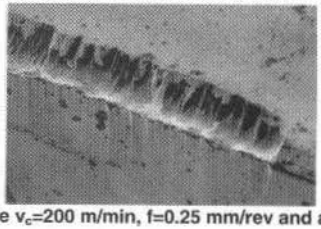

f) Amborite v_c=200 m/min, f=0.25 mm/rev and a_p=2.0 mm

Fig. 5 Tool wear when turning hardened AISI E52100 bearing steel.

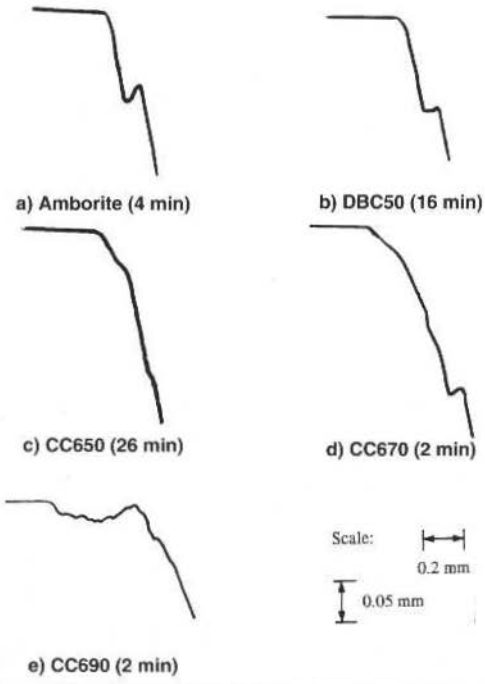

Fig. 6 Profile of the rake and flank faces after finish turning (v_c=200 m/min, f=0.06 mm/rev and a_p=0.5 mm) hardened AISI E52100 steel with: a) Amborite, b) DBC50, c) CC650, d) CC670 and CC690.

When finish turning , CC650 showed the best crater wear resistance followed by DBC50 and Amborite. CC670 showed a rapid loss of the cutting edge and excessive wear was observed on CC690. When rough turning Amborite gave the best result. Both CC670 and CC690 presented insufficient crater wear resistance and the profile of DBC50 and CC650 tools after roughing are not shown due to tool fracture.

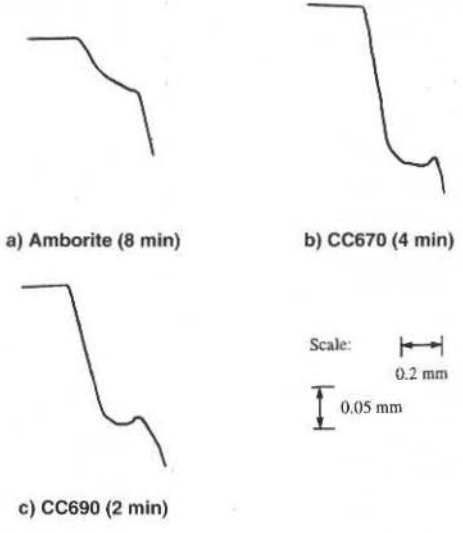

Fig. 7 Profile of the rake and flank faces after rough turning (v_c=70 m/min, f=0.25 mm/rev and a_p=2.0 mm) hardened AISI E52100 steel with: a) Amborite, b) CC670 and c) CC690.

Discussion

When cutting with a depth of cut of 0.5 mm and a feed rate of 0.06 mm/rev (Fig. 1), CC650 and DBC50 gave comparable results, followed by CC670 (at lower cutting speeds). Amborite tool life was shorter and CC690 shortest of all. When the feed rate was increased to 0.25 mm/rev, however, the tool life of the mixed alumina cutting tool showed a drastic reduction ending in catastrophic failure. The v-T curves for f=0.25 mm/rev (Fig. 2) shows that DBC50 provided the best flank wear resistance, followed by Amborite instead of CC650. This is an indication that when machining materials within this level of hardness, the mechanical properties of the tool, particularly hot hardness and fracture toughness, are crucial for a satisfactory performance. The fracture toughness of Amborite is approximately five times higher than reported values for CC650.

When the depth of cut was increased to 2.0 mm (Fig. 3) the same trend observed previously was maintained, however, as the cutting speed increased, the flank wear rate increased considerably, even so CC650 exhibited superior tool wear resistance. Nevertheless, with an increase in feed rate to 0.25 mm/rev none of the tool materials was able to produce a satisfactory performance. DBC50 gave the longest tool life results at 70 and 140 m/min but was outperformed by Amborite at 200 m/min. It would appear that when rough turning at cutting speeds as high as 200m/min, the mechanical and thermal stresses imposed are too high for most of the tool materials. Failure occurred within a short period of time either due to lack of toughness or as a consequence of accentuated diffusion wear caused by the high temperatures generated at the tool/chip interface. The overall poor performance of Amborite compared to DBC50 when rough cutting was a surprise since the former product is particularly recommended for heavy/rough cutting operations. In spite of its high hot hardness, the inferior wear resistance of Amborite could be explained in terms of grain size. According to Enomoto (1988), reducing the CBN grain size the contact area between the CBN crystals and the binder phase is increased leading to a greater bonding force. This would be an advantage in favour of DBC50 whose grain size is approximately one tenth of that of Amborite. Furthermore, the presence of titanium carbide increased the wear resistance of DBC50 due to its lower solubility in steel compared to CBN (Kramer, 1987) and also because of its good atmospheric etching resistance (Hooper et al., 1989).

The micrographs of worn cutting tools (Fig. 5) together with the profile of the rake and clearance faces after finish and rough turning (Figs. 6 and 7) give an insight into the possible wear mechanisms acting when machining such high hardness workpiece materials. When finish turning with Amborite, the smooth appearance of the crater was one possible indication that diffusion had occurred and the grooves on the clearance face suggested that abrasion was also a factor. Since these grooves were not as distinctive when using the other tool materials, it would seem logical to assume that they were not caused by hard carbide particles present in the workpiece, but by loose CBN grains which rubbed against the clearance face. They were also noticed, to a much lesser extent, when turning at v_c=140 m/min, f=0.25 mm/rev and a_p=0.5 mm but were not observed with DBC50 tools. Therefore their appearance was associated with a combination of high cutting speed and feed rate. They could be a result of chemical wear when high temperatures are reached in the tool/chip interface, which did not occur with DBC50 because of the presence of titanium carbide and the lower thermal conductivity of the low CBN content product. This form of localised wear may also be associated with the manufacturing route of the compact. It has been reported by Hooper et al. (1989) that during the synthesis of the tool blanks, the CBN grains in DBC50 are subjected to much less plastic deformation than in Amborite. As a result, DBC50 will possess higher resistance to wear caused by the development of structural defects in the CBN grains.

Similar wear patterns were observed in DBC50 and CC650. When turning at v_c=70 m/min, f=0.06 mm/rev and a_p=0.5 mm minimal wear was observed after 30 minutes, but when the cutting speed was increased to 200 m/min signs of chipping of the cutting edge were evident. The texture of the crater produced in CC650, particularly in Fig. 5a, and of the crater and rake faces of DBC50 (Fig. 5d) indicated the occurrence of diffusion wear. The profile of the cutting edge when finish turning suggested that the mixed alumina product had a higher crater wear resistance than DBC50. In contrast, the gross fracture observed when rough turning using both materials indicated insufficient fracture toughness (k_{Ic}=3.7 MPa.m$^{0.5}$ for DBC50 and typically k_{Ic}=2.9 MPam$^{0.5}$ for Al_2O_3 + 30% TiC according to De Beers, 1990). Certainly, this difference accounted for the fact that the CC650 failed after 30 seconds of cutting whereas the DBC50 lasted for 4 minutes.

During the cutting tests on the hardened bearing steel the whisker reinforced alumina suffered from cratering and spalling on the rake face. Accentuated loss of the cutting edge was also observed suggesting that despite the smaller contact area, the greater hardness of the bearing steel and associated higher forces resulted in higher chip/tool interface temperatures and consequently accelerated wear of

CC670. The wear of the silicon nitride-based product when finishing was characterised by spalling and fracture, possibly caused by the weakening of the cutting edge due to the high diffusion wear rates evident from rapid cratering.

Conclusions

When continuous turning hardened bearing steel using PCBN and ceramic cutting tools, the following conclusions can be drawn:

- Superior wear resistance was obtained by the mixed alumina tool and by the low content PCBN at low feed rate (f=0.06 mm/rev);
- When the feed rate was increased to 0.25 mm/rev, the low and high content PCBN compacts gave best results, in this order;
- Tool wear micrographs and profile samples suggest that diffusion and abrasion (caused by dislodged CBN grains) were the principal reasons for tool wear of the high content PCBN compact, whereas the low content compact and the mixed alumina tool failed due to diffusion at low feed rates and plastic deformation followed by catastrophic failure at high feed rates.

References

Bhattacharyya, S.K., Aspinwall, D.K. and Nicol, A.W., 1978, "The application of polycrystalline compacts for ferrous machining", Proceedings, 19th International Machine Tool Design and Research Conference, Manchester, UK, pp. 425-434.

Calabrese,S.J. and Murray,S.F., 1989, "SEM observations of the sliding behavior of Al_2O_3 and CBN against steel", Scanning, Vol. 11(5), pp. 231-236.

Chen,W., 1993, "The machining of hardened steels using superhard CBN tooling and CBN tipped rotary cutting tools", PhD Thesis, University of Birmingham, UK.

De Beers Industrial Diamond Division, 1990, "DBC50", Technical catalogue nº. H4000890.

Enomoto, S., Kato,M. and Miyazawa,S., 1988, "Flank wear of CBN cutting tools of various compositions", Journal of Mechanical Working Technology, Vol. 17, pp. 177 - 186.

Gane, N. and Stephens, L.W., 1983, "The wear and fracture resistance of ceramic cutting tools", Wear, Vol. 88, pp. 67 - 83.

Hooper, R.M., Shakib,J.1., Parry,A. and Brookes,C.A., 1989, "Mechanical properties, microstructure and wear of DBC50", Industrial Diamond Review, Vol. 4, pp. 170 - 173. Hooper,R.M. and Brookes,C.A., 1984, "Microstructure and wear of cubic boron nitride aggregate tools", Proceedings, 2d International Conference Science Hard Materials, Rhodes, pp. 907 - 917. IS03685, 1977, "Specification for tool life testing with single point turning tools", International Standards Organization.

Klimenko,S.A., Mukovoz,Y.A., Lyashko,V.A., Vashchenko,A.N. and Ogorodnik, V.V., 1992, "On the wear mechanism of cubic boron nitride base cutting tools", Wear, Vol. 157, pp. 1 - 7.

König,W. and Neises,A., 1993, "Wear mechanisms of ultrahard, non-metallic cutting materials", Wear, Vol. 162-164, pp. 12-21.

Kramer, B.M., 1987, "On tool materials for high speed machining", Journal of Engineering for Industry (Transactions of the ASME), Vol. 109, pp. 87 - 91.

Nakai,T., Goto,Y. and Nakatani,S., 1988, "Cutting performance of PCBN and PCD for P/M parts", Proceedings, Modern Developments in Powder Metallurgy, Vol. 19, Orlando, USA, pp. 379 393.

Narutaki, N. and Yamane, Y., 1979, "Tool wear and cutting temperature of CBN tools in machining of hardened steels", Annals of the CIRP, Vol. 28(1), pp. 23 - 28.

Notter, A. T. and Heath, P. J., 1980, "Machining of hard ferrous materials with Amborite", De Beers Industrial Diamond Division, Technical Service Centre, Charters, Ascot, England, pp. 6 - 13.

Ohtani, T., and Yokogawa,H., 1988, "The effects of workpiece hardness on tool wear characteristics/Machining of cold work tool steel with CBN, ceramic and carbide tools", Bulletin of Japan Society of Precision Engineering, Vol. 22(3), pp. 229 - 23 1.

Oishi,K. and Nishida,T., 1992, "Study on the fracture characteristics of ceramic cutting tools - first report", Wear, Vol. 154, pp. 361 - 370.

Takatsu,S., Shimoda,H. and Otani,K., 1983, "Effects of CBN content on the cutting performance of polycrystalline CBN tools", International Journal of Refractory and Hard Metals, Vol. 2(4), pp. 175 - 178.

Vander Voort, G. and Lesher,J.A., 1994, "Preparation of high alloy martensitic steels", Struers Journal of Metalography, Vol. 1, pp. 3-8.

Xiangning,W. and Guangmin,L., 1994, "Study on the tool wear of PCBN face milling cutter", Proceedings, Advancement of Intelligent Production, The Japan Society for Precision Engineering, pp. 401-406.

Xin,Y., 1980, "The influence of cutting atmosphere on the wear of CBN turning tool Elbor-IC", Tool Engineering, Vol. 5, pp. 25-27.

RBCM - J. of the Braz. Soc. Mechanical Sciences
Vol. XXI - No.1 - 1999 - pp. 10-16

ISSN 0100-7386
Printed in Brazil

Analysis of Polyethylenes Used to Coat Telephone Wires and Cables Submitted to Severe Wether-Ometer Conditions

Derval dos Santos Rosa
José Eduardo Volponi
Sebastião Sahão Júnior
CPqD-Fundação
Rodovia Campinas Mogi-Mirim, Km 118,5
Campinas, SP Brazil
derval@cpqd.com.br

Abstract

Polyethylenes, used to coat telephone cables and wires, are the materials that have shown the best behavior when submitted to the action of the environment; in many cases they last over twenty years. Among them, we highlight low-density polyethylene (LDPE), that, however, has low resistance to abrasion: this makes impossible its use in networks that undergo a great incidence of kites and cutting materials. An alternative for this material is the high-density polyethylene (HDPE). Detailed studies have shown that both, in the laboratory as in the field, have similar behavior as to resistance to severe weather conditions, with the additional advantage that HDPE has a much higher mechanical resistance. This work presents an assessment of the behavior of these materials and demonstrate why they have an excellent resistance to severe weather conditions.
Keywords: *Wire and Cable Coating, Polyethylenes, Aging*

Introduction

The presence of polymeric materials in the telephone network has been increasing along the years due to the high cost/benefit ratio these materials deliver to telecommunications products: low costs, good mechanical properties, high performance and long life, provided they are used adequately. Among those most used, one can mention polyethylenes, which can be: High-Density Polyethylene (HDPE), Low-Density Polyethylene (LDPE), Low Linear Density Polyethylene (LLDPE), etc.

These polymeric materials are rated as "commodities" and are widely used in coating of telephone cables and wires, with some applications also in Optical Splice Closures, Sub-Ducts, Insulation of Telephone Cable Conductors, etc, and have excellent performance, when submitted to severe weather conditions: heat, rain, pollutants and, above all, UV radiation from the sunlight. Although they belong to the same family of materials, polyethylenes have significant differences in their properties due to minor differences in their structures. Figures 1(a), 1(b) and 1(c), below, illustrate the structures of High-Density, Low-Density and Low Linear Density Polyethylenes:

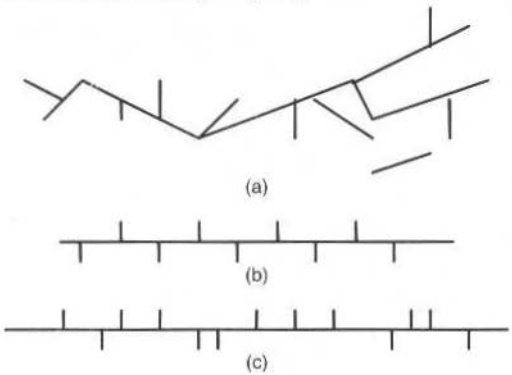

Fig. 1 Schema of the molecular structure of: (a)-LDPE; (b) - HDPE and (c)-LLDPE

Manuscript received: April 1998; revision received: August 1998. Technical Editor: Leonardo Goldstein Jr.

These structure differences determine different physical and mechanical properties, and have a direct influence on the behavior of these materials in telecommunication products, mainly with respect to dimensional stability and resistance to abrasion, and, at times, resistance to being cut.

LDPE's low cutting and abrasion resistances have been observed in telephone wires installed in areas with great incidence of kites prepared with cutting strings, as illustrated in Figs. 2 and 3.

Fig. 2 Telephone wires and cables involved with kite strings.

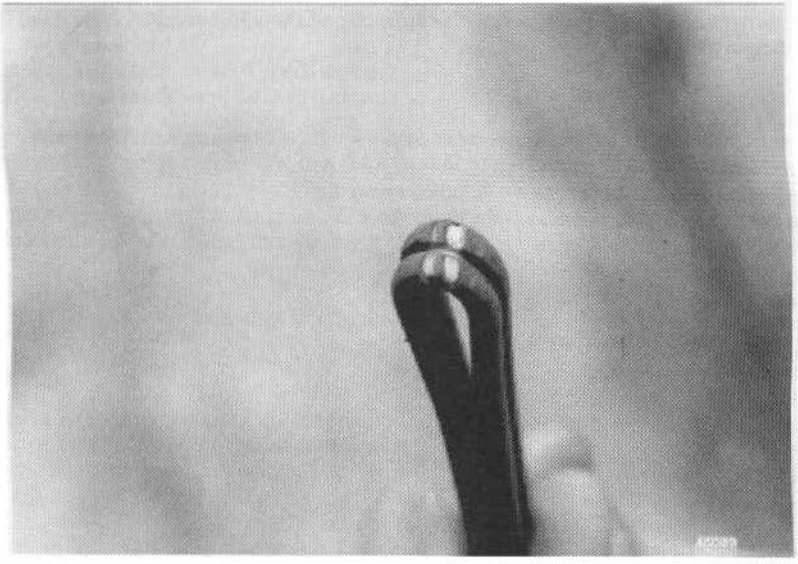

Fig. 3 Detail of a cut in a telephone wire

Nevertheless, LDPE has been used in sheath of wires and cables, and has shown an excellent behavior and performance in severe weather conditions. Currently there are reports of cables that have been installed for over 20 years in the Brazilian Telecommunication Company telephone network, with no problems of degradation of their polymeric sheathing.

As HDPE has a more uniform molecular structure, that is, more crystalline, its resistance to cuts or abrasion is higher than LDPE, and this feature is even more evident in the presence of heat, because the LDPE hardening and softening points are very low. Our studies, have shown that HDPE has the same behavior as LDPE when submitted to severe weather conditions, both in laboratory and in the field, and these results will be presented next.

Materials and Methodology

The materials used in developing this work were:

- Pure LDPE;
- Pure HDPE;
- LDPE with 2.5% carbon black, plus chemical stabilizers, and
- HDPE with 2.5% carbon black plus chemical stabilizers.

where

- Low-Density Polyethylene:
  Density: 0.92-0.94 g/cm^3
  Melt Flow Index: 0.6 g/10min.
- High-Density Polyethylene:
  Density: 0,95-0,97 g/cm^3
  Melt Flow Index : 0.8 g/10min.
- Carbon Black N 220

From these formulations, standard specimens were prepared for tensile strength tests. They were submitted to natural and accelerated aging tests, so that their mechanical properties could be assessed before and after aging.

The purpose of the addition of carbon black and chemical stabilizers to polyethylene was to increase stability of the material to severe weather conditions, particularly to ultraviolet radiation from sunlight, and heat. Carbon black is an absorber of ultraviolet rays and, in order to deliver an effective protection to the polymer, its grain size should be smaller than 25μm (N220 carbon black) and the concentration should be 2 to 3 percent of the polymeric matrix mass. Above 3%, no significant protection improvement was noticed, due to the difficulty of incorporating and dispersing carbon black particles in the polymer matrix.

Aging

To study the behavior of the polyethylenes when submitted to severe weather conditions, two types of aging procedures were used: natural aging in test fields and accelerated aging in laboratory.

The accelerated aging test is usually conducted on an apparatus named "Weather-Ometer ®", which supplies weather conditions as close as possible to those found in nature. It simulates sunlight radiation with a xenon arc lamp; it also simulates temperature, humidity and rain. The test parameters used were the following, in accordance with ASTM G-26:

- Xenon arc lamp 6500 W with borosilicate filters
- Two-hours cycles (102 minutes of light + 18 minutes of light and water spray)
- Black panel temperature = 63 ± 5 °C
- Relative humidity = 65 ± 5%
- Radiation at 340 nm = 0.35 W/m^2

In the natural aging test, samples were exposed directly to the same conditions of product use, but the response time was very long. In this work, materials were installed in different locations of the country, including climates that are very aggressive to polymers. The three cities chosen were: Campinas - SP, Fortaleza - CE and Belém - PA.

Laboratory Tests

Many physical and chemical tests have been applied to predict the performance of plastics submitted to severe weather. Visual aspect, change in color, mechanical resistance, melt flow index, change in weight and spectroscopic methods are some of the most important parameters and procedures used to characterize degradated polymers. In this work, due to application of polyethylenes as sheathing for telephone wires and cables, three properties were chosen to follow up the degradation of these materials: tensile strength, elongation at break and resistance to cutting.

In general, when polymers are submitted to degradation, they tend to reduce their tensile strength and their resistance to abrasion and become more brittle; therefore they reduce their elongation at break.

Tensile strength and elongation at break are parameters measured in standard test specimens, in accordance to the ASTM D-638 norm. To measure resistance to cutting, there is a specific test which simulates a real situation, where a standard "cerol"(kite string with little fragments of glass and glue) cutting kite string is placed in contact with the telephone wire, and the number of cycles required to cut the string is measured with a frequency of 1,5 Hz. A schematic drawing of the test assembly is shown in Fig. 4.

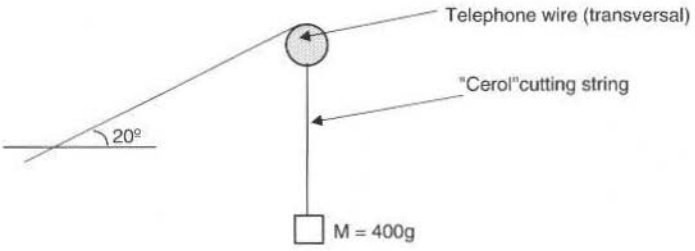

Fig. 4 Resistance to cutting test assembly

In addition to the previously described tests to follow degradation, another widely used test to assess the performance of polyethylenes, before aging, is the measurement of the coefficient of carbon black absorption in ultraviolet. The purpose of this spectroscopic technique is to evaluate the degree of dispersion of carbon black particles in the polymeric matrix, since this property is directly linked to the stability of the material to weather, particularly to ultraviolet radiation.

Another technique to evaluate carbon black dispersion is optical microscopy, where one can check qualitatively if the carbon black particles are well dispersed in the polymeric matrix.

Results and Discussion

Initiably the carbon black (C.B.) formulation was characterized by measuring its absorption coefficient in the ultraviolet:

LDPE 2.5% carbon black $\Rightarrow$ *3607 ± 64 abs/cm*

HDPE 2.5% carbon black $\Rightarrow$ *4084 ± 110 abs/cm*

and dispersion by optical microscopy. These results are shown in Fig. 5.

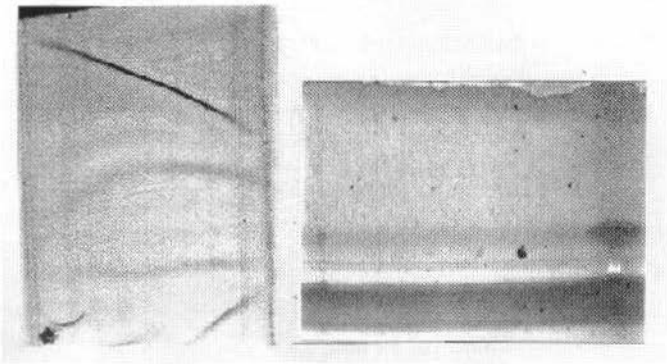

Fig. 5 Micrographies showing carbon black dispersion in LDPE and HDPE.

The analysis of these results, showed that both formulations with carbon black had good dispersion (there are no particle clusters - Fig. 5). Also, they have a high absorption coefficient in the ultraviolet, above 3,500 abs/cm. Therefore, both formulations have good stability against severe weather conditions and this ensures standardization for comparing between LDPE and HDPE after aging.

The mechanical properties after accelerated aging in the Weather-Ometer are shown in Figs. 6 and 7, where small difference between pure polyethylene and with addition of carbon black can be obserwed. Before 1,000 hours of aging the same behavior was maintained, however, after that, one can see a sharp decrease in the mechanical properties of the pure material. As to the polymers with additive, both preserved their mechanical properties up to the end of the test, i.e., approximately 3,500 hours. Note that the values for the HDPE tensile strength are greater than for LDPE.

In the case of natural aging, despite the short time exposure (two years), Figs. 8, 9 and 10 show that no differences were found among polyethylenes as to their tensile strength during the period analyzed.

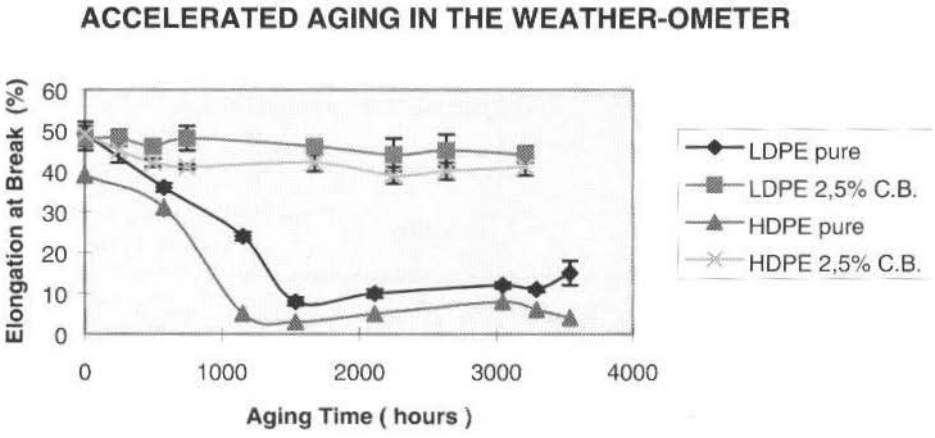

Fig. 6 Results of the elongation at break after aging in the Weather-Ometer

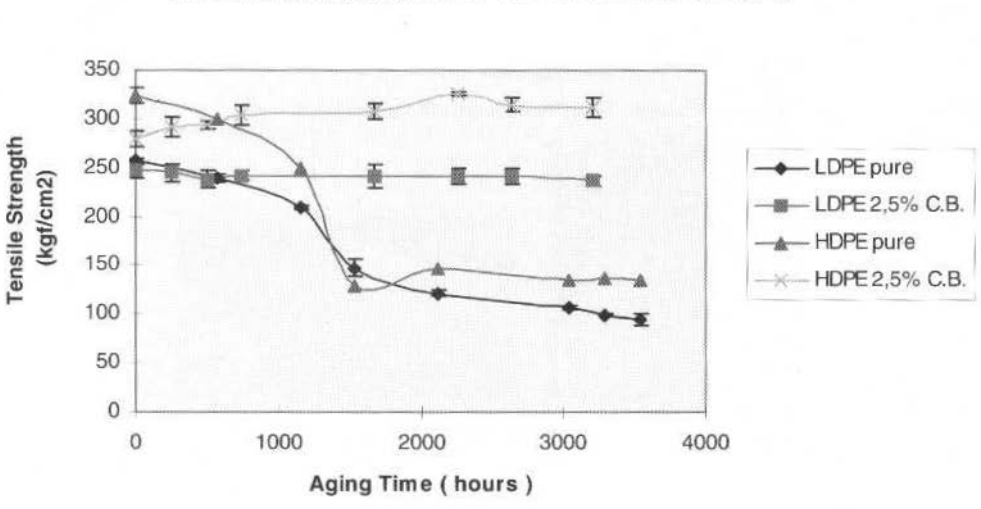

Fig. 7 Results of the tensile strength after aging in the Weather-Ometer

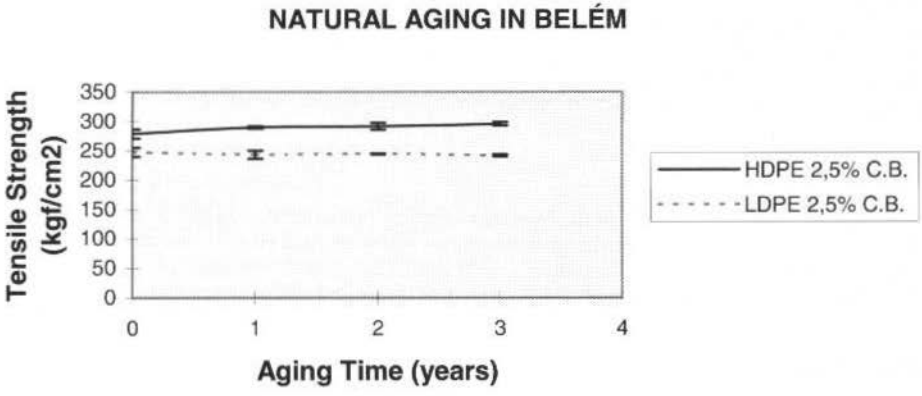

Fig. 8 Tensile strength after natural aging in Belém

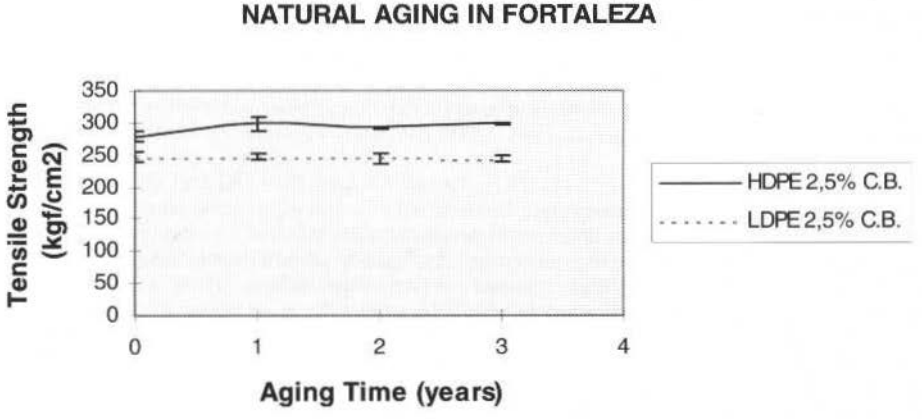

Fig. 9 Tensile strength after natural aging in Fortaleza

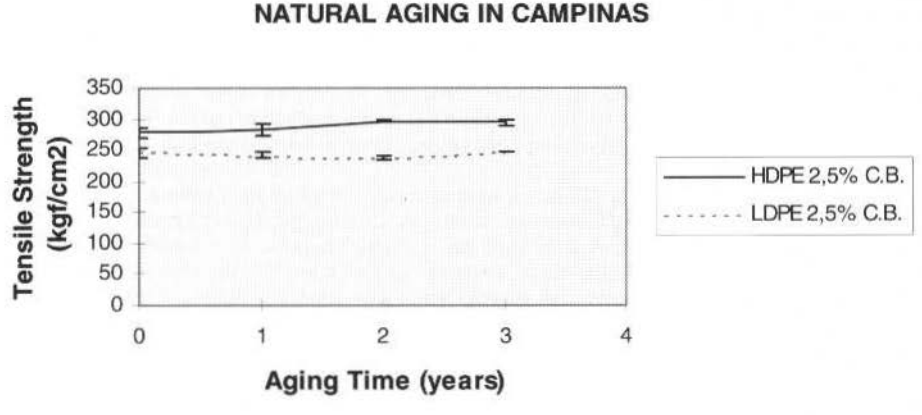

Fig. 10 Tensile strength after natural aging in Campinas

The resistance to cutting tests, conducted on telephone wires with the same configuration, but with different coating materials gave:

Wire coated with LDPE: *34±2 cycles*

Wire coated with HDPE: *125±7 cycles*

Which shows that HDPE's resistance to cutting with cerol string was much higher than LDPE's.

Conclusions

After up to 3,500 hours aging in the Weather-Ometer, and after two years of natural aging in three test fields, the analysis of the mechanical properties showed that HDPE and LDPE have the same performance under severe weather conditions. HDPE also has greater resistance to cutting and abrasion, a critical property for which the sheathing of telephone wires and cables is applied.

Acknowledgement

The authors thank TELEPARÁ and TELECEARÁ for the installation of the test specimens in their test fields.

References

Allen, N.S., 1983, "Degradation and Stabilization of Polyolefins", Applied Science Publishers, Essex, p.384.

American Society for Testing and Materials, 1995, ASTM G-26/95 - Standard Practice for Operating Light Exposure Apparatus (Xenon Arc Type) with and without water for Exposure of Nonmetallic Materials, p.10.

American Society for Testing and Materials, 1996, ASTM D-638/96 - Standard Test Method for Tensile Properties of Plastics, p.13.

Bagarolli, A., Silva, M.C. and Lopes, S.J.C, 1995, Technical Report PD.12.AT.CST.0005A/RT-01-AA; CPqD TELEBRÁS, p.52 (internal communicative).

Brydson, J.A., 1975, "Plastics Materials", Newnes Butherworths, p. 182-216.

Davis, A. and Davis, S., 1986, "Weathering of Polymer", Applied Science Publishers Ltd., 1 ed. New York, 289p.

Gilroy, H.M. and Chan, M.G., 1984, "Polymer Science and Technology", v.26. p. 273-287.

Gugumus, F. , 1989, Polymer Degradation and Stability, v.24, p.289-301.

Gugumus, F. , 1993, Polymer Degradation and Stability, v.39, p.117-135.

Ogorkiewicz, R.M., 1974, "Thermoplastics – Properties and Design", John Wiley & Sons, New York, p. 155-160.

Parris, D.R. and Gao, Z., 1997, "International Wire & Cable Symposium Proceedings", p.122-125.

Sahão Junior, S., 1996, Report of Research Project Applicated in Special Polymers - Telebrás - S/A P.A. PER - PD.33.PE.004.0001A/RT-04-AA, p.29 (internal communicative) .

Sahão Junior, S., 1996, Report on Field Operational Test -Telebrás - S/A - P.A. PER - PD.24.IA.001.0001A/RT-12-AA, p.48 (internal communicative).

Schnabel, W., 1982, "Polymer degradation principles and practical applications, Macmillan, New York, p.227.

Verdu, J., 1993, International Polymer Science and Technology, v.20, p. T64-T70.

Verdu, J., Langlois, V. and Audouin, L., 1995, "Die Angewandte Makromolekulare Chemie", v. 232, p.1-12.

RBCM - J. of the Braz. Soc. Mechanical Sciences
Vol. XXI - No.1 - 1999 - pp. 17-28

ISSN 0100-7386
Printed in Brazil

Theoretical and Experimental Study of a CPL Using Freon 11 as the Working Fluid

Edson Bazzo
Sergio Colle
UFSC - Federal University of Santa Catarina
Department of Mechanical Engineering
88040-900 Florianópolis, SC Brazil
ebazzo@emc.ufsc.br

Manfred Groll
IKE - Institute for Nuclear Technology and Energy Systems
University of Stuttgart
70550 Stuttgart, Germany

Abstract

Theoretical and experimental analysis are presented for a Capillary Pumped Loop (CPL), using Freon 11 as the working fluid. A mathematical model to predict the hydrodynamic behavior and the heat transport capability on the basis of capillary limitation is presented. Circumferentially grooved heat pipes are considered to be used as the capillary pumps. The capillary pumps consist of 19 mm O.D. aluminum tubes, with fine circumferential grooves machined along their inner surfaces. Start-up, heat transport limits and repriming after dryout were investigated. Experimental results up to 1.7 W/cm^2 were found. A good agreement between measured values and those computed by using the theoretical model has been observed.
***Keywords**: CPL, Capillary Pumped Loop, Heat Pipe, Two-Phase Heat Transfer Loop.*

Introduction

Heat pipes have found wide acceptance in the thermal management of current spacecraft and in many industrial applications. As conventional two-phase loops, with a common line for the vapor and liquid flows, heat pipes are able to transfer a large amount of thermal energy, at small temperature drop, and without need of a noisy mechanically driven pump to circulate the working fluid. Typical applications of heat pipes in the range of 100 to 200 W have been identified to the need to transport waste heat from electronic components of communication satellites over radiator areas. The most common heat pipes for space application have been made of axially grooved aluminum tube. However, due to new requirements related to the increased heat loads and reduction in weight, high composite heat pipe configurations (Schlitt, 1995; Dubois et al., 1997), loop heat pipes (Goncharov et al., 1995; Maidanik et al., 1997) and capillary pumped loops (Ku, 1993; Hoang, 1997) are being developed.

The performance of Capillary Pumped Loops (CPL) have been satisfactory in most ground tests in order to attend the heat transport capability or temperature control as required for space applications. Up to date, several ground tests and also flight tests have been already carried out using different types of capillary pumps. Most capillary pumps have been built using tubular porous material as the capillary structure. Porous material currently used in the capillary pumps are made of high density polyethylene or sintered nickel powder. Porous material has the advantage to produce higher capillary pumping pressure, when compared with axially or circumferentially grooved surfaces. However, some operational problems related to the startup and to the repriming ability in case of dryout must still to be effectively solved. Also, porous material is more sensitive to non-condensable gases or to vapor bubbles formation inside of its structure.

Circumferentially grooved heat pipes are also proposed as capillary pumps to be used in two-phase heat transfer loops. Theoretical and experimental results are presented here for capillary pumps made of aluminum tubes assembled as the evaporator plate mounted in a two-phase heat transfer loop. The capillary structure consists of circumferential grooves with slightly different geometry. The corresponding capillary pumping pressure was calculated in the range of 1.3 kPa to 2.0 kPa. First results regarding ground tests were reported (Bazzo et al., 1997). As an extension of this work, additional information regarding the tests, a mathematical model and theoretical results are now presented. The experimental results have demonstrated its ability to transfer heat fluxes up to 1.7 W/cm^2, for an effective internal heat transfer surface of the capillary pump equal to 0.0166 m^2, using Freon 11 as the working fluid. Success in startup and success in repriming a capillary pump in case of dryout have been observed. The corresponding values for ammonia was found to be up to 11 W/cm^2.

Manuscript received: July 1998; revised: September 1998. Technical Editor: Angela Ourívio Nieckele.

Despite the low capillary pumping pressure, a circumferentially grooved capillary pump is a reliable candidate to be used in small CPLs, or in those cases where the pressure drops through the vapor and liquid lines are not high enough to lead the system to the dryout condition.

The Capillary Pump Design

The capillary pump consists of a 19 mm O.D. aluminum tube with fine circumferential grooves machined on its inner surface. An insert is used to separate the inlet liquid channel from two outlet vapor channels. The internal structure of the capillary pump is schematically shown in Fig. 1. Heat is applied, along the vapor section, onto the outer surface of the capillary pump. The circumferential grooves create the required surface tension forces to move the working fluid from the liquid line, through the grooved surface, from where the heat is removed by phase changing. The active length is considered to be equal to the length of the insert. The internal surface is equal to $2.\pi.r_i.L = 0.025\ m^2$, where $r_i = 7.93$ mm is the internal radius and $L = 500$ mm is the active length of the tube. Due to the position of the insert, the effective internal heat transfer surface of the capillary pump is considered to be equal to $0.0166\ m^2$ (2/3 of the total value). The geometrical characteristics of the capillary pump are also schematically shown in Fig. 2.

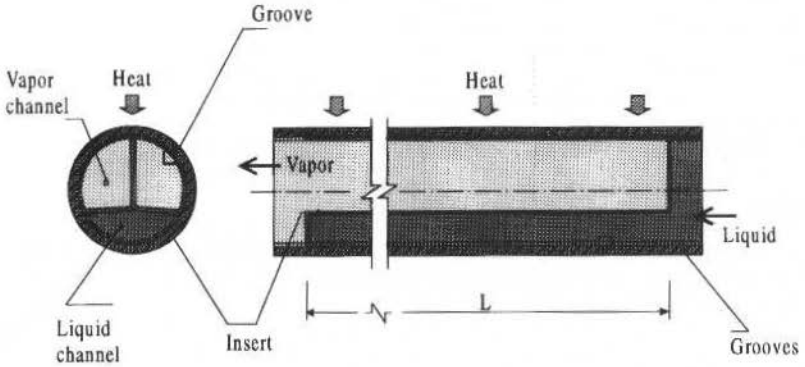

Fig. 1 The internal configuration of the capillary pump.

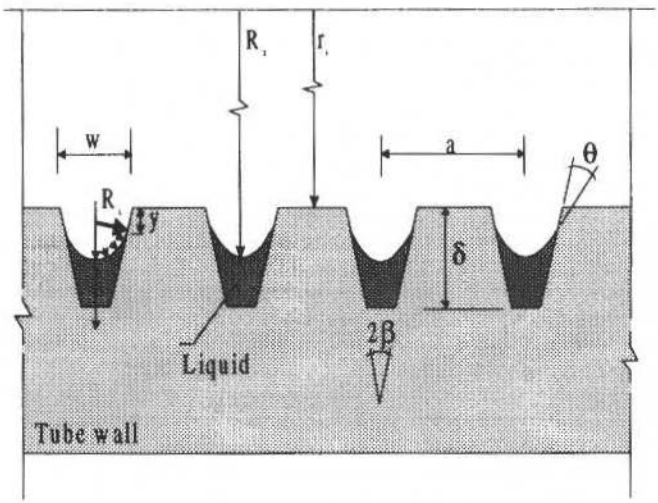

Fig. 2 Cross-section of the grooved wall.

According to the scheme of Fig. 2, w is the groove width, δ is the groove depth, 2β is the groove opening angle, a is the groove pitch, r_i is the internal radius of the tube, R_1 is the smaller meniscus radius and θ is the contact angle. The second meniscus R_2 is relatively large and its influence is neglected in this study ($R_2 > r_i >> R_1$). To measure the parameters of the capillary structure, several samples were prepared in the laboratory, cutting the capillary pumps after the tests.

A microphotograph related to one sample is shown in Fig. 3, where one sees in cross-section the aluminum tube. It was found that the groove structure of the capillary pump is not uniform. According to the microphotograph analysis of 10 samples from 5 different capillary pumps, the following parameters were measured as average values:

- $w = 33.0 \pm 6.7$ μm
- $\delta = 309.7 \pm 59.2$ μm
- $a = 214.7 \pm 9.7$ μm
- $\beta = 0.57 \pm 0.4$ degree

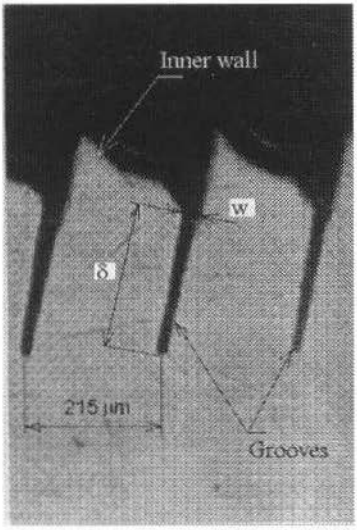

Fig. 3 Microphotograph of the grooved wall.

Theoretical Analysis

A computer program was developed to observe the capillary pump behavior and to estimate the maximum heat transport capability of the CPL. A nonlinear equation system was derived accounting for the geometrical characteristics of the capillary pump. The maximum heat input is found when

$$p_{cm} - \Delta p_{cp} - \Delta p_{loop} = 0 \tag{1}$$

where p_{cm} is the maximum capillary pumping pressure, Δp_{cp} is the pressure drop inside the capillary pump and Δp_{loop} is the pressure drop along the loop. The maximum capillary pumping pressure is

$$p_{cm} = \frac{2\sigma}{r_c} \tag{2}$$

where σ is the surface tension of the working fluid and r_c is the effective capillary radius of the groove. The physical meaning and the corresponding values for r_c of some of the more common wicking structures can be found in the literature for heat pipes (see Faghri, 1995 or Peterson, 1994). For circumferential grooves,

$$r_c = 2\frac{\cos\beta}{1-\sin\beta}\left(\frac{w}{2} - \delta\tan\beta\right) \tag{3}$$

Equations (2) and (3) should be used if the circumferential grooves are the only connection between the liquid channel and vapor channel. That means, there is no gaps at the interface along the insert and the grooved wall. Existing gaps are strongly associated to the capillary action of the capillary pump. In reality, an effective capillary pumping pressure related to the gaps, so called p_{cmg}, must be also calculate, or even measured in the laboratory. The larger the gaps, the smaller p_{cmg}. It is expected that the system works only while $p_{cmg} > \Delta p_{loop}$.

The term Δp_{loop} is easily calculated applying existing correlations available in the literature of fluid mechanics. On the other hand, to calculate Δp_{cp}, one should consider the changes of the mass flow rate, m, liquid velocity, v, liquid cross section, A, meniscus contact angle, θ, meniscus radius, R_l and the meniscus position from the inner surface of the tube, y, along a groove length of the capillary pump (see Fig. 4). The pressure drop along the liquid channel and vapor channels is relatively small and can be neglected. The pressure drop along one single groove of the capillary pump is calculated taking into account the geometrical characteristics of the capillary structure and the momentum equation,

$$\frac{d}{d\psi}(p_l A) = -\rho_l g r_i \cos\psi A - 4f\frac{r_i}{d_h}\frac{\rho_l v^2}{2}A - \frac{1}{2}\frac{d}{d\psi}\left(\frac{\rho_l v^2}{2}A\right) \tag{4}$$

subjected to the following boundary condition

$$p_{ll} = p_l\left(\psi = -\frac{\pi}{6}\right) = p_v - \Delta p_{loop} \tag{5}$$

where p_v is assumed to be equal to the saturation pressure as a function of the loop operation temperature, set through the reservoir. In Figure 4, p_v is the vapor pressure inside the capillary pump and $p_l(\psi)$ is the liquid pressure along the groove as a function of the angle ψ (see also Fig. 5). Concerning the right hand side of Eq. 4, the first term represents the gravity effect, the second term represents the viscous forces, and the third term represents the inertial effects. The third term is relatively small and can be neglected.

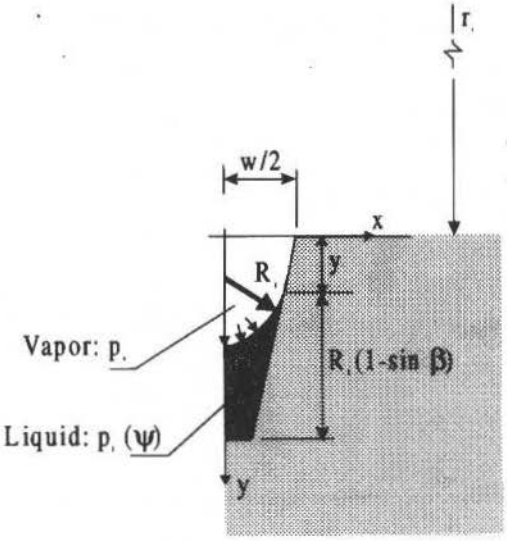

Fig. 4 Cross-section of one half groove and its geometrical characteristics.

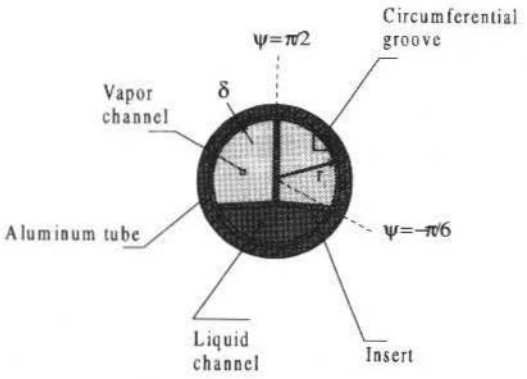

Fig. 5 Cross-section of the capillary pump.

The problem is easily solved dividing the groove in n equal elements (i = 1,2,...,n), making $\Delta p_{cp} = \sum \Delta p_i$ so that all these variables can be considered constant along every element, without significant effects on the evaluation of the pressure drop. Thus, neglecting the inertial effects, one finds:

$$\Delta p_{cp} = \sum \left(\rho_l g r_i \phi_{1i} + 4 f_i \frac{r_i}{d_{hi}} \frac{\rho_l \bar{v}_i^2}{2} \phi_{2i} \right) \tag{6}$$

where

$$\bar{v}_i = \frac{1}{2\rho_l A_i} \left(\frac{L}{a} \int_{\psi_0}^{\frac{\pi}{2}} d\psi \right)^{-1} \frac{Qt}{\Delta h} \tag{7}$$

$$v_i = \bar{v}_i \left(\frac{\pi}{2} - \psi_i \right) \tag{8}$$

$$\phi_{1i} = \int_{\psi_i}^{\psi_{i+1}} \cos\psi \, d\psi \tag{9}$$

$$\phi_{2i} = \int_{\psi_i}^{\psi_{i+1}} \left(\frac{\pi}{2} - \psi \right)^2 d\psi \tag{10}$$

$$A_i = (\delta - y_i)[R_{1i} \cos(\beta + \theta_i) + \frac{w}{2} - \delta \tan\beta] - R_{1i}^2 [(\frac{\pi}{2} - \beta - \theta_i) - \frac{1}{2} \sin 2(\beta + \theta_i)] \tag{11}$$

$$R_{1i} = \frac{\sigma}{p_v - p_{li}} \tag{12}$$

$$d_{hi}=\frac{4A_i\cos\beta}{w\cos\beta+2(\delta-y_i-\sin\beta)} \tag{13}$$

$$y_i=\frac{2R_{li}\cos\beta-w}{r_c\cos\beta-w}\left[\delta(1+\sin\beta)-\frac{w}{2}\cos\beta\right] \tag{14}$$

$$\theta_i=arcos\left(\frac{w}{2R_{li}}\right)-\beta \tag{15}$$

where Q_l is the total heat input, ρ_l is the liquid density, g is the gravitational acceleration, f_i is the friction factor of the *ith* element, d_{hi} is the hydraulic diameter of the *ith* element and v_i is the liquid velocity of the *ith* element. Additional information about the mathematical model described here were reported for Bazzo (1996). At such conditions, for a desired heat input applied onto the capillary pump, assuming the above boundary condition, the problem is solved iteratively, step by step, for every element along the groove.

Despite the evident non-uniformity of the grooves, in this work the geometrical values obtained from the microphotograph analysis are used to estimate the maximum heat input capability and to determine the characteristic curve of the capillary pump. Freon 11 is assumed to be the working fluid at an operation temperature equal to 300 K. The characteristic curve of the capillary pump is plotted in Fig. 6. The influence of the groove width and the inner radius is shown in Figs. 7 and 8.

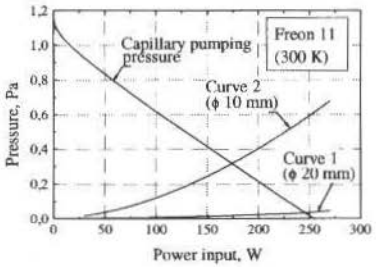

Fig. 6 Characteristic curves for the capillary pump. Comparison with pressure losses along the loop.

The pressure losses concerning two different pipes for the CPL are also plotted in Fig. 6, for a length of 10 m of liquid and vapor lines. Curve 1 is plotted taking into account obtained results for O. D. 20 mm. Curve 2 is plotted taking into account obtained results for O. D. 10 mm. The values found for Curve 1 are equivalent to the pressure losses found for the CPL set-up shown in Fig. 9. In case of curve 1, and according to the characteristic curve shown in Fig. 6, it is expected to find a power input of approximately 250 W as the maximum heat input to the transported by the CPL. In case of curve 2, this value falls to 170 W.

Despite their low capillary pumping pressure, circumferentially grooved capillary pumps could be also applied in large two-phase heat transfer loops. One could select liquid lines and vapor lines of larger diameters, once the increase in weight of the loop is not so high. So, the pressure losses to be overcome can be as small as desirable, or possible. In fact, there is no reason to dismiss circumferentially grooved capillary pumps as possible candidates in two-phase heat transport loops for space applications. However, special care about their manufacture must be taken. The manufacture of a circumferentially grooved capillary pump is not so easy as the manufacture of tubular porous material capillary pumps. Special tools are required to machine fine circumferential grooves along the inner surface of small tubes. Also, special care must be taken in fitting the insert inside the tube in order to avoid any damage or any gap at the interface with the grooved wall.

The influence of the inner radius over the capillary limit is shown in Fig. 7, for constant values of w, δ, β and *a*. It was also found that the maximum heat input decreases asymptotically with increasing inner radius of the capillary pump. The larger the radius, the smaller the capillary limit.

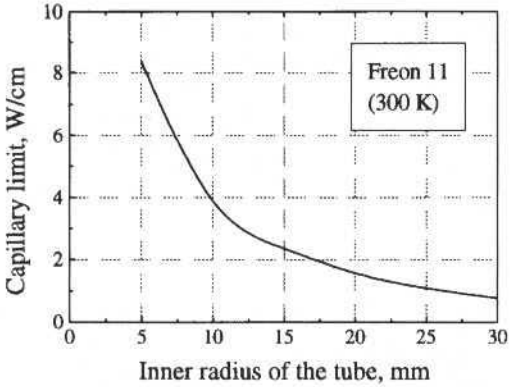

Fig. 7 Capillary limit as a function of the inner radius of the capillary pump.

The groove width and the groove opening angle also have a strong influence over the capillary limitation of the pump. The influence of the groove width is shown in Fig. 8 for two different values of groove opening angles (β = 0.57° and β = 3°). The value β = 0.57° represents the average groove opening angle of the capillary pumps tested in the laboratory. The remaining parameters related to δ, a and r were kept constant and also equal to the average values found from the microphotograph analysis. For β = 0.57°, one can see a maximum heat input of about 34 W/cm at groove width near to 130 μm. But it is also shown in Fig. 8 that the maximum capillary pumping pressure decreases steeply for higher values of groove widths. Therefore, it stands to reason that the best choice does not mean finding the point where the heat input is maximum. A small value for the groove width is preferable because of its higher capillary pumping pressure. So, by comparing the two curves, rectangular grooves (β = 0°) look better than trapezoidal grooves (β > 0°).

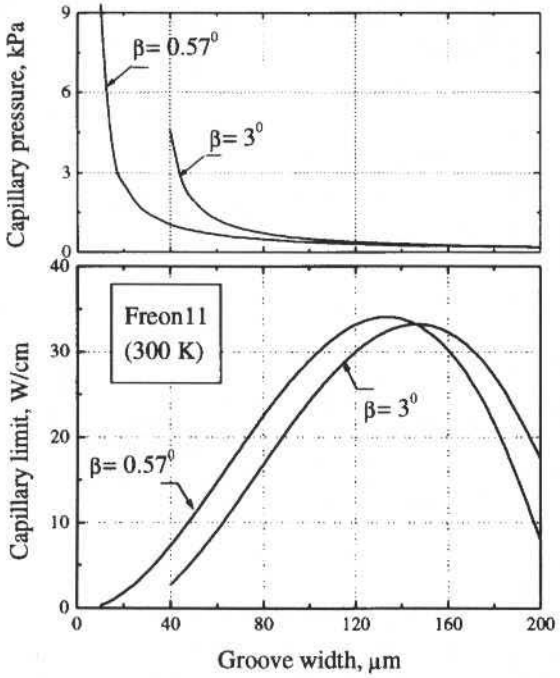

Fig. 8 Capillary limit as a function of the groove width and groove opening angle.

Due to its smaller effective capillary radius, one should expect higher capillary pumping pressure for a trapezoidal groove than for a rectangular groove. However, for high inputs applied to a CPL, trapezoidal grooves are not able to maintain the capillary pumping pressure as rectangular grooves. In fact, good performance is possible only for very small heat input applied onto the evaporator. It was demonstrated that the higher the β angle, the higher the influence of the loop pressure drop over the meniscus radius of the grooves (see Bazzo et al., 1994). So, it is possible to transport higher heat inputs and to overcome higher pressure losses with rectangular grooves. Anyway, to overcome any additional pressure drop during the startup, or even during the normal operation of the loop, one should make the option for capillary pumps with narrow grooves.

Experimental Set-up

All the tests were carried out at IKE (Institut für Kernenergetik und Energiesysteme) of the University of Stuttgart. The set-up consisted basically of one evaporator with seven capillary pumps, one condenser and one reservoir (see Fig. 9). All the capillary pumps have similar groove structure. The reservoir is used to control the liquid inventory in the loop. It was designed to contain enough liquid to ensure a good performance of the loop. A nearly blocked condenser section must occur when a minimum heat input is applied to the evaporator at the minimum condenser sink temperature. On the other hand, the condenser must be fully active when a maximum heat input is applied to the evaporator at the maximum condenser temperature.

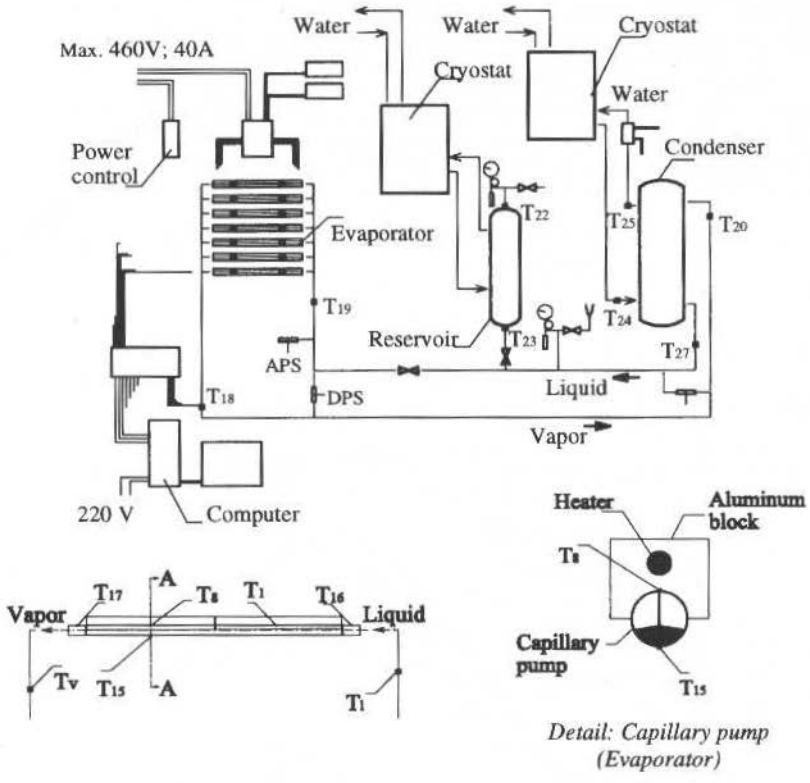

Fig. 9 Schematic of the CPL set-up.

The CPL was instrumented with 27 thermocouples, two differential pressure sensors (DPS), one absolute pressure sensor (APS), one digital voltmeter, one digital amperemeter and one water-cooling flowmeter. Two cryostats and one DC-power supply were used operate the CPL. A first cryostat was used to control the temperature of the reservoir. The second cryostat was used to remove heat from the

condenser. During the tests, the temperature and the pressure signals were measured and saved at every 3 seconds, by using a data acquisition system connected to a computer. Heat was supplied to each capillary pump through a pair of aluminum blocks with cartridge heaters (see detail on the right side of Fig. 9). T_1 and T_8 correspond to the thermocouples used to measure the outer surface temperatures of the capillary pump number 7. T_{15} represents the wall temperature of the liquid channel. T_{16} and T_{17} represents the inlet and outlet temperatures of the capillary pump. Finally, T_l and T_v correspond to the inlet and outlet temperatures of the evaporator.

Performance Testing

Various tests were performed in order to determine the performance of the loop. The tests comprised individual heating of each pump and uniform heating of two or more capillary pumps. The start-up, heat transport limits and repriming after dry out were investigated using Freon 11 as the working fluid. The reservoir temperature was fixed around 300 K. In Figure 10 one can see the temperature profiles obtained with individual heating of the capillary pump number 7, for stepwise increasing power inputs of 200, 260 and 280 W. After 300 minutes of operation, the system deprimed when the heat input was increased to 280 W. At this point, T_8 increased steeply and indicated no more capillary action in the grooves of the capillary pump. Individual tests carried out with all other capillary pumps also indicated heat transport capabilities about 280 W. For an effective internal heat transfer area of the capillary pump equal to 0.0166 m^2, the corresponding heat flux is calculated to be about 1.7 W/cm^2. For ammonia as working fluid, the equivalent value is estimated to be approximately equal to 11 W/cm^2 . As expected, uniform heating of two or more capillary pumps in parallel indicated higher values for the evaporator, but substantially lower values for each pump when compared with testing of individual capillary pumps. The higher the heat input, the higher the mass flow rate. In consequence, the higher is the pressure drop along the loop. As already discussed, the increase in pressure drop along the loop reduces the heat input capability of the capillary pump (see Fig. 6).

All star-up were successful. The thermal behavior of the start-up related to the capillary pump N° 7. is shown in Fig. 11. At the beginning, the whole loop was flooded by liquid. Then, after 33 minutes a power input of 200 W was applied to the capillary pump to start the system. In the next 10 minutes all temperature changed. A first and larger peak is observed in T_1, somewhat about 47°C, at least 15°C above the peak observed in T_v. Larger or smaller peaks are associated to the required forces to displace liquid back to the reservoir. That is, the corresponding saturation pressure must be sufficient to partially displace the cold liquid from the vapor channel and vapor line, through the condenser, and back to the reservoir. Smaller peaks are expected in the cases of smaller volumes of liquid inside the vapor channels of the capillary pump.

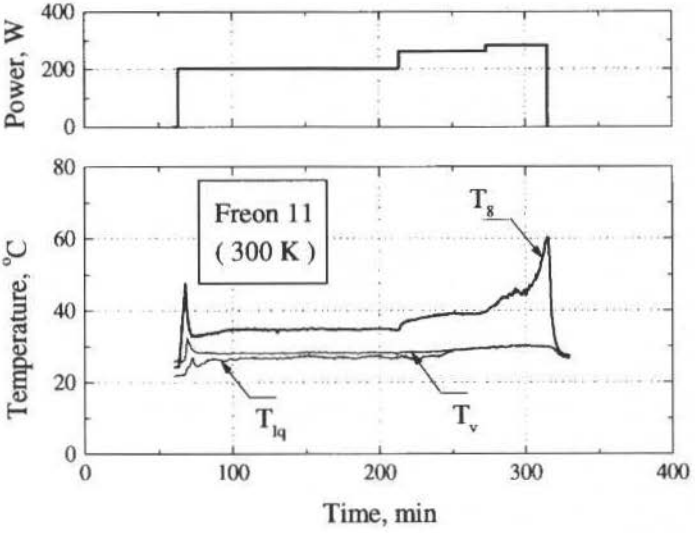

Fig. 10 Thermal behavior of the capillary pump number 7.

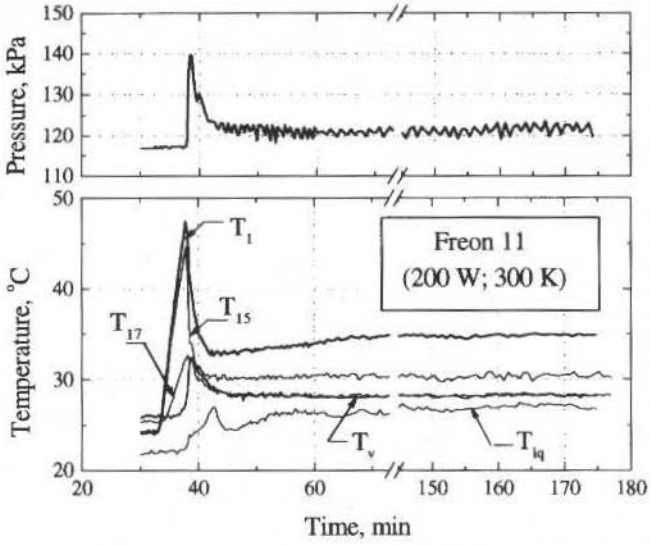

Fig. 11 Start-up of the capillary pump Nº 7 (200 W).

As can be seen in Fig. 11, the internal pressure is not constant. It is observed a substantial increase in the internal pressure at the moment when T_1 is maximum. The internal pressure was measured by means an absolute pressure sensor (APS) installed before the evaporator (see Fig. 9). At steady state condition, is has been observed that the corresponding values of the saturation temperature are approximately equal to T_v. The pressure oscillations observed after the start-up are frequently observed in two-phase systems. Further investigations are still required to better understand these oscillations. After the peak in the pressure, one sees that T_1 falls to a minimum and then increase again, slightly to reach the steady state condition. This indicates that cold liquid from the liquid lines is being pumped by capillary action along the grooved wall. During the start-up, the temperature T_1 and T_8 are approximately the same, which means a uniform behaviour of the capillary pump.

A strong increase in T_{15}, the wall temperature of the liquid channel, is also observed. Although undesirable, the increase in T_{15} is inevitable because of the high thermal conductivity of the aluminum tube. Also, at steady state condition, T_{15} has the tendency to be higher than T_v. In consequence, it is reasonable to suppose that there also is evaporation inside the liquid channel. Nevertheless, existing vapor bubbles in the liquid channel may be a minor problem, because these tubes bubbles tend to recondense in the sub-cooled liquid that flows from the condenser section. The relatively sharp angle between the insert and the grooved wall provides a continuous evaporator feeding, even in presence of the vapor bubbles. In fact, it was observed that the loop still worked, even in case of liquid inlet temperature, T_{lq}, equal to the vapor outlet temperature, T_v.

Other start-ups at lower or higher heat input levels were also successful, but always for condenser elevations slightly above the evaporator section. In this work, loop operations with the condenser position below the evaporator section were not possible because of the existing gaps between the insert and the grooved wall of the capillary pumps. In Figure 3 is shown a microphotograph of the capillary structure, where it is clear that the surface wall is not smooth. As a consequence, there are gaps between the insert and the surface wall connecting the vapor channels to the liquid channel of the capillary pump. In fact, according to the measurements, differential pressures of about 200 Pa across the evaporator were sufficient to lead the system to dry out. Improvements in the capillary pumps are still in course in order to minimize this problem. Since all external pressure drops could be compensated by an adjustable vertical condenser position, the performance limits of the capillary pumps were evaluated approximately at zero available capillary pumping pressure (see Fig. 6). A comparison between predicted and measured values is shown in Fig. 12, where good agreement is observed. The solid line represents the theoretical values and the dark symbols represent the measured values. The theoretical values were found taking into account the mathematical model presented here and the average values obtained from the microphotograph analysis of the capillary structure. The two dotted lined represent

the uncertainty range of the predicted values. The measured values of power input were plotted considering the corresponding average groove width for each capillary pump.

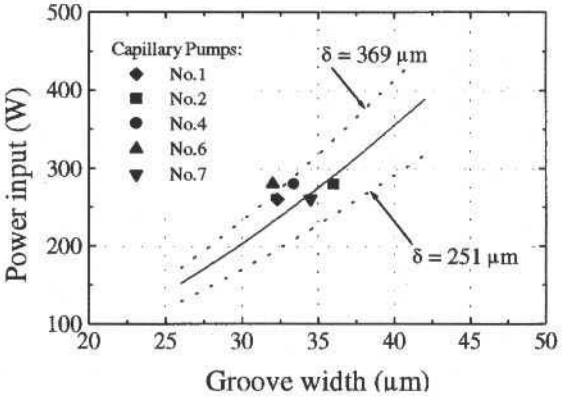

Fig. 12 Comparison between predicted and measured values.

Finally, from the experimental results, the following points have been observed:

- The loop temperature was successfully controlled by the reservoir. The vapor temperature was maintained approximately constant under changing evaporator heat inputs and even under changing sink temperature, by compensating the liquid inventory in the loop.
- The loop was able to recover from a depriming without the need to turn the equipment off. There was no need either to inject subcooled liquid into the evaporator. By reducing the heat input by about 20% from its maximum heat input capability, is was found that it is possible to restart the loop and resume steady state operation.
- The loop was able to work even in case of liquid inlet temperature equal to the vapor outlet temperature. Heat transfer occurs also in the liquid channel. Vapor bubbles may form in the liquid channel. But it was not considered a great problem because these bubbles tend to recondense in the presence of the subcooled liquid that comes from the condenser section. Also, the relatively sharp angle between the insert and the grooved wall may provide a continuous evaporator feeding, even in presence of vapor bubbles. Anyway, further studies are recommended to minimize this problem.
- The capillary pumps were unable to suck cold fluid from the liquid line for differential pressures between the evaporator inlet and outlet above 200 Pa. After the tests, existing gaps were detected between the insert and the grooved wall of the capillary pump. The existing gaps are associated with a very weak capillary action. To minimize this problem, special care must be taken during the manufacture of the capillary pump.
- Higher heat inputs were possible for operation of capillary pumps in parallel. In that case, the increase in mass flow rate leads to an increase of the liquid velocity and vapor along the loop. Also, more subcooled liquid was displaced from the condenser to the reservoir. Thus, the liquid level in the condenser was reduced and the total pressure drop along the loop was no longer compensated. So, the maximum heat input for each capillary pump was found to be smaller than that obtained from testing of an individual capillary pump.

Conclusions

Theoretical and experimental results have demonstrated that the CPL is able to achieve high heat transport capabilities. Using Freon 11 as the working fluid, heat fluxes up to 1.7 W/cm^2 have been

measured for an effective internal heat transfer surface of the capillary pump equal to 0.0166 m^2. The several ground tests performed up to now have demonstrated success in startup and success in repriming a capillary pump in case of dry-out. As expected, the best performance of the capillary pump is obtained using small values of groove width and small values of the tube inner radius. Theoretical results have demonstrated somewhat better performance for rectangular grooves than trapezoidal grooves. Capillary pumping pressures up to 1500 kPa are expected for groove widths of about 30 μm and groove opening angle of about 1°. Further experimental work is still needed to establish this point. Special care related to the manufacturing of the capillary pump and its corresponding pumping capacity has to be taken.

Acknowledgments

The authors would like to acknowledge the financial support received from KFA-Forschungszentrum Jülich, ERNO Raumfahrtechnik GmbH from Germany and CNPq-Conselho Nacional de Desenvolvimento Científico e Tecnológico from Brazil.

References

Bazzo, E., Groll, M., Brost, O. y Colle, S., 1994. "Hydrodynamic Analysis and Capillary Limitation of Circumferentially Grooved Heat Pipe Evaporators". Proceedings of 4th International Heat Pipe Symposium, Tsukuba, Japan, pp. 77-84.

Bazzo, E., 1996. "Theoretical and Experimental Investigation on Capillary Pumped Loops" (in Portuguese), Ph. D. Thesis, Federal University of Santa Catarina, Florianópolis, SC, Brazil.

Bazzo, E., Colle, S., Groll, M. y Brost, O., 1997. "Capillary Pumps Applied to two-phase Heat Transfer Loops" (in Spanish). Información Tecnológica, Vol. 8 N° 4, pp. 355-364.

Delil, A. A. M., Dubois, M. and Supper, W., 1997. "In-orbit Demonstration of Two-phase Heat Transport Technology: TPX/II: Ready for Launch", 27th International Conference on Environmental System, Technical Paper 972479, Lake Tahoe, Nevada.

Dubois, M., Mullender, B. and Supper, W., 1997, "Space Qualification Results of High Capacity Grooved Heat Pipes". Proceedings of 27th International Conference on Environmental Systems, Lake Tahoe, USA, Paper 972453.

Faghri, A., 1995. "Heat Pipe Science and Technology", Taylor & Francis, Washington, USA, 874p.

Goncharov, K. A., Nikitkin, M. N., Golovin, O. A., Fershtater, Yu. G., Maidanik, Yu. F. and Piukov, S. A., 1995. "Loop Heat Pipes in Thermal Control Systems for OBZOR Spacecraft". Proceedings of 25th International Conference on Environmental Systems, San Diego, USA, Paper 951555.

Hoang, T., 1997. "Development of an Advanced Capillary Pumped Loop". Proceedings of 27th International Conference on Environmental Systems, Lake, Tahoe, USA, Paper 972325.

Ku, J., 1993. "Overview of Capillary Pumped Loop Technology". ASME 29th National Heat Transfer Conference, Atlanta, USA, HTD-Vol. 236.

Maidanik, Yu. F., Fershtater, Yu. G. and Vershinin, S. V., 1997. "Heat Transfer Enhancement in a Loop Heat Pipe Evaporator". Preprints of 10th International Heat Pipe Conference, Stuttgart, Germany.

Peterson, G. P., 1994. "An Introduction to Heat Pipes", John Wiley & Sons, New York, USA, 356p.

Schlitt, R., 1995. "Performance Characteristics of Recently Developed High-Performance Heat Pipes". Heat Transfer Engineering, Vol. 16, N° 1, pp. 44-52.

RBCM - J. of the Braz. Soc. Mechanical Sciences
Vol. XXI - No.1 - 1999 - pp. 29-40

ISSN 0100-7386
Printed in Brazil

Finite Element Approximation for the Heat Transfer in Incompressible Oldroyd-B Flows

Sérgio Frey
Universidade Federal do Rio Grande do Sul
Departamento de Engenharia Mecânica
90050-170 Porto Alegre, RS Brazil
frey@mecanica.ufrgs.br

José Henrique Carneiro de Araujo
Universidade Federal Fluminense
Departamento de Ciência da Computação
24210-000 Niterói, RJ Brazil
jhca@dcc.uff.br

Marco Antônio M. Silva Ramos
Universidade Federal Fluminense
Departamento de Ciência da Computação
24210-000 Niterói, RJ Brazil
marco@dcc.uff.br

Abstract

The main purpose of this article is the numerical simulation of the heat transfer in an incompressible viscoelastic flow via a stable finite element method. The chosen nonlinear model was the differential Oldroyd-B *liquid with constant viscoelastic properties. The proposed numerical scheme is based upon a four-field finite element formulation whose main features are the optimal representation of the stress tensor in the Stokes context and the use of upwind strategies in order to stabilize both stress and temperature fields in advective-dominated situations. Some two-dimensional simulations illustrate the stable and accurate performance of the finite element method employed.*
Keywords: *Viscoelastic Flows, Heat Convection, Finite Elements, Bubble Functions, Stabilized Methods.*

Introduction

A characteristic of some solids is that they respond to external stress by deforming and returning to their original shape when external solicitation vanishes - such kind of response is called *elastic*. Under the influence of deformation, stretching of intermolecular bonds occurs in the solid material and the resulting internal stress balances the external stress; thus, an equilibrium deformation is established. In the simplest case there is a direct proportionality between the stress and the deformation. The rheological properties of such a material may be described by *Hooke's law* (Billigton et al., 1981). There are also elastic materials, however, which do not obey Hooke's law and which exhibit a non-linear dependence between stress and deformation.

A characteristic of fluids is that, if an external stress is applied, they deform and continue to deform as long as the shear stress is present. Moreover, removal of the stress will not result in a return of the fluid to the undeformed state - such a response is called *viscous*. The fluid deforms under an stress, however small, because of the great mobility of molecules, but internal frictional forces retard the rate of deformation and cause an *equilibrium* state, in which a constant external stress results in a constant rate of deformation. In the simplest case there is a proportionality between the stress and the rate of deformation. The rheological properties of such a fluid may be described by *Newton's law* (Billigton et al., 1981). There also are the so-called viscous fluids, however, which do not obey Newton's law and exhibit a non-linear dependence between stress and rate of deformation. We call such fluids non-Newtonian (Bird et al. 1987), *pure viscous* fluids - as in the *power-law* and *Carreau* rheological models (Baranger et al., 1996).

Viscoelastic Behavior

The elastic and viscous behavior represent two extremes of response to external stress between which there can be an infinite number of intermediate ones. An especially important field of research of modern rheology, however, is concerned with more complex materials which exhibit some elastic and viscous simultaneously and are called *viscoelastic* substances (Bird et al. 1987). Strictly speaking, these substances may be either viscoelastic solids - i.e. elastic solids which during deformation exhibit some

Manuscript received: July 1997: revision received: February 1998. Technical Editor: Angela Ourívio Nieckele.

viscous effects resulting from energy dissipation - or elasticoviscous fluids - viscous fluids which exhibit some elastic effects - giving rise to more complex phenomena such as non-null normal stresses and recoil (Bird et al. 1987). As classical examples of viscoelastic fluids, we can cite the *Maxwell* and *Oldroyd* liquids (Baranger et al., 1996) and, as their industrial applications, we can mention some oils, paints, polymeric solutions under engineering flow processes such as mechanical extrusion.

Numerical Approximation

Numerical simulations of incompressible viscoelastic flows (Karan Filho et al., 1996, Soares et al., 1997) suffer from two major difficulties. Initially, the need of satisfying two mathematical *inf-sup* conditions: one relating stress and velocity finite subspaces and the well-known Babuska-Brezzi condition involving pressure and velocity subspaces (Babuska, 1973 and Brezzi, 1974 and Ruas et al., 1993). As a second shortcoming, we shall yet consider the instability inherent to Galerkin formulations in the presence of high advective situations (Brooks et al., 1982), when flows are subjected to very high Péclet and Reynolds numbers.

In the present work, stable finite element simulations of thermal incompressible viscoelastic flows have been performed. The adopted mechanical model was an *Oldroyd-B* liquid with constant viscoelastic properties. This kind of fluid is characterized by three parameters, namely a relaxation time of stress, a retardation time of strain and a fluid dynamic viscosity (Baranger et al., 1996). The finite element method employed consists of a four-field bubble formulation in terms of extra-stress, velocity, pressure and temperature, whose main characteristic is the optimal stable representation of the extra-stress tensor in the linear context of the Stokes problem (Ruas et al., 1992 and Ruas et al., 1993 and Silva Ramos et al., 1997). In order to generate stable finite element approximations even for high advective situations, the method uses a non-consistent streamline upwind scheme (Brooks et al., 1982 and Marchal et al., 1987) to approximate the advective term of the stress constitutive law and a Galerkin/least-squares philosophy (Hughes et al., 1987 and Hughes et al., 1986 and Macedo et al., 1997 and Sampaio, 1991) for the temperature convection in the energy equation. The non linear system associated was solved by an incremental Newton's method (Silva Ramos, 1993). Some two-dimensional computational experimentation of thermal incompressible flows of an *Oldroyd-B* liquid illustrate the good performance of the numerical procedure employed.

Preliminaries and Some Notation

The problems considered herein are defined on a bounded domain $\Omega \subset R^2$, with a boundary Γ,

$$\begin{cases} \Gamma = \overline{\Gamma}_g \cup \overline{\Gamma}_h, \\ \Gamma_g \cap \Gamma_h = \phi, \Gamma_g \neq 0 \end{cases} \tag{1}$$

where Γ_g is the region of the boundary Γ on which essential (Dirichlet) conditions are imposed and Γ_h is subjected to the natural (Neumman) ones. A partition C_h of $\overline{\Omega}$ into elements consisting of convex quadrilaterals is performed in the usual way (Ciarlet, 1978),

$$\begin{cases} \overline{\Omega} = \bigcup_{K \in C_h} \overline{\Omega}_K \\ \Omega_{K_1} \cap \Omega_{K_2} = \phi, \ \forall K_1, K_2 \in C_h \end{cases} \tag{2}$$

In what follows $L^2(\Omega)$ stands for the space of square-integrable functions in Ω, $L^2_0(\Omega)$ is the space of square-integrable functions with zero mean-value in Ω, $H^1(\Omega)$ is the Sobolev space of functions with square-integrable value and 1st derivatives in Ω,

$$L^2(\Omega) = \{ q \mid \int_\Omega q^2 \, d\Omega < \infty \}, \tag{3}$$

$$L_0^2(\Omega)=\{q\in L^2(\Omega)\,|\int_\Omega q\,d\Omega=0\}, \tag{4}$$

$$H^1(\Omega)=\{v\in L^2(\Omega)\,|\frac{\partial v}{\partial x_i}\in L^2(\Omega),\ for\ i=1,2\}, \tag{5}$$

Finally, $(\cdot,\cdot)$ denotes the L^2-inner product in Ω and $(\cdot,\cdot)_K$ the L^2-inner product in the element domain K.

Conservative Principles

The wide scope and great success of variational principles in classical dynamics have stimulated many efforts to formulate the laws of continuum mechanics in a similar way. The variational principle appropriate to a given dissipative system is little more than a reformulation of the equations of motion; it may, however, provide methods for handling constraints otherwise beyond the scope of the original equations. In the particular case of fluid dynamics, the *Virtual Power Principle* (VPP) establishes an alternative way to enunciate Euler axioms for momentum conservation in fluids. This major principle may be summarized as: *the expended power on a fluid volume Ω by the surface and body forces is equal to the rate of change of its kinetic energy plus the stress power* (Gurtin, 1981).

Let $\boldsymbol{v}$ be a virtual velocity of the fluid particles from their instantaneous position. The vector function $\boldsymbol{v}$ is assumed to be finite valued and continuously differentiable; moreover, it should conform to any restriction placed on the fluid position. Then, the VPP may be mathematically expressed by the following theorem,

Theorem (VPP) Let $(\boldsymbol{t},\boldsymbol{f})$ be a system of forces in a flow $(\boldsymbol{v},\rho,\boldsymbol{T})$, with $\boldsymbol{t}$ denoting the surface force density, $\boldsymbol{f}$ the body force per mass unit, $\mathbf{T}$ the symmetric Cauchy tensor and ρ the fluid density. Then a necessary and sufficient condition that the mechanical conservation in the fluid be satisfied is that given any fluid volume Ω and time instant t,

$$\int_\Gamma t(n)\cdot v\,d\Gamma+\int_\Omega \rho f\cdot v\,d\Omega=\int_\Omega T\cdot\varepsilon(v)\,d\Omega+\frac{d}{dt}\int_\Omega \rho\frac{v\cdot v}{2}d\Omega \tag{6}$$

with $\boldsymbol{n}$ standing for the outward normal vector to Γ and $\varepsilon(v)$ the symmetric part of the gradient of velocity tensor,

$$\varepsilon(v)=\frac{1}{2}(\nabla v+\nabla v^T) \tag{7}$$

(The theorem proof can be found, for instance, in (Gurtin, 1981) or (Truesdell et al., 1960).)

Remarks:

1. We can extract the equation of motion from VPP integrating-by-parts Eq. (6), exploiting the symmetry of the stress tensor $\mathbf{T}$ and employing Reynolds and divergence theorems (Billigton et al., 1981),

$$\int_\Omega[\rho\frac{Dv}{Dt}-\nabla\cdot T-\rho f]\cdot v\,d\Omega+\int_\Gamma[Tn-t(n)]\cdot v\,d\Gamma=0 \tag{7}$$

where the symbol D/Dt stands for the material derivative of a vector field (Gurtin, 1981). Now, applying Cauchy (Truesdell et al., 1960) and localization (Gurtin, 1981) theorems, we will achieve the *differential equation of conservation of the mechanical energy*,

$$\rho\frac{Dv}{Dt}=\nabla\cdot T+\rho f \tag{8}$$

2. The alternative way of VPP to postulate the conservation of mechanical energy has the great virtue of integrating the kinematics and dynamics of fluid motion. In the VPP, the concept of forces naturally emerges from the power expended by virtual velocities. According to (Sampaio, 1985), we may consider the space of all forces acting on the fluid as the dual space of virtual velocities. From the numerical point-of-view, the VPP carries the advantage of formulating mechanical problems in a variational context, introducing in a natural way variational methods in Mechanics, in particular the finite element method.

First Law of Thermodynamics

Energy can have many different forms such as nuclear, potential and thermal. As these forms can all be converted from one into other, it is desirable to have a balance equation to include all forms of energy. Such an equation, which is taken as a fundamental postulate, is called the 1st Law of Thermodynamics, which takes the form

$$\frac{d}{dt}K(\Omega)+\frac{d}{dt}U(\Omega)=H(\Omega)+P(\Omega) \tag{9}$$

where $K(\Omega)$ is the kinetic energy of the fluid volume Ω, $U(\Omega)$ its internal energy, $H(\Omega)$ the rate at which thermal energy is transferred to Ω and

$$P(\Omega)=\int_{\Gamma} t(n)\cdot v\,d\Gamma+\int_{\Omega}\rho f\cdot v\,d\Omega \tag{10}$$

is the rate that work is being done on Ω, i.e., the mechanical power $P(\Omega)$. From VPP (Eq. (6)), we have that the kinetic energy $K(\Omega)$ may be expressed by

$$\frac{d}{dt}K(\Omega)=P(\Omega)-\int_{\Omega}T\cdot\varepsilon(v)\,d\Omega \tag{11}$$

Then, substituting Eq. (11) into Eq. (9), we will obtain the so-called *equation of conservation of thermal energy*,

$$\frac{d}{dt}U(\Omega)=H(\Omega)+\int_{\Omega}T\cdot\varepsilon(v)\,d\Omega \tag{12}$$

Using that the internal energy $U(\Omega)$ is an additive set function (Billigton et al., 1981) like mass (i.e., that exists a scalar field ε such that $U(\Omega)=\int_{\Omega}\rho\varepsilon\,d\Omega$) and applying Reynolds theorem (Truesdell et al., 1960), we may write Eq. (12) as

$$\int_{\Omega}\rho\frac{D\varepsilon}{Dt}d\Omega=\int_{\Omega}\rho r\,d\Omega+\int_{\Gamma}h\,d\Gamma+\int_{\Omega}T\in(v)\,d\Omega \tag{13}$$

where r denotes a heat source per mass unit and h the heat flux on the boundary Γ. Now, supposing the existence of a heat flux vector $\boldsymbol{q}$ such that $h = \boldsymbol{q}\cdot\boldsymbol{n}$ (similar to concept of the stress vector $t(n)$ (Truesdell et al., 1960)), we will have

$$\int_{\Omega}\left[\rho\frac{D\varepsilon}{Dt}-\rho r-T\cdot\varepsilon(v)\right]d\Omega-\int_{\Gamma}q\cdot n\,d\Gamma=0 \tag{14}$$

with $\boldsymbol{q}$ directed opposite to the heat flux. Then, using the divergence (Billigton et al., 1981) and localization (Gurtin, 1981) theorems, we eventually achieved the *differential equation of the conservation of thermal energy*,

$$\rho\frac{D\varepsilon}{Dt}=\nabla\cdot q+\rho r+T\cdot\varepsilon(v) \tag{15}$$

Constitutive Hypothesis

For a given fluid there must exist some relation between the dynamical and kinematical states of the fluid at some instant and possibly the kinematical state of the fluid at all instants of the fluid's past history. The equations which express the relation between the kinematical and dynamical variables are called *constitutive equations*. Continuum physics is concerned with establishing the equation of state for a given material and with showing how values can be assigned to the material coefficients appearing in the equation of state. In general, these coefficients are functions of thermodynamic variables such as pressure or temperature, and therefore the constitutive equation of a fluid is influenced by its thermodynamic state.

Assuming in Eqs. (8) and (15) steady state and low Reynolds regime, the system describing an incompressible viscoelastic thermal flow may be written as,

$$\begin{aligned} -\nabla\cdot\sigma+\nabla p&=f\\ \nabla\cdot v&=0\\ \rho c(v\cdot\nabla\theta)+\nabla\cdot q&=r \end{aligned} \tag{16}$$

where v, f, p, ρ, q and r are defined as above, σ is the extra-stress tensor, θ the temperature field and c the specific heat. This system shall be yet supplemented with constitutive laws relating σ to v and q to θ.

Viscoelastic Models

Differential constitutive models for viscoelastic fluids are capable of describing most of the sophisticated mechanical behaviors of non-newtonian fluids. These models may be accommodated into the following set of constitutive equations,

$$\begin{aligned} \sigma&=\sigma_1+\sigma_2,\\ \sigma_2&=2\eta_2\varepsilon(v),\\ \sigma_1+\lambda\frac{D_a}{Dt}\sigma_1+\beta(\varepsilon(v),\sigma_1)&=2\eta_1\varepsilon(v) \end{aligned} \tag{17}$$

with σ, v and $\varepsilon(v)$ defined as above, η_1, η_2 are fluid viscosities, λ a relaxation time, $\beta(\varepsilon(v), \sigma_1)$ is a tensor function submitted to restrictions due to objectivity (Baranger et al., 1996), D_a/Dt an objective derivative of a symmetric tensor (Marchal et al., 1987),

$$\frac{D_a}{Dt}(\cdot)=\frac{\partial}{\partial t}(\cdot)+(v\cdot\nabla)(\cdot)+(\cdot)W(v)-W(v)(\cdot)-a(\varepsilon(v)(\cdot)+(\cdot)\varepsilon(v)) \tag{18}$$

with the parameter $-1\le a\le 1$ and $W(v)$ is the anti-symmetric vorticity tensor,

$$W(v)=\frac{1}{2}(\nabla v-\nabla v^T)$$

Remark:
The tensor σ_2 corresponds to a Newtonian contribution or to a fast relaxation mode; models with $\eta_2 = 0$ will be called *of Maxwell type*, those with $\eta_2 > 0$ will be called *of Jeffreys type*.

Taking advantage of a wise selection of the β-functions, most of all viscoelastic differential models can be written in the form of system (17). Following (Baranger et al., 1996), taking, for instance, $\beta = 0$ in Eq. (17) we will obtain a version of an *Oldroyd* fluid; in addition, if $\eta_2 = 0$, the parameter a = -1, 0, and 1 correspond, respectively, to the lower-convected, Jaumann and upper-convected *Maxwell* models. On the other hand, if we select in Eq. (17),

$$\beta(\varepsilon(v),\sigma)=2tr(\sigma\varepsilon(v))\alpha(tr\sigma)(\sigma+I);\ a=1$$

we will get the *Larson* models, with $\alpha(tr\sigma)$ representing a scalar function of $tr\sigma$. Finally, choosing in Eq. (17) $\beta = 0$ and λ, η_1 being functions of the second invariant of $\varepsilon(v)$, $II_{\varepsilon(v)}$, we will have the *White-Metzner* models. In particular, $\eta_1=\eta_0\{1+(\lambda_0 II_{\varepsilon(v)})^{2\alpha}\}^{\frac{n-1}{2\alpha}}$, n > 0 corresponds to the classical *Carreau law*.

In the present article, we have selected an *Oldroyd-B* fluid whose constitutive law may be constructed from Eqs. (17) and (18) taking $\beta = 0$ and a = 1,

$$\begin{aligned}
&\sigma=\sigma_1+\sigma_2,\\
&\sigma_2=2\eta_2\varepsilon(v),\\
&\sigma_1+\lambda[v\cdot\nabla\sigma_1-\nabla u\sigma_1-\sigma_1\nabla u^T]=2\eta_1\varepsilon(v)
\end{aligned} \tag{19}$$

In addition, in order to characterize the thermal behavior of the fluid, we must still impose the Fourier constitutive law on the heat flux vector $\boldsymbol{q}$,

$$q=-\kappa\nabla\theta \tag{20}$$

with $k\nabla$ representing the classical thermal conductivity.

Finite element approximation

Employing constitutive relations defined by Eqs. (19) and (20) into conservation equations (8) and (15), respectively, we can state a boundary-value problem for thermal incompressible viscoelastic flows as follows,

$$\begin{aligned}
&-\nabla\cdot\sigma_1-2\eta_2\nabla\cdot\varepsilon(\boldsymbol{u})+\nabla p=\boldsymbol{f} \quad in\ \Omega\\
&\sigma_1+\lambda[(u\cdot\nabla)\sigma_1-\nabla u\sigma_1-\sigma_1\nabla u^T]-2\eta_1\varepsilon(\boldsymbol{u})=0 \quad in\ \Omega\\
&\nabla\cdot u=0 \quad in\ \Omega\\
&\rho c(\boldsymbol{u}\cdot\nabla\theta)-\kappa\Delta\theta=r \quad in\ \Omega\\
&\boldsymbol{u}=\boldsymbol{u}_g \quad on\ \Gamma_g\\
&\sigma_1=\sigma_g \quad on\ \Gamma_g^-\\
&\theta=\theta_g \quad on\ \Gamma_g\\
&[\sigma_1-pI+2\eta_2\varepsilon(u)]n=\sigma_h \quad on\ \Gamma_h\\
&\boldsymbol{q}\cdot\boldsymbol{n}=q_h \quad on\ \Gamma_h
\end{aligned} \tag{21}$$

where p, σ_1, $\varepsilon(v)$, $\boldsymbol{f}$, η_1, η_2, λ, κ, θ, ρ, c, r, $\boldsymbol{q}$, $\boldsymbol{n}$, Γ_g and Γ_h are described in the previous sections, $\boldsymbol{u}$ is the admissible velocity (i.e., a velocity field with the same regularity as the virtual velocity $\boldsymbol{v}$ satisfying the essential boundary condition $\boldsymbol{u} = \boldsymbol{u}_s$ *on* Γ_s) and boundary Γ_g^- is defined by

$$\Gamma_g^- = \{ x \in \Gamma_g ; \boldsymbol{n}(\boldsymbol{x}) \boldsymbol{u}_g(\boldsymbol{x}) < 0 \}$$

Remark:

One may set system (21) in dimensionless form by introducing the Deborah number De, which represents the viscoelastic nature of the flow (Bird et al. 1987) and the Péclet number Pe, which establish a relationship between advective and diffusive fluxes of thermal energy. These numbers can be expressed by

$$De = \lambda \left(\frac{\partial u_1}{\partial x_2} + \frac{\partial u_2}{\partial x_1} \right)\Bigg|_w \qquad \text{and} \qquad Pe = \frac{uL}{\kappa} \tag{22}$$

where λ, $\boldsymbol{u}$, κ are defined as above, u_i the cartesian i-compotent of velocity field, L a characteristic length for the thermal phenomenon and with the characteristic shear rate computed at a chosen wall boundary point.

A Stable Method

In this subsection we present a finite element method employing a four-field (σ_1, $\boldsymbol{u}$, p, θ) bubble formulation to approximate Eqs. (21). In a partition C_h of Ω defined by quadrilateral elements, velocity and temperature fields are approximated by continuous piecewise biquadratic elements and the pressure field by discontinuous piecewise linear ones. The extra-stress tensor is approximated by continuous piecewise isoparametric bilinear elements in direct sum with twelve bubble tensors in each element as defined in (Ruas et al., 1992 and Ruas et al., 1993).

The finite elements subspaces for extra-stress $\boldsymbol{\Sigma}_h$, velocity $\boldsymbol{V}_h$, pressure P_h and temperature W_h are defined by,

$$P_h = \{ q \in L_0^2(\Omega) | q_{|K} \in P_1(K), K \in C_h \} \tag{23}$$

$$W_h = \{ \phi \in H^1(\Omega) | \phi_{|K} \in Q_2(K), K \in C_h, \phi = 0 \quad on \, \Gamma_g \} \tag{24}$$

$$\boldsymbol{V_h} = \{ \boldsymbol{v} \in H^1(\Omega)^2 | \boldsymbol{v}_{|K} \in Q_2(K)^2, K \in C_h, \boldsymbol{v} = \boldsymbol{0} \quad on \, \Gamma_g \} \tag{25}$$

$$\sum_h = \{ \tau \in H^1(\Omega)^{2\times 2}, \tau_{ij} = \tau_{ji} | \tau_{|K} \in (Q_1(K) \oplus B(K))^{2\times 2}, K \in C_h, \tau = \boldsymbol{0} \quad on \, \Gamma_g^- \} \tag{26}$$

$$W_h^g = \{ \phi \in H^1(\Omega) | \phi_{|K} \in Q_2(K), K \in C_h, \phi = \theta_g \quad on \, \Gamma_g \} \tag{27}$$

$$\boldsymbol{V_h^g} = \{ \boldsymbol{v} \in H^1(\Omega)^2 | \boldsymbol{v}_{|K} \in Q_2(K)^2, K \in C_h, \boldsymbol{v} = \boldsymbol{u}_g \quad on \, \Gamma_g \} \tag{28}$$

$$\sum_h^g = \{ \tau \in H^1(\Omega)^{2\times 2}, \tau_{ij} = \tau_{ji} | \tau_{|K} \in (Q_1(K) \oplus B(K))^{2\times 2}, K \in C_h, \tau = \sigma_g \quad on \, \Gamma_g^- \} \tag{29}$$

where $Q_2(K)$ denotes the space of polynomials of degree two in each one of the independent variables on K, $P_1(K)$ the space of polynomials of degree one over K, $L^2(\Omega)$, $L^2_0(\Omega)$ and $H^1(\Omega)$ the functional spaces described by Eqs. (3)-(5) and $B(K)$ is a family of bubble tensors on K defined as: Let K be a quadrilateral and F_K be the bilinear mapping from a reference unit square $\hat{K} = [-1,1] \times [-1,1]$ in the reference plane $\hat{O}\hat{x}\hat{y}$ onto K. Defining $\hat{\phi}(\hat{x},\hat{y}) = (1-\hat{x}^2)(1-\hat{y}^2)/4$ (the bubble function of $\hat{K}$) the twelve tensors ξ_i are the reciprocal images through mapping F_K, of twelve tensors $\hat{\xi}_i$ defined in $\hat{K}$, where

$$\hat{\xi}_1=\begin{bmatrix}\hat{\varphi} & 0\\ 0 & -\hat{\varphi}\end{bmatrix};\quad \hat{\xi}_2=\begin{bmatrix}\hat{x}\hat{\varphi} & 0\\ 0 & -\hat{x}\hat{\varphi}\end{bmatrix};\quad \hat{\xi}_3=\begin{bmatrix}\hat{y}\hat{\varphi} & 0\\ 0 & -\hat{y}\hat{\varphi}\end{bmatrix};\quad \hat{\xi}_4=\begin{bmatrix}0 & \hat{\varphi}\\ \hat{\varphi} & 0\end{bmatrix}$$
$$\hat{\xi}_5=\begin{bmatrix}0 & \hat{x}\hat{\varphi}\\ \hat{x}\hat{\varphi} & 0\end{bmatrix};\quad \hat{\xi}_6=\begin{bmatrix}0 & \hat{y}\hat{\varphi}\\ \hat{y}\hat{\varphi} & 0\end{bmatrix};\quad \hat{\xi}_7=\begin{bmatrix}\hat{x}\hat{y}\hat{\varphi} & 0\\ 0 & 0\end{bmatrix};\quad \hat{\xi}_8=\begin{bmatrix}0 & \hat{x}\hat{y}\hat{\varphi}\\ \hat{x}\hat{y}\hat{\varphi} & 0\end{bmatrix} \tag{30}$$
$$\hat{\xi}_9=\begin{bmatrix}\hat{x}\hat{\varphi} & 0\\ 0 & \hat{x}\hat{\varphi}\end{bmatrix};\quad \hat{\xi}_{10}=\begin{bmatrix}0 & 0\\ 0 & \hat{x}\hat{y}\hat{\varphi}\end{bmatrix};\quad \hat{\xi}_{11}=\begin{bmatrix}\hat{y}^2\hat{\varphi} & 0\\ 0 & \hat{x}^2\hat{\varphi}\end{bmatrix};\quad \hat{\xi}_{12}=\begin{bmatrix}\hat{y}\hat{\varphi} & 0\\ 0 & \hat{y}\hat{\varphi}\end{bmatrix}$$

Based upon the approximated sets described by Eqs. (23)-(30), a stable finite element method to approximate system (21) can be written as: Find $(\sigma_{1h}, \boldsymbol{u}_h, p_h, \theta_h) \in \sum_h^{\boldsymbol{g}} \times V_h^{\boldsymbol{g}} \times P_h \times W_h^{g}$ such that

$$B(\sigma_{1h},\boldsymbol{u}_h,p_h,\theta_h;\tau,v,q,\phi) = F(\tau,v,q,\phi)\ \ \tau,v,q,\phi \in \sum_h \times V_h \times P_h \times W_h \tag{31}$$

with

$$\begin{aligned} B(\sigma_1,\boldsymbol{u},p,\theta;\tau,v,q,\phi) &= (\sigma_1,\varepsilon(v)) + (2\eta_2\varepsilon(\boldsymbol{u}),\varepsilon(v)) - (p,\nabla\cdot v) + (\nabla\cdot\boldsymbol{u},q)\\ &+ (\kappa\nabla\theta,\nabla\phi) + (\rho c(\boldsymbol{u}\cdot\nabla\theta),\phi) + (\sigma_1,\tau)\\ &+ (\lambda(\boldsymbol{u}\cdot\nabla)\sigma_1,\tau) - (\lambda\nabla\boldsymbol{u}\sigma_1,\tau) - (\lambda\sigma_1\nabla\boldsymbol{u}^T,\tau)\\ &- (2\eta_1\in(u),\tau) + \sum_{K\in C_h}(\rho c(\boldsymbol{u}\cdot\nabla\theta)\\ &- \kappa\Delta\theta,\alpha_\phi(\rho c(v\cdot\nabla\phi) - \kappa\Delta\phi))_K + (\lambda(\boldsymbol{u}\cdot\nabla)\sigma_1,\alpha_\tau(\boldsymbol{u}\cdot\nabla)\tau) \end{aligned} \tag{32}$$

and

$$F(\tau,v,q,\phi) = (f,v) + (\sigma_h,v)_{\Gamma_h} + (r,\phi) + (q_h,\phi)_{\Gamma_h} + \sum_{K\in C_h}(r,\alpha_\phi(\rho c(v\cdot\nabla\phi) - \kappa\Delta\phi))_K \tag{33}$$

where the stability parameters α_ϕ and α_τ are defined as follows:

$$\alpha_\tau = \frac{h_K}{2|\boldsymbol{u}(x)|_p} \tag{34}$$

$$\alpha_\phi = \frac{h_K}{2|\boldsymbol{u}(x)|_p}\xi(Pe_K(x)) \tag{35}$$

$$Pe_K(x) = \frac{m_\kappa|\boldsymbol{u}(x)|_p h_K}{2\kappa} \tag{36}$$

$$\xi=\begin{cases} Pe_K(x), 0 \le Pe_K(x) < 1 \\ 1 \quad , Pe_K(x) \ge 1 \end{cases} \tag{37}$$

$$|u(x)|_p = \begin{cases} \left(\sum_{i=1}^{N} |u_i(x)|^p \right)^{1/p} , 1 \le p < \infty \\ \max\limits_{i=1,N} |u_i(x)| \quad , p = \infty \end{cases} \tag{38}$$

in which m_k denoting a positive constant introduced in (Franca et al., 1992) dependent of the thermal finite element interpolation adopted.

Remarks

1. It is well known that the classical Galerkin method applied to hyperbolic equations results in spurious oscillations in the finite element approximation. In formulation (31)-(33), we have employed a non-consistent *streamline upwind* strategy (Marchal et al., 1987) to treat the advective term of the stress material law of system (21) and a *Galerkin/least-squares* one (Franca et al., 1992 and Franca et al.,1992) for the convective term of its energy equation.
2. The usual definition of the element Péclet number Pe_K was modified by including the constant m_k, which takes into account the effect of the degree of the interpolation used. This definition may be viewed as a rescaling of the usual element Péclet number, such that, for all interpolations employed, the locally advective dominated thermal flows are given by $Pe_K(x) > 1$ and the locally diffusive dominated thermal flows are given by $Pe_K(x) < 1$.

Numerical Results

In this section we present some two-dimensional simulations of the incompressible viscoelastic thermal problem defined by Eqs. (21), employing a stable finite element method introduced in Eqs. (31)-(33). All computations were performed in microcomputers equipped with the P200 Intel chip, using the finite element code FEM and graphics post-processor VIEW, both codes under development at the *Laboratory of Theoretical and Applied Mechanics* (LMTA) of the Universidade Federal Fluminense.

Flow Through an Abrupt Contraction Channel

The geometry and boundary conditions of the problem are sketched in Fig.1: the domain is a plane channel with a sudden 4:1 contraction. The boundary conditions for velocity and extra-stress tensor at the channel entrance are fully developed profiles and, at its exit, a fully developed profile was considered only for the velocity field - taking into account the mass conservation. For the temperature field, we have imposed at channel entrance a flat profile θ_1; upstream contraction, a greater constant value θ_2; and, after the contraction, a maximum value θ_3 was prescribed (These conditions intend to simulate the heating generated by a mechanical extrusion process.).

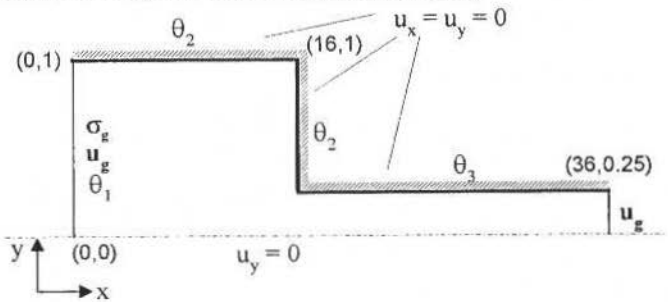

Fig. 1 Flow into a sudden contraction: Problem statement.

The computational domain Ω was discretized by a non-uniform mesh consisting of 472 quadrilateral elements with 4110 degrees-of-freedom for velocity, 2055 for temperature, 1416 for pressure and 7332 for the extra-stress tensor - see Fig.2 for a detail of the mesh near the contraction. In the numerical tests, we have selected a viscosity ratio $\eta_2 / (\eta_1 + \eta_2) = 0.11$ in the Eqs. (21) - as usual in Oldroyd-B simulations (Marchal et al., 1987 and Silva Ramos, 1993) - and the Deborah and Péclet numbers (Eq. (22)) were have measured at downstream fully developed region. The non-linear strategy to solve the set of non-linear equations resulting from the discretization of system (21) was an incremental Newton's method (Silva Ramos et al., 1997) with a continuation strategy on the stress relaxation time λ (Eq. 19). We used, for its first step, the velocity and pressure fields for the Stokes flow (taking $\lambda = 0$ in Eq. (21)) and employed as Newton's increment a Deborah number De equal to 1.0 (Eq. (22)).

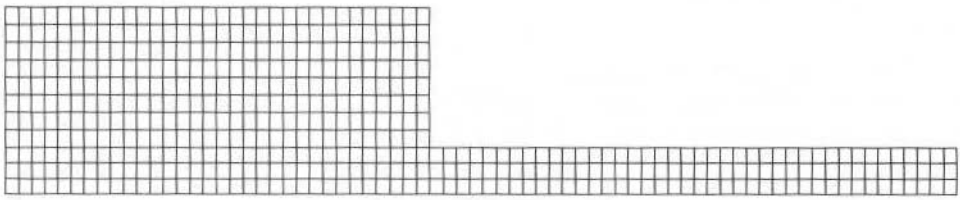

Fig. 2 The finite element mesh: 472 quadrilateral elements.

Figures 3-5 show a detail of the flow streamlines near the contraction. The numerical simulations have indicated a similar streamline pattern for Deborah numbers from 0 to 15 and, for this reason, we will only present the flows for De = 1.2, 9 and 15, respectively. As it can be seen in the Figures, the finite element formulation defined by Eqs. (31)-(33) was able to capture a well-defined back-flow region nearby the channel contraction.

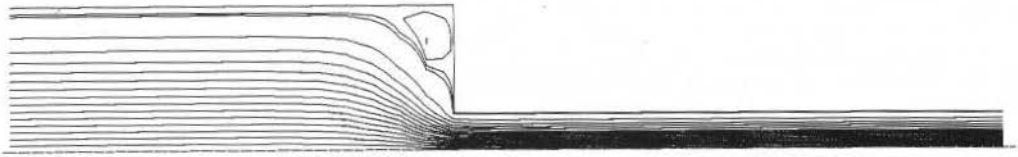

Fig. 3 Flow into a sudden contraction: streamlines for De = 1.2.

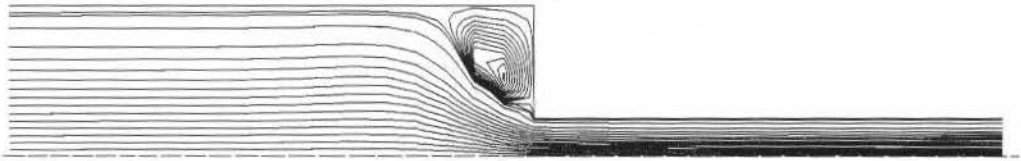

Fig. 4 Flow into a sudden contraction: streamlines for De = 9.

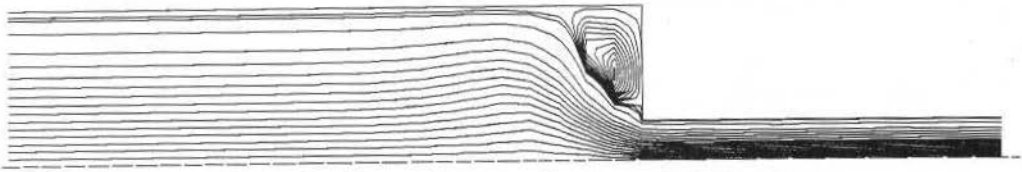

Fig. 5 Flow into a sudden contraction: streamlines for De = 15.

In Figures 6-8 temperature contours were shown for Deborah number equal to 15. These pictures illustrate three distinct thermal regimes. First, in Fig.6, a classical diffusive dominated flow has been found: the temperature distribution is due almost to heat conduction with no significant contribution of

convective heat transport (low Péclet flow, $Pe = 10^2$). At the channel centerline, we may observe that the computed natural (Neumman) boundary conditions were able to generate accurate maximum points for the temperature transversal profiles (remembering that, according to the finite element methology, these boundary values are unknown degrees-of-freedoms to be calculated, instead of prescribed nodal values to be imposed). Secondly, in Fig.7, the Péclet value $Pe = 10^3$ was sufficient to create a moderate advective-diffusive pattern: two thermal boundary layers close to the walls with the second layer thinner than the first one. Eventually, in Fig.8 we already have a very high thermal flow. It can be noticed that the fluid heating was confined to very thin boundary-layers, as expected from the high value of Péclet number ($Pe = 10^4$). Besides, the back-flow zone disturbs the boundary layer diffusive mechanism on the vertical wall of the contraction. These results were expected and are qualitatively in accordance with experimental visualizations introduced in (Evans, 1986).

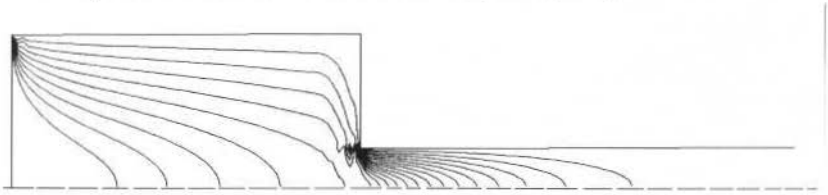

Fig. 6 Flow into a sudden contraction: temperature contours for Pe = 10^2 and De = 15.

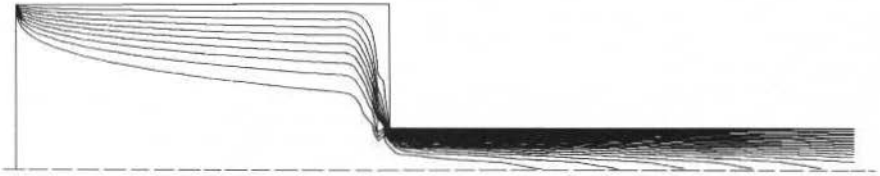

Fig. 7 Flow into a sudden contraction: temperature contours for Pe = 10^3 and De = 15.

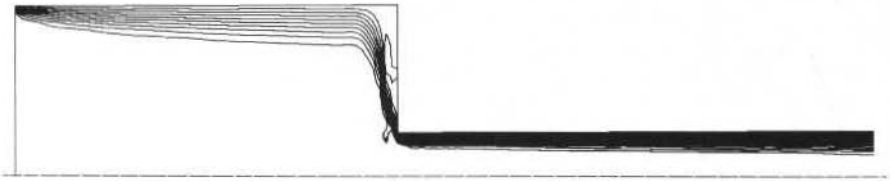

Fig. 8 Flow into a sudden contraction: temperature contours for Pe = 10^4 and De = 15.

Conclusions

In this paper, stable finite element simulations of thermal incompressible viscoelastic flows have been performed. The adopted mechanical model was the *Oldroyd-B liquid* with constant viscoelastic properties. The finite element method employed consists of a four-field bubble formulation in terms of $(\sigma_l, \boldsymbol{u}, p, \theta)$, with velocity and temperature fields approximated by continuous biquadratic elements (Q2) and pressure by discontinuous linear ones (P1). The extra-stress tensor is approximated by continuous bilinear elements in direct sum with twelve bubble tensors in each element $K(Q1 \oplus B(K))$.

In order to generate stable and accurate approximations for high advective situations, the method makes use of upwind stabilization strategies. To discretize the advective term of the stress material law of the system (21), it was used a non consistent *Streamline Upwind* scheme and, for the temperature convective term of the energy equation, a Galerkin/Least-squares methodology has been employed. Some two-dimensional simulations in a plane channel subjected to a sudden contraction indicate that the numerical scheme introduced was able to produce stable finite element approximations even in those situations in which it is known *a priori* that the Galerkin formulation with standard Lagrangean elements will generate unstable results.

Acknowledgements

During the course of this work, the author S. Frey has been partially supported by CNPq Proc. 350747/93-8.

References

Babuska, I., 1973, "The finite element method with Lagrangean multipliers", Numer. Math. 20 179-192.

Baranger, J., Guillopé, C. and Saut, C., 1996, "Mathematical Analysis of Differential Models for Viscoelastic Fluids, Rheology for Polymer Melt Processing", J-M. Piau and J-F. Agassant, Ed., (Elsevier Science) pp.199-236.

Billigton, E. W. and Tate, A., 1981, "The Physics of Deformation and Flow" (McGraw-Hill, N.Y., 1981).

Bird, R. B., Armstrong, R. C. and Hassager, O., 1987, "Dynamics of Polymerics Liquids". Vol. 1 - Fluid Mechanics (John Wiley and Sons, N.Y.).

Brezzi, F., 1974, "On the existence, uniqueness and approximation of saddle-point problems arising from Lagrange multipliers", RAIRO/Ser.Rouge 8 129-151.

Brooks, A. N. and Hughes, T. J. R., 1982, "Streamline upwind/Petrov-Galerkin formulations for convective dominated flows with particular emphasis on the incompressible Navier-Stokes equations", Comput. Methods Appl. Mech. Engrg. 32 199-259.

Ciarlet, P. G., 1978, "The finite element method for elliptic problems". (North-Holland, Amsterdam).

Evans, R. E. and Walters, K., 1986, "Flow characteristics associated with abrupt changes in geometry in the case of highly elastic liquids", J. Non-Newtonian Fluid Mechs., 20 11-29.

Franca, L. P. and Frey, S., 1992, "Stabilized finite element methods: II. The incompressible Navier-Stokes equations", Comput. Methods Appl. Mech. Engrg. 99 209-233.

Franca, L. P., Frey, S. and Hughes, T. J. R., 1992, "Stabilized finite element methods: I. Application to the advective-diffusive model", Comput. Methods Appl. Mech. Engrg. 95 253-276.

Gurtin, M. E., 1981, "An Introduction to Continuum Mechanics". (Academic Press, N.Y.).

Hughes, T. J. R. and Franca, L. P., 1987, "A new finite element formulation for computational fluid dynamics: VII. The Stokes problem with various well-posed boundary conditions", Comput. Methods Appl. Mech. Engrg. 65 85-96.

Hughes, T. J. R., Franca, L. P. and Balestra, M., 1986, "A new finite element formulation for computational fluid dynamics: V. Circumventing the Babuska-Brezzi condition: A stable Petrov-Galerkin formulation of the Stokes problem accomodating equal-order interpolations", Comput. Methods Appl. Mech. Engrg. 59 85-99.

Karam Filho, J., Loula, A. F. D. and Guerreiro, J. M. C., 1996, "A finite element formulation for coupled-thermal creep flow problems", Proc. Joint Conference of IGCM and CILANCE96, pp.197-200, Pádova, Itália, Setembro.

Macedo, A.P. and Brasil Junior, A.C.P., 1997, "A GLS-finite element method for turbulent flows", Preprint in preparation.

Marchal, J. M. and Crochet, M., 1987, "A new mixed finite element for calculating viscoelastic flow", J. Non-Newtonian Fluid Mechs., 26 77-117.

Ruas, V. and Carneiro de Araujo, J. H., 1992, "Un método mejorado de segundo orden para la simulatión de flujo viscoelástico con elementos finitos quadrilaterales", Revista Internacional de Métodos Numéricos para Cálculo y Diseno en Ingeniería, 8/1 77-85.

Ruas, V. and Carneiro de Araujo, J. H. and Silva Ramos, M. A., 1993, "Approximation of the three-field Stokes system via optimized quadrilateral finite elements", Math. Model. Num. Anal., 27/1 107-127.

Sampaio, R., 1985, "Introdução à Termomecânica dos Meios Contínuos, VI Escola de Matemática Aplicada" (Laboratório Nacional de Computação Científica, Rio de Janeiro).

Sampaio, P.A.B., 1991, "A Petrov-Galerkin formulation for the incompressible Navier-Stokes equations using equal-order interpolation for velocity and pressure", Int. Journal for Numerical Methods in Engineering, 31 1135-1149.

Silva Ramos, M.A., 1993, "Um Modelo Numérico para a Simulação do Escoamento de Fluidos Viscoelásticos via Elementos Finitos", Doctor Thesis (Pontifícia Universidade Católica do Rio de Janeiro, R.J).

Silva Ramos, M.A., Frey, S. and Carneiro de Araujo, J.H., 1997, "Stable finite element approximations of thermal viscoelastic flows", Mechanics Research Communications 24/2 203-208.

Soares, M. Souza Mendes, P.R. and Naccache, M.F., 1997, "Heat transfer to viscoplastic fluids in laminar flow through isothermal short tubes", Journal of the Brazilian Society of Mechanical Sciences, 19/1 1-14.

Truesdell, C. and Toupin, R. A., 1960, "The classical field theory", Handbuch der Physik III/1 Springer-Verlag, Berlin.

RBCM - J. of the Braz. Soc. Mechanical Sciences
Vol. XXI - No.1 - 1999 - pp. 41-50

ISSN 0100-7386
Printed in Brazil

A Finite Element Approximation for the Heat Transfer Process in a Plate with a Nonuniform Temperature-Dependent Source

Rogério Martins Saldanha da Gama
Laboratório Nacional de Computação Científica
25651-070, Petrópolis, RJ Brazil

Abstract

In this work the steady-state heat transfer process in an opaque plate with a nonuniform temperature-dependent source is modelled assuming that there exists a heat transfer from/to the plate following Newton's law of cooling. It is presented a quadratic functional whose minimization corresponds to the solution of the heat transfer problem. A finite element approximation is proposed for carrying out numerical simulations through the minimization of the functional. Some particular problems are simulated.

Keywords: *Conduction Heat Transfer, Minimum Principle, Plate Approximation, Finite Elements.*

Introduction

Let us consider a body represented by the bounded open set Ω given by

$$\Omega = \{ (x,y,z) \in \Re^3 \text{ such that } (x,y) \in \Gamma \subset \Re^2 , -L < z < L \}$$

in which Γ is a bounded open set of $\Re^2$ and L is a positive constant.

The set Ω is called a plate. If L is small it seems to be convenient to describe the heat transfer process in Ω taking into account its geometrical features. In other words, form small L, the heat transfer phenomenon in Ω may be, in a certain sense, described in the set Γ (Saldanha da Gama, 1997).

At this point a question arises naturally: Why to study the heat transfer in a thin plate? A possible answer is: Because there exist bodies that may be regarded as thin plates and, in such cases, the plate approximation in the most convenient mathematical approach for describing the heat transfer process in these bodies, avoiding a three-dimensional description or some inaccurate approximation.

The main subject of this work in the mathematical description and the numerical simulation of the heat transfer process in a thin plate that, originarily, is represented by (three-dimensional)

$$\begin{aligned}
&\frac{\partial}{\partial x}\left(k\frac{\partial T}{\partial x}\right)+\frac{\partial}{\partial y}\left(k\frac{\partial T}{\partial y}\right)+\frac{\partial}{\partial z}\left(k\frac{\partial T}{\partial z}\right)+\dot{q}=0 \quad in \ \ \Omega \\
&k\left(\frac{\partial T}{\partial x},\frac{\partial T}{\partial y},\frac{\partial T}{\partial z}\right)\boldsymbol{n}_{\partial\Gamma}=0 \quad for\ (x,y)\in\partial\Gamma \\
&-k\left(\frac{\partial T}{\partial x},\frac{\partial T}{\partial y},\frac{\partial T}{\partial z}\right)\boldsymbol{e}_z=h_+(T-T_+) \quad for\ z=+L \\
&k\left(\frac{\partial T}{\partial x},\frac{\partial T}{\partial y},\frac{\partial T}{\partial z}\right)\boldsymbol{e}_z=h_-(T-T_-) \quad for\ z=-L
\end{aligned} \tag{1}$$

in which $\partial\Gamma$ is the boundary of Γ (a plane curve); $\boldsymbol{n}_{\partial\Gamma}$ the unit outward normal defined on $\partial\Gamma$; $\boldsymbol{e}_z$ is the vector (0,0,1); k is a known functions of x and y ($k = \hat{k}(x,y)$); h_+, h_-, T_+ and T_- are known functions of x and y ($h_+ = \hat{h}_+(x,y)$, $h_- = \hat{h}_-(x,y)$, $T_+ = \hat{T}_+(x,y)$ and $T_- = \hat{T}_-(x,y)$; $\dot{q}$ is a linear function of T given by

$$\dot{q}=\alpha-\beta T, \quad \alpha=\hat{\alpha}(x,y) \text{ and } \beta=\hat{\beta}(x,y)\geq 0 \tag{2}$$

and T is the unknown of problem (1).

Manuscript received: November 1996; revision received: January 1998. Technical Editor: Angela Ourívio Nieckele.

The above linear relationship (between $\dot{q}$ and T) is mathematically interesting when employed with the plate approximation, since the source $\dot{q}$ will behave like the boundary conditions on $z = +L$ and $z = -L$ giving rise to a convenient description.

In problem (1) k represents the thermal conductivity (always positive), h_+ and h_- the convection heat transfer coefficients (always positive), T_+ and T_- the temperatures of reference, $\dot{q}$ energy supply (per unit time and volume) and T the temperature.

The plate (in general a thin plate) is assumed to be insulated on $\partial\Gamma$. In other words, the heat transfer from/to the plate takes place on the surfaces $z = +L$ and $z = -L$.

Despite of its large range of application, the plate approximation is not an usual approach for engineering heat transfer problems. In general, even for describing the heat transfer process in a thin plate, engineers employ standard three-dimensional heat transfer approaches in order to ensure the availability of the necessary mathematical tools, widely found in the current literature of numerical heat transfer (e.g.: Dan-ping, 1992; Ciarlet, 1978; and Cranck and Nicholson, 1947) or represents the plate as a fin (Kern and Kraus, 1985) giving rise to ordinary differential equations.

The Plate Approximation

Integrating the first equation of (1) over the thickness 2L we have

$$\int_{-L}^{L}\left\{\frac{\partial}{\partial x}\left(k\frac{\partial T}{\partial x}\right)+\frac{\partial}{\partial y}\left(k\frac{\partial T}{\partial y}\right)+\frac{\partial}{\partial z}\left(k\frac{\partial T}{\partial z}\right)\dot{q}\right\}dz=0 \quad for(x,y)\in\Gamma \tag{3}$$

so, taking into account the boundary conditions of (1), the following can be written

$$\begin{aligned}&\int_{-L}^{L}\left\{\frac{\partial}{\partial x}\left(k\frac{\partial T}{\partial x}\right)+\frac{\partial}{\partial y}\left(k\frac{\partial T}{\partial y}\right)+\dot{q}\right\}dz=-\left[h_+(T-T_+)\right]_{z=+L}+\left[h_-(T-T_-)\right]_{z=-L}=0 \quad for(x,y)\in\Gamma\\ &k\left(\frac{\partial T}{\partial x},\frac{\partial T}{\partial y},\frac{\partial T}{\partial z}\right)\boldsymbol{n}_{\partial\Gamma}=0 \quad for(x,y)\in\partial\Gamma\end{aligned} \tag{4}$$

Let us define the following mean temperature (evaluated over the thickness of the plate)

$$\overline{T}=\frac{1}{2L}\int_{-L}^{L}T\,dz \tag{5}$$

When $\dot{q}$ belongs to $L^2(\Omega)$ and Ω has the cone property (Maz'ja, 1985), T is a continuous and bounded function as well as $\overline{T}$. So, for a thin plate (very small L), the following approximation may be considered

$$\overline{T}\equiv T \quad for\ (x,y)\in\Gamma\ and\ z\in(-L,L) \tag{6}$$

and, therefore, problem (4) gives rise to

$$\begin{aligned}&\frac{\partial}{\partial x}\left(k\frac{\partial\overline{T}}{\partial x}\right)+\frac{\partial}{\partial y}\left(k\frac{\partial\overline{T}}{\partial y}\right)+\dot{q}-\frac{1}{2L}\left[h_+(\overline{T}-T_+)+h_-(\overline{T}-T_-)\right]=0 \quad for(x,y)\in\Gamma\\ &k\left(\frac{\partial\overline{T}}{\partial x},\frac{\partial\overline{T}}{\partial y}\right)\boldsymbol{n}_{\partial\Gamma}=0 \quad for(x,y)\in\partial\Gamma\end{aligned} \tag{7}$$

in which the unknown is $\overline{T}$ (this function depends only on x and y).

Taking into account (2), problem (7) may be expressed as

$$\begin{aligned} &\frac{\partial}{\partial x}\left(k\frac{\partial \bar{T}}{\partial x}\right)+\frac{\partial}{\partial y}\left(k\frac{\partial \bar{T}}{\partial y}\right)+\lambda-\mu\bar{T}=0 \quad for(x,y)\in\Gamma \\ &k\left(\frac{\partial \bar{T}}{\partial x},\frac{\partial \bar{T}}{\partial y}\right)\boldsymbol{n}_{\partial\Gamma}=0 \quad for(x,y)\in\partial\Gamma \end{aligned} \tag{8}$$

in which λ ($\lambda=\hat{\lambda}(x,y)$) *and* μ ($\mu=\hat{\mu}(x,y)$) are the known functions defined as

$$\lambda=\alpha+\frac{1}{2L}(h_+T_+ + h_-T_-) \tag{9}$$

$$\mu=\beta+\frac{1}{2L}(h_+ + h_-) \tag{10}$$

Variational Formulation

Problem (8) has an equivalent minimum principle. The function $\bar{T}$ which satisfies (8) is the one that minimizes the functional *I[W]* defined below

$$I[w]=\int_\Gamma \left\{\frac{k}{2}\left(\frac{\partial w}{\partial x}\right)^2+\frac{k}{2}\left(\frac{\partial w}{\partial y}\right)^2-\lambda=w+\frac{\mu}{2}w^2\right\}^2 dxdy \tag{11}$$

in which w is any admissible field ($w\in H^1(\Gamma)$).

The functional I[w] is quadratic, convex and coercive (Berger, 1977 and Saldanha da Gama, 1992), since k and μ are positive valued functions. In other words this functional admits one, and only one, minimum which is reached when $w\equiv u$, being u the solution of the following problem (Euler-Lagrange equation and natural boundary condition)

$$\begin{aligned} &\frac{\partial}{\partial x}\left(k\frac{\partial u}{\partial x}\right)+\frac{\partial}{\partial y}\left(k\frac{\partial u}{\partial y}\right)+\lambda-\mu u=0 \quad for(x,y)\in\Gamma \\ &k\left(\frac{\partial u}{\partial x},\frac{\partial u}{\partial y}\right)\boldsymbol{n}_{\partial\Gamma}=0 \quad for(x,y)\in\partial\Gamma \end{aligned} \tag{12}$$

which is exactly problem (8).

An Application - Numerical Simulation of a Heat Transfer Problem

Now, the variational formulation presented in this work will be employed for simulating the heat transfer process in a rectangular plate by means of a finite element approximation.

Let us suppose that the set Γ is given by (rectangular plate)

$$\Gamma = \{(x,y)\in\Re^2 \text{ such that } 0<x<L_x \text{ and } 0<y<L_y\}$$

that k and μ are constants and that λ is piecewise constant.

In this case problem (8) yields

$$k\left(\frac{\partial^2 \overline{T}}{\partial x^2}+\frac{\partial^2 \overline{T}}{\partial y^2}\right)+\lambda-\mu\overline{T}=0 \quad for \quad 0<x<L_x,\ 0<y<L_y$$

$$\frac{\partial \overline{T}}{\partial x}=0 \quad for\, x=0,\ \ 0<y<L_y \ and \ for \ \ x=L_x,\ \ 0<y<L_y \tag{13}$$

$$\frac{\partial \overline{T}}{\partial y}=0 \quad for\, y=0,\ \ 0<x<L_x \ and \ for\, y=L_y,\ \ 0<x<L_x$$

It will be considered the following finite element approximation for the admissible fields w ($w = \tilde{w}(x,y)$)

$$w=w_i\left(\frac{1}{2}-r\right)\left(\frac{1}{2}+s\right)+w_{i+1}\left(\frac{1}{2}+r\right)\left(\frac{1}{2}+s\right)+w_{i+M}\left(\frac{1}{2}-r\right)\left(\frac{1}{2}-s\right)+w_{i+M+1}\left(\frac{1}{2}-r\right)\left(\frac{1}{2}+s\right); \tag{14}$$
$$for\ j=1,2,.....,(M-1)(N-1),\ \overline{x}_j-\Delta x/2\le x\le \overline{x}_j+\Delta x/2 \ and \ \overline{y}_j-\Delta y/2\le y\le \overline{y}_j+\Delta y/2$$

in which w_i represents the approximation for w at the node i, i and j related by ("int" denotes the integer part of)

$$i = j + int\,[\,(j\text{-}1)/(M\text{-}1)\,] \tag{15}$$

$$r=\frac{x-\overline{x}_j}{\Delta x} \tag{16}$$

$$s=\frac{y-\overline{y}_j}{\Delta y} \tag{17}$$

$$\overline{x}_j=\{(j-1/2)-(M-1)int[(j-1)/(-1)]\}\Delta x \tag{18}$$

$$\overline{y}_j=\{(N-3/2)-int[(j-1)/(M-1)]\}\Delta y \tag{19}$$

In the above equations M represents the number of nodes in the x direction while N is the number of nodes in the y direction.

It is to be noticed that $(\overline{x}_j, \overline{y}_j)$ represents the position of the center of the element j. The position of the node i is given by (x_i, y_i) where

$$x_i = \{(i\text{-}1) - M\ int\,[\,(i\text{-}1)/M\,]\,\}\ \Delta x \tag{20}$$

$$y_i = \{(N\text{-}1) - int\,[\,(i\text{-}1)/M\,]\,\}\ \Delta y \tag{21}$$

Inserting the approximation (14) into functional I[w], defined by (11), we obtain the following function

$$g=\hat{g}(w_1, w_2, ..., w_{MN})=\sum_{j=1}^{(M-1)(N-1)} A_j \tag{22}$$

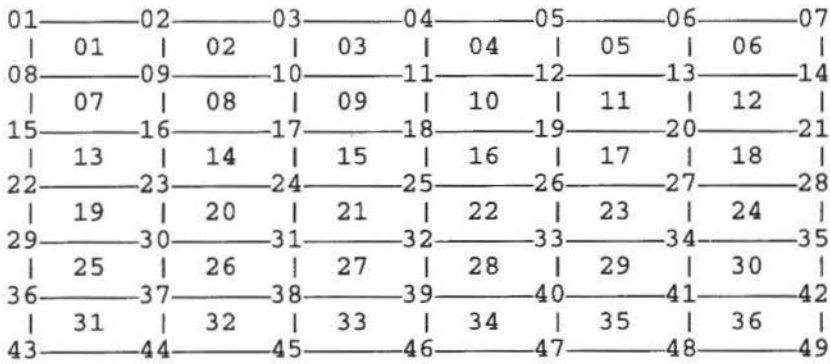

Fig. 1 The considered finite element approximation for the particular case in which M=7 and N=7 (1≤j≤36 and 1≤i≤49).

Assuming that λ is constant over each considered element and denoting by λ_j the value of λ at the element j we have

$$A_j=\frac{k}{6}\left\{\left(w_{i+1}-w_i\right)^2+\left(w_{i+M+1}-w_{i+M}\right)^2+\left(w_{i+1}-w_i\right)\left(w_{i+M+1}-w_{i+M}\right)\right\}\frac{\Delta y}{\Delta x}+$$
$$+\frac{k}{6}\left\{\left(w_i-w_{i+M}\right)^2+\left(w_{i+1}-w_{i+M+1}\right)^2+\left(w_i-w_{i+M}\right)\left(w_{i+1}-w_{i+M+1}\right)\right\}\frac{\Delta x}{\Delta y}$$
$$-\frac{1}{4}\lambda_j\left\{w_i+w_{i+1}+w_{i+M}+w_{i+M+1}\right\}\Delta x\Delta y+\frac{\mu}{36}\left(2w_i^2+2w_{i+1}^2+2w_{i+M}^2+2w_{i+M+1}^2+\right. \tag{23}$$
$$\left.+2w_i w_{i+1}+2w_{i+1}w_{i+M+1}+2w_{i+M}w_{i+M+1}+2w_i w_{i+M}+w_i w_{i+M+1}+w_{i+1}w_{i+M}\right)\Delta x\Delta y$$
$$i=j+int\{(j-1)/(M-1)\}$$

The minimum of g is reached when

$$\frac{\partial g}{\partial w_i}=0 \quad for\, i=1,2,\ldots,NM \tag{24}$$

The solution of the above linear system of NM equations represent the approximation for $\overline{T}$ at each node i.

Some selected results are shown in Figs. 2 to 8 in which the (modified) temperature θ defined as

$$\theta=\overline{T}\left(\frac{k}{\mu}\right)\left(\frac{1}{L_x}\right)^2 \tag{25}$$

is represented as a function of the independent dimensionless variables X and Y given by

$$X=\frac{x}{L_x};\quad Y=\frac{y}{L_x} \tag{26}$$

In Figures 2 and 3 a comparison among four different *approximations (M=N=11, M=N=21, M=N=31 and M=N=41)* for the same problem is presented. It is remarkable that the upper and lower bounds for θ have not a strong dependence on M and N.

Figures 4, 5, 6, 7 and 8 present θ as a function of x and y for some particular cases. It is to be noticed that $\theta = \theta$ (x,y) depends only on the ratios λ / μ and L_y / L_x.

The effect of the ratio λ / μ can be illustrated from the integration of (8) over the set Γ. This integration leads us to

$$\int_{\Gamma} \left(\lambda - \mu \overline{T}\right) dS = 0 \tag{27}$$

So, since μ does not dependent on the position , we can conclude that the ratio $\overline{\lambda} / \mu$ (where $\overline{\lambda}$ is the mean value of λ in Γ) represents the mean temperature over the plate.

The (geometric) ratio L_y / L_x determines the upper bound for the dimensionless variable Y ($0 \le Y \le L_y / L_x$ *while* $0 \le X \le 1$). Since the boundary $\partial\Gamma$ is insulated, this parameter affects directly the derivatives $\partial \overline{T} / \partial X$ and $\partial \overline{T} / \partial Y$.

In all the considered situations a Gauss-Seidel iterative scheme (Todd, 1962) was used for solving system (24).

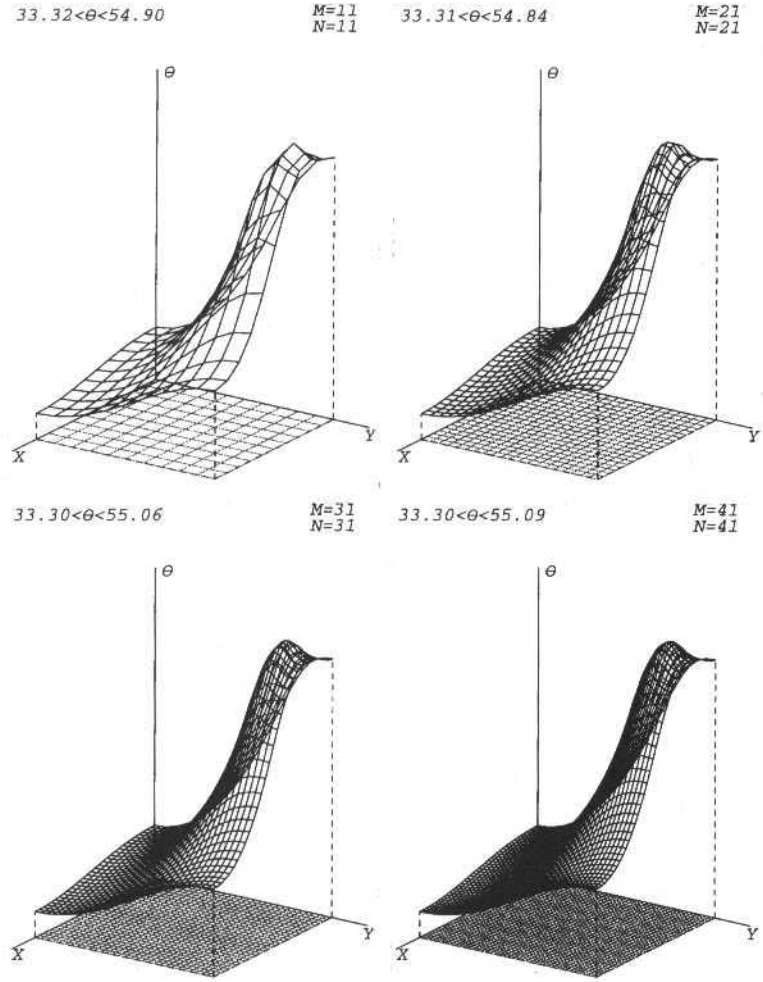

Fig. 2 The modified temperature θ as a function of X and Y, obtained with four different approximations, for L_y/L_x = 1.0 and λ/μ = 1000.0 for 0.10 <X<0.50 and 0.80<Y<0.90 (λ/μ = 0.0 otherwise).

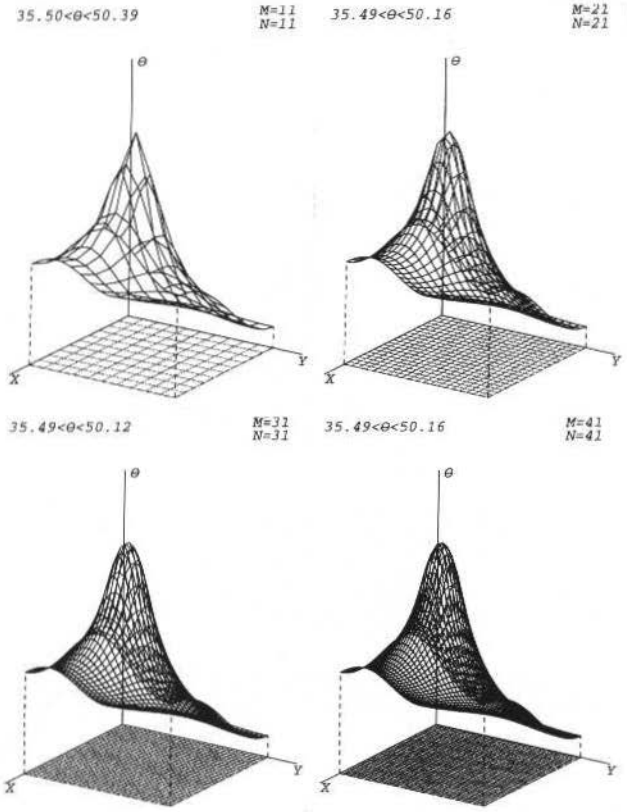

Fig. 3 The modified temperature θ as a function of X and Y, obtained with four different approximations, for $L_y/L_x = 1.0$ and $\lambda/\mu = 1000.0$ for $0.60<X<0.80$ and $0.40<Y<0.60$ ($\lambda/\mu = 0.0$ otherwise).

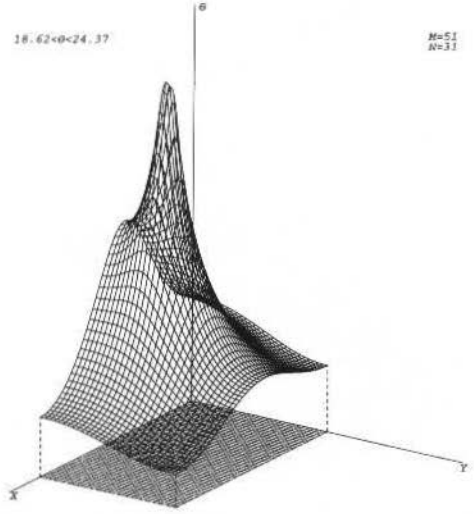

Fig. 4 The modified temperature θ as a function of X and Y, obtained with M=51 and N=31, for $L_y/L_x = 0.6$ and $\lambda/\mu = 5000.0$ for $0.40<X<0.52$ and $0.18<Y<0.20$ ($\lambda/\mu = 0.0$ otherwise). Here $18.62<\theta<24.37$

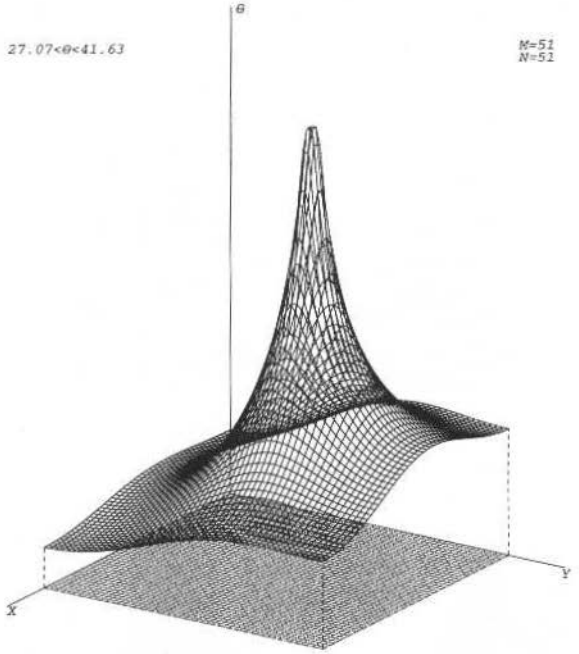

Fig. 5 The modified temperature θ as a function of X and Y, obtained with M=51 and N=51, for L_y/L_x = 1.0 and λ/μ = 15000.0 for 0.40<X<0.50 and 0.58<Y<0.60 (λ/μ = 0.0 otherwise). Here 27.07<θ<41.63

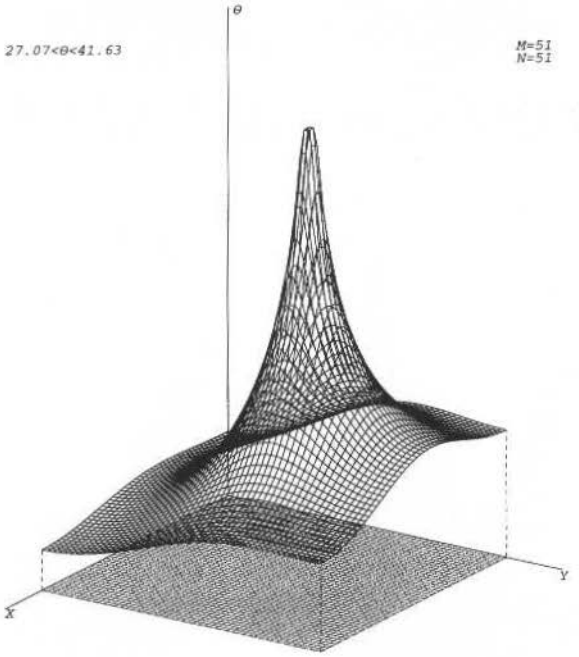

Fig. 6 The modified temperature θ as a function of X and Y, obtained with M=51 and N=31, for L_y/L_x = 1.0 and λ/μ = 5000.0 for 0.92<X<0.96 and 0.92<Y<0.98 and for 0.04<X<0.08 and 0.02<Y<0.08 (λ/μ = 0.0 otherwise). Here 21.56<θ<36.36.

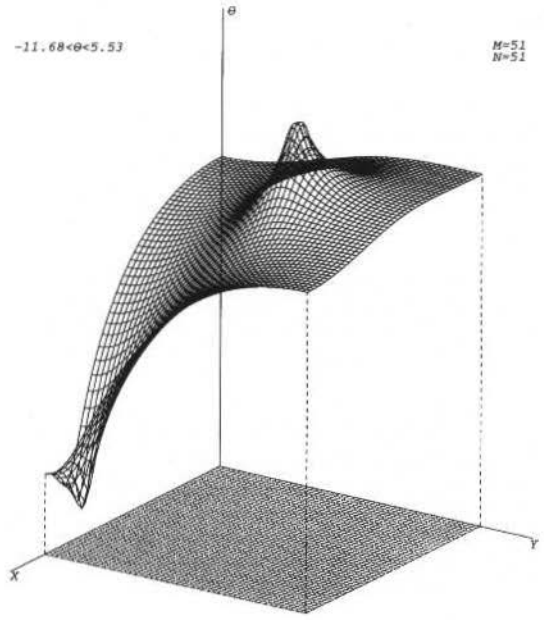

Fig. 7 The modified temperature θ as a function of X and Y, obtained with M=51 and N=51, for $L_y/L_x = 1.0$ and $\lambda/\mu = 5000.0$ for $0.40<X<0.52$ and $0.58<Y<0.60$ and $\lambda/\mu = -5000.0$ for $0.84<X<0.90$ and $0.04<Y<0.08$ ($\lambda/\mu = 0.0$ otherwise). Here $-11.68<\theta<5.53$.

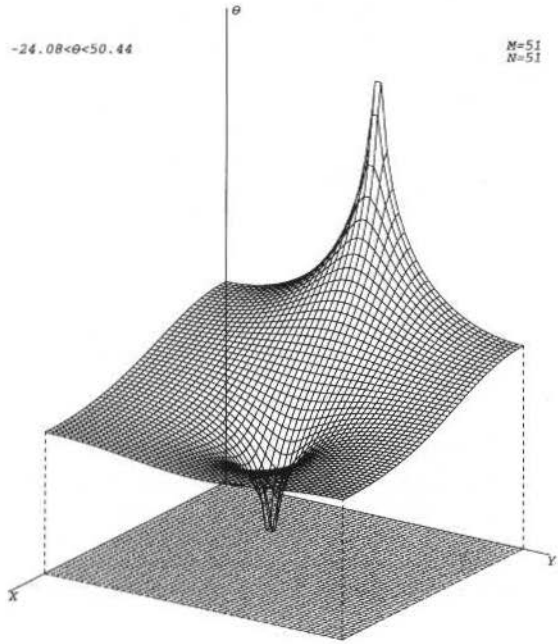

Fig. 8 The modified temperature θ as a function of X and Y, obtained with M=51 and N=51, for $L_y/L_x = 1.0$ and $\lambda/\mu = 100000.0$ for $0.40<X<0.42$ and $0.58<Y<0.60$ and $\lambda/\mu = -100000.0$ for $0.58<X<0.60$ and $0.50<Y<0.52$ ($\lambda/\mu = 0.0$ otherwise). Here $-24.08<\theta<50.44$.

Conclusions

In this work a powerful tool for solving a large class of linear conduction heat transfer problem in plates was presented.

The energy transfer from/to the plate (by convection) and the liner temperature-dependent source term $\dot{q}$ plays the same (mathematical) role giving rise to an interesting and simple description with a convenient variational formulation.

References

Berger, M. S., 1977, "Nonlinearity and Functional Analysis", Academic Press, London.

Maz'ja, V. G., 1985, "Sobolev Spaces", Springer-Verlag, Berlin.

Saldanha da Gama, R. M., 1992, "Simulation of the Steady-State Energy Transfer in Rigid Bodies, with Convective/Radiative Boundary Conditions, employing a Minimum Principle", J. Comp. Phys., 99, n°.2, pp. 310-320.

Saldanha da Gama, R. M., 1997, "Mathematical Modelling of the Non-Linear Heat Transfer Process in a Gray Shell Surrounded by a Nonparticipating Medium", Int. J. Non-Linear Mech., 32, n° 5, pp. 885-904.

Todd, J., 1962, "Survey of Numerical Analysis", McGraw-Hill, New York.

Dan-ping, Yang, 1992, "Global Maximum Norm Error Estimates of Boundary Finite Element Methods for Elliptic Boundary Value Problems", J. Comp. Math., 10, suppl. issue, pp. 144-157.

Ciarlet, P. G., 1978, "Finite Element Methods for Elliptic Problems", North-Holland, Amsterdam.

Kern, D. Q. and Kraus, A. D., 1985, "Extended Surface Heat Transfer", McGraw-Hill, New York.

Cranck, J. and Nicholson, P., 1947, " A Practical Method for Numerical Type", Proc. Camb. Phil. Soc., 43, pp. 50-55.

RBCM - J. of the Braz. Soc. Mechanical Sciences
Vol. XXI - No.1 - 1999 - pp.51-60

ISSN 0100-7386
Printed in Brazil

Friction Factor in Annular Conduits with Tubular Fins

J. R. Sodré
Pontifícia Universidade Católica de Minas Gerais
Departamento de Engenharia Mecânica
30535-610 Belo Horizonte, MG Brazil
ricardo@pucminas.br

J. A. R. Parise
Pontifícia Universidade Católica do Rio de Janeiro
Departamento de Engenharia Mecânica
22453-900 Rio de Janeiro, RJ Brazil
parise@mec.puc-rio.br

Abstract

The friction factor for turbulent fully developed flow of air at steady state conditions through an annular conduit with tubular fins has been determined. The tubular fins consisted of tubes inserted in the annular gap to increment heat transfer. The finned annular section was built to simulate the heat exchangers (cooler and heater) of a Stirling engine. Tests were carried out in an annular section with a radius ratio of 1.083, covering Reynolds numbers between 1000 and 6000. The results have shown that the utilization of annular fins increased the pressure loss by friction by a factor of 7 to 12, within the range studied.
Keywords: *Annular Pipe, Stirling Engines, Friction Factor.*

Introduction

Finned annular sections has been studied previously by other authors. Flat fins placed along the internal pipe diameter of the annular conduit, longitudinal to the flow direction, are well investigated (Patankar et al., 1979, Braga, 1987). However, a work considering annular conduit with tubular fins has not been found in the literature. Tubular fins consist of circular pipes placed along the perimeter of the annular section, which external diameter coincide with the annular gap (Fig. 1). This type of fin has been used in the cooler and heater of the Stirling engine described by Bartolini and Naso (1984), to increment heat exchange.

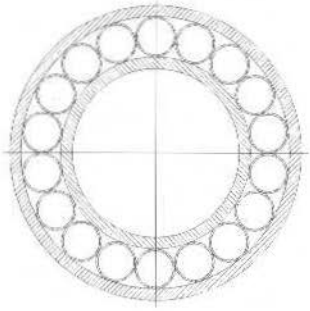

Fig. 1 Annular section with tubular fins.

In this work, the friction factor has been studied for turbulent fully developed flow of air in an annular conduit with tubular fins. Experiments have been carried out in a test section built to simulate the heat exchangers of a Stirling engine (heater and cooler), to determine the pressure loss along the finned region. The results are, thus, expected to be of direct application to the mentioned engine, and to furnish information for future analysis on the performance of this type of fin.

Experiments

The test section used in the experiments, built to simulate the heat exchangers (cooler and heater) and the regenerator of a Stirling engine, was connected to an air circuit, shown schematically in Fig. 2.

Manuscript received: September 1997. Technical Editor: Angela Ourívio Nieckele.

The air circuit comprised an air filter, a silencer, a compressor, two valves for flow control, an orifice plate, plenum chambers, dampening chamber and straighteners. Air was blown by a Roots compressor, driven by an electric motor. The flow amount was controlled by two butterfly valves, one of them restricting the flow to by-pass, and the other, to the test section. The flow amount to the test section was measured by an orifice plate, installed according to specifications of ASME (1971). The pressure drop in the orifice plate was read by a Dwyer well-type inclined manometer or by a Dwyer U-tube water column manometer, with resolutions of 0.5 mm and 2 mm, respectively. The inclined manometer was used for low flows. The tube used in the air circuit had a diameter of 106.75mm ± 0.05mm ID. A silencer was installed between the filter and the compressor, to reduce noise. A plenum chamber and a dampening chamber were located after the compressor, to eliminate pulsation effects. A flow straightener was used after the flow control valve, before the developing length to the orifice plate. Another straightener was used between a second plenum chamber and the test section.

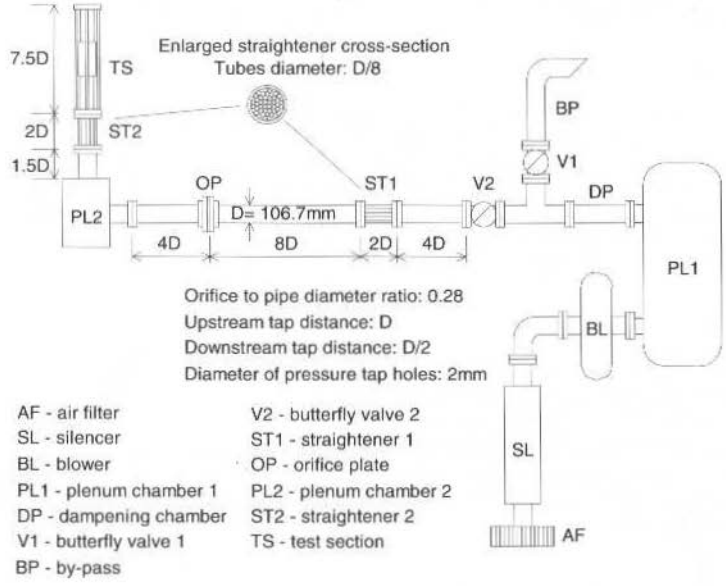

Fig. 2 Schematic of the air circuit

Copper-constantan ATP/H-TEK T type thermocouples were used to measure the temperature of the air flowing in the orifice plate and in the test section. The readings from the thermocouples were registered by a voltmeter, with resolution of 0.01 mV. Ambient air temperature was read by a mercury-in-glass Incotherm thermometer, with resolution of 0.1 °C. Atmospheric pressure was taken by a Fisher Scientific mercury column barometer, with resolution of 0.1mmHg. Room air humidity was measured by a Henni-René Graf thermohygrometer, with resolution of 2 %.

The test section had a single internal pipe and external pipes with different diameters for the cooler, regenerator and heater locations (Fig. 3). That was done to reproduce the radius ratios of the heat exchangers and regenerator of the Stirling engine, as quoted by Bartolini and Naso (1984). The cooler and the heater were located in the extremes of the test section, with the regenerator in the middle. That

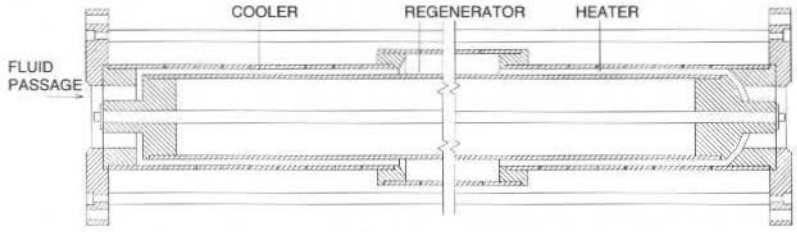

Fig. 3 Longitudinal view of the test section.

was in accordance with the project of the Stirling engine. The internal pipe of the test section had a diameter of 71.21 mm ± 0.01 mm OD, the diameter of the external pipe of the heater was 76.63 mm ± 0.03 mm ID , and the external pipe diameter of the cooler was 77.56 mm ± 0.02 mm ID . With these pipes, radius ratios of 1.076 and 1.089 were obtained for the heater and cooler, respectively, reproducing the Stirling engine described by Bartolini and Naso (1984). The section of the heater had a total length of 180 mm, and seven locations of pressure reading were spaced in intervals of 30 mm ± 0.3 mm. The length of the cooler was 210 mm, with eight pressure reading locations spaced as in the heater. To obtain an averaged pressure, each location of reading had four taps, distant 90 degrees from each other along the perimeter (Fig. 4). The pressure taps were built with holes of 0.8 mm. A multi-point valve was used to select the location of reading.

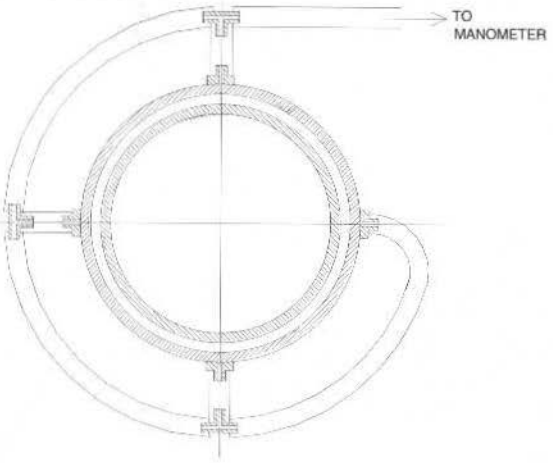

Fig. 4 Pressure taps distribution in a section of reading.

The pressure drop along the test section was measured with one Dwyer well-type inclined manometer, one Dwyer U-tube water column manometer, and one Dwyer U-tube mercury column manometer. The instruments had resolutions of 0.2 mm, 1 mm, and 1 mm, respectively. For the tests without fins, the readings from the first tap in the entrance of the cooler and the heater were neglected in the evaluation of the pressure drop, to assure that the readings considered were not affected by the changes in the flowing area. The changes in the flowing area are characterized by the tiny annular area of the cooler and the heater, to the larger cross-sectional area in the regenerator, and the curved regions in the extremes of the section (see Fig. 3). The fully developed condition was quickly reached, as demonstrated by the uniform pressure distribution in Figs. 5 and 6.

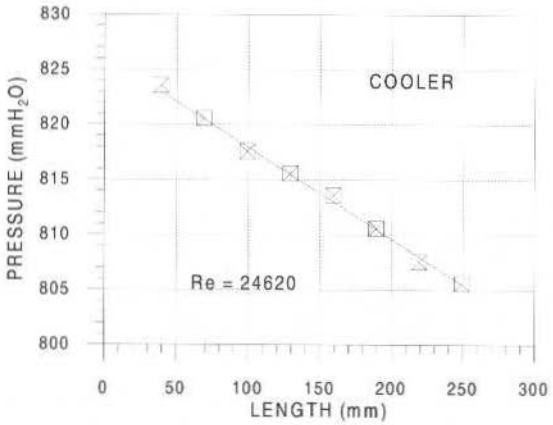

Fig. 5 Pressure distribution in the bare annular region.

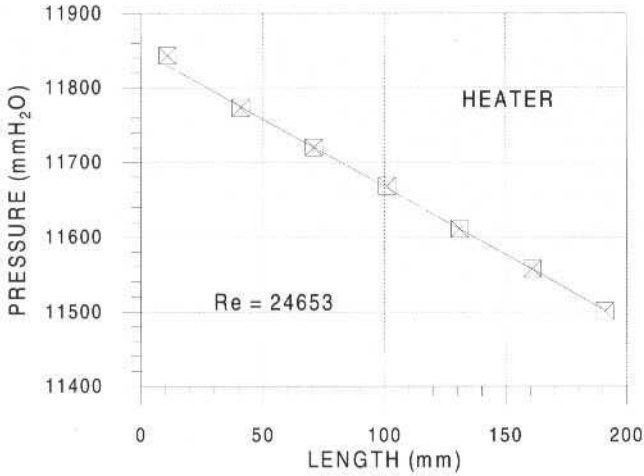

Fig. 6 Pressure distribution in the bare annular region.

For the tests with finned region, pressure readings were made in three locations at the inlet and in two locations in the outlet, as shown in Fig. 7. It can be seen the intensity of drop in pressure after the flow enters the finned region, and the rise in pressure at the exit of the region, due to an abrupt expansion. The pressure drop was determined from the readings of the second tap before and the second tap after the finned region. The taps located right at the entrance and at the exit of the finned regions were under effects of flow contraction and expansion, respectively.

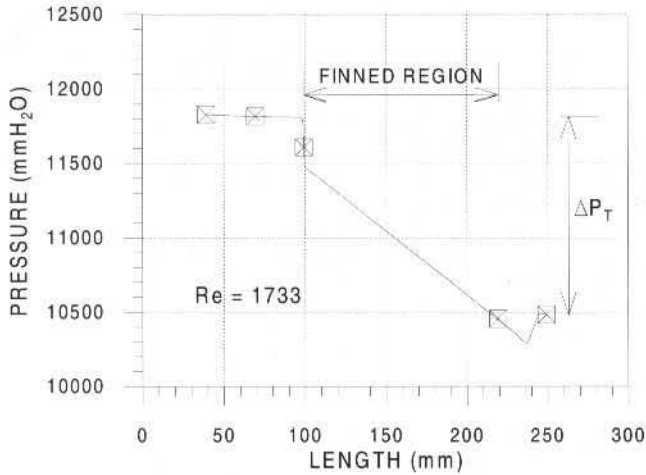

Fig. 7 Pressure distribution in the finned annular region.

The fins were plastic tubes (nylon) of external diameter 3.00 mm ± 0.05 mm, and internal diameter 2.00 mm ± 0.05 mm. The fins were fitted in the cooler only, as the gap of the heater were too small (2.71 mm). The original gap in the cooler was 3.175 mm, and had to be reduced to the diameter of the fins (3.00 mm). To solve it, the external diameter of the internal pipe of the annular section was augmented, by sticking two layers of adhesive tape on it, which thickness was 0.1 mm. It was verified that the inclusion of the tape did not alter the friction factor of the bare section. Seventy eight tubular fins were fitted in the section.

The apparatus was constructed in the laboratories of PUC-Rio, where all the experiments were performed. For the tests without fins, the estimated uncertainties associated to the determination of the mass flow rate and Reynolds number were ± 1.4 % and ± 1.9 %, for the cooler and heater, respectively.

The uncertainty associated to the friction factor for the cooler was ± 5.0 %, and for the heater, ± 4.5 %. The total uncertainty related to the determination of the friction factor from Eq. (1) was estimated in ± 9.3 % and ± 7.6 %, for the cooler and heater, respectively. The uncertainties for the mass flow rate, Reynolds number and friction factor for the finned section were ± 1.4 %, ± 5.2 % and ± 7.3 %. The total uncertainty associated to the determination of the friction factor through Eq. (10) was estimated in ± 11.3 %. The uncertainties were calculated according to the method proposed by Kline and McClintock (1953).

The procedure adopted in the execution of the experiments involved a regular check of the ambient air condition for each test run. Atmospheric pressure, room air temperature and humidity were always registered. Soon after a new flow was set though the butterfly valves, the steady state condition was obtained. The readings from the instruments were taken manually, and each test run took approximately 5 min. Both flow directions, cooler-regenerator-heater and heater-regenerator-cooler, were tested.

The measured quantities during the experiments were: atmospheric pressure, ambient air temperature, room air humidity, air temperature at the orifice plate inlet, air temperature at the test section entrance, pressure difference across the orifice plate, pressure difference between the test section exit and the atmosphere, pressure difference through the test section, pressure difference between the orifice plate inlet and the test section entrance, and pressure difference between the compressor outlet and the test section entrance. The preliminary data were converted by a data reduction computer program, written in BASIC language. The output from the program included the corresponding mass flow rate, Reynolds number and friction factor.

Data Reduction

In the analysis applied for data reduction, the fluid is considered to be at a steady state flow regime, and the boundary layer is fully developed. Spatial dependence of fluid properties in the radial direction is not taken into account. All fluid properties are written as an average value in time and space, except when indicated.

Bare Section

The pressure drop due to friction of the flowing fluid with the walls of the annular conduit along a length L, ΔP_b, is given by the expression from Darcy-Weissbach,

$$\Delta P_b = f_b \frac{L}{D_h} \overline{\rho} \frac{\overline{v}^2}{2} \tag{1}$$

where $\overline{\rho}$ is the fluid density.

The hydraulic diameter of the annular section, D_h, is so described,

$$D_h = D_e - D_i \tag{2}$$

where D_e and D_i are the external and internal diameters of the annular section, respectively. The average velocity of approach, $\overline{v}$, is so given,

$$\overline{v} = \frac{\dot{m}}{\overline{\rho} A_b} \tag{3}$$

where $\dot{m}$ is the total mass flow rate, and A_b is the cross-sectional area of the annular conduit. The friction factor for the bare section, f_b, can be written from Eq. (1),

$$f_b = \frac{\Delta P_b}{\frac{L}{D_h} \overline{\rho} \frac{\overline{v}^2}{2}} \tag{4}$$

and can be represented in terms of Reynolds number,

$$f_b = a_1 Re^{b1} \tag{5}$$

where a_1 and b_1 are constant coefficients determined experimentally. The Reynolds number, Re, is so written,

$$Re = \frac{\overline{\rho v} D_h}{\overline{\mu}} \tag{6}$$

where μ is the viscosity of the fluid.

There are additional pressure losses which arise from the flow and test section characteristics. According to Kays and London (1964), alterations in the fluid density due to variations of pressure and temperature along the section generate a pressure drop, ΔP_d, which is thus calculated,

$$\Delta P_d = \left(\frac{\dot{m}}{A_b}\right)^2 \left(\frac{1}{\rho_o} - \frac{1}{\rho_i}\right) \tag{7}$$

where ρ_i and ρ_o are the respective fluid densities calculated at the entrance and at the exit of the length considered.

If the flow is upwards on the vertical, there is a pressure drop due to the elevation, ΔP_h (Kays and London, 1964),

$$\Delta P_h = \overline{\rho} g L \tag{8}$$

where g is the free-fall acceleration.

So, for the bare section, the total pressure drop, ΔP_T, is so given,

$$\Delta P_T = \Delta P_b + \Delta P_d + \Delta P_h \tag{9}$$

Re-writing Eq. (9), the pressure drop due to friction in the bare annular section is expressed,

$$\Delta P_b = \Delta P_T - \left(\Delta P_d + \Delta P_h\right) \tag{10}$$

ΔP_T is the measured pressure; ΔP_d and ΔP_h are evaluated from Eqs. (7) and (8). With the value of ΔP_b from Eq. (10), f_b is obtained in Eq. (4) and is plotted against Reynolds number, determining the values of coefficients a_1 and b_1 [Eq. (5)]. The density and the viscosity of the fluid are calculated as function of pressure, temperature and humidity.

Finned Section

The presence of fins generates an additional pressure drop, ΔP_f, which is thus calculated,

$$\Delta P_f = nK_f \overline{\rho} \frac{\overline{v}^2}{2} \tag{11}$$

where n is the number of fins, and K_f is the pressure loss coefficient associated to a row of fins.

The total pressure drop by friction through the finned annular region, ΔP_{ft}, is the sum of the pressure drop due to friction with the walls of the annular conduit, plus the additional pressure drop due to the presence of fins,

$$\Delta P_{ft} = \Delta P_b + \Delta P_f \tag{12}$$

ΔP_{ft} can also be expressed by Darcy-Weissbach equation,

$$\Delta P_{ft} = f_f \frac{L}{D_h} \bar{\rho} \frac{\bar{v}^2}{2} \tag{13}$$

where f_f is the friction factor for the finned region, defined by the sum,

$$f_f = f_b + K_f \frac{D_h}{L} \tag{14}$$

The friction factor f_f can be explicit from Eq.(13),

$$f_f = \frac{\Delta P_{ft}}{\frac{L}{D_h} \bar{\rho} \frac{\bar{v}^2}{2}} \tag{15}$$

and can also be represented in terms of Reynolds number,

$$f_f = a_2 \, Re^{b_2} \tag{16}$$

where a_2 and b_2 are constant coefficients determined experimentally.

The thickness of the fins reduces the free-flow cross sectional area and, as a consequence, the flow is contracted at the entrance of the finned region and expanded at the exit, generating additional losses. If the pressure taps are located at the entrance and at the exit of the finned region, these additional pressure drops must be considered. According to Kays and London (1964), the pressure drop due to contraction of the flow, ΔP_c, is so described,

$$\Delta P_c = \left(\frac{\dot{m}}{A_f} \right)^2 \frac{1}{\rho_i} \left[1 - \left(\frac{A_f}{A_b} \right)^2 + K_c \right] \tag{17}$$

A_f is the minimum flow area in the finned region, given by,

$$A_f = A_b - n\pi \frac{d_e^2 - d_i^2}{4} \tag{18}$$

where d_e and d_i are the respective tubular fin external and internal diameters.

Tew (1978) proposed the following expression for the contraction coefficient K_c, tested against the experimental data on different geometry by Kays and London (1964),

$$K_c = 0.5 - 0.4 \frac{A_f}{A_b} \tag{19}$$

The pressure drop due to expansion of the flow is calculated in a similar way (Kays and London, 1964),

$$\Delta P_e = \left(\frac{\dot{m}}{A_f} \right)^2 \frac{1}{\rho_o} \left[1 - \left(\frac{A_f}{A_b} \right)^2 + K_e \right] \tag{20}$$

The expansion coefficient, K_e, is given by the following expression (Tew, 1978),

$$K_e = 1 - 2.0928\frac{A_f}{A_b} + 0.996\left(\frac{A_f}{A_b}\right)^2 \tag{21}$$

Thus, effects of flow entrance and exit in the finned region are taken into account by ΔP_c and ΔP_e. These effects should not influence the friction factor f_f, as it is based on ΔP_{ft} only.

The overall pressure drop measured between the entrance and the exit of the finned region, ΔP_T, is given by the parcels,

$$\Delta P_T = \Delta P_{ft} + \Delta P_d + \Delta P_h + \Delta P_c + \Delta P_e \tag{22}$$

Re-writing Eq. (22) to express ΔP_{ft}, results,

$$\Delta P_{ft} = \Delta P_T - \left(\Delta P_d + \Delta P_h + \Delta P_c + \Delta P_e\right) \tag{23}$$

ΔP_T is measured experimentally; ΔP_d, ΔP_h, ΔP_c and ΔP_e are calculated through Eqs. (7), (8), (17) and (20). From the value determined for ΔP_{ft} by Eq. (23), f_f is evaluated from Eq. (15) and is plotted against Reynolds number in Eq. (16), establishing the constants a_2 and b_2. As for the bare section, Reynolds number is also based on the velocity of approach to the finned region [Eq. (6)].

Results and Discussion

The friction factor for the bare sections of the cooler and heater are displayed in Figs. 8 and 9. The data shown were obtained for tests made with both flow directions, cooler-regenerator-heater and heater-regenerator-cooler. Covering Reynolds numbers between 4000 and 27000, the application of linear regression to the data resulted in the following curves:

Cooler: $f_b = 0.190\,Re^{-0.183}$ (24)

Heater: $f_b = 0.234\,Re^{-0.204}$ (25)

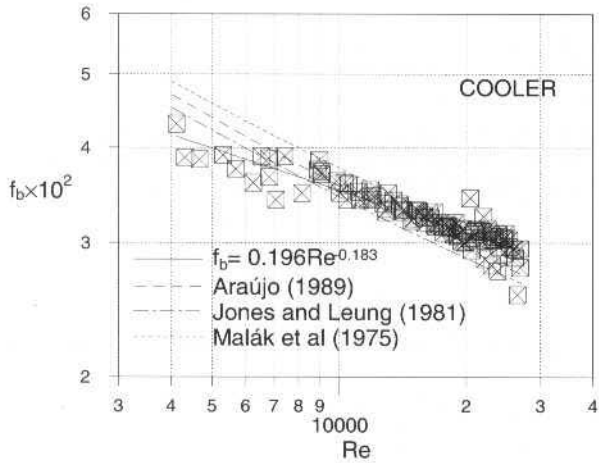

Fig. 8 Friction factor in the bare annular region.

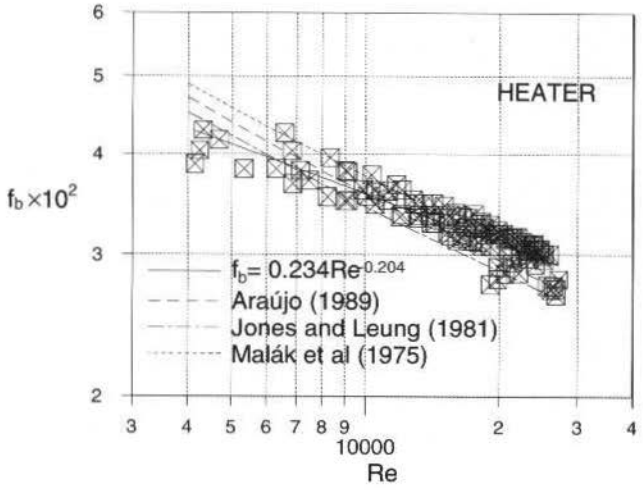

Fig. 9 Friction factor in the bare annular region.

Chauvenet's criterion has been used to eliminate inconsistent data (Holman, 1994). Though the coefficients are not the same, the maximum difference between the curves in the range is 3.5 %, for Reynolds equal to 4000.

Although numerous empirical works on annular sections are found in the literature, larger radius ratios than the ones dealt with in the present work were always used. Thus, comparisons have been made with authors who treated the problem analytically, proposing methods to cover any radius ratio. Friction factor expressions for flow through annulus proposed by Malák et al. (1975), Jones and Leung (1981) and Araújo (1989) are plotted in Figs. 8 and 9. Good agreement is found throughout the range studied between the present work and the ones from the other authors. A maximum discrepancy of 14.8 % is found in the lower limit of Reynolds, near the transition region.

Figure 10 shows the friction factor for the finned cooler. Again, the data was obtained for flow in both directions, covering Reynolds numbers between 4000 and 20000. Linear regression applied to the data yielded the expression below,

$$f_f = 32.713\,Re^{-0.501} \tag{26}$$

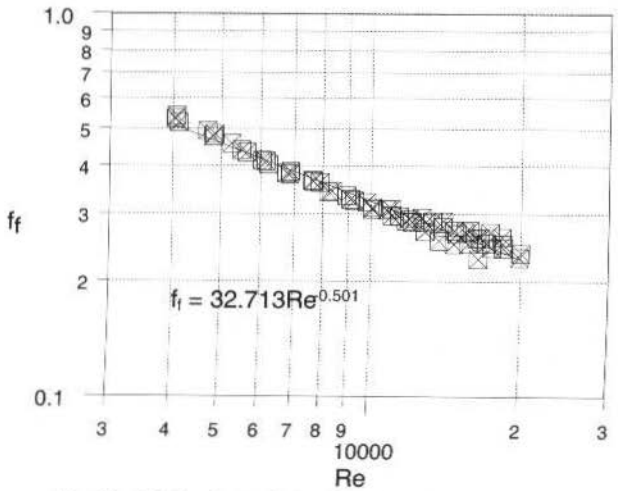

Fig. 10 Friction factor in the finned annular region.

Chauvenet's criterion has also been applied to eliminate inconsistent data. Comparisons with results by other authors have not been made, as studies on similar finned sections have not been found in the literature. The friction factor in the finned annulus is about 7 to 12 times larger than in the bare section.

Conclusion

Experiments carried out in an annular section, simulating the heat exchangers (cooler and heater) of a Stirling engine, have shown that the introduction of tubular fins increases the pressure loss by friction by a factor of seven to twelve times. The results were obtained for an annular section of radius ratio 1.083, ratio of the fin thickness to the hydraulic diameter of the annular section of 0.084, and Reynolds numbers between 4000 and 20000.

Acknowledgments

The authors wish to thank the Brazilian Government's Science and Technology body, CNPq, for the financial support to this project.

References

Araújo, P. M. S., 1989, "A Semi-analytical Approach to Turbulent Flow through Concentric Annuli", Heat and Technology, Vol. 7, n. 3-4, pp. 45-56.

ASME, 1971, "Fluid Meters, their Theory and Application", Report from the Research Committee on Fluid Meters, 6th ed..

Bartolini, C. M., and Naso, V., 1984, "Theoretical Predictions of the Performance of Stirling Engines Metallic Regenerators", The 2nd Int. Conference on Stirling Engines, Shangai.

Braga, C.V.M., 1987, "Thermo-Hydraulic Analysis of Bare and Finned Annular Sections ", D.Sc. Thesis, PUC-Rio. (In Portuguese)

Holman, J. P., 1994, "Experimental Method for Engineers", McGraw-Hill Book Co., 6th ed..

Jones, O. C., Jr., and Leung, J. M. C., 1981, "An Improvement in the Calculation of Turbulent Friction in Smooth Concentric Annuli", J. of Fluids Engineering, Vol. 103, pp. 615-623.

Kays, W.M., and London, A.L., 1964, "Compact Heat Exchangers", McGraw-Hill Book Company.

Kline, S. J., and McClintock, F. A., 1953, "Describing Uncertainties in Single Sample Experiments", Mech. Eng., pp. 3-8.

Malák, J., Hejna, J., and Schmid, J., 1975, "Pressure Losses and Heat Transfer in Non-circular Channels with Hydraulically Smooth Walls", Int. J. Heat Mass Transfer, Vol. 18, pp. 139-149.

Patankar, S.V., Ivanovic, M., and Sparrow, E. M., 1979, "Analysis of Turbulent Flow and Heat Transfer in Internally Finned Tubes and Annuli", Journal of Heat Transfer, Vol. 101, pp. 29-37.

Sodré, J.R., 1991, "Experimental Determination of Friction Factor for Annular Regions with Tubular Fins or Filled with Regenerative Porous Matrices", M.Sc. Dissertation, PUC-Rio. (In Portuguese)

Tew, R., 1978, "A Stirling Engine Computer Model for Performance Calculations", NASA - TM - 78884.

RBCM - J. of the Braz. Soc. Mechanical Sciences
Vol. XXI - No.1 - 1999- pp. 61-70

ISSN 0100-7386
Printed in Brazil

A Simplified Method for Axial-Flow Turbomachinery Design

Andre Luiz Amarante Mesquita
Cláudio Mauro Vieira Serra
Daniel Onofre de Almeida Cruz
Universidade Federal do Pará
Centro Tecnológico
Departamento de Engenharia Mecânica
66075-900 Belem, PA Brazil
gtdem@amazon.com.br

Nelson Manzanares Filho
Escola Federal de Engenharia de Itajubá
Departamento de Engenharia Mecânica
37500-000 Itajubá, MG Brazil
nelson@poisson.iem.efei.br

Abstract

This paper presents a methodology for design of axial-flow turbomachinery using the cascade flow model and the boundary-layer theory. The inviscid cascade flow is treated by means of a panel method with an empirical correction to take in account the viscous effects. By applying the momentum equation the drag coefficient of the cascade airfoils is related to the loss coefficient, the deflection coefficient, the inflow angle, and all the cascade geometric parameters. The applicability of the design criterion and the validity of the prediction method are analyzed by using experimental data from axial-flow fan rig tests.
Keywords: *Axial-Flow Turbomachinery, Cascade, Boundary-Layer, Fan.*

Introduction

Recent developments in computational fluid dynamics (CFD) allow the treatment of most of the complex flow structures found in turbomachinery (Keck *et al.*, 1996; Riedelbauch *et al.*, 1996). However, at the initial step of a turbomachinery design, there is a lack of information about the necessary geometrical definition for advanced CFD code application. At this step the designer needs to employ some design criteria in order to attend certain performance requirements, such as optimal operational parameters, aerodynamic loading, cavitation, shock effects, stall limits, etc. It is desirable that these criteria have good characteristics of selectivity and flexibility. In a very large universe of design options, they must be capable of selecting the eligible ones at a relatively low computational cost. In view of these aspects, it is natural to implement the design criteria by means of simplified CFD tools.

A good comparative review of various aerodynamic performance criteria for axial flow cascades was conducted by De La Fuente (1982). By employing the experimental data of Herrig et al. (1957) for NACA 65-series-airfoil cascades, De La Fuente (1982) concluded that the criterion based on the minimum suction pressure coefficient was the more adequate for selecting the minimum aerodynamic loss cascades. This criterion was initially proposed by Sholz (1965) for isolated airfoils, and was tested in axial-flow pump design by Fernandes (1973). However more studies are necessary in order to evaluate its real applicability in axial-flow turbomachinery design (Amarante Mesquita *et al*, 1996).

After the initial geometry definition, the advanced CFD codes can be employed in order to estimate the machine losses, and to determine the final geometry through an iterative process (designer's criteria versus losses minimization). Finally, its is necessary to preview the characteristic curves of the machine in order to evaluate its operational performance. This can be achieved by applying the CFD codes to several working conditions in the overall machine operational range. This procedure, however, requires a large amount of computer time. If the initial investment to purchase the full-version of advanced CFD codes is taken into account, the design costs can become too high for small size turbomachinery companies. In view of these aspects, the use of alternative methods with a low computational cost can be attractive.

The principal aim of this paper is to analyze in details a methodology for axial-flow turbomachinery design based on the minimum suction pressure coefficient criterion. The pressure distribution around the impeller blades is computed by using a cascade panel method (Manzanares Filho, 1994; Amorim,

Manuscript received: September 1997; revision received: October 1998. Technical Editor: Angela Ourívio Nieckele.

1986). In this inviscid method, a correction is applied for accounting the boundary layer effect on the cascade deflection angle, following the Gostelow procedure (Gostelow,1974). The cascade losses are accessed by applying a two-dimensional incompressible boundary-layer model (Cebeci and Bradshaw, 1977).

In order to verify the applicability of the methodology under consideration, experimental data from axial-flow fan rig tests were utilized. The fans were designed with five different values of the required minimum pressure coefficient at the impeller hub. The results indicated the validity of this present methodology as an useful tool for axial-flow turbomachinery design.

Cascade Geometry and Aerodynamic Coefficients

Figure 1 presents the cascade geometry, which performs the required flow deflection, and the corresponding velocity diagrams, where c is the absolute velocity, w is the relative velocity, and u is the cascade speed. The cascade deflection angle is defined as

$$\Delta\beta = \beta_1 - \beta_2 \tag{1}$$

where $\beta_1 = \beta + \alpha_1$ is the inlet flow angle, β is the stagger angle, α_1 is the angle of attack, and β_2 is the outlet flow angle. This effect can be also characterized by the dimensionless cascade deflection coefficient, δ_u

$$\delta_u = \frac{\Delta w_u}{w_a} = tg\ \beta_1 - tg\ \beta_2 \tag{2}$$

where Δw_u is the difference between the tangential velocity components and w_a is the axial velocity component (see Fig. 1).

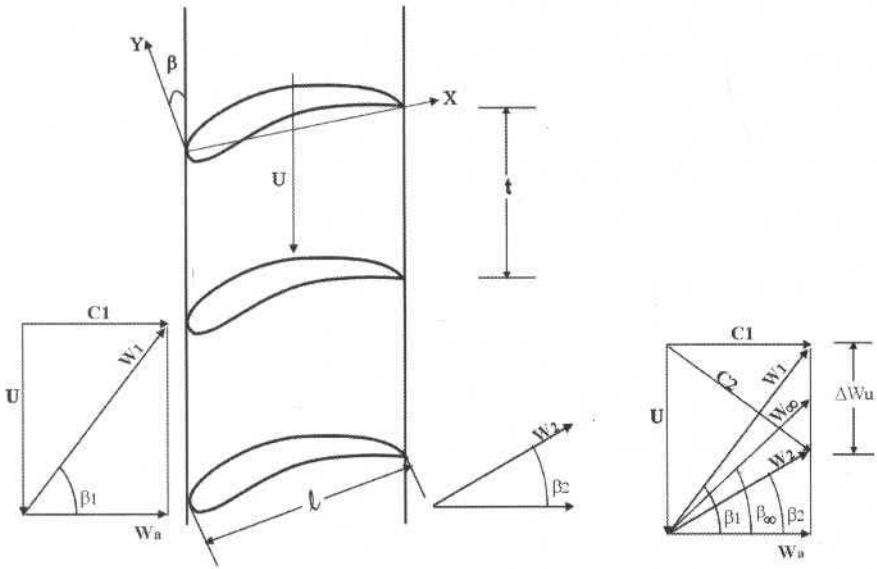

Cascade **Velocity Diagrams**

Fig. 1 The cascade geometry

The flow is considered as two-dimensional, incompressible, isothermal, and in steady-state condition. By applying the momentum equation in both axial and tangential directions one can obtain the following expressions (Gostelow, 1984)

$$c_L\sigma = 2\,\delta_u \cos\beta_\infty - \xi_v \sin\beta_\infty \cos^2\beta_\infty \tag{3}$$

$$c_D\sigma = \xi_v \cos^3\beta_\infty \tag{4}$$

In Eqs.(3) and (4), the lift coefficient, c_L, and the drag coefficient, c_D, are defined by

$$c_L = \frac{L}{1/2\,\rho w_\infty^2 \ell h} \tag{5}$$

$$c_D = \frac{D}{1/2\,\rho w_\infty^2 \ell h} \tag{6}$$

where w_∞ is the modulus of the mean velocity vector, $\mathbf{w}_\infty = (\mathbf{w}_1 + \mathbf{w}_2)/2$; β_∞ is the angle between the vector $\mathbf{w}_\infty$ and the axial direction; ℓ and h are the blade chord and blade length; L and D are the lift and drag forces; $\sigma = \ell/t$ is the cascade solidity, and ξ_v is the dimensionless loss coefficient of the cascade, defined by

$$\xi_v = \frac{\left[\left(p_1 + 1/2\,\rho w_1^2\right) - \left(p_2 + 1/2\,\rho w_2^2\right)\right]}{1/2\,\rho w_a^2} \tag{7}$$

where p_1 and p_2 are the inlet and outlet static pressures. For inviscid flow, $c_D = 0$, and Eq. (3) reduces to

$$c_L\sigma = 2\frac{\Delta w_u}{w_\infty} \tag{8}$$

Equations (3-4) relate the loss coefficient, the deflection coefficient, the angle of inflow, and all geometric parameters of the cascade (i.e., solidity, stagger angle, and profile geometry). Eq. (8) is the classical relation employed in turbomachinery design, which can be also derived from the Kutta-Joukowsky theorem (Gostelow, 1984).

Nomenclature

c = absolute velocity (m/s)
c_D = drag coefficient, related to the mean velocity (dimensionless)
c_{D1} = drag coefficient, related to the inlet velocity (dimensionless)
c_L = lift coefficient (dimensionless)
C_{psmin} = minimum suction pressure coefficient (dimensionless)
D = drag force (N); outlet fan diameter (m)
d = hub fan diameter (m)
h = blade length (m)
L = lift force (N)
ℓ = chord length (m)
n = rotational speed (rps)
n_q = specific speed (dimensiogless)
p_1 = inlet static pressure (N/m^2)
p_2 = outlet static pressure (N/m^2)
Q = volumetric flow rate (m^3/s)
t = distance between the airfoil cascade (m)
u = cascade speed (m/s)
w = relative velocity (m/s)
w_a = axial velocity component (m/s)
w_{max} = maximum surface velocity on the suction profile side (m/s)
w_1 = inlet velocity (m/s)
w_2 = outlet velocity (m/s)
w_∞ = mean velocity (m/s)
Y = specific energy (J/kg)
Y_r = design specific energy (dimensionless)
α_1 = angle of attack (degree)
β = stagger angle (degree)
β_1 = inlet flow angle (degree)
β_2 = outlet flow angle (degree)
β_∞ = angle of the vector w_∞ (degree)
$\Delta\beta$ = cascade deflection angle (degree)
Δw_u = difference between the tangential velocity components (m/s)
δ_u = cascade deflection coefficient (dimensionless)
ϕ = pressure coefficient (dimensionless)
η = efficiency (dimensionless)
ν = diameter ratio (dimensionless)
ρ = fluid density (kg/m^3)
σ = cascade solidity (dimensionless)
θ_{bf} = wake momentum thickness (dimensionless)
ξ_v = cascade loss coefficient (dimensionless)
ψ = pressure coefficient (dimensionless)

The drag coefficient can be also defined by using the inlet velocity instead of the mean velocity. In this form it is denoted c_{D1} and can be related to the c_D coefficient by

$$c_D = \left(\xi_v \cos^3 \beta_\infty\right) / \sigma = c_{D1} (\cos \beta_\infty / \cos \beta_1)^2 \tag{9}$$

The Minimum Suction Pressure Coefficient Criterion

The pressure coefficient is an important parameter, and give information on the aerodynamic loading of the cascade blades. It is defined as

$$C_p = \frac{p - p_0}{1/2\, \rho w_\infty^2} \tag{10}$$

where p is the static pressure on the airfoil, and p_0 is a reference pressure.

The minimum suction pressure coefficient, C_{psmin}, is defined as the minimum value of the pressure coefficient on the airfoil suction side. Normally, p_0 is the upstream static pressure, and this gives a negative value for C_{psmin}. This coefficient can be used as an aerodynamic loading criterion, allowing the selection of cascades with relatively low profile losses. Fig. 2 illustrates this concept. There is a C_{psmin} interval limited by an inferior value, C_{psi}, and a superior value, C_{pss}, which corresponds to a cascade with a low loss coefficient. It is important to note that both C_{psi} and C_{pss} have negative values. For $C_{psmin} > C_{pss}$, a slightly loaded blade is obtained, and the danger of boundary layer separation is reduced, but comparatively large area is exposed to the flow, i.e., the friction losses are augmented. In contrast, for a cascade with $C_{psmin} < C_{psi}$, the frictional area is relatively small but a comparatively high pressure loading is observed, increasing the danger of separation. So, in order to apply this criterion it is essential to determine with confidence the interval $C_{psi} < C_{psmin} < C_{pss}$. A properly way to accomplish this task is to test a series of turbomachines especially designed for this purpose.

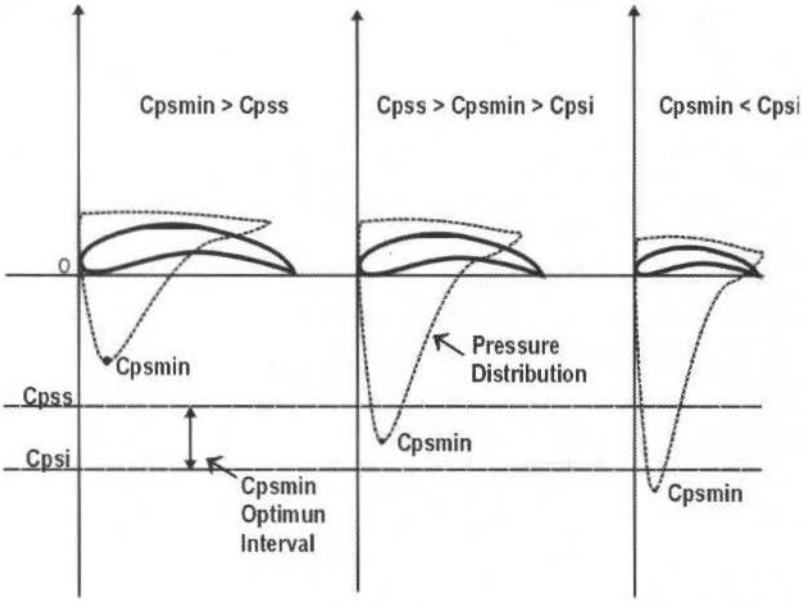

Fig. 2 The minimum suction pressure coefficient criterion concept.

Inviscid Method and Boundary-Layer Calculation

The minimum suction pressure coefficient criterion is established by potential flow calculation. The inviscid flow is calculated by a panel method (Manzanares Filho, 1994; Amorim, 1986). The numerical strategy involves the representation of the flow by a distributed vorticity sheet clothing the whole airfoil. The resulting boundary integral equation is solved through a computational scheme proposed by Lewis (1991).

In order to furnish an acceptable value for the deflection angle, an empirical correction is employed to take into account the viscous effects. This correction was proposed by Gostelow (1974) and consists in fairing-in the pressure distributions to avoid non-natural strong pressure gradients at the trailing edge region. Gostelow proposes that the fairing-in be done by extrapolating tangentially the pressure curves on both airfoil sides, from 85% chord location.

In the present paper, the Gostelow's procedure is generalized and the fairing-in chord location is treated as a function of a suitable loading coefficient. Fig. 3 shows some results obtained for the deflection angle of a typical cascade. The theoretical results corresponding to the inviscid flow with the Kutta condition (potential theory) and those obtained with the Gostelow correction procedure (corrected theory) are confronted with the experimental data obtained by Herrig *et al.* (1957). A good agreement is observed between the experiments and the Gostelow method. This kind of result was systematically observed in a series of computations made for various cascades with NACA 65-series airfoils. Furthers details can be found in Manzanares Filho (1994).

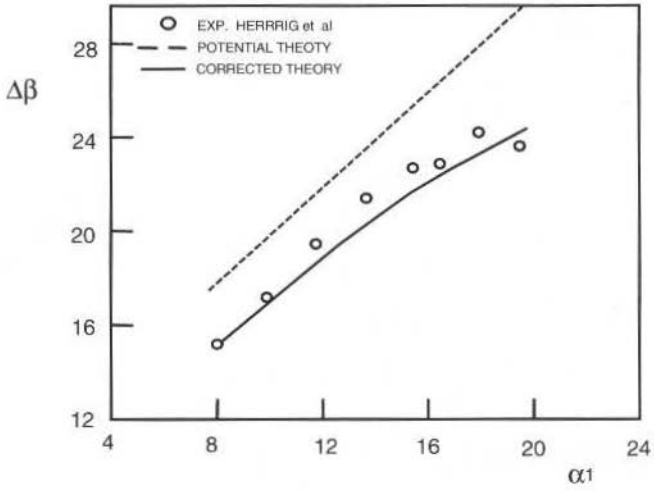

Fig. 3 Results for the deflection angle.

The two components of the drag force (shear stress and pressure distribution) are calculated separately. The contribution of the shear stress at the airfoil surface is obtained using the boundary-layer formulation, which also furnishes the location of the separation point. The component due the pressure distribution is obtained assuming that the pressure is constant in the separated region, with the same value computed at the separation point. The resultant force is then performed integrating the pressure distribution over the suction and pressure side of the airfoil. The total drag force is given by the sum of the both components.

The boundary-layer calculation is performed by applying the model reported by Cebeci and Bradshaw (1977) with an empirical correlation for the laminar-turbulent transition (Michel, 1952). The turbulent modeling is achieved by using the method proposed by Cebeci (1970).

An approximate form to compute the drag coefficient in cascades was proposed by Schlichting (1959)

$$c_{Dl} = 2\theta_{bf} \frac{cos^2 \beta_1}{cos^3 \beta_2} cos\beta_\infty \tag{11}$$

with

$$\theta_{bf} = \frac{0{,}004}{1{,}17\, ln(w_{max}/w_2)} \tag{12}$$

where θ_{bf} is the dimensionless wake momentum thickness (Lieblein, 1959) and w_{max} is the maximum local free-stream velocity outside the boundary layer on the suction profile side.

Figure 4 shows some results for the drag coefficient calculated by the present methodology in comparison with experimental data available in the literature (Herrig *et al.*,1957), and those obtained from the empirical method of Schlichting (1959). It is observed that the results from the present method and the experimental data have a similar behavior, and also that the Schlichting's method fails in this prediction. In spite of the good qualitative result found for the present method, the maximum relative deviation from the experimental data was about 30 %, with a mean value of 11 %, which allows, at least for engineering design purposes, an estimate of the airfoil drag and then the energy loss of the cascade.

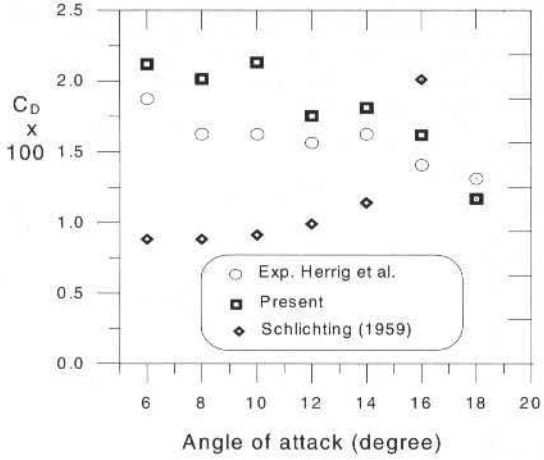

Fig. 4 Results for the drag coefficient.

Axial Fan Design and Testing

In order to evaluate the optimal C_{psmin} interval, five axial flow fans were designed, employing NACA 65-series airfoil for the blade geometry. Tab. 1 presents the main dimensionless fan coefficients: mass-flow coefficient, ϕ, pressure coefficient, ψ, specific speed, n_q, and diameter ratio, ν, defined by

$$\phi = \frac{w_a}{u} \tag{13}$$

$$\psi = \frac{2Y}{u^2} \tag{14}$$

$$n_q = \frac{n\sqrt{Q}}{Y^{3/4}} \tag{15}$$

$$\nu = \frac{d}{D} \tag{16}$$

where u is the cascade tangential velocity, defined as the product of the rotor angular velocity by the the blade radius for the cascade considered; Y is the specific energy, defined as the ratio of the rotor power by the mass flow rate; Q is the volumetric flow rate; n is the rotational speed; d is the hub diameter; and D is the outlet fan diameter.

Table 1 Dimensionless fan coefficients.

n_q	ψ	ϕ	ν
0,60	0,299	0, 293	0,50

The adopted procedure was to impose a different C_{psmin} value for the impeller hub cascade for each designed fan. Tab. 2 shows the main aerodynamic and geometrical parameters of the impeller hub cascade at the design operation point. The C_{psmin} values were computed by using the inviscid method already described. In this table, the value of the product $C_L.\sigma$ was evaluated by Eq.(8), with the nominal values for the flow rate (1.2 m^3/s) and specific energy (360 J/kg). The inner and outer fan diameters of the fans are, respectively, 195 mm and 390 mm, respectively. The cascade design for the other radial stations was made by assuming the free-vortex radial equilibrium, which involves the neglecting of the curvature term in the radial momentum equation. This flow distribution results in a constant axial velocity component and also in an uniform radial distribution of the specific energy, and, consequently, in highly twisted blades.

Table 2 Designed fan data for the impeller hub cascades.

Design	C_{psmin}	C_b	$C_L\sigma$ req.	ℓ mm	σ	C_L comp.	α deg.	β deg.
A	-6.84	1.2	1.32	65	0.85	1.55	12.4	38.2
B	-6.01	0.8	1.31	88	1.15	1.14	12.3	38.0
C	-3.90	1.2	1.31	83	1.09	1.21	9.7	40.6
D	-3.11	0.8	1.29	125	1.63	0.79	11.0	38.4
E	-2.32	1.2	1.31	90	1.17	1.11	9.2	40.9

The fans were built and tested in a specific test rig, constructed in accordance to AMCA 210-74 standard (1975). The systematic experimental uncertainties were evaluated as ±1% for the specific energy, ±1% for the mass flow rate and ±1.5% for the maximum efficiency values. Table 3 presents the fan test results obtained for the maximum efficiency, η_{max}, and the corresponding nominal specific energy related to the design value, Y_r (Y_r =1 at design). It is clearly observed that the specific energy approximates the design point of operation and a best efficiency is attained as C_{psmin} increases. These results indicate the validity of the C_{psmin} as a criterion for axial-flow turbomachinery design.

Table 3 Fan testing results.

Design	Y_r	η_{max}
A	0.45	0.22
B	0.60	0.32
C	0.70	0.33
D	0.80	0.36
E	0.90	0.55

Based on theses results, on experimental data of the NACA 65-series-blades (De La Fuente, 1982), and on pump testing data (Fernandes, 1973), it was possible to evaluate with confidence the interval $-2 \leq C_{psmin} \leq -1.6$ for the application of the minimum suction pressure coefficient criterion. This range will be used as a basis for the present study. It is important to note that these C_{psmin} values are related to the pressure distribution from the inviscid flow calculation.

Analysis of the Minimum Pressure Coefficient Criterion

It is possible to find a set of cascade that can satisfy both the minimum suction pressure coefficient criterion and the required aerodynamic conditions (Manzanares Filho, 1994). By adopting a specific airfoil, the cascade geometrical parameters (β, σ) are computed in order to satisfy both the cinematic condition (for instance the design defection angle, $\Delta\beta$) and a required value for C_{psmin}. Nevertheless, it is possible to adopt a new profile and then determine a new set of parameters (β, σ) which satisfies the same requisites for $\Delta\beta$ and C_{psmin}. Thus, one obtains a family of design solutions, and, for this reason, the C_{psmin} criterion can not be employed alone, but in conjunction with a loss prediction method. The design must be refined in order to select the optimal cascade in this family. This is achieved by minimizing the loss energy resulting from a viscous action, which, in the present study, is calculated by the boundary-layer model, as presented in the previous section.

The criterion analysis is carried out by using the same fan coefficients shown in Tab. 1. With these data, and using the NACA 65-C_b010 profiles (C_b is the camber coefficient), five cascade were selected with the minimum suction pressure coefficient, settled equal to -2,0, for the application of the criterion. The parameters of theses cascades are shown in Table 4. To maintain the same angle of deviation, the cascade solidity decreases to compensate the raise in the profile curvature. The corresponding pressure distribution for all cascades are shown in Fig. 5, and the lift coefficient was obtained by integration of these curves.

Table 4 Cascades Parameters

$C_{psmin} = -2{,}0$ e $\Delta\beta = 25{,}3°$, $\beta_1 = 59{,}6°$, $\beta_\infty = 50{,}1°$.

β	C_b	σ	α_1	$\Delta\beta_{corr}$	C_{L1}
38,6	08	2,5	21,0	25,3	0,32
39,4	10	2,0	20,2	25,5	0,43
39,9	12	1,5	19,7	25,7	0,56
40,5	15	1,0	19,05	25,8	0,75
41,4	18	0,9	18,2	25,4	0,89

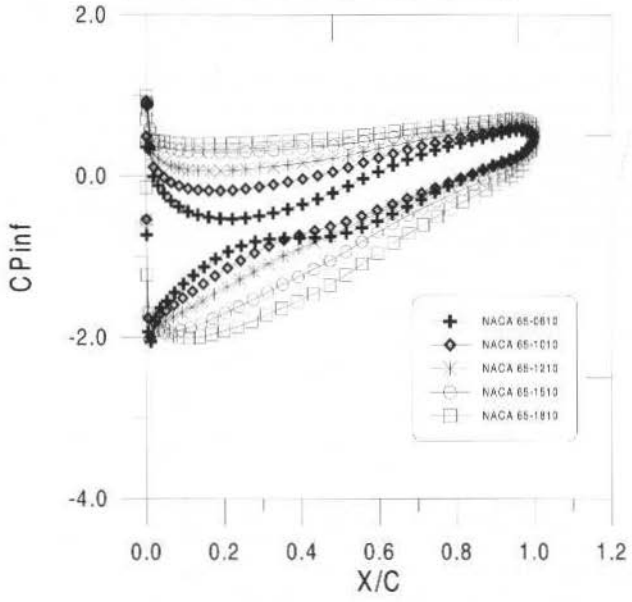

Fig. 5 Pressure distribution for cascades with same C_{psmin} value.

The boundary-layer calculation was then performed for these cascades in order to calculate the drag coefficient. Using the momentum balance, Eq. (4), and the relation between c_D and c_{D1}, Eq. (9), one can obtain the cascade loss coefficient. These results are shown in Tab. 5. For a small camber coefficient, the airfoil has a low lift coefficient, but the product $c_D.\sigma$ is large since the solidity presents a extremely great value. For a large camber coefficient the solidity is small and the lift coefficient is large. In this case the product $c_D.\sigma$ is large again since the c_D value is large. Thus, one observes that the loss coefficient presents a minimum, which corresponds to the optimum cascade for the required aerodynamic conditions. In this particular example, this minimum corresponds to a cascade with solidity equal to 1, stagger angle 40.5° and NACA 65-1510 airfoils (the camber coefficient equals to 1.5). An important fact, observed from the boundary-layer results, is that part of the flow around the optimum cascade airfoils is separated on the suction side. This means that the optimum cascade problem is closely related to the stall phenomena.

Table 5 Cascade Loss Coefficient Behavior.

C_b	C_{D1}	ξ_v
08	0,0125	0,234
10	0,010	0,150
12	0,011	0,129
15	0,015	0,116
18	0,025	0,166

Conclusion

A simplified methodology for axial-flow turbomachinery design was presented. It is based on the minimum suction pressure coefficient, C_{psmin}, at the impeller hub cascade. The cascade geometric parameters are determined in order to obtain a C_{psmin} value that furnish the required flow condition with a minimum aerodynamic flow loss. Five axial fans were designed and tested in order to access the methodology capability. The fan testing results have shown the validity of the presented methodology as an useful design guide for axial-flow turbomachinery. Nevertheless, the establishment of the optimum cascade geometry requires the determination of the loss through the cascade, due to the fact that it is possible to find a set of cascades that satisfies both the minimum suction pressure coefficient criterion and the required aerodynamic conditions.

A boundary-layer method was employed to calculate the cascade loss coefficient, and good results were found in comparisons with the experimental data available in the literature. By applying this method, it was possible to conclude that the loss coefficient attains a minimum, allowing to define an optimum cascade for a given nominal condition. It was also observed that the flow through this optimum cascade is partly stalled.

The proposed methodology furnishes a cheap procedure to obtain a good indication of the design geometric configuration of an axial-flow turbomachine, but in order to develop a better design methodology, other influences must be considered, as the secondary flows and tip clearance effects, not considered in a pure cascade model.

Acknowledgments

This work was supported by CNPq (Brazilian National Research Council) through the research project No. 523211/94-5 and CAPES-COFECUB program through the research project No. 001N/95.

References

AMCA 210-74 Standard, 1975 "Laboratory Methods of Testing Fans for Rating Purposes".

Amarante Mesquita, A. L., Manzanares Filho, N. and Fernandes, E. C., 1996, "A Methodology for Axial Flow Turbomachine Design", Proceedings of the VI ENCIT-LATYCIM, vol. 3, pp. 1883-1886, Florianópolis, Brasil.

Amorim, J. C. C., 1986, "Potential Flow Calculation Around Isolated Airfoils and Through Turbomachine Cascades" (in Portuguese), M.Sc Thesis, Escola Federal de Engenharia de Itajubá, Minas Gerais, Brasil.

De La Fuente, R. P., 1982, "Performance Evaluation Criteria for Linear Cascades" (in Portuguese), M.Sc. Thesis, Instituto Tecnológico de Aeronáutica, S. J. Campos, Brasil.

Fernandes, E. C., 1973, "Analysis of the Geometric Parameter Influences on the Axial Flow Turbomachine Design" (in Portuguese), M.Sc. Thesis, Instituto Tecnológico de Aeronáutica, S. J. Campos, Brasil.

Cebeci, T., 1970, "Behavior of Turbulent Flow Over a Porous Wall with Pressure Gradients", AIAA Journal, vol. 8, pp. 2152-2156, 1970.

Cebeci, T., and Bradshaw, P., 1977, "Momentum Transfer in Boundary Layers", Hemisphere Publishing Corporation.

Gostelow, J. P., 1984, "Cascade Aerodynamics", Pergamon Press, Elmsford, N.Y.

Gostelow, J. P., 1974, "Trailing Edge Flows Over Turbomachine Blades and the Kutta-Joukowsky Condition", ASME Paper 75-GT-94, pp. 2-16.

Herrig, L. J., Emery, J. C. and Erwin, J. R., 1957, "Systematic Two-Dimensional Cascades Tests of NACA 65-Series Compressor Blades at Low Speeds", NACA TN 3916.

Keck, H., Drtina, P. and Sick, M., 1996, "Numerical Hill Chart Prediction by Means of CFD Simulation for a Complete Francis Turbine", in Hydraulic Machinery and Cavitation, ed. Cabrera, E., Espert, V. and Martínez, F., vol. I, pp. 170-179, Kluwer Academic Publishers.

Lewis, R. I., 1991, "Vortex Element Methods for Fluid Dynamic Analysis of Engineering Systems", Cambridge University Press.

Lieblein, S., 1959, "Loss and Stall Analysis of Compressor Cascades", Journal of Basic Engineering, pp. 387-400.

Manzanares Filho, N., 1994, "Flow Analysis in Axial-Flow Turbomachines" (in Portuguese), Ph.D. Thesis, Instituto Tecnológico de Aeronáutica, S. J. Campos, Brasil.

Michel, R., 1952, "A Study of Flow Transition on Wing Sections: Establishment of a Transition Criterion and Section Drag Determination for Incompressible Flow" (in French), ONERA Rep. 1/1578 A.

Riedelbauch, S., Klemm, D. and Hauff, C., 1996, "Importance of Interaction Between Turbine Components in Flow Field Simulation", in Hydraulic Machinery and Cavitation, ed. Cabrera, E., Espert, V. and Martínez, F., vol. I, pp. 238-247, Kluwer Academic Publishers, 1996.

Schlichting, H., 1959, "Application of Boundary-Layer Theory in Turbomachinery, Journal of Basic Engineering", pp. 543-551.

RBCM - J. of the Braz. Soc. Mechanical Sciences
Vol. XXI - No.1 - 1999 - pp. 71-81

ISSN 0100-7386
Printed in Brazil

High Speed Cinematography of Dynamical Processes in Microdevices

Eberhard P. Hofer
Christian Rembe
Michael Beuten
Department of Measurement, Control and Microtechnology
university of Ulm
Albert-Einstein-Allee 41, 89081 Ulm, Germany
mrm.office@e-technik.uni-ulm.de

Abstract

Testing of micro devices, especially micro mechanical systems with movable parts, seems to be an essential step prior to introduction into the market. The acceptance of the micro device and its market share strongly depend on reliability which requires advanced testing methods.
In this paper, a testing equipment for visualizing and recording of highly dynamical phenomena of very short time durations in micro structures is presented. The cinematographic image sequences allow the extraction of position, velocity and acceleration of moving parts in micro devices.
In a first application, results for thermal ink jet print heads with emphasis on the fluid dynamical processes in the ink chamber were presented at DINAME 95 by Hofer, Patzer and Beurer (1995). For this microactuator - most sold world wide - the whole life cycle of droplet generation can be shown as it appears in real time. In addition to experimental testing, analytical and numerical studies have been carried out for a better understanding of the governing physical phenomena in thermal ink jet printing. As a consequence, valuable information about the design of ink jet print heads, wear of its heating element, printing at very high frequencies and the existence of satellite droplets during printing could be extracted.
The second application, which is presented in this paper, studies the dynamics of an electromagnetic micro relay in detail. The dynamical behavior of the free and bounded oscillations of the switching of the relay has been visualized in order to identify material parameters which are included in a state space model. This example clearly demonstrates the capability of a combined approach using cinematographic visualization together with systems theoretic methods for the development of high performance micro devices.
An outlook towards future research within the framework of high speed cinematography of dynamical processes in micro devices with emphasis on gaining more insight in transient behaviors concludes this research work
Keywords: *High-Speed-Photomicrography, Cinematography, Highly Dynamical Phenomena, Parameter Identification, Microactuators*

Introduction

In recent years, the technology progress of miniaturization and integration made it possible to massproduce systems with very small dimensions. The combination of integrated circuits and micromechanical sensors and actuators leads to powerful microsystems for signal processing, measurement, and automation technology.

However, micromechanical components are - in comparison with microelectronic circuitry - at the very beginning of their history of development. The production technology for mechanical microdevices is widely investigated but there are few suitable means of verifying the quality of the prototypes yet (Egelhaaf and Mayer, 1996).

This gap, especially the dynamic behavior of such micromechanical devices, can be filled by cinematographic visualization technique. This technique has been successfully applied for the first time to study ink chambers of thermal ink jet print heads. Experimental and numerical results are summarized in Fig. 1. These non-destructive measuring technologies are applicable to a wide variety of dynamical processes in microdevices. The processes can be observed directly without manipulating the microsystem.

Therefore we have developed two experimental setups to study high speed processes in micro devices. From cinematographic image sequences discrete motion data are available. One image furnishes information about the position of an object, two images provide velocity data.

By identifying the system parameters of a state space model of the investigated micro device the corresponding physical properties can be determined. This is a very important aspect in developing micro devices. Because of the very small dimensions of the microsystem, the measurement of material

Presented at DINAME 97 – 7th International Conference on Dynamic Problems in Mechanics, 3 – 7 March 1997, Angra dos Reis, RJ, Brazil. Technical Editor: Agenor de Toledo Fleury.

properties is difficult or, in some cases, impossible. The major problem is that most sensors are larger than the object to be measured.

In this paper, the investigation of the dynamic behavior of an electromagnetic micro switch using cinematographic data is presented in detail.

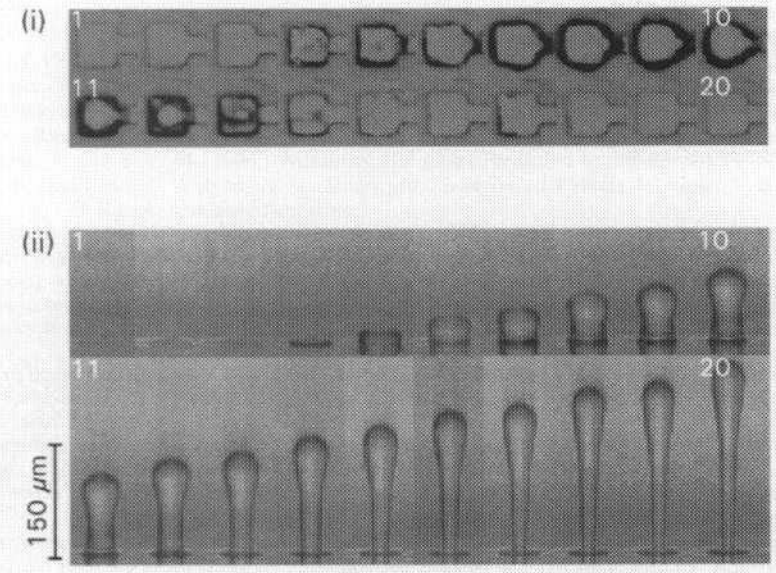

Fig. 1a Visualization of bubble nucleation, growth, and collapse (i) and droplet ejection (ii) in thermal ink jet printing. For both visualizations the interframe time is 1 µs and the exposure time is 250 ns.

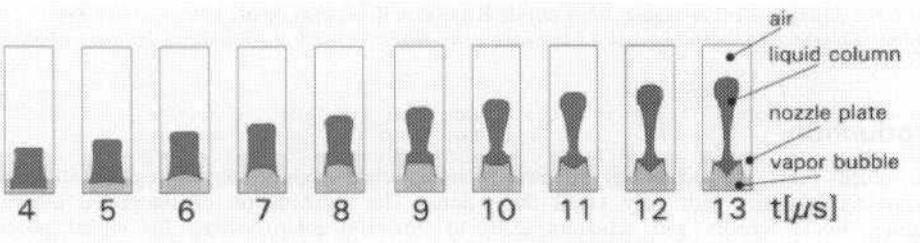

Fig. 1b Numerical simulation of droplet ejection.

Nomenclature

δ_0 = Width of air gap in steady state position [m]

μ_0 = Magnetic field constant $[\frac{Vs}{Am}]$

μ_r = Magnetic permeability [1]

$\omega_0 = 2\pi f_0 = \frac{2\pi}{T_0}$ = Natural frequency of undamped oscillation $[\frac{1}{s}]$

$\omega_d = 2\pi f_d = \frac{2\pi}{T_d}$ = Natural frequency of damped oscillation $[\frac{1}{s}]$

A_G = Cross-sectional area of air gap [m^2]

A_{Fe} = Cross-sectional area of magnetic core [m^2]

c_g = Spring constant $[\frac{N}{m}]$

d = Attenuation of lever oscillation [1]

F_{fr} = Frictional force [N]

F_{mag} = Magnetic force [N]

F_{sp} = Spring force [N]

I_c = Exciting current through coil [A]

$\hat{I}$ = Measured current values [m]

l_{Fe} = Effective length of magnetic core [m]

M = Mass of the micro relay lever [kg]

N = Number of coil windings [1]

r = Friction constant $[\frac{kg}{s}]$

T_1 = Time constant [s]

z = Deviation of micro relay lever from steady state position [m]

$\hat{z}$ = Measured deviation values [m]

Cinematographic Visualization Methods

The visualization technology is suited to measure position, velocity and acceleration. There are two different visualization methods, the pseudocinematographic and the realcinematographic visualization.

Pseudocinematographic visualization can be applied to reproducible transient processes. During the measurement, the reproducible process is repeated several times and visualized at different points of time, respectively. This method is based on the stroboscopic principle. The delay time between second shooting and the reference point of first shooting (Fig. 2a) corresponds to the interframe time. This procedure results in a series of sequential images.

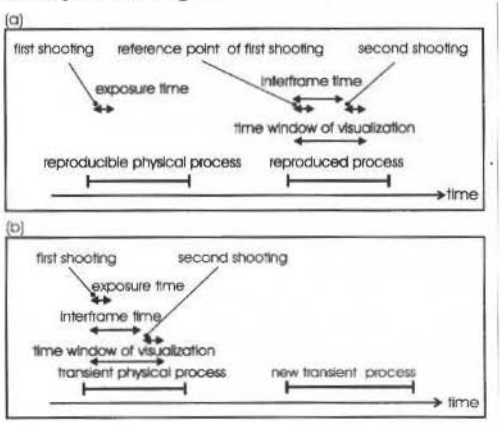

Fig. 2 (a) Pseudocinematographic and (b) realcinematographic visualization

Non-reproducible transient processes *must* be observed using realcinematographic visualization technology. This method allows registration of several frames of one single process. For extremely fast processes high speed framing cameras must be utilized to obtain sufficient frame rates and exposure times. Fig. 2b shows the principle of realcinematographic visualization.

Pseudocinematographic Setup

The experimental setup shown in Fig. 3 enables automatic registration of a series of images based on the pseudocinematographic visualization principle (Beurer, Hofer and Patzer, 1994). A stroboscope

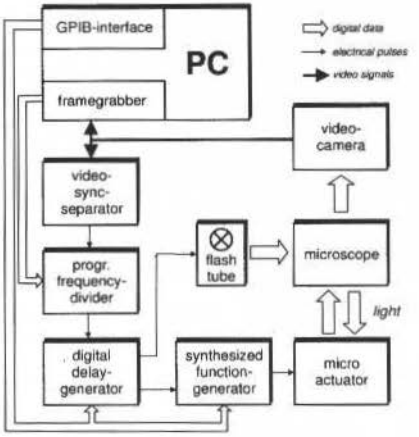

Fig. 3 Experimental setup for pseudocinematographic visualization

light attached to a microscope allows data registration with a time resolution of 250 ns and a spatial resolution better than 660 nm depending on the resolution of diffraction and the pixel size of the CCD-

sensor of the camera. The stroboscope light source has peak intensity in the blue wavelength area (400 nm < λ < 500 nm). Using a microscope lens with numeric aperture NA=0.75 the minimum distance between two objects to be separately perceptible is calculated (Hecht, 1990) as

$$d=0.61\frac{\lambda}{NA}=407nm$$

Images are recorded using a standard color CCD-camera with a pixel size of 11 μm. This is another limiting factor for the spatial resolution.

The microscope lens has a magnification factor of n = 50, which augments the resolution of the CCD-sensor to 220 nm. Hence, the image of an edge which is blurred by diffraction is imaged on two or three pixels. Therefore, the error for each measured position is smaller than 660 nm.

The microactuator is supplied with driving pulses by a function generator. A delay generator produces trigger signals for either the flash tube and the function generator such that an event of interest can be frozen and visualized at a selected time. A frame grabber board built in a personal computer (PC) digitizes the video images for further processing. After receiving the video image, the PC changes the settings of the delay generator in order to increase the time between the starting point of the process and the flash. The visualization process is triggered by the vertical synchronization pulse extracted from the analog video signal. Thus, the driving frequency of the microactuator equals to 25 Hz. To observe processes of longer duration a programmable frequency divider is used to reduce the driving frequency by a user-defined factor.

The computer contains a GPIB-interface which allows the user to set the parameters of measurement - e.g., interframe delay or the number of pictures to register - remotely by software. This software also provides various options for viewing, measuring, and saving a collection of images. The input signals for the microactuator are also dealt with comfortably by a signal editor.

Realcinematographic Setup

Visualizing short non-reproducible transient processes requires a very high temporal resolution of the imaging device. In our experimental setup we have attached the commercially available high speed camera IMACON 468, manufactured by Hadland Photonics, to a microscope. The principle of the setup is described as follows: The microscope images the object. The camera, including a beamsplitter composed of eight lenses and a prism, is adjusted to record the image. The beamsplitter parcels the image into eight images which, at most, can be detected by eight microchannel plate (MCP) sensors. Our setup includes six channels so that we can shoot a maximum of six frames of one transient process. The spatial resolution of this setup is also limited by the resolution of diffraction and the pixel size of the MCP-sensors and results in d=550 nm. The error of position measurement is higher because the complex beam path in the camera leads to distortion of the images. This error can be corrected by digital image processing. Exposure and interframe times are selectable with a resolution of 10 ns.

This results in a maximum frame rate of 100 million frames per second.

Another important part of our setup is a powerful flashlight source (Krehl et. al., 1996) which produces a light pulse of very high constant intensity (approx. 50 Mcd) over a period of 100 μs. This light source ensures a satisfactory image quality even at shortest exposure times. For longer and slower processes like the oscillation of the micro relay lever, a commercial permanent light source is used (Xenon High-Pressure Lamp XBO 75 W, Carl Zeiss Jena GmbH).

The principle of the setup is depicted in Fig. 4.

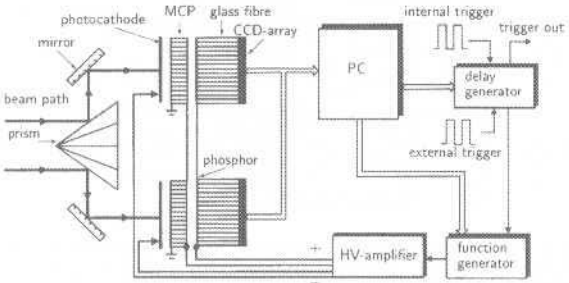

Fig. 4 Principle of the high speed camera IMACON 468

Experimental Results

As an example for the investigation of dynamic processes in microsystems, a micro relay (Rogge et al., 1995) developed at the Institute of Microstructure Technology - a joint institution of Research Centre Karlsruhe and the University of Karlsruhe - was analyzed. The outline of this micro relay is shown in Fig. 5. The dimensions of the microactuator are 4 mm x 2.3 mm x 100 µm. The gap width

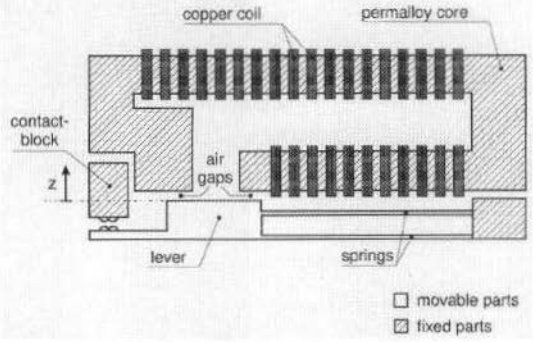

Fig. 5 Outline of the micro relay

between the contact block and the lever is approx. 30 µm. A current applied to the coil results in a magnetic field in the permalloy core. The resulting magnetic force moves the lever towards the contact block and closes the contact. When the current is switched off, the springs force the lever back into its steady state position.

In a first experiment, a 2 ms current pulse of 60 mA was chosen as input signal. Using pseudocinematographic visualization the process was repeated with a frequency of 6.25 Hz (vertical video-sync clock divided by 4). Figure 6 shows an image sequence recorded with an interframe delay of 50 µs. It is obvious that the micro relay lever performs an almost undamped oscillation. The lever touches the contact block several times after switching off the current - this is an undesirable effect, of course. The images show, that the switching process of the micro relay is reproducible for low frequency input signals. When applying current pulses with higher frequency to the coil, non-reproducible phenomena occur. In this case pseudocinematographic visualization fails and the lever seems to flutter.

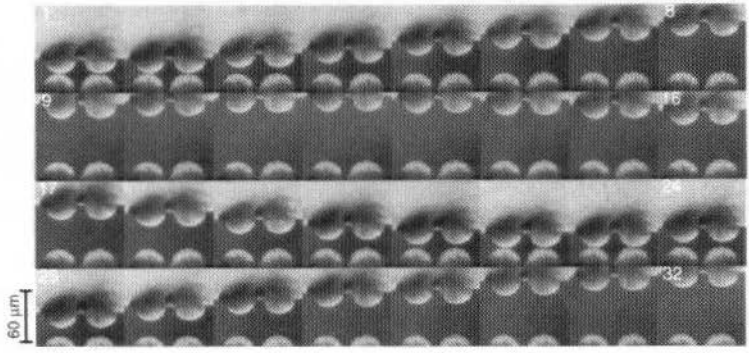

Fig. 6 Pseudocinematographic image sequence showing the oscillation of the lever. The interframe time is 50 µs, the exposure time is 250 ns.

Therefore, realcinematographic visualization is the appropriate means to investigate these non-reproducible processes. Fig. 7 shows two series of images taken with the IMACON 468 camera. The interframe delay is 200 µs. The input signal was a rectangular burst with three pulses and a delay time of 2 ms. The images show the first closing of the contact after the third pulse of the burst. The comparison shows different lever positions at corresponding points of time. Consequently, the dynamical process is not reproducible any more.

The presented images show the contact area of the micro relay which give an idea of the functionality of the micro system. However, to obtain motion data for system identification the air gap width has to be measured because it has a direct influence on the magnetic force.

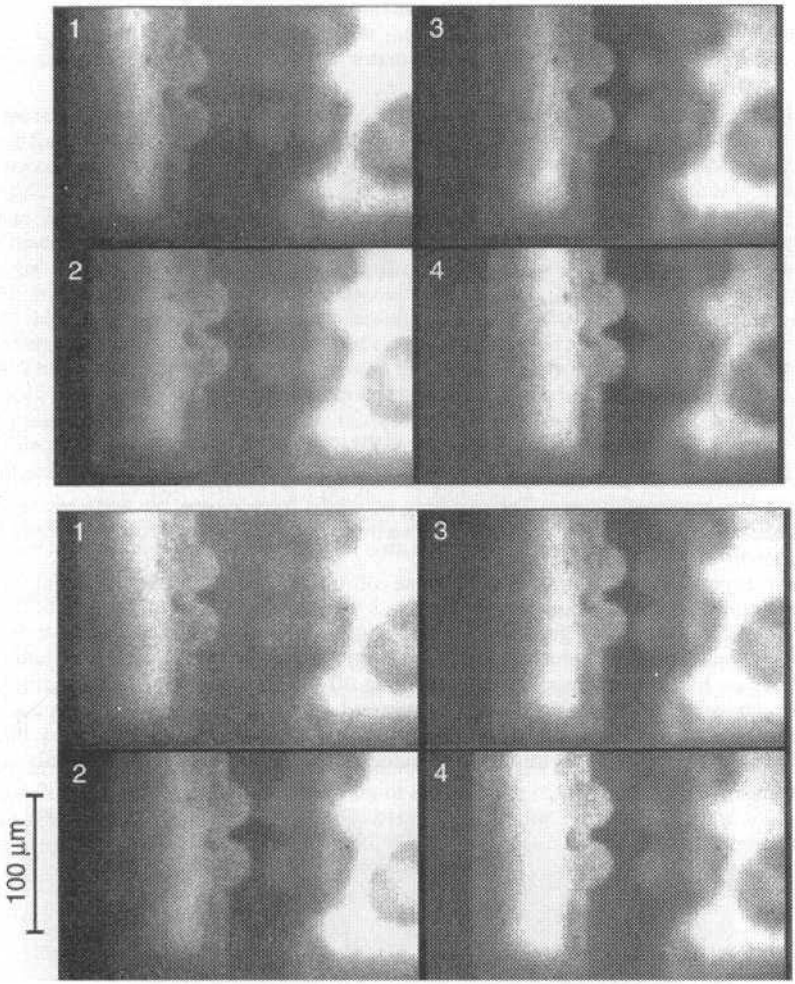

Fig. 7 Realcinematographic image sequences showing the oscillation of the lever. The interframe time is 200 µs, the exposure time is 1 µs.

Characterization of a Micro Relay

Modelling of System Dynamics

The dynamical behavior of the contact lever is described by a spring-mass-damper-system (Rogge 1996). The magnetic coil produces an exciting force in positive z-direction measured from the steady state (Fig. 5). The

spring force counteracts lever deviation and is calculated using Hooke's law. Depending on the lever velocity frictional effects cause a damping force. Newton's law describes the system's dynamics

$$M\ddot{z}(t) = F_{mag}(t) + F_{fr}(t) + F_{sp}(t) \qquad (1)$$

where M is the mass of the lever. By

$$F_{mag}(t)=\left(\frac{N\mu_0\mu_r I_c(t)}{\frac{A_G}{A_{Fe}}l_{Fe}+2\delta(t)\mu_r}\right)^2\frac{A_G}{\mu_0}$$

the magnetic force is denoted. The effective length of the magnetic core is represented by l_{Fe}, $\delta(t) = \delta_0 - z(t)$ denotes the width of the air gap between lever and core. N represents the number of coil windings, μ_0 the magnetic field constant, A_G the cross-sectional area of the air gap and A_{Fe} the cross-sectional area of the permalloy core. The exciting current is denoted by $I_c(t)$, μr is the permeability of the core material. The velocity dependent frictional force can be written as

$$F_{fr}(t)=r\dot{z}(t).$$

In this equation, r is the friction constant. The parallel springs with spring constant c_g produce the force

$$F_{sp}(t)=-c_g z(t)$$

if the deviation z is sufficiently small.

The natural frequency ω_d of a damped harmonic oscillator differs from the natural frequency ω_0 in the undamped case. The equation

$$\frac{\omega_d}{\omega_0}=\sqrt{1-d^2}\approx 1-\frac{1}{2}d^2$$

describes the relation between this frequency shift and the damping coefficient d. Cinematographic image sequences of unbounded oscillations of the micro relay lever clearly showed that the system's damping coefficient is very small ($d << 1$). Therefore, the frequency shift is negligible and the approximation

$$\omega_d\approx\omega_0 \; resp. \; T_d\approx T_0 \qquad (2)$$

with T_0 as time duration of the oscillation can be used to replace the lever mass M and the friction constant r by parameters which are identifiable by evaluating cinematographic data. With

$$M=c_g\frac{T_0^2}{4\pi^2} \; and \; r=2d\sqrt{c_g M}$$

the equation of motion (1) results in

$$\ddot{z}(t)=\frac{4\pi^2}{c_g T_0^2}\left(\frac{N\mu_0\mu_r I_c(t)}{\frac{A_G}{A_{Fe}}l_{Fe}+2\mu_r(\delta_0-z(t))}\right)^2=\frac{A_G}{\mu_0}d\frac{4\pi}{T_0}\dot{z}(t)-\frac{4\pi^2}{T_0^2}z(t).$$

This dynamic equation can be rewritten as a nonlinear state space representation with two state variables, deviation $x_1(t) = z(t)$ and velocity $x_2(t) = \dot{z}(t)$. Due to self-induction the exciting current through the coil is the step response of the input signal $u(t) = u_0\,\sigma(t)$ and can be modelled as

$$T_1 \dot{I}_c(t) + I_c(t) = u(t)$$

with the time constant T_1. The input signal $u(t)$ results from a voltage controlled current supply and u_0 denotes $I_{c0} = \lim_{t \to \infty} I_c(t) = const.$. Therefore, the third state variable $x_3(t) = I_c(t)$ is introduced. The resulting nonlinear state space equations read as

$$\begin{pmatrix} \dot{x}_1(t) \\ \dot{x}_2(t) \\ \dot{x}_3(t) \end{pmatrix} = \begin{pmatrix} x_2(t) \\ -a_0 x_1(t) - a_1 x_2(t) + b(x_1(t)) x_3^2(t) \\ \frac{1}{T_1} x_3(t) + \frac{1}{T_1} u(t) \\ y(t) = x_1(t) \end{pmatrix} \tag{3}$$

with the parameters

$$a_0 = \frac{4\pi^2}{T_0^2}, a_1 = d\frac{4\pi}{T_0}, b(x_1(t)) = \frac{4\pi^2}{c_g T_0^2} \left(\frac{N\mu_0\mu_r}{\frac{A_G}{A_{Fe}} l_{Fe} + 2\mu_r(\delta_0 - x_1(t))} \right)^2 \frac{A_G}{\mu_0}$$

The system has only one output, the lever deviation $y(t) = x_1(t)$.

Identification of System Parameters

Damping coefficient d and Natural Frequency f_0 of the Micro Relay Lever

The attenuation of the micro relay can be calculated using the decay coefficient of the oscillation,

$$\Delta = \frac{\ln q \omega_d}{2\pi} \text{ with } q = \frac{\hat{z}_i}{\hat{z}_{i+1}} \tag{4}$$

where q denotes the quotient of two successive maxima of the harmonic oscillation. The parameter Δ can also be expressed as

$$\Delta = \omega_0 d \tag{5}$$

with the natural frequency ω_0 of the undamped oscillation. Assuming that d is very small the approximation (2)

$$\omega_d \approx \omega_0 = 2\pi f_0$$

can be used; thus equations (4) and (5) result in

$$d \approx \frac{\ln q}{2\pi}$$

To determine the parameter d the maximum amplitudes of ten successive periods of the oscillation were measured. The average damping coefficient of the investigated relay equals to

$$\bar{d} \approx 0.0118 \pm 0.002$$

The time points corresponding to the maxima and minima of the oscillations were used to measure the frequency f_0. The measurement error consists of two components: the limited spatial resolution of the setup leads to a frequency error $\Delta f_0 = 0.73$ Hz. The approximation $f_s \approx f_0$ causes an additional relative error of $\Delta f_0 / f_0 = 7 \cdot 10^{-3}$. The average value of the natural frequency of the micro relay lever oscillation and the approximation error result in

$$\bar{f}_0 = 829.7 \pm 0.79 Hz$$

Spring Constant c_g and Magnetic Permeability μ_r

The stationary values of the micro relay lever deviation can be calculated from equation (3) by setting the derivative of the state vector to zero. This results in

$$c_g z = \left(\frac{N \mu_0 \mu_r}{\frac{A_G}{A_{Fe}} l_{Fe} + 2\mu_r (\delta_0 - z)} \right)^2 \frac{A_g}{\mu_0} I_c^2 \qquad (6)$$

with the two unknown parameters spring constant c_g and magnetic permeability μ_r. It is obvious, that the exciting current I_c is time independent in the characteristic line $z(I_c)$. Equation (6) is a third order equation in z and can be solved numerically or analytically by Cardano's formula. Here the numerical technique was utilized.

Therefore, the parameters can be identified by minimizing a cost function $J(\mu_r, c_g)$. In this case, the cost function is the sum of squared errors of the calculated deviations z and measured data $\hat{z}[n]$, n = 1...N. Thus,

$$J(\mu_r, c_g) = \sum_{n=1}^{N} \left\{ \hat{z}[n] - z(\mu_r, c_g, \hat{I}[n]) \right\}^2,$$

where $\hat{I}[n]$, n = 1...N, are the values of the input current corresponding to the $\hat{z}[n]$.

The minimization $J(\mu_r, c_g)$ was performed by a Nelder-Mead simplex algorithm (Nelder and Mead, 1964) implemented in the numerical mathematic software MATLAB from The Math Works, Inc. Fig. 8 shows the measured deviations from steady state (circles) and the solution of Eq. (6) after

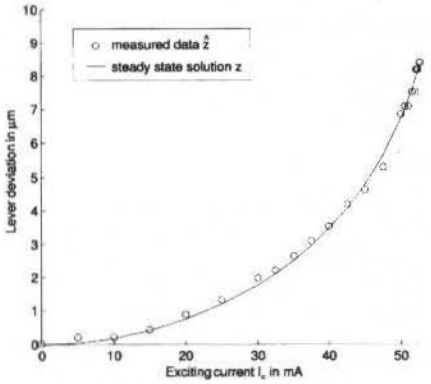

Fig. 8 Identification of the parameters μ_r and c_g

minimizing $J(\mu_r, c_g)$. The results of this identification are

$$\mu_r = 697 \text{ and } c_g = 5.3 \frac{N}{m}$$

In this case, a discussion of errors is difficult, because the error is influenced by the quality of the model.

Time Constant T_1 of the Exciting Current I_c

The identification of the parameter T_1 was carried out by investigating the dynamical behavior of the micro relay after applying a current pulse of constant amplitude to the coil. The resulting step response was visualized and the lever trajectory was extracted for different input signal amplitudes. The circles in Fig. 9 represent the measured lever positions plotted over the time *t*. The amplitudes of the input pulse were 55 mA, 60 mA, 70 mA, 80 mA and 90 mA.

Using the differential equation system (3), the dynamical behavior can be calculated numerically, e.g. using a Runge-Kutta algorithm. Again, minimizing the sum of squared errors between measured and calculated data relative to T_1 results in an optimal estimate for the time constant

$$T_1 = 20 \mu s$$

The graphs in Fig. 9 depict the calculated step responses of the fully identified state space model for the microrelay.

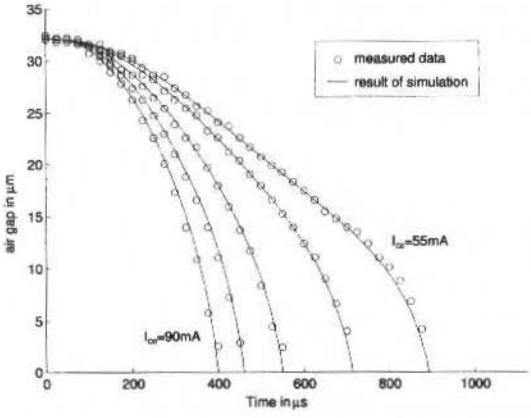

Fig. 9 Dynamical behavior of the micro relay lever, simulation versus measured data

Obviously, the model output shows a very good correspondence to the real data obtained by pseudocinematographic visualization.

Conclusion and Outlook

In this paper, the applicability of cinematographic visualization methods to determine material properties in microsystems has been demonstrated. Two experimental setups were described which allow automatic PC-based registration of cinematographic motion data.

The pseudocinematographic setup was used to identify the parameters of a state space model of an electromagnetic microactuator. It has been proved by numerical simulations of the dynamic behavior of the system that the model represents the system dynamics very accurately.

In a second experiment, non-reproducible phenomena which occured when the microactuator was operated with high frequency driving pulses were visualized using the realcinematographic visualization method.

Future research is directed towards studying more micro devices. Next step is the real high speed framing photomicrography of the non-reproducible transient phenomena in a microturbine. The turbine rotates with approximately 200000 revolutions per minute.

Acknowledgments

The authors would like to thank B. Rogge, J. Schulz, J. Mohr, A. Thommes and W. Menz from the Institute of Microstructure Technology in Karlsruhe, Germany for the possibility to investigate the micro relay.

References

Beurer, G., Hofer, E.P., and Patzer, J., 1994, "Process Control for Improvement of Print Quality and Life Time of Bubble-Jet Printers". Proc. of IS\&T/SPIE Symposium on Electronic Imaging: Science and Technology, Feb., San Jose, California, USA

Egelhaaf, P.and Mayer, K. M., 1996, "Mikrosystemtechnik: Von der Forschung zu innovativen Produkten". Physikalische Blätter 52, Nr. 9, pp. 900-902

Hecht, E., 1990, "Optics Addison-Wesley series in physics".

Hofer, E.P., Patzer, J., and Beurer, G., 1995, "Numerical and Experimental Studies on Bubble Jet Printheads". Proc. of 6th International Conference on Dynamic Problems in Mechanics, Brazil

Krehl, P., Engemann, S., Rembe, Ch., and Hofer, E.P., 1996, "Versatile Microscope-Coupled High-Intensity Pulsed Light Source for High-Speed Cine Photomicrography of Microactuators". Proc. of 22nd International Congress on High-Speed Photography and Photonics, October, Santa Fe, USA

Nelder, J.A., and Mead, R., 1964, "A Simplex Method for Function Minimization". Computer Journal, Vol. 7, pp. 308-313.

Rembe, Ch., Patzer, J., Hofer, E.P., and Krehl, P., 1996, "Realcinematographic Visualisation of Droplet Ejection in Thermal Ink Jets". Journal of Imaging Science and Technology, Vol. 40, No. 5, Sept./Oct., pp. 401-404

Rogge, B., Schulz, J., Mohr, J., Thommes, A., and Menz, W., 1995, "Fully Batch Fabricated Magnetic Microactuators Using a Two Layer Liga Process". Proc. of International Conference on Solid-State Sensors and Actuators, Transducers 95, June, Stockholm, Sweden

Rogge, B., 1996, "Entwicklung, Optimierung und Test von elektromagnetischen Linearaktoren basierend auf LIGA-Mikrotechnik". Dissertation zur Erlangung des akademischen Grades eines Doktors derIngenieurwissenschaften. Fakultät für Maschinenbau, Universität Karlsruhe, Februar.

RBCM - J. of the Braz. Soc. Mechanical Sciences
Vol. XXI - No.1 - 1999- pp. 82-90

ISSN 0100-7386
Printed in Brazil

On the Usefulness of Antiresonances in Structural Dynamics

Domingos Alves Rade
Leandro Afonso da Silva
Federal University of Uberlândia
Fhysical Sciences Department P. O. Box 593
38400-902 Uberlândia, MG Brazil
domingos@ufu.br
lafonsos@ufu.br

Abstract

In this paper a study focusing the zeros of frequency response functions (FRFs) of linear mechanical systems is presented. Two major aspects are focused: the underlying theory, including a physical interpretation of the zeros of both transfer and driving point FRFs in terms of structural modifications, and the possibility of practical exploration of the FRF in some structural dynamics applications, namely: finite element updating, structural damage identification and vibration attenuation using dynamic vibration absorbers. After presentation of the theory, some results of applications performed on both numerically simulated and experimental mechanical systems are presented o illustrate the practical use of the zeros.

Keywords: *Antiresonances, System Identification, Modal Analysis, Structural Modifications, Damage Localization*

Introduction

The dynamic behavior of linear mechanical systems can be modeled, in the frequency domain, by a set of frequency response functions (FRFs) which, in turn, can be expressed in terms of their *poles* and *zeros*, related to the *resonance frequencies* and *antiresonance frequencies*, respectively. The large majority of modal-based analysis and identification techniques are founded on the utilization of natural frequencies and mode shapes associated with the poles of the FRFs, while much less attention has been paid to the FRF zeros. One of the reasons for this is the belief that an accurate identification of the antiresonances from experimentally measured FRFs is hard to be achieved. In fact, due to their dependence on spatial input and output measurement locations and their typically low signal to noise ratio, FRF zeros are more likely to be affected by experimental errors than are the poles. Nevertheless, it must be remembered that the incessant improvements of the vibration testing equipment and procedures as well as of the digital signal processing and experimental techniques have been making it possible to obtain experimental vibration data with an ever increasing accuracy. So, the use of the antiresonances seems to be a very attractive alternative in the realm of various structural dynamics problems.

Important contributions to clarifying the physical and mathematical nature of the antiresonances were made by Flannely (1971) and Miu (1991). The authors of this paper have been investigating the potential usefulness of the antiresonances in practical structural dynamics applications (Rade, 1994), (Silva, 1996), (Rade, Lallement and Silva, 1996). In this paper, two major aspects concerning the zeros of FRFs are examined namely: 1st) some key properties and physical interpretation of FRF zeros and, 2nd) some practical applications for which the antiresonances can be conveniently used. These applications are illustrated through numerical results recently obtained by the authors.

Basic Definitions and Properties of Poles and Zeros of FRFS

Consider a self-adjoint undamped structure, modeled with mass matrix $[M] \in \mathrm{R}^{N,N}$ (symmetric, positive definite) and stiffness matrix $[K] \in R^{N,N}$ (symmetric, positive semidefinite), for which the equations of motion in the time domain are written:

$$[M]\{\ddot{x}(t)\}+[K]\{x(t)\}=\{f(t)\} \tag{1}$$

where $\{f(t)\}$ and $\{x(t)\}$ are the vectors of forcing functions and displacement time responses, respectively. For a set of harmonic external forces given by:

Presented at DINAME 97 - 7th International Conference on Dynamic Problems in Mechanics, 3-7 March 1997, Angra dos Reis, RJ, Brasil. Technical Editor: Agenor de Toledo Fleury.

$$\{f(t)\} = \{F(\omega)\}e^{i\omega t} \in C^{N,1}, \tag{2}$$

the steady state solution to (1) takes the form:

$$\{x(t)\} = \{X(\omega)\}e^{i\omega t} \in C^{N,1} \tag{3}$$

Introducing Eqs. (2) and (3) into Eq. (1), the following relation between the amplitudes of the response and the amplitudes of the excitation forces is obtained:

$$\{X(\omega)\} = [Z(\omega)]^{-1}\{F(\omega)\} = [H(\omega)]\{F(\omega)\}, \tag{4}$$

where $[Z(\omega)] = ([K] - \omega^2[M]) \in R^{N,N}$ is the dynamic stiffness matrix and $[H(\omega)] = [Z(\omega)]^{-1}$ is the receptance matrix, dynamic flexibility matrix or FRF matrix. From the properties of matrix inversion, it follows that:

$$[H(\omega)] = [Z(\omega)]^{-1} = \frac{1}{det([Z(\omega)])} Adj([Z(\omega)]) \tag{5}$$

From (5), a single FRF $H_{ij}(\omega)$, which represents the amplitude of the response at coordinate i, for a single force of unitary amplitude applied at coordinate j is given by the expression:

$$H_{ij}(\omega) = (-1)^{i+j}(K_{ij} - \omega^2 M_{ij}) \frac{det([K_{ij}] - \omega^2[M_{ij}])}{det([K] - \omega^2[M])} \tag{6}$$

where $[M_{ij}]$ and $[K_{ij}] \in R^{N-1,N-1}$ are non symmetric matrices, obtained by canceling the j-th lines and i-th columns of matrices *[M]* and *[K]*. Development of the determinants indicated above leads to:

$$H_{ij}(\omega) = \frac{a_0 + a_1\lambda + a_2\lambda^2 + \cdots + a_{N-1}\lambda^{N-1}}{b_0 + b_1\lambda + b_2\lambda^2 + \cdots + a_N\lambda^N} = \alpha_{ij} \frac{\prod_{r=1}^{N-1}(\lambda - {}^{ij}\lambda_r)}{\prod_{r=1}^{N}(\lambda - \lambda_r)}, \tag{7}$$

where $\lambda_r = \omega_r^2$, $\lambda = \omega^2$. In Equation (7), λ_r, $r = 1,2,...$ are the poles, and ${}^{ij}\lambda_r$, $r = 1,2,...$ are the zeros of $H_{ij}(\lambda)$. As it can be seen in Eq. (6), the poles are all real and non negative, since they correspond to the eigenvalues of the undamped, self-adjoint, positive definite (or positive semidefinite) structure. As for the zeros, they can be either real or complex, since they are the roots of a characteristic polynomial associated with matrices $[M_{ij}]$ and $[K_{ij}]$, which are generally non symmetric. In the particular case of a driving point FRF (i=j), both matrices $[M_{ii}]$ and $[K_{ii}]$ are symmetric, positive definite (or positive semidefinite) and all the zeros are then real, non negative. Physically, the poles are associated with the resonance frequencies, for which the amplitude of the response tends to become infinite, while the real zeros are related to the antiresonance frequencies, i.e., the frequencies for which the harmonic response at the i-th coordinate vanishes. Another important feature, which can be deduced from Eq. (6) is that the poles are global properties, i.e, they do not depend upon the particular FRF considered, while the zeros are local properties, which depend on the choice of coordinates i and j where the response is observed and the excitation force is applied, respectively.

Physical Interpretation of FRF Zeros in Terms of Structural Modifications

In this section, a novel physical interpretation of the real zeros of transfer FRFs is presented, in terms of structural modifications. Consider a structure which is acted upon by a single control force applied at coordinate j, given by: $f_j = -k_{ij}x_i$, where x_i is the displacement at coordinate i. The pertaining dynamic stiffness relation is written:

$$([K]-\lambda\,[M])\{x(\lambda)\} = -k_{ij}\{I_j\}\{I_i\}^T\{x(\lambda)\}, \tag{8}$$

where $\{I_i\}$ denotes the i-th column of the identity matrix of order N. This last relation can be re-written under the form:

$$\left([K]+k_{ij}\{I_j\}\{I_i\}^T-\lambda\,[M]\right)\{x(\lambda)\} = \{0\} \tag{9}$$

Equation (9) can be interpreted as an eigenvalue problem, associated with a modified structural configuration, obtained by a fictive addition of a stiffness k_{ij}, connecting coordinates i and j, represented by $[\delta K] = k_{ij}\{I_i\}\{I\}^T$. Further development of (9) leads to the following frequency equation (whose roots correspond to the eigenvalues of the modified configuration), expressed in terms of the receptance matrix:

$$1 + k_{ij}H_{ij}(\lambda_r) = 0 \Rightarrow H_{ij}(\lambda) = -\frac{1}{k_{ij}} \tag{10}$$

This last equation can be interpreted with the aid of Fig. 1.

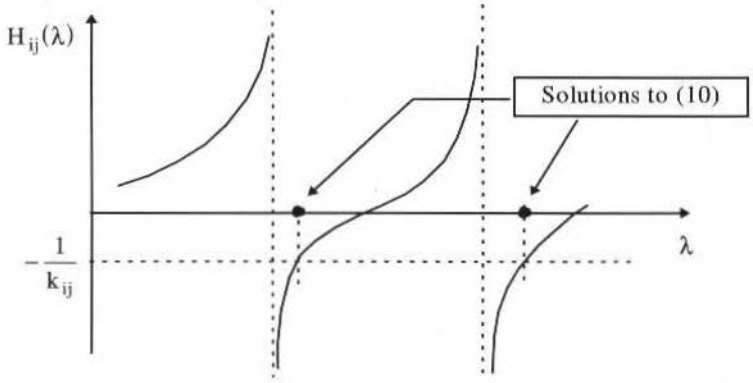

Fig. 1 Graphical interpretation of the characteristic Equation (10).

When $k_{ij} \to \infty$, Eq. (10) becomes:

$$H_{ij}(\lambda) = 0, \tag{11}$$

whose solutions are precisely the zeros of the FRF $H_{ij}(\lambda)$

It can thus be concluded that the real zeros of a transfer FRF $H_{ij}(\lambda)$ correspond to the eigenfrequencies of a modified structural configuration obtained by a fictive stiffness addition given by $[\delta K] = \lim_{k_{ij}\to\infty} k_{ij}\{I_i\}\{I_j\}^T$. In the particular case where i=j, this stiffness addition corresponds to the

physical grounding of coordinate i to the fixed space, the zeros of a driving point FRF $H_{ii}(\lambda)$ correspond to the natural frequencies of the structure with coordinate i grounded.

Antiresonance Eigenvalues and Eigenvectors

In this paragraph, it is formally demonstrated that the antiresonances of transfer FRFs are the eigensolutions of non self-adjoint systems.

For a single harmonic force applied at coordinate i, the dynamic stiffness and flexibility relations can be partitioned as follows:

$$\left[\begin{array}{c|c} \{Z_{Ii}\}(\lambda) & [Z_{ij}(\lambda)] \\ \hline Z_{ji}(\lambda) & [Z_{jI}(\lambda)] \end{array}\right]\left\{\begin{array}{c} x_i(\lambda) \\ \hline \{x_I(\lambda)\} \end{array}\right\}=\left\{\begin{array}{c} \{0\} \\ \hline f_j \end{array}\right\} \tag{12}$$

$$\left[\begin{array}{c|c} H_{iI}(\lambda) & H_{ij}(\lambda) \\ \hline [H_{II}(\lambda)] & \{H_{Ij}(\lambda)\} \end{array}\right]\left\{\begin{array}{c} \{0\} \\ \hline f_j(\lambda) \end{array}\right\}=\left\{\begin{array}{c} x_i(\lambda) \\ \hline \{x_I(\lambda)\} \end{array}\right\} \tag{13}$$

Imposing the relation $[Z(\lambda)][H(\lambda)] = [I]$ under the condition $\lambda = {}^{ij}\lambda_r$, r=1,2,...(such that $H_{ij}({}^{ij}\lambda_r) = 0$), it follows that:

$$[Z_{ij}({}^{ij}\lambda_r)]\ \{H_{Ij}({}^{ij}\lambda_r)\}=0\,.$$

From the definition of the dynamic flexibility matrix, this last equation can be written as:

$$\left([K_{ij}]-{}^{ij}\lambda_r[M_{ij}]\right)\{H_{Ij}({}^{ij}\lambda_r)\}=0 \tag{14}$$

where matrices $[K_{ij}]$ and $[M_{ij}]$ were already defined in Eq. (6).

Equation (14) represents a non self-adjoint eigenvalue problem whose eigenvalues are the zeros of the FRF, $H_{ij}(\lambda)$, ${}^{ij}\lambda_r$, r =1,2,... and the corresponding eigenvectors, designated as $\{{}^{ij}x_r\}= \{H_{ij}(\lambda), {}^{ij}\lambda_r\}$, are collinear to the vectors of the amplitudes of the forced response evaluated at the antiresonance frequencies.

The adjoint eigenvalue problem associated with (14) is written:

$$\left([K_{ij}]^T-{}^{ij}\lambda_r^*[M_{ij}]^T\right)\{{}^{ij}x_r^*\}=0 \tag{15}$$

It can be shown that the following properties hold:

$${}^{ij}\lambda_r^*={}^{ij}\lambda_r \tag{16}$$

$$\{{}^{ij}x_r^*\}^T[M_{ij}]\{{}^{ij}x_s\}=\delta_{rs}{}^{ij}\eta_s \tag{17}$$

$$\{{}^{ij}x_r^*\}^T[K_{ij}]\{{}^{ij}x_s\}=\delta_{rs}{}^{ij}\eta_s{}^{ij}\lambda_r \tag{18}$$

where δ_{rs} is the Kronecker is delta and ${}^{ij}\eta_s$ are arbitrarily chosen scaling factors.

Antiresonance Sensitivities

Similarly to the system global eigenvalues, analytical expressions can be derived for the derivatives (or sensitivities) of the antiresonance eigenvalues, with respect to scalar stiffness and mass parameters, denoted by K and m, respectively. This is achieved by deriving Eqs. (14), (17) and (18) with respect to these parameters. The Equations obtained this way are (Murthy and Haftka, 1988):

$$\frac{\partial\, {}^{ij}\lambda_r}{\partial k} = \frac{1}{{}^{ij}\eta_r} \left\{ {}^{ij}x_r^* \right\}^T \frac{\partial \left[K_{ij} \right]}{k} \left\{ {}^{ij}x_r \right\} \tag{19}$$

$$\frac{\partial\, {}^{ij}\lambda_r}{\partial m} = -\frac{{}^{ij}\lambda_r}{{}^{ij}\eta_r} \left\{ {}^{ij}x_r^* \right\}^T \frac{\partial \left[M_{ij} \right]}{m} \left\{ {}^{ij}x_r \right\} \tag{20}$$

Exploring Antiresonances in Practical Applications

Analysis of Modified Structures Subjected to Changes in Boundary Conditions

As was seen in Paragraph 3, the antiresonance frequencies of a driving point FRF $H_{ii}(\lambda)$ of a given structural configuration and the corresponding displacement shapes are equivalent to the natural frequencies and mode shapes of a modified configuration, obtained by grounding of the i-th coordinate. This property can be directly used for identifying the eigenfrequencies and eigenvectors of more constrained configurations, given the FRFs of less constrained configurations, without any physical grounding of coordinates during vibration tests. This way, technical drawbacks and increase in the test costs can be avoided. Figure 2 illustrates this methodology when applied to an experimental beam-like structure. Another application to a real-world industrial structure is presented by Rade and Lallement (1996).

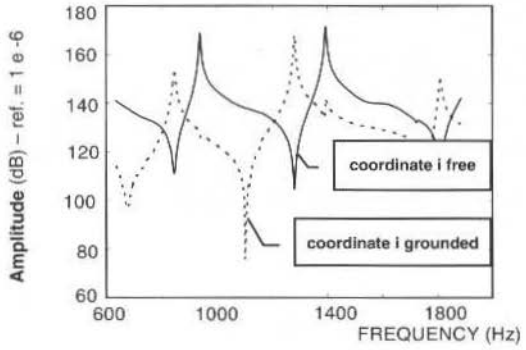

Fig. 2 Equivalence between the antiresonance frequencies of $H_{ii}(\lambda)$ and the natural frequencies of the structure with coordinate i grounded.

The dynamic vibration absorber

A vibration absorber is essentially a spring-mass appendage (see Fig. 3) which is added to the original structure with the aim of reducing, for a given forcing frequency, the vibration level at the coordinate to which it is attached. Its underlying principle can be interpreted in terms of antiresonances as follows. The vibration at coordinate i, due to a harmonic force applied at coordinate j, can be suppressed by choosing a set of absorber parameter values - mass and stiffness - so that a zero of the FRF $H_{ij}(\lambda)$ is made to coincide with the forcing frequency. Using coupling techniques based on dynamic flexibilities, it can be shown that the FRF $\hat{H}_{ij}(\lambda)$ for the coupled system structure+absorber is given, in terms of the corresponding FRF of the original structure, $H_{ij}(\lambda)$ and, by the following expression:

$$\hat{H}_{ij}(\lambda) = H_{ij}(\lambda)\frac{\lambda^* - \lambda}{\lambda^* - \lambda\left[1 + kH_{ii}(\lambda)\right]}, \quad \text{with} \quad \lambda^* = \frac{k}{m} \tag{21}$$

This last equation shows that the addition of the dynamic absorber enables the creation of an antiresonance with frequency, $\omega^* = \sqrt{k/m}$ which corresponds to the natural frequency of the appendage when grounded at its base. It should be noted that this antiresonace frequency is created not only in the FRF $H_{ii}(\lambda)$, but in each FRF $H_{ij}(\lambda)$, n=1,2,.... A simple numerical application to a finite element model of a uniform simply-supported beam is illustrated in Fig. 3. Appending multiple absorbers to a given coordinate of the original structure leads to creating multiple antiresonances to its FRFs. This situation is illustrated in Fig. 4 for the case of appending two absorbers simultaneously.

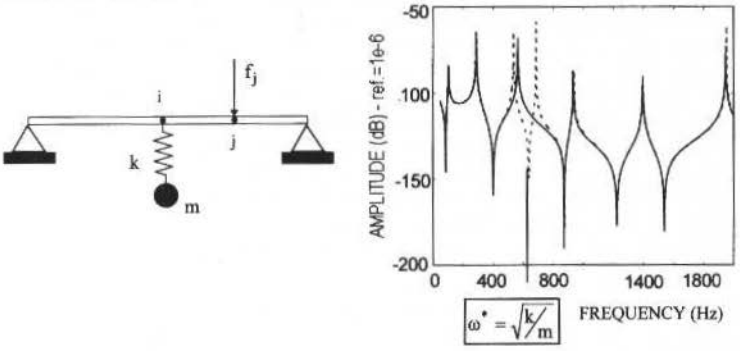

Fig. 3 Illustration of antiresonance generation as a consequence of adding a vibration absorber
___: without absorber _ _ _: with absorber

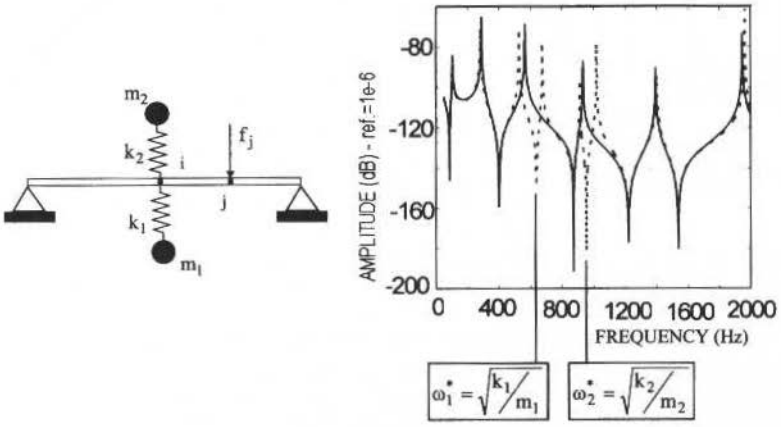

Fig. 4 Illustration of multiple antiresonances generated by various dynamic absorbers
___: without absorbers _ _ _: with absorbers

Finite element model updating and structural failure detection

The use of antiresonances in techniques addressing these problems was adopted by Sheppard and Milani (1990), Lallement and Cogan (1992), Rade (1994), Rade, Lallement and Silva (1996), Silva(1996). A classical parameter identification method, based on the sensitivity of eigenvalues and eigenvectors was extended to explore simultaneously the natural frequencies and the antiresonance frequencies (Rade, 1994). The latter were treated as eigenvalues of non self-adjoint structures, using Eqs. like (19) and (20). Several numerical applications to the problems of finite element model updating and structural damage localization, formulated as a parameter identification, demonstrated the possibility of achieving additional information and improving the calculation results, with respect to the

classical methodology based on the sole exploitation of natural frequencies. Some important observations regarding the improvements the antiresonances can provide are:

- It is well known that a sufficiently high degree of sensitiveness of the dynamic responses with respect to physical parameter variations is required for achieving meaningful model updating and damage localization from noisy experimental data. It was demonstrated (Rade, Lallement and Silva, 1996) that the antiresonance frequencies can be, in certain cases, much more sensitive to physical parameter variations than the natural frequencies. Thus, their utilization can lead to improved observability of the influence of the physical parameters on the dynamic responses.
- Most model updating and damage localization methods exploring eigenvalues experience difficulties when applied to symmetric structures. In this case, symmetric distributions of modal energies make it impossible, for the identification methods, to distinguish between the effects of the "coupled" physical parameters. This can lead to erroneous model corrections or damage localizations. Since, as it was previously seen, the antiresonances can be associated with the natural frequencies of structures with modified boundary conditions, they can be used to reduce the degree of symmetry of the structure, thus avoiding the problem of non unique parameter identification solutions owing to the symmetry (Silva, 1996).

In the following, the main results of a experimental study of damage localization and quantification, performed on a free-free beam, using a parameter identification method based on the inverse sensitivity of poles and zeros are presented. The FRFs explored were obtained from impact hammer excitation. A complete description of this study is given by Silva (1996).

Figure 5 depicts the test structure, where the damage was simulated by making a saw-cut whose dimensions b and t were varied to account for different damage severities. It is also indicated the

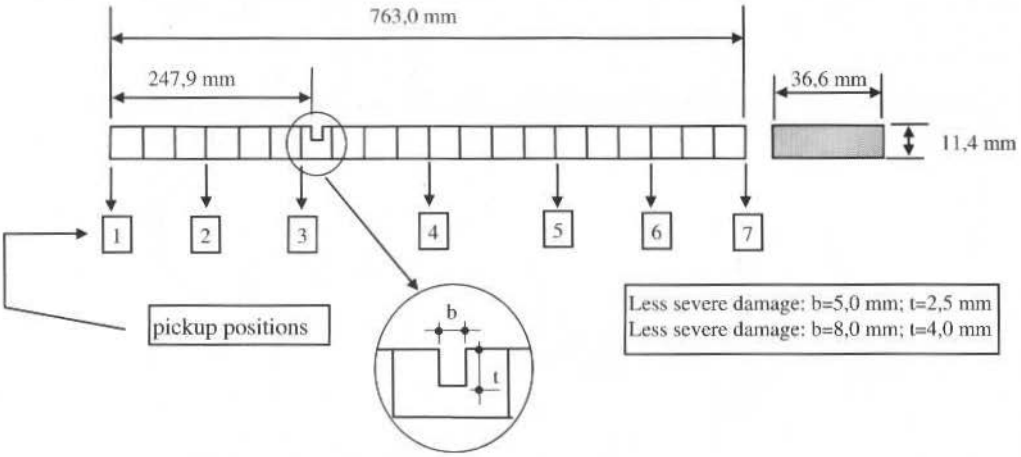

Fig. 5 Characteristics of the test structure

positions of the sensors used to acquire the experimental FRFs. Figure 6 shows the characteristics of the finite element model used for localization. Figure 7 shows a FRF of the undamaged structure, superimposed to the corresponding FRF of the damaged structure, for the less severe damage scenario.

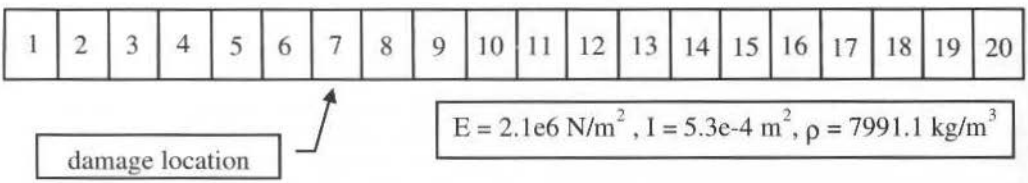

Fig. 6 Characteristics of the finite element model used for damage identification

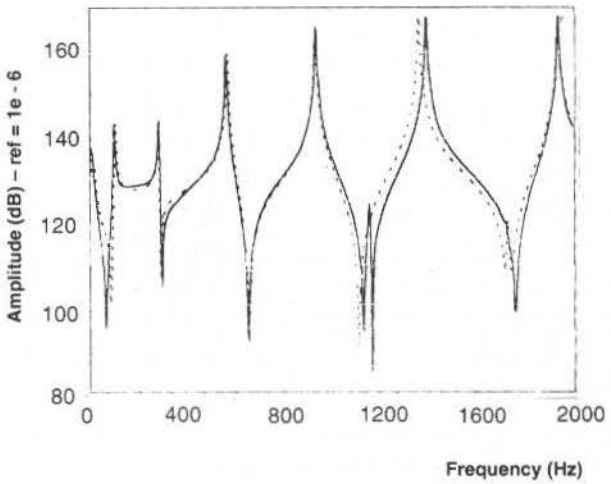

Fig. 7 Comparison between FRFs of the undamaged and damaged structures
.....: undamaged structure ____ : damaged structure

Table 1 presents some damage identification results. In this table, parameters k_i are understood as dimensionless damage indicators associated with the bending stiffness of the i-th finite element of the model shown in Fig. 6. This parameters are defined such as k_i =1 indicates no damage, k_i <1 indicates a stiffness reduction and k_i >1 represents an increase in stiffness. It can be seen that, while the identification of the damage using sole the natural frequencies led to erroneous results (due to the symmetry of the structure) the use of poles and zeros simultaneously enabled to achieve a correct damage localization. Furthermore, the technique was able to indicate the degree of severity of damage.

Table 1 Damage identification results

Explored data	Damage indicators
Poles of FRF $H_{67}(\lambda)$	k_{14}
Poles and zeros of FRF $H_{67}(\lambda)$	k_7 =0.91 (less severe damage) k_7 =0.65 (more severe damage)

Conclusions

Some aspects concerning the zeros of FRFs were examined. Theoretical developments were presented to clarify their basic properties and physical interpretation. Based on these properties, the practical use of the zeros in the realm of some structural dynamics applications was investigated. Many numerical results obtained by the authors led to the conclusion that the practical exploration of the FRF zeros is not only possible but also very convenient in applications such as: analysis of modified structures and structural damage identification. Moreover, a clear interpretation of the basic principle of single and multiple dynamic vibration absorbers was presented in terms of antiresonances. It was also verified that, as long as enough care is take during tests (concerning frequency spectra resolution, experimental noise, etc.) antiresonances can be experimentally identified with enough accuracy so as to provide meaningful results. Nevertheless, further investigations have still to be conducted aiming at quantifying the uncertainties affecting experimentally identified antiresonances.

Acknowledgments

The first author wishes to express his gratitude to FAPEMIG which, through contract TEC 1305/95, has provided the financial support for his research work. The second author is grateful to CAPES for having granted him a scholarship during his graduate studies.

References

Flannelly, W. G., 1971, "Natural Antiresonances in Structural Dynamics", Internal Report, Kaman Aerospace Corporation, Bloomfield, Connecticut, USA.

Lallement, G., Cogan, S., 1992, "Reconciliation Between Measured and Calculated Dynamic Behavior: Enlargement of the Knowledge Space", Proceedings, 10th IMAC - International Modal Analysis Conference, San Diego, California, USA, pp. 487-493.

Miu, D. K., 1991, "Physical Interpretation of Transfer Function Zeros for Simple Control Systems with Mechanical Flexibilities", Journal of Dynamic Systems, Measurement and Control, Transactions of the ASME, Vol. 13, pp. 419-424.

Murthy, D., Haftka, R., 1988, "Derivatives of Eigenvalues and Eigenvectors of a General Complex Matrix", International Journal of Numerical Methods in Engineering, Vol. 26, pp. 293-311.

Rade, D. A., 1994, "Parametric Correction of Finite Element Models: Enlargment of the Knowledge Space", (in French), Doctoral Thesis, Université de Franche-Comté, UFRST, Besançon, France.

Rade, D. A., Lallement, G., 1996, "Vibration Analysis of Structures Subjected to Boundary Condition Modifications Using Experimental Data", Journal of the Brazilian Society of Mechanical Sciences, Vol.XVIII, nb. 4, pp. 374-382.

Rade, D. A., Lallement, G., Silva, L. A., 1996, "An Strategy for the Enrichment of the Experimental Data as Applied to an Inverse Eigensensitivity-Based FE Model Updating Method", Proceedings, 14th IMAC - International Modal Analysis Conference, Dearborn, Michigan, USA, pp. 1078-1085.

Sheppard, G. D., Milani, J., 1990, "Frequency Based Localisation of Structural Discrepancies", Mechanical Systems and Signal Processing, Vol. 4, nb. 2, pp. 173-184.

Silva, L. A., 1996, "Structural Damage Identification Based on the Inverse Sensitivity of FRFs Poles and Zeros", (in Portuguese), M.Sc. Dissertation, Federal University of Uberlândia, Uberlândia, Brazil

RBCM - J. of the Braz. Soc. Mechanical Sciences
Vol. XXI - No.1 - 1999 - pp. 91-98

ISSN 0100-7386
Printed in Brazil

Controller Design for a Bearingless Electric Motor

José Andrés Santisteban
Arthur Ripper
Richard M. Stephan
Universidade Federal do Rio de Janeiro
COPPE - EE C.P. 68504
21945-970 Rio de Janeiro, RJ Brazil
jasl@coe.ufrj.br
richard@coe.ufrj.br

Domingos David
Roberto Noronha
Universidade Federal Fluminense
Rua Passo da Pátria, 156
24210-240 Niterói, RJ Brazil

Abstract

An electromagnetic and a mechanical model for a bearingless electric motor are presented. Based on these models, a controller structure is proposed and simulations presented. A laboratory prototype of this motor was constructed and experimental results validated the model. The proposed approach can also be used for the design of better controllers.

Keywords: *Magnetic Bearing, Bearingless Motor, Modeling.*

Introduction

The use of magnetic bearings has been investigated for more than 50 years (Haberman, 1979, Schweitzer et al., 1994). Its characteristics of no mechanical friction, absence of lubrication and capacity of working at high rotating speed have application in light and heavy industries, when the use of conventional mechanical bearings is unacceptable.

The conventional magnetic bearing system has the basic structure shown in Fig. 1(a). It consists of four blocks. The proposed system, shown in Fig. 1(b), has just three blocks, since the electric motor works also as a bearing (Ortiz and Stephan, 1993). This means that the proposed solution requires less space and fewer components.

Ortiz and Stephan (1993) have already described this proposal. In the present paper, a better formulation for the mechanical and electromagnetic models is presented.

The structure used for the analysis is shown in Fig. 1(c). The axis is in the vertical position to avoid the gravitational force and to allow any direction of external radial force to be applied for testing. Mechanical bearings are present at both ends of the rotor. However, the one at the top is normally not in contact. The bottom bearing is used for experimental purposes to simplify this first prototype. In a practical system it will be necessary to use two motors in a dumbbell arrangement on the same shaft to provide the necessary positioning action. This is shown in Fig. 1(b).

The machine used has a 4-pole, 2-phase configuration. The first phase is split into four windings, each one supplied with sinusoidal currents. These currents have their amplitude given by a closed loop control of the shaft position, which is measured through Hall-effect sensors.

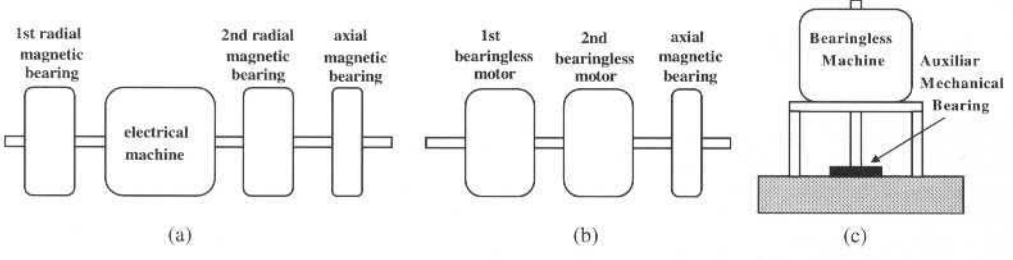

Fig. 1 a) Conventional Magnetic Bearing. b) Proposed system. c) Laboratory prototype.

Presented at DINAME 97 – 7th International Conference on Dynamic Problems in Mechanics, 3-7 March 1997, Angra dos Reis, RJ, Brazil. Technical Editor: Agenor de Toledo Fleury.

Electromagnetic Model

An equivalent magnetic scheme for phase A is shown in Fig. 2 and its equivalent magnetic circuit in Fig. 3.

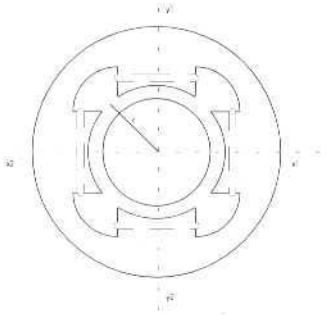

Fig. 2. Equivalent magnetic scheme

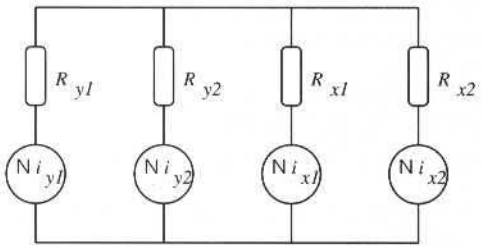

Fig. 3. Magnetic circuit

The linked fluxes are related to the currents as given by Eq. (1). The magnetic circuit equations are given in Eq. (2). The components of the inductance matrix $[L(h)]$ are a function of the radial rotor displacement, where each reluctance is calculated as: $R = \mu h/A$, with "A" being the mean area of each magnetic pole, "h" the correspondent airgap (x1,x2,y1,y2) and $\frac{1}{R_{eq}} = \frac{1}{R_{y1}} + \frac{1}{R_{y2}} + \frac{1}{R_{x1}} + \frac{1}{R_{x2}}$.

$$[\lambda] = [L(h)][I] \tag{1}$$

$$\begin{bmatrix} \lambda_{y1} \\ \lambda_{y2} \\ \lambda_{x1} \\ \lambda_{x2} \end{bmatrix} = N^2 \begin{bmatrix} \frac{1}{R_{y1}} - \frac{R_{eq}}{R_{y1}^2} & -\frac{R_{eq}}{R_{y1}R_{y2}} & -\frac{R_{eq}}{R_{y1}R_{x1}} & -\frac{R_{eq}}{R_{y1}R_{x2}} \\ -\frac{R_{eq}}{R_{y2}R_{y1}} & \frac{1}{R_{y2}} - \frac{R_{eq}}{R_{y2}^2} & -\frac{R_{eq}}{R_{y2}R_{x1}} & -\frac{R_{eq}}{R_{y2}R_{x2}} \\ -\frac{R_{eq}}{R_{x1}R_{y1}} & -\frac{R_{eq}}{R_{x1}R_{y2}} & \frac{1}{R_{x1}} - \frac{R_{eq}}{R_{x1}} & -\frac{R_{eq}}{R_{x1}R_{x2}} \\ -\frac{R_{eq}}{R_{x2}R_{y1}} & -\frac{R_{eq}}{R_{x2}R_{y2}} & -\frac{R_{eq}}{R_{x2}R_{x1}} & \frac{1}{R_{x2}} - \frac{R_{eq}}{R_{x2}^2} \end{bmatrix} \begin{bmatrix} i_{y1} \\ i_{y2} \\ i_{x1} \\ i_{x2} \end{bmatrix}. \tag{2}$$

Then, the radial forces (F_e) are calculated from the derivatives of the stored magnetic energy (W_e) as explained in Eqs. (3), (4) and (5).

$$W_e = \frac{1}{2}[i]^T [L(h)][i] \tag{3}$$

$$F_e = \frac{dW_e}{dh} \tag{4}$$

$$F_e = \frac{1}{2}[i]^T \frac{d[L(h)]}{dh}[i]. \tag{5}$$

With the new variables "x" and "y" such that: $y1 = y = h_o + \Delta y$; $y2 = (2 * h_o - y) = h_o - \Delta y$; $x1 = x = h_o + \Delta x$; $x2 = (2 * h_o - x) = h_o - \Delta x$, where h_o is the nominal airgap in the centered condition, the first term of the inductance matrix $L_{11}(h)$ will be:

$$L_{11} = \mu A N^2 \left[\frac{1}{y} - \frac{1}{2h_o \left(\frac{y^2}{x(2h_o - x)} + \frac{y}{(2h_o - y)} \right)} \right]. \tag{6}$$

Analogously, the other terms can be calculated and, with some simplifications, the derivative of $[L(h)]$ with respect to the displacement y_1 will be:

$$\frac{\partial [L(h)]}{\partial y_1} = -\frac{1}{2} N^2 \mu \frac{A}{y^2} \begin{bmatrix} 1 & 0 & -\frac{1}{2} & -\frac{1}{2} \\ 0 & -1 & +\frac{1}{2} & +\frac{1}{2} \\ -\frac{1}{2} & +\frac{1}{2} & 0 & 0 \\ -\frac{1}{2} & +\frac{1}{2} & 0 & 0 \end{bmatrix}. \tag{7}$$

Using Eq. (5), the equivalent force along direction y1 will be:

$$F_{y1} = -\frac{1}{4} N^2 \mu \frac{A}{y^2} \left[{i_{y1}}^2 - {i_{y2}}^2 - i_{y1}(i_{x1} + i_{x2}) + i_{y2}(i_{x1} + i_{x2}) \right]. \tag{8}$$

Analogously, $\frac{\partial [L(h)]}{\partial y2}$ can be calculated and then F_{y2} , the equivalent force along direction $y2$:

$$F_{y2} = -\frac{1}{4} N^2 \mu \frac{A}{y^2} \left[{i_{y2}}^2 - {i_{y1}}^2 - i_{y2}(i_{x1} + i_{x2}) + i_{y1}(i_{x1} + i_{x2}) \right]. \tag{9}$$

In the same way, the forces along the "x" axis can also be obtained.

On the other hand, given that the AC machine has 4 poles, the imposed sinusoidal currents onto phase A have the following expressions:

$$i_{y1} = (i_o + \Delta i_y) \cos\omega t \; ; \qquad i_{y2} = (i_o - \Delta i_y) \cos\omega t$$

$$i_{x1} = (i_o + \Delta i_x) \cos\omega t \; ; \qquad i_{x2} = (i_o - \Delta i_x) \cos\omega t$$

where i_o is a mean value, which determines a particular stiffness for the magnetic bearing, and Δi is the incremental value supplied by the position control. Ortiz and Stephan (1993) have shown that these currents imposed on the coils of a conventional motor produce both torque and radial positioning forces. Unlike other methods, which use separate windings for positioning and torque (Bichsel, 1991; Chiba et al., 1990, 1991; Isely, 1986; Studer, 1987; Wehde, 1974), this technique modulates the magnitude of the winding currents.

With this, Eqs. (8) and (9) will be:

$$F_{y1} = -\frac{1}{4} N^2 \mu \frac{A}{y^2} \left[8 i_o \Delta i_y \right] \cos^2 \omega t \tag{10}$$

$$F_{y2} = -\frac{1}{4} N^2 \mu \frac{A}{y^2} \left[-8 i_o \Delta i_y \right] \cos^2 \omega t \tag{11}$$

As expected they have opposed sign, but any one of them represents the force along the "y" axis:

$$F_y = -2 N^2 \mu \frac{A}{y^2} \left[i_o \Delta i_y \right] \cos^2 \omega t \, . \tag{12}$$

This force is non linear, but for small displacements ($\Delta y < y$) it depends basically on Δi_y. As $\cos^2 \omega t = (1/2)[1+\cos 2\, \omega t]$ this force can be split in two terms: a continuous force and a harmonic component. As long as the natural frequencies of the rotor are kept reasonably lower than this harmonic value, the oscillatory term should produce a negligible effect on the dynamic behavior of the system.

Mechanical Model

A schematic drawing of the vertical rotor is shown in Fig. 4. The lower ball bearing does not restrict angular displacements. Since the rotor is considered to be pivoted at the lower bearing, only the magnetic bearing forces acting at an axial distance "*b*" from "O" contribute to the dynamical behavior of the rotor.

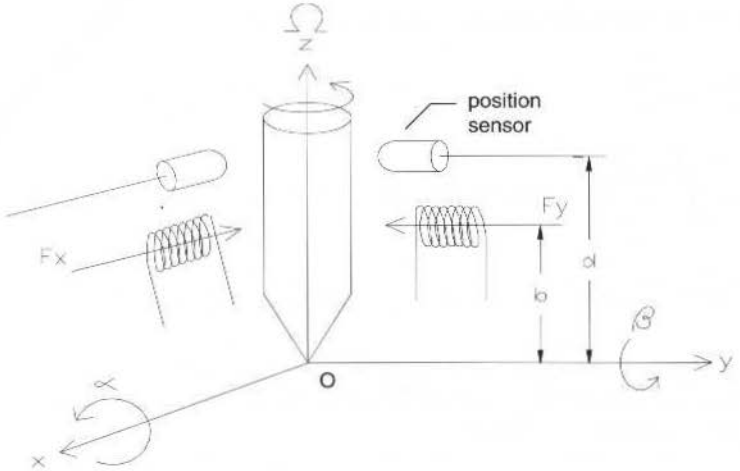

Fig. 4 Mechanical model

The system is a two degrees of freedom one, leading to the following equation:

$$\begin{bmatrix} I_O & 0 \\ 0 & I_O \end{bmatrix} \begin{Bmatrix} \ddot{\alpha} \\ \ddot{\beta} \end{Bmatrix} + \begin{bmatrix} 0 & -I_p \Omega \\ I_p \Omega & 0 \end{bmatrix} \begin{Bmatrix} \dot{\alpha} \\ \dot{\beta} \end{Bmatrix} = \begin{Bmatrix} -bF_y \\ bF_x \end{Bmatrix} \tag{13}$$

where I_O is the transverse moment of inertia at point "O", I_p is the polar moment of inertia of the rotor and Ω its spin velocity.

It is convenient to represent Eq. (13) in terms of the linear radial displacement coordinates "*x*" and "*y*" furnished by the feedback displacement sensors positioned at an axial distance "d" from the pivot

point "O". Considering that the angular displacements $\alpha = -y/d$ and $\beta = x/d$ are small, eq(13) in terms of "x" and "y" is:

$$\begin{bmatrix} I_O & 0 \\ 0 & I_O \end{bmatrix}\begin{Bmatrix} \ddot{x} \\ \ddot{y} \end{Bmatrix} + \begin{bmatrix} 0 & -I_p\Omega \\ I_p\Omega & 0 \end{bmatrix}\begin{Bmatrix} \dot{x} \\ \dot{y} \end{Bmatrix} = \begin{Bmatrix} bdF_x \\ bdF_y \end{Bmatrix}. \tag{14}$$

This matrix equation may be written as a system of two coupled differential equations:

$$\ddot{x} = \frac{I_p}{I_o}\Omega\dot{y} + \frac{bd}{I_o}F_x \ , \tag{15a}$$

$$\ddot{y} = -\frac{I_p}{I_o}\Omega\dot{x} + \frac{bd}{I_o}F_y \ . \tag{15b}$$

The moments of inertia I_o and I_p of the prototype were measured and found to be:

$I_o = 0.134078\ kg\text{-}m^2$ $\qquad$ $I_p = 0.003996\ kg\text{-}m^2$,

while the heights "b" and "d":

$b = 0.195\ m.$ $\qquad$ $d = 0.345\ m.$

Taking these values into account, Eq. (15) leads to the following block diagram

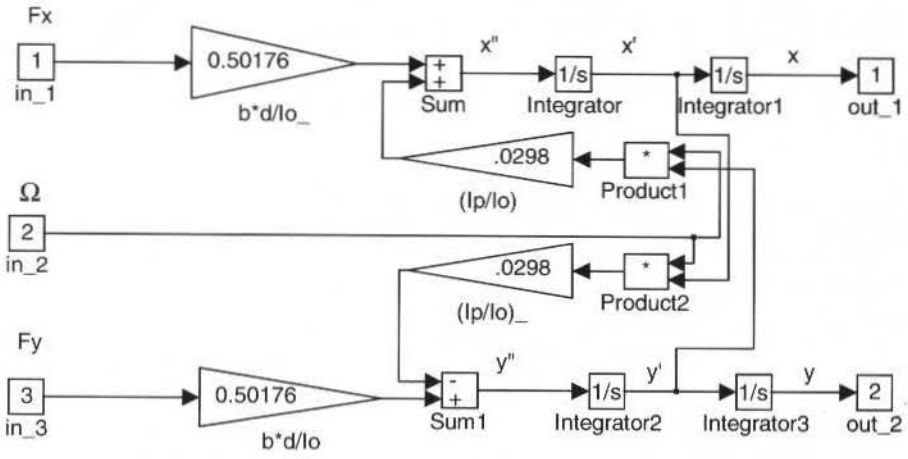

Fig. 5 Block diagram of the mechanical model.

Controller Structure, Simulation and Experimental Results

The above proposed model takes into account gyroscopic coupling. However for low speeds it may be considered decoupled. Based on this assumption, two independent PD controllers have been designed as shown in Fig. 6 and implemented as shown in Fig. 7.

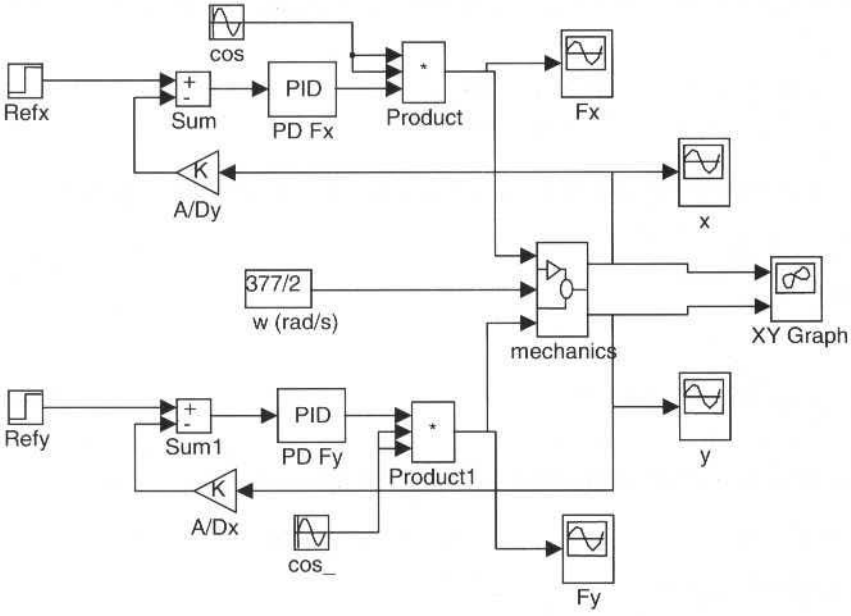

Fig. 6 Block diagram of the control system.

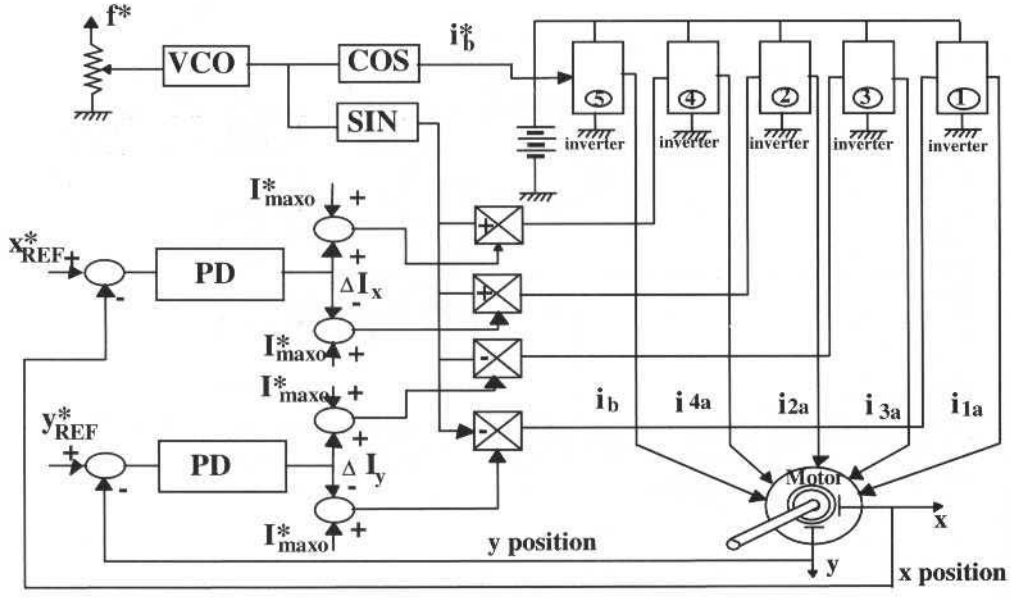

Fig. 7 Actual control structure

Simulation results showing the effect of the speed over the transient responses of the position control, for the same initial condition, are presented in Fig. 8.

The experimental orbital path of the rotor with and without control is compared in Fig. 9. The controlled system shows a small error that is explained by the residual unbalance. The outer circular path represents the restraint of the auxiliar mechanical bearing. The central dots represent the closed loop control response while the rotor is rotating at 1800 rpm.

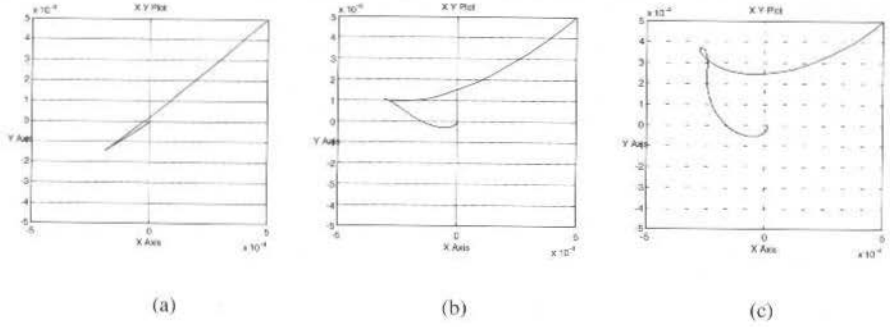

(a) (b) (c)

Fig.8 Simulated transient responses (initial condition x=0.5mm, y=0.5mm): a) 180rpm, b) 1800rpm, c) 3600rpm.

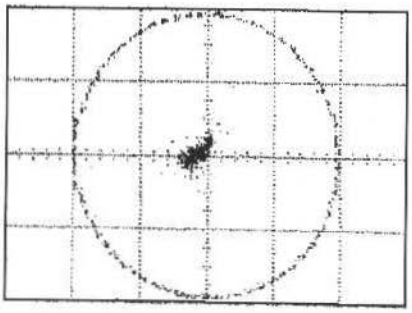

Fig. 9 Experimental orbital path with and without position control. (1 div = 0.5 mm)

Conclusion

New electromagnetic and mechanical models for a previously designed bearingless machine have been described.

These more accurate models allows for:

a) the realization of numerical simulation of the dynamical behavior of the prototype, either at low or at high speeds,

b) the design of more sophisticated controllers (e.g., multivariable, robust, fuzzy), taking into account the variables coupling.

Experimental and simulation results validate this approach.

Acknowledgments

The authors would like to thank Eng. A.C.Siqueira de Lima, Eng. Paulo Roberto Guimarães, Dr. A. Ortiz and Prof. W. Dunford for their helpful suggestions.

References

Bichsel, J., 1991, "The Bearingless Electrical Machine", NASA Conference Publication 3152, part2.

Chiba, A., Ciba, K., Fukao, T., 1990,"Principles and characteristics of a reluctance motor with winding of magnetic bearing", International Power Electronics Conference, Tokyo, Japan, v.2, pp919-26.

Chiba, A., Power, D.T., Rahman, M.A., 1991,"Characteristics of a bearingless induction motor", IEEE Trans. Magn., v.27, pp 5199-5201.

Haberman, W., 1979, "Practical Magmetic Bearing", IEEE Spectrum, Sep.79.

Isely, W., 1986, "Magnetically supported and torque momentum reaction sphere", US Patent n. 4,611,863.

Ortiz, A., Stephan, R.M., 1993, "A bearingless method for induction machines", IEEE Trans. on Magnetics, v.29, no.6, pp 2965-2967.

Schweitzer, G., Bleuler H., Traxler A., 1994, "Active Magnetic Bearings", v/dlf Hochschulverlag AG an der ETH Zürich.

Studer, P., 1987, "Radial and torsionally controlled magnetic bearing", US Patent n. 4,634,191.

Wehde, H., 1974,"Magnetically mounted rotor", US Patent n. 3,845,995.

RBCM - J. of the Braz. Soc. Mechanical Sciences
Vol. XXI - No.1 - 1999 - pp. 99-108

ISSN 0100-7386
Printed in Brazil

Automation In Fault Detection Using Neural Network and Model Updating

João Antonio Pereira
Vicente Lopes Jr.
UNESP - Universidade Estadual Paulista
Faculdade de Engenharia de Ilha Solteira
Departamento Engenharia Mecanica
15385-000 Ilha Solteira, SP Brazil
japereir@dem.feis.unesp.br

Hans Ingo Weber
UNICAMP - Universidade Estadual de Campinas
Faculdade de Engenharia Mecânica
Departamento de Projeto Mecânico
13083-970 Campinas, SP Brazil
hans@mec.puc-rio.br

Abstract

In this article, an implementation of structural health monitoring process automation based on vibration measurements is proposed. The work presents an alternative approach which intent is to exploit the capability of model updating techniques associated to neural networks to be used in a process of automation of fault detection. The updating procedure supplies a reliable model which permits to simulate any damage condition in order to establish direct correlation between faults and deviation in the response of the model. The ability of the neural networks to recognise, at known signature, changes in the actual data of a model in real time are explored to investigate changes of the actual operation conditions of the system. The learning of the network is performed using a compressed spectrum signal created for each specific type of fault. Different fault conditions for a frame structure are evaluated using simulated data as well as measured experimental data.
Keywords: *Neural Network, Fault Detection, Model Updating, Predictive Maintenance*

Introduction

The entire life cycle of a product involves an iterative engineering effort. The initial design concept is likely to give rise to a variety of design options each of which will be evaluated against the requirements of the product specification. At this stage, usually, is constructed a prototype and their properties are evaluated and compared with the design requirement. The Structural Dynamic Modification (SDM) is a term usually used in modal analysis and implies the incorporation, into an existing model, of design modification or new information gained either from experimental testing or other source, in order to evaluate the accuracy of the model.

The SDM algorithm is useful for solving the forward variational problems for structures, i.e., for a given variation into the mass, stiffness or damping properties, it leads to the corresponding changes in the modal properties of the model. However, to access a high performance against the requirements of the product specification demands a safety and reliable monitoring of the operation conditions and failure diagnostic of the model. This involves a solution of an inverse problem, or modal sensitivity problem. That is, for a given variation in the modal properties of the structure, which corresponding changes in its mass, stiffness and damping properties have taken place. Application as fault detection requires solutions of this kind of inverse problem. Unlike the forward variational problem, fault detection applications can not be solved in a straightforward manner. Its solution, for most practical cases, requires the inversion of a rank deficient matrix, which creates numerical difficulties to identify the correct changes of the structural properties that have to taken place into the model.

Numerous researches have proposed solutions using modal sensitivity problem to damage detection of structures through vibration changes. As modal testing has become more widespread, finite element model updating using measured modal test data has also become popular in the field of damage detection. The relative success and the potentiality demonstrated by these techniques, mainly, those based on vibration properties have shown that they are promising tools for damage detection purpose (Pereira, 1994; Hemez, 1993; Zimmerman, 1995). However, for purpose of monitoring, they are still under investigation (far to be consolidated). The recent literature has been shown some attempts to use permanently working monitoring system, based on natural excitation source actuating in the system to evaluate its health condition (Rohrmann and Rucker, 1994) but the results are still limited.

Presented at DINAME 97 - 7th International Conference on Dynamic Problems in Mechanics, 3-7 March 1997, Angra dos Reis, RJ, Brasil. Technical Editor: Agenor de Toledo Fleury.

Artificial Neural Networks (ANN) have recently emerged as a good tool for pattern recognition turning their application in promising tools for monitoring and fault classification of machines and equipments. The technique offers promise for solving inverse varational problem in the context of monitoring and fault detection because of their pattern recognition and interpolation capabilities. In order to identify the fault in the model, it must be trained using a set of solutions to its corresponding forward variational problem. In this case, the neural networks should be designed to classify the input patterns in pre-defined classes or to create categories of group patterns according to their similarity. An important feature of the neural networks, in this context, is their inherent ability to operate on noisy, incomplete or sparse data and to model process from actual system parameters (Uhl, 1994). The neural network could respond in real time to the changes in the system state, provided by continuous sensor inputs. Hence this technique should facilitate fault identification in real time, providing a good Non-Destructive Evaluation (NDE) tool to investigate the state of operation and health condition of a system based on measured vibration data. Nevertheless, several attempts to use neural networks faced difficulties to generate reliable set of information to train the net. It demands a wide range of experimental tests to cover the whole possibility of damages of the model, which makes its use prohibitive.

This work presents an alternative proposal to exploit the capability of neural network associating it with model updating technique to investigate the state of operation and health condition of the system. It creates a very reliable updated finite element model, using a FRF-based model updating approach (Larson, 1992; Lammens, 1994; Pereira, 1996) and uses SDM to generate the patterns faults to feed the ANN during the training phase. The approach initially adjusts the finite element model and validates its response properties in terms of the dynamic measured data of the real system. Following, it simulates different types of damage conditions to train the network.

The proposed approach is addressed to fault detection on the frequency analysis domain, where each machine defect generally produces a set of vibration components that allows the recognition of different faults. However, its application is similar for others kind of signal since there are many others parameters that can be measured to evaluate the operation condition of a machine such as pressure, temperature, sound, oil particles, etc.

Methodology

An Artificial Neural Network approach associated with a Finite Element Model Updating Procedure (MUP) has been used to operate the monitoring and failure diagnosis of machines and equipments. The updating approach performs an improvement of the FE-Model in order to define a representative mathematical model of the actual system. The improved model permits to create the various damage conditions required to define the reliable set of information data concerning each kind of failure liable to occur in the life cycle of the system. The network is designed to classify the input patterns of the model in pre-defined classes of inputs or to create categories of group patterns according to their similarity, by a training process phase. In the monitoring phase, it compares the actual measured data with the input patters aiming at recognising the existence of fault in the system. The updated FE-model permits to generate the various damage conditions necessary for the training of the network. So, the ANN may lead to diagnose of the system in real time, facilitating the identification of faults in the operating system.

The approach comprehends a definition of a reliable FE-Model, the generation of whole expected failure conditions, the training of the ANN and finally, the recognition and location of each kind of fault. The ANN learns by example and the pattern of damaged signal used to feed the training of the network, frequency response functions, is created in a straight forward manner by applying SDM. Once the network is trained, it can execute any patter recognition task.

The classification of the vibration signal, generated from the improved finite element model, comprehend a separation of the vibration data in signals of components operating normally, signals of components operating with fault; a compression of the signals and finally, classification of the compressed patterns using a backpropagation algorithm. The compression of the pattern data is important because it transforms a large set of data in an equivalent reduced set containing the same information provided by the original signal. This reduction decreases significantly the time spent to train the network as well as the reduction of the instability in the recognition process (Lopes Jr. and Turra, 1996). The compression process consists in the compression of the spectrum size of the signal in a reduced number of points. It constructs a new equivalent signature for the system based on the maximum amplitude and corresponding frequencies points of the original signal. The algorithm

searches the maximum amplitude points in the original signal at an earlier specified frequency range and considers a band width of 3.0% around each frequency point related with maximum amplitude points.

Background of the Neural Network

ANN is made by a number of processing elements which are connected to form layers of neurons. Each neuron is a simple mathematical processing unit that, when it is interconnected, produces a complex structure with different architectures, which can be trained to recognise defined patters. It is common to specify the architecture of the network by referring to the number of hidden layers; layers that are neither inputs nor outputs. The topologies and size of the network depend on the specific application, and the definition of an optimal choice is case dependent (Bernieri, 1994; Worden and Tomlinson, 1994; Yuedong and Du, 1996). Figure 1 shows the architecture used, in this approach, it has one hidden layer with 500 neurons for an output layers with 31 neurons.

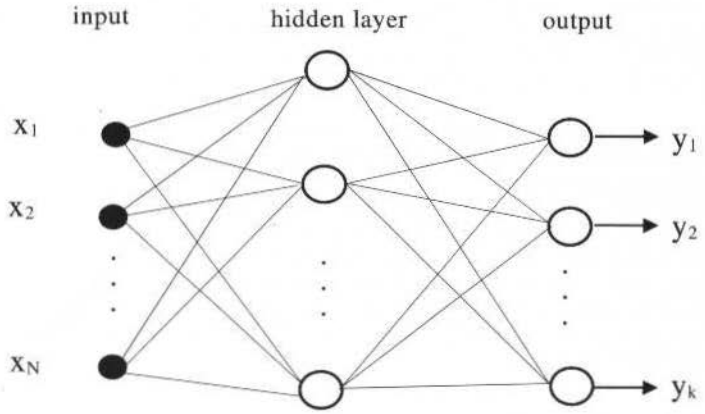

Fig. 1 Architecture of the neural network with one hidden layer

The input x's are weighted by $w_{j,i}^{h}$ and by the bias b_j^h , and the output results feed the hidden layer. The output of the j^{th} hidden unit can be described by:

$$y_j^h = F_1\left(b_j^h + \sum_{i=1}^{N} W_{i,j}^h . x_i\right) \qquad (1)$$

where the superscript (h) means that the quantities pertain to the hidden unit and $\mathbf{F_1}(\,.\,)$ is a sigmoid nonlinear function. The output of the net is biased and weighted by sum of the hidden layer outputs:

$$y_l = F_2\left(b_l^o + \sum_{j=1}^{H} W_{j,l}^o . y_j^h\right) \qquad l = 1, 2, \ \ldots, k \qquad (2)$$

where the superscript (o) refers to the output unit. **H** is the number of units in the hidden layer and $\mathbf{F_2}(.)$ is a linear activation transfer function. The net is trained starting with a random set of weights and biases and calculating the output for every input set. Then, the error E is computed from the output layer backwards, which has historically been called the backpropagated error, and the learning algorithm the backpropagation. Several publications (Hecht and Nielsen, 1990; Wasserman, 1989; Hush and Horne, 1993) have presented details of this algorithm.

$$E = sumsqr(\{T\} - \{y\}) \tag{3}$$

where sumsqr is the sum of square of the elements, and T is the desired output. The error E is formulated as a function of the weights and biases and then, the minimisation is performed by means of the usual steepest algorithm. The error E is denoted by $\{\alpha_j\}$, where the index j aking on as many values as there are weights and biases. When the parameter α_j changes by $\delta\alpha_j$, the error E changes by

$$\delta E = \frac{\partial}{\partial \alpha_j}(E)\,\delta\alpha_j \tag{4}$$

where $\delta/\delta\alpha_j$ is evaluated using the current values of the parameter. To ensure that changes in α_j results in a decrease in E, it selects

$$\delta\alpha_j = -\eta \frac{\partial}{\partial \alpha_j}(E) \tag{5}$$

where η is a positive constant. The parameter η determines how large a step is made in the direction of the steepest descent and therefore how quickly the optimum parameters are obtained. For this reason η is called the learning coefficient.

The training of the network uses a set of inputs for which a specified output is known and in this case, the process finishes when the error $\boldsymbol{E}$ is smaller than a desired value or it reaches a maximum specified number of iterations. In the later case, the training set is considered unsatisfactory. The error E considered here, is the sum of the squared error between the output value provided by the trained network and the value obtained for a specific input. The outputs are combination of zeros and ones for each state of operation of the machine, for the intact structure the outputs are equal one for the first component and zero for the others.

Model Updating Procedure

The MUP used to improve the original finite element model is based on the measured frequency response functions (FRF(s)). A detailed discussion can be found in Lammens, 1995 and Pereira, 1996. The procedure operates at an element level and the model changes are directly related to the variation of the parameters of each element. It describes the discrepancy between analytical and experimental models as a force residue written in terms of the analytical dynamic stiffness matrix $[Z^A]$, and the experimental FRF matrix $[H^X]$.

$$\{\varepsilon\} = \varepsilon\left([Z^A(p_1 + \Delta p_1, p_2 + \Delta p_2, \ldots, p_m + \Delta p_m)],[H^X]\right) \equiv \{0\} \tag{6}$$

This discrepancy of the models is used to define the updating set of equations and the solution of the updating problem consists in finding m analytical parameter changes that minimises the difference between the two models. The p-parameters can represent any physical or geometrical property of the model, they can be a parameter of an element in the case of the elements being adjusted independently or a parameter of a set of elements when some elements are adjusted proportionally. The Δp's are parameters correction of the p-parameters that minimise the discrepancy between the two models. The formulation of an approximated solution of the problem, through a first order linearization of the expression (6) in the p-parameters, leads an overdetermined set of linear equations:

$$\{\varepsilon\} = [S]\{\Delta p\} - \{B\} \tag{7}$$

where the elements of the sensitivity matrix [S] and these of the difference vector {B} are known elements. They are obtained from the analytical dynamic stiffness matrix and the experimental measured frequency response functions at each selected measured frequency points respectively. The

elements of the vector $\{\Delta p\}$ are unknown parameter corrections to be estimated. The solution of this system of linearised equations system provides an improved analytical model. If the discrepancy between the models is not yet sufficiently small, the procedure is iteratively repeated.

Experimental Test

To demonstrate the applicability of the proposed methodology, a laboratory spatial frame structure, Fig. 3, has been investigated. An analytical modelling by finite elements and a modal test of the structure were carried out and compared aiming at defining a representative analytical-numerical model able to predict the real behaviour of the structure. The initial comparison of modal parameters from both, analytical and experimental models, showed a deviation of the predicted data from the experimental one, Table 1 and Fig. 4.a. The adjustment of the analytical finite element model and the consequent improvement of the correlation of the models was performed by a FRF based model updating procedure (Pereira, 1996). The spatial parameters of the finite element model were successfully updated by using the FRF based model updating and, the correlation of the models was improved satisfactory, table 1. The elements selected to be adjusted during the updating process were those elements evolved into the welding connections. Figure 4.b shows the superposition of the FRF(s) in the drive point for the experimental test and the corresponding new reliable finite element model. The updating process, as shown in Table 1 and Fig. 4, allowed the definition of a representative mathematical model of the actual system.

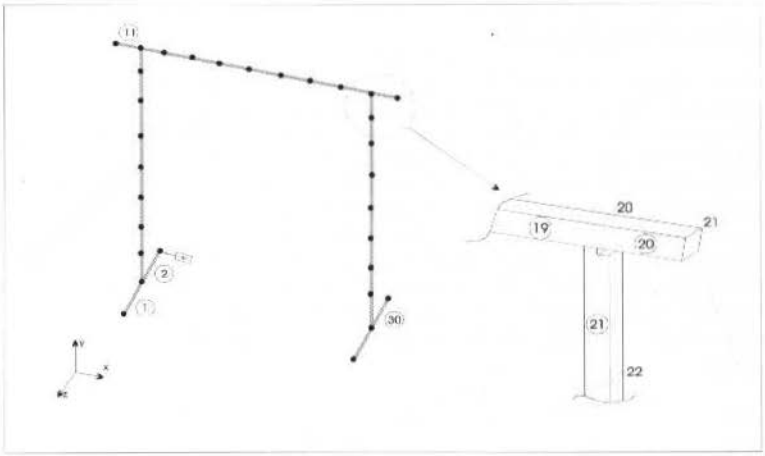

Fig. 3 Frame structure - Detail of the cut bar

Table 1 Experimental, Analytical and Updated models correlation

Experimental model		Analytical model		Updated model		Initial correlation		Final correlation (iteration 5)	
mode	freq. [Hz]	mode	freq. [Hz]	mode	freq. [Hz]	Δf [%]	MAC-val.	Δf [%]	MAC-val.
1	17.06	1	17.26	1	16.98	1.17	0.994	-0.43	0.995
2	22.10	2	25.30	2	22.38	14.47	0.991	1.26	0.991
3	42.44	3	43.86	3	42.73	3.34	0.990	0.68	0.990
4	97.54	4	102.06	4	97.04	5.71	0.978	-0.02	0.985
5	112.86	5	121.63	5	112.91	8.73	0.975	0.66	0.974
6	142.36	6	144.93	6	141.60	2.73	0.834	-0.53	0.881
7	153.83	7	155.03	7	153.71	0.78	0.954	-0.07	0.953
8	171.13	8	176.21	8	172.56	2.96	0.978	0.83	0.982

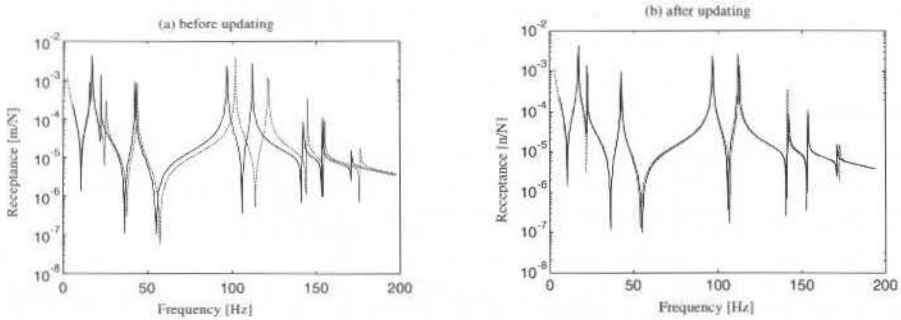

Fig. 4 Experimental (full line) and analytical (dashed line) receptances (point 1, x-direction)

Different damage conditions of the structure were obtained numerically by using the updated FE-model of the structure. Each fault introduced to the structure consisted of a reduction of 50% of the sectional area of the associated element. A frequency range covering the first eleven mode shapes of the structure was analysed. For each damaged element a set of FRF(s) was created which contains the whole informations used to feed the training of the network. The training was based on the compressed set of data obtained from the original one.

Compression of the Signal

A compression method based on the maximum amplitudes of the spectrum signal has been used to reduce the number of points of the signal and to construct a new equivalent signature for the system. The method localises the frequency points related with the maximum amplitudes and creates a masked signal with a band width of 3% of the frequency points of maximum amplitudes. This permits to comprise small deviations of the measured FRF(s) since, in practical cases, it is almost impossible to calculate FRF(s) that matches exactly the measured ones, due to problems related with the modelling approach as well as the experimental test. Once the reduction is effective, the procedure tries to associate the compressed signal response with a set of specific faults. Figures 5.a-b show an original measured FRF (512 points) and the corresponding compressed or masked curve (57 points) respectively for the intact frame structure and the damaged structure (element 13). The number of points of the compressed signal depends on the number of frequencies point related with the maximum amplitude peaks of the signal.

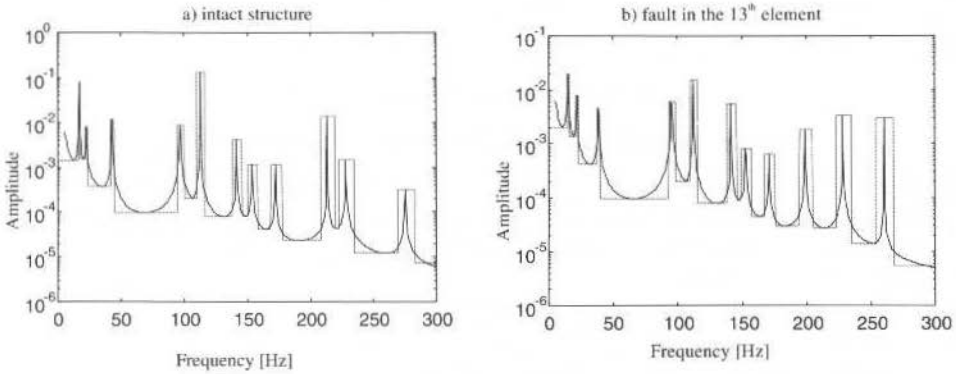

Fig. 5 Original (full line) and compressed (dotted line) signal

Numerical Results

Machines failure is a phenomenon liable to occur during the service life of most machines and equipaments. However, in some cases, the analyst may have previous information of the region more

susceptible to failure and should take it into account to search the failure. Nevertheless, to evaluate the robustness of the approach it is assumed that all elements of the structure are likely to failure and the procedure tries to identify the fault in the element without any previous information. In this case, the frame structure was divided in 30 elements and the procedure was trained to identify fault in any element. All conditions of failure were investigated, elements of low probability to failure (elements in the mid of bars), elements more liable to failure (elements in the welding connections) and elements of very low sensitivity to the damage. Table 2 shows the error obtained when each specific curve is submitted to the trained network and compared with the patterns curves used for the training of the network.

Table 2 Error value of the recognition of the faults.

Fault Condition / Curves	Undamaged	Fault Element 1	Fault Element 2	...	Fault Element 30
input 1 (intact struct.)	**9.6063e-006**	4.8641e+000	3.7970e+000		1.1696e+001
input 2 (fault elem. 1)	6.7413e+000	**9.7144e-006**	9.7573e-001		4.0104e+001
input 3 (fault elem. 2)	1.7271e+001	2.5262e+000	**9.6776e-006**		2.0471e+001
input 4 (fault elem. 3)	3.2935e+001	3.2589e+001	3.3665e+001		5.4743e+001
input 5 (fault elem. 4)	1.6834e+001	1.7251e+001	1.5313e+001		1.3523e+001
input 6(fault elem. 5)	1.7713e+001	2.0244e+001	2.0787e+001		9.6019e+000
input 7 (fault elem. 6)	2.9976e+001	3.0634e+001	3.0579e+001		1.8342e+001
input 8 (fault elem. 7)	3.9097e+001	4.7494e+001	4.5525e+001		1.3870e+001
input 9 (fault elem. 8)	2.0037e+001	1.6979e+001	1.5710e+001		1.3138e+001
input 10 (fault elem. 9)	1.5272e+001	2.6424e+001	2.2509e+001		1.1539e+001
input 11 (fault elem. 10)	1.3199e+001	1.7504e+001	1.3277e+001		2.5670e+001
input 12 (fault elem. 11)	3.9884e-002	1.7489e+001	1.7140e+001		2.6266e+001
input 13 (fault elem. 12)	3.4204e+001	3.0950e+001	3.0608e+001		3.4119e+001
input 14 (fault elem. 13)	9.8143e+000	1.1770e+001	1.2617e+001		1.5352e+001
input 15 (fault elem. 14)	4.5487e+000	5.7721e+000	6.3547e+000		1.7717e+001
input 16 (fault elem. 15)	1.9961e+001	1.9895e+001	1.6745e+001		2.6779e+001
input 17 (fault elem. 16)	3.1467e+001	2.1154e+001	2.1000e+001		4.4202e+001
input 18 (fault elem. 17)	3.1031e+001	5.4119e+001	5.4335e+001		6.8628e+001
input 19 (fault elem. 18)	1.5390e+001	7.2700e+000	5.9768e+000		1.7626e+001
input 20 (fault elem. 19)	4.0137e+000	2.7592e+000	4.0291e+000		2.5086e+001
input 21 (fault elem. 20)	3.2059e-002	9.4283e+000	5.1077e+000		2.2617e+001
input 22 (fault elem. 21)	1.7899e+001	1.7955e+001	1.6803e+001		4.1428e+001
input 23 (fault elem. 22	5.5282e+000	6.6056e+000	6.2168e+000		1.7987e+001
input 24 (fault elem. 23)	2.0025e+000	2.1186e+000	2.3363e+000		5.8111e+001
input 25 (fault elem. 24)	4.1322e+001	2.7704e+001	2.4730e+001		4.8111e+001
input 26 (fault elem. 25)	3.2059e-002	9.4283e+000	5.1077e+000		2.2617e+001
input 27 (fault elem. 26)	1.7899e+001	1.7955e+001	1.6803e+001		4.1428e+001
input 28 (fault elem. 27	5.5282e+000	6.6056e+000	6.2168e+000		3.7987e+001
input 29 (fault elem. 28	2.0025e+000	2.1186e+000	2.3363e+000		4.8111e+001
input 30 (fault elem. 29)	2.0025e+000	2.1186e+000	2.3363e+000		4.7111e+001
input 31 (fault elem. 30)	4.1322e+001	2.7704e+001	2.4730e+001	...	**9.1069e-006**

Figures 6.a-6.s give an overview of the normalised errors for some investigated failure conditions. The plots show the errors, normalized in relation to the minor component, obtained through a "comparison" of each specific "measured" curve with all others curves used for the training of the network.

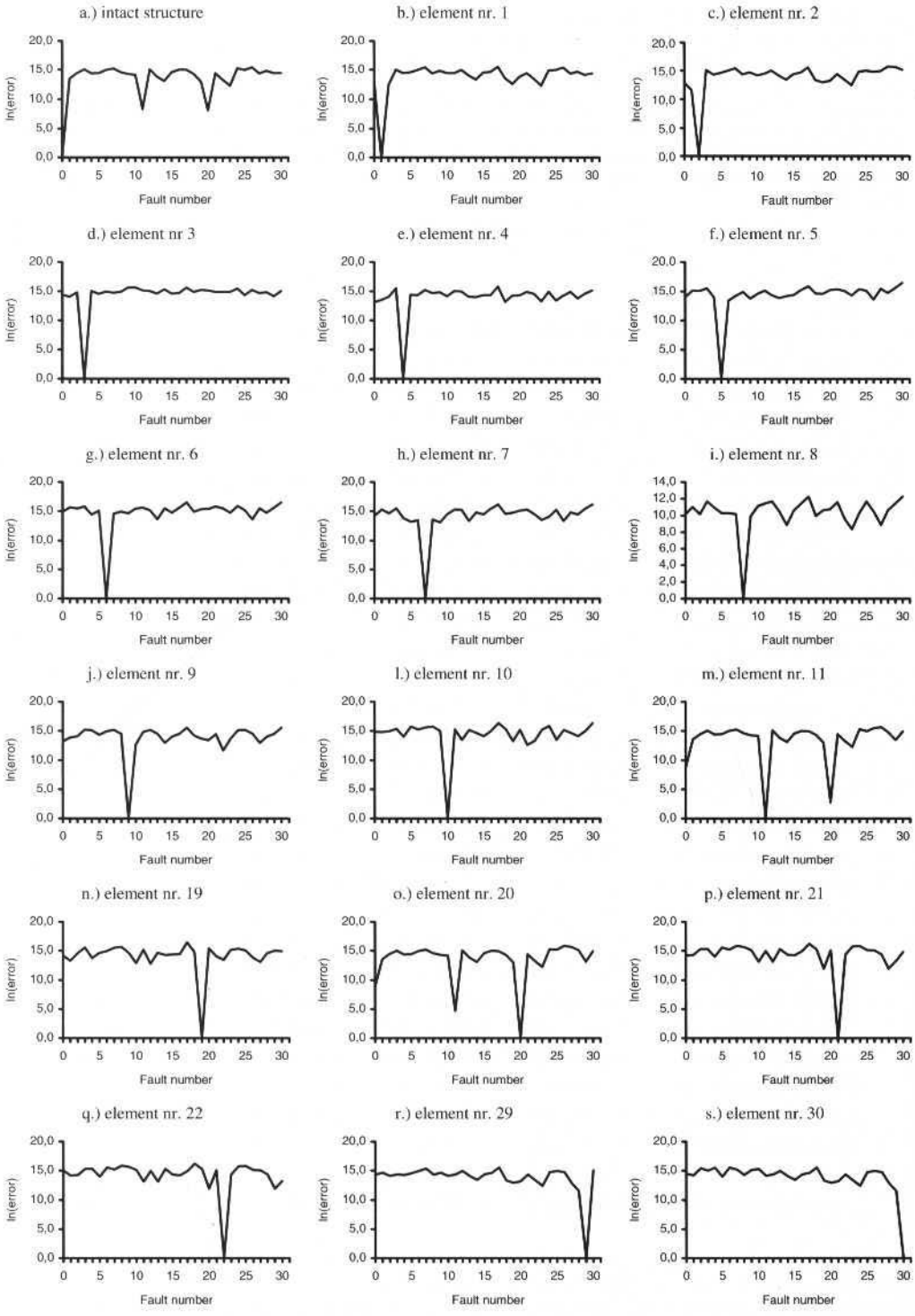

Fig. 6 Identification of the fault in the frame structure

The lower errors show the similarities of the curves and consequently the searched fault. As expected in this case, all faults as well as the intact condition of the structure were clearly identified since the training of network was based on these curves. The identification of the damaged element in Fig. 6.m is not very clear since the error for element 20 is very low too. It happens because elements 11 and 20, due their position in the structure, have few influences in the dynamic behaviour of the model, and even a very large damage in these elements does not affect the dynamic properties of the model. The same effect is verified in Fig. 6.o. Therefore, recognition faults in these elements, based on the changes of the dynamic properties of the model, is a difficult task

Experimental Results

In the above investigated case, the data of the damaged structure was created through the same numerical model used to train the network. Thus, the simulated data used in the training of the net and the "experimental" data of the damaged structure are identical. Howevep, for a real case the experimental measurement data present a light difference in relation to the simulated data used to train the network, turning more difficult the comparison of the data and the recognition of the fault. Hence the compression of the measured data is performed in two stages aiming to comprise this light difference. Initially, the measured FRF curve is compared with the simulated compressed curves utilised to train the network aiming to define if the frequency band of the simulated compressed data includes the frequency points of maximum amplitude of the measured curve. If the points are within the frequency band of the simulated curve, the procedure uses the same points of frequency used in training phase to compress the measured signal. In sequence, the signal is compared with the curves used in the training phase in order to detect the probable fault. Figure 7 shows the measured experimental curve of the damaged structure (element 21) and the masked one utilised to train the network. The mask was derived, from the improved FE-model, during the simulation of the failure condition of the model. Figure 8 shows the normalised error when the measured experimental curve is compared with all curves used to train the net. As it can be seen, the smallest error occurs for curve number 21, that means the real damaged element (element nr. 21).

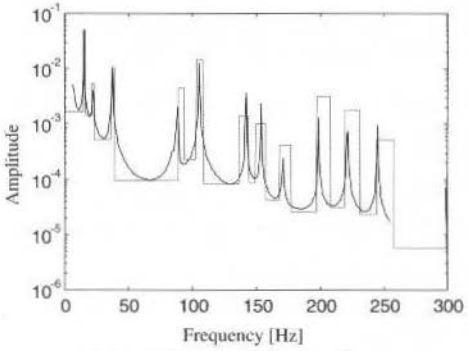

Fig. 7 Original (full line) and compressed (doted line) response signal

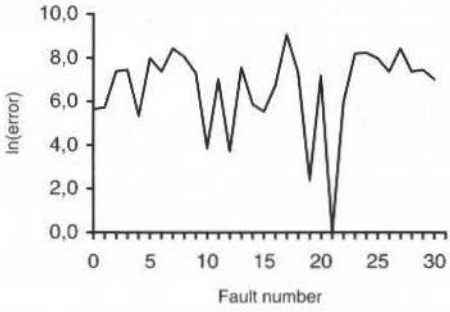

Fig. 8 Identified error among the curves

Conclusion

A fault detection methodology using neural networks and model updating for identifying the presence of structural damage has been presented and demonstrated with an application to a frame structure. The feasibility of the approach is evaluated for simulated numerical data and experimental test. As discussed, the approach compares the current characteristic response of the model with previous pattern of the state of operation which were defined by applying SDM in the representative FE-model.

A compression method has been used to reduce the number of point of the signal that will feed the ANN. It creates an equivalent signature for the system based on the maximum amplitudes of the original spectrum signal. Considering a frequency range of 3% around of the points of maximum amplitudes is satisfactory in this study case. It seems to suppress the effects of small oscillation

(variations) in experimental measurements. The architecture of the network has been defined by tests since it does not comply a criterion to define the optimum architecture. However, the results seem to be better when the neurons number in the hidden layer increase. Parallel issues such as fault into elements of low sensitivity and robustness when the measured data comprise small deviation of previous pattern due measurement difficulties have been addressed.

In general for condition monitoring such issues are extremely important since it is essential to recognise a fault in time to permit action to be taken in order to avoid failure of the component. The preliminary results show that the proposed methodology can be applied to classify an unknown signal in patterns fixed beforehand. Although the approach has successfully identified the damaged element for all simulated test cases as well as for the experimental test, its success is not unconditional. In order to explore in depth the potential for application of such propose to monitoring health condition and failure location in real structures, further research addressing more complex case studies must to be done.

References

Bernieri, A. at all; 1994, "A Neural Network Approach for Identification and Fault Diagnosis on Dynamic Systems," IEEE Trans. on Instrumentation and Meas., vol. 43, n° 6 pp. 867-873. Dec.

Hecht-Nielsen R.; 1990, Neurocomputing - Addison-Wesley Publishing Company.

Hush D.R. and Horne, B.G.; 1993, "Progress in Supervised Neural Networks - What's New Since Lippmann," - IEEE Signal Proc. Mag., pp. 8-39 - Jan.

Lammens. S., 1995, "Frequency Response Based Validation of Dynamic Structural Finite Element Models," Ph.D., Thesis, Katholieke Universiteit Leuven, Belgium.

Larsson, P. O. and Sas, P., 1992, "Model Updating Based on Forced Vibration Testing Using Numerically Stable Formulations," Proceedings of the X-IMAC.

Lippmann, R.P.; 1987, "An Introduction to Computing with Neural Nets," IEEE - ASSP Magazine, pp. 4-22, April.

Lopes Jr., V. and Turra, A. E., 1996, "Diagnosis of Rotating Systems Using Artificial Neural Networks", Application of Artificial Intelligence in Engineering XI, includes CD Rom - Computational Mechanics Publications, Sep.

Narenda, K.S. and Parthasarathy, K., 1990, "Identification and Control Dynamical Systems Using Neural Networks," IEEE Trans. on Neural Networks, vol. 1, n° 1 pp. 4-24, March.

Pereira, J. A., 1996, "Structural Damage Detection Methodology using a Model Updating Procedure based on Frequency Response Functions - FRF(s)," Tese de Doutorado, Universidade Estadual de Campinas, Faculdade de Engenharia Mecânica, Campinas.

Schwaarz, B. J., et all; 1996, "Using SDM to train Neural Networks for Solving Modal Sensitivity Problems",. Proceedings of the XIV-IMAC.

Uhl,T.; 1994, "Automation of monitoring and diagnostic process for rotating machinery using neural networks," ISMA - Intern. Seminar of Modal Analysis - Leuven, Belgium, Sept.

Yuedong, C., and Du, R.; 1996, "Artificial Neural Network Architecture Design Using Similarity Measure with Applications in Engineering Monitoring and Diagnosis," ASME Journal of Dynamic System, Measurement, and Control, , vol 118, pp. 635-639, sept.

Wasserman, P.D., Neural Computing, 1989, Theory and Practice - Van Nostrand Reinhold.

Warden, K. and Tomlinson G. R.; 1994, " Modeling and Classification of Non-linear System Using Neural Networks," Mechanical Systems and Signal Processing, pp. 319-356.

RBCM - J. of the Braz. Soc. Mechanical Sciences
Vol. XXI - No.1 - 1999 - pp. 109-122

ISSN 0100-7386
Printed in Brazil

Availability of a Component Subject to an Erlangian Failure Model Under Wearout by Supplementary Variables

Marcos Oliveira de Pinho
CEFET - RJ
Rua General Canabarro 495
20271-201 Rio de Janeiro, RJ Brazil

Héctor Crispín Noriega Fernández
Universidad Austral de Chile
Instituto de Disegno y Métodos Industriales
Campus Miraflores
Casilla 567 Valdevia, Chile
h.noriega@computer.org

Antonio Carlos Marques Alvim
Paulo Fernando Ferreira Frutuoso e Melo
Universidade Federal do Rio de Janeiro
COPPE - Programa de Engenharia Nuclear - C. P. 68509
21945-970 Rio de Janeiro, RJ Brazil
(alvim, frutuoso)@lmn.com.ufrj.br

Abstract

This paper presents the availability analysis of a component by means of supplementary variables taking wearout into account. An Erlangian failure model is adopted, so as to allow comparison of the results with those obtained from the device of stages, which, for this failure model, theoretically gives exact results. The component availabilities obtained from both methods are well in agreement, although the results obtained from the supplementary variables method are less conservative. A point worth mentioning is that the solutions have been obtained for the transient period, a feature not commonly approached in the literature. The supplementary variables method is more general, although it may present numerical instability problems if proper care is not taken when discretization of the system is made. In this paper, the indirect method of Lax is shown to be stable for the problem modeled.
Keywords: *Availability Analysis, Wearout, Non-Markovian Models, Device of Stages, Supplementary Variables*

Introduction

For those components which are no longer in their useful life period, the use of exponential failure models implying constant failure rates is not adequate as long as it results in an overestimation of the reliability figure of interest (Billinton and Allan, 1983).

The hypothesis of a constant failure rate is quite convenient because it is then possible to use a time-homogeneous Markovian model for evaluating reliability figures of interest. By means of a time-homogeneous Markovian model, we may obtain both time-dependent reliability characteristics and treatment of failure dependencies and interactions; for example, common cause failures and shared-load components.

The consideration of the component wearout implies the use of an increasing failure rate model, for example, as in the Weibull or the lognormal distributions (Kececioglu, 1991).

To model the problem under discussion, two approaches are available (Singh and Billinton, 1977).

The first approach consists of introducing supplementary variables in the model (Cox, 1955, Cox and Miller, 1965, Singh and Billinton, 1977), taking into account the age of components which do not have constant failure rates. This is due to the fact that the operational records of each component must be taken into account since the Markovian lack of memory property is no longer valid.

Theoretically, the supplementary variables technique allows consideration for any wearout model. However, to obtain the reliability figures of interest, one has to solve a system of coupled differential equations where both ordinary and partial equations appear, as well as the additional difficulty of time-dependent boundary conditions. Generally, the solution of these equations is performed by finite difference methods.

Some recent applications of the supplementary variables method can be found in Dhillon (1992), Dhillon and Anude (1993), Dhillon and Yang (1993a), Dhillon and Yang (1993b), and Dhillon and Anude (1994). In general, only asymptotic solutions are obtained.

Manuscript received: November 1997; revised: September 1998. Technical Editor: Paulo Eigi Miyagi. An abridged version of this paper has been presented at COTEQ'96 - Conferência sobre Tecnologia de Equipamentos, Rio de Janeiro, RJ, November 1996.

It is uncommon to find general solutions for this problem in reliability literature. We have found a few references where analytical solutions for the transient phase are approached.

Analytical solutions considering the transient phase may be found in Kumar et al (1988), Singh (1989), and Singh and Murari (1984). In all of them, exponential failure times and general repair times are taken into account.

On the other hand, general solutions for the transient case considering arbitrary failure time distributions have not been found.

For the second approach mentioned above, which is termed the device of stages (Cox and Miller, 1965, Singh and Billinton, 1977), fictitious states, called stages, are taken into account. In this respect, the Non-Markovian model is cast into a Markovian one. A limitation of this device is that it is not as general as the supplementary variables method (Singh and Billinton, 1977).

The purpose of this paper is to present the application of the supplementary variables technique to a component which undergoes wearout, in order to obtain its time-dependent availability. Both the transient behavior and the asymptotic availability were investigated. Our aim is to present general numerical solutions by means of the indirect method of Lax, which is shown to be stable for the problem modeled.

The problem faced here is not new [this may be confirmed by the fact that the first published reference on this subject matter is Cox (1955)]. However, the employment of appropriate numerical methods for solving the resulting system of coupled differential equations has not as yet been found in the literature, so as to our knowledge, the analysis of the transient phase has not been performed.

The hypotheses undertaken for calculating the results are discussed, and the numerical features of relevance are also presented.

This paper is organized as follows. The next section discusses the employed methodology, both from the point of view of supplementary variables, and also from the device of stages. Next, specific analyzed cases are displayed. Finally focused are the generated results allowing conclusions and recommendations for further research.

Methodology

The cases to be analyzed in this paper will make use of the Erlangian distribution for the failure times. This distribution has a probability density given by:

$$f_T(t) = \frac{\lambda^{\rho} t^{\rho-1} e^{-\lambda t}}{(\rho-1)!} \tag{1}$$

for which $t \geq 0$, $\lambda \geq 0$ and ρ is a positive integer. Figure 1 displays the density function for this distribution for different values of its parameter ρ. It should be noted that for $\rho = 1$, one has the exponential distribution.

The failure rate for the Erlangian distribution may be written as:

$$h(t) = \frac{t^{\rho-1}}{(\rho-1)! \sum_{k=0}^{\rho-1} \frac{t^k}{k! \lambda^{\rho-k}}} \tag{2}$$

Nomenclature

$f_T(t)$ = failure times probability density
M = state transition matrix
$P(t)$ = state vector, $[P_1(t), P_2(t), P_3(t)]^T$
$h(t)$ = failure rate [year^{-1}]
$P_i(\infty)$ = asymptotic probability of a component being in state i
$P_i(t)$ = probability of a component being in a state (considers a constant transition rate out of the state)
$p_I(x,t)$ = probability density of a component being in a state (considers a time-dependent transition rate out of the state) [year^{-1}]
$\tilde{p}_I(x,s)$ = Laplace transform
t = time [year]
x = component age [year]
λ = scale parameter for the Erlangian distribution [year^{-1}]
μ = repair rate [year^{-1}]
ρ = shape parameter for the Erlangian distribution

Figure 2 presents the failure rate behavior considering different values for ρ. It may be seen that the failure rate approaches similar asymptotic values for longer time periods (over 80 years).

The Erlangian distribution is a specific gamma distribution case when ρ is an integer (McCormick, 1981, Soong, 1981).

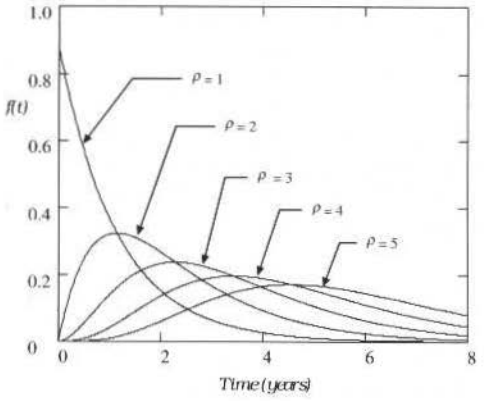

Fig. 1 Erlangian Densities for Different Values of ρ

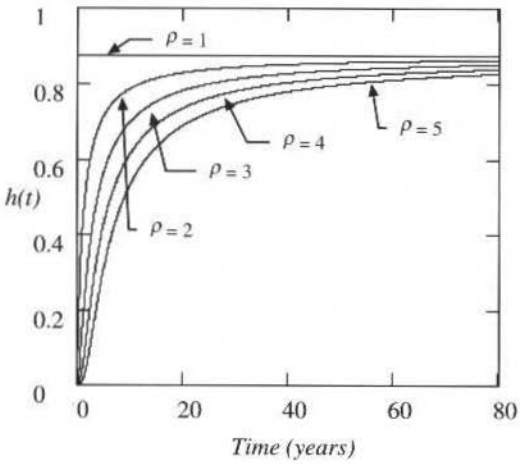

Fig. 2 Erlangian Failure Rates dor Different ρs

It is convenient to consider the Erlangian distribution as the first failure model because, if a random variable follows this distribution, it can be written as the sum of ρ, independent and identically distributed exponential random variables with parameter λ (Soong, 1981). This fact makes it theoretically possible to obtain exact results by the device of stages (Singh and Billinton, 1977). In this sense, one has the exact solution to compare to that which was obtained from the supplementary variables method.

Specifically, let $T = Y + W$ and let Y and W be independent and continuous random variables. Then, the probability density function of T is the convolution of the densities associated with Y and W; that is,

$$f_T(t) = \int_{-\infty}^{\infty} f_Y(t-w) f_W(w)\,dw = \int_{-\infty}^{\infty} f_W(t-y) f_Y(y)\,dy \qquad (3)$$

It is easy to generalize Eq. (3) for the case where the sum is composed of ρ independent random variables.

Now consider that both Y and W follow an exponential distribution with parameter λ [by putting ρ = 1 in Eq. (1)]. Then, by applying Eq. (3) one has:

$$f_T(t) = \int_0^t \lambda^2 e^{-\lambda(t-w)} e^{-\lambda w} dw = \lambda^2 t e^{-\lambda t}, t \geq 0 \tag{4}$$

This is the Erlangian distribution. Notice that since t-$w \geq 0$, the integration on w is from 0 to t.

Repeated application of Eq. (3) gives as a result Eq. (1). For example, consider that Y follows the Erlangian distribution displayed in Eq. (4), and W again follows an exponential distribution with parameter λ. One then has,

$$f_T(t) = \int_0^t \lambda^2 (t-w) e^{-\lambda(t-w)} \lambda e^{-\lambda w} dw = \frac{1}{2} t^2 e^{-\lambda t} \tag{5}$$

Recall that Eq. (5) may be obtained from Eq. (1) when using ρ = 3.

Finally, consider that Y follows the Erlangian distribution displayed in Eq. (5), and W still follows the exponential distribution. One has,

$$f_T(t) = \int_0^t \frac{1}{2} \lambda^3 (t-w)^2 e^{-\lambda(t-w)} \lambda e^{-\lambda w} dw = \frac{1}{3!} t^3 e^{-\lambda t} \tag{6}$$

which is the Erlangian distribution obtained by putting ρ = 4 in Eq. (1).

When the situation of interest in this paper occurs in which failure times follow an Erlangian distribution and, consequently, wearout is present, the lack of memory property of Markovian models (Ross, 1993) is no longer valid. To solve this problem, a supplementary variable, x, is introduced in order to account for the component age (Cox and Miller, 1965, Singh and Billinton, 1977).

The state transition diagram for the component problem is displayed in Figure 3. State 1 (which is the functioning state) is modeled by means of a probability density, termed $p_1(x,t)$, which is interpreted as follows: $p_1(x,t)\Delta x$ is the probability that the component is in state 1 at time t, and its age is between x and $x+\Delta x$. In this sense, the probability that the component is in state 1 at time t, $P_1(t)$, is given by:

$$P_1(t) = \int_0^\infty p_1(x,t) dx \tag{7}$$

In Figure 3, $h(x)$ is the component age-dependent failure rate and μ is its constant repair rate. $P_i(t)$ is the probability that the component is in state i at time t.

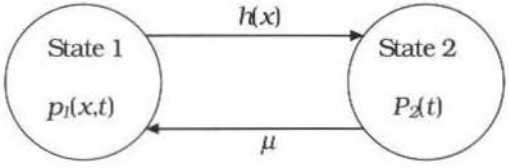

Fig. 3 State Transition Diagram for the Supplementary Variables Method

The solution of the equations for the supplementary variables method will be discussed in the next section, where the analyzed cases will be presented.

The device of stages (Cox and Miller, 1965, Sing and Billinton, 1977, Nunes, 1995) has been the result of a simple fact: transitions which occur with time-dependent rates (corresponding to nonexponential failure time distributions) can, in certain cases, be cast into combinations of fictitious states with constant transition rates. In this sense, a Markovian model results.

The model for this case, particularly, in terms of states, will always be a series of ρ stages. In this sense, an exact solution will be obtained (in fact, numerical methods must be used if one has many coupled equations, since analytical solutions may become tedious; therefore, the meaning of the exact word should be taken only on conceptual grounds, unless a symbolic computer program is available). For other failure time distributions, as the Weibull and the lognormal, one should search for convenient combinations of stages (series and/or parallel) so that adequate approximations are obtained (Singh and Billinton, 1977, Nunes, 1995).

Solutions for the models developed by means of the device of stages will also be discussed in the next section.

Description of the Analyzed Cases

Before discussing the analyzed cases, a comment is due. As opposed to the general procedure when applying the device of stages, which means a better choice of the combination of stages to represent the real failure distribution, we focus attention on two different failure time distributions which have different means, defined by different shape parameter values, as will be seen later.

Considered is the general model of a component which may be in one of two possible states. It can be on (state 1) or failed (state 2), as depicted in Figure 3. Its failure rate is represented by $h(x)$, where x represents its age. On the other hand, μ represents its repair rate.

The first case to be analyzed, hereafter denoted as case 1, is that for which an Erlangian distribution with $\rho = 2$ is assumed for the component failure times [Eq. (1) and Figure 1].

The corresponding failure rate function is obtained by putting $\rho = 2$ in Eq. (2) (see Figure 2).

The supplementary variables method for this problem is the solution of the following system of coupled equations, Singh and Billinton (1977):

$P_i(t)$ = the probability that the component is in state i at time t. (8)

$$p_i(x,t) = \lim_{\Delta x \to 0} \frac{P\left[\textit{The system is in state i and its age is in } (t-x-\Delta x, t-x)\right]}{\Delta x} \tag{9}$$

Performing a probability balance, one has:

$$p_1(x+\Delta t, t+\Delta t) = p_1(x,t)\left[1-h(x)\Delta t\right] \tag{10}$$

$$P_2(t+\Delta t) = P_2(t)\left[1-\mu\Delta t\right] + \Delta t \int_0^\infty h(x)\,p_1(x,t)\,dx \tag{11}$$

By means of a Taylor series expansion to linear terms,

$$p_1(x+\Delta t, t+\Delta t) \equiv p_1(x,t) + \frac{\partial p_1}{\partial x}\Delta t + \frac{\partial p_1}{\partial t}\Delta t + o(\Delta x^2, \Delta t^2), \tag{12}$$

one obtains the resulting differential equations as $\Delta t \to 0$ [Eq. (12) is substituted in Eq. (10) and an equation for the Taylor expansion of $P_2(t+\Delta t)$ is substituted in Eq. (11)]:

$$\frac{\partial p_1(x,t)}{\partial x}+\frac{\partial p_1(x,t)}{\partial t}=-h(x)p_1(x,t) \tag{13}$$

$$\frac{dP_2(t)}{dt}=-\mu P_2(t)+\int_0^{\infty} h(x)p_1(x,t)dx \tag{14}$$

The initial conditions for solving this system are given by

$$p_1(x,0)=f_X(x) \tag{15}$$

$$P_2(0)=0 \tag{16}$$

and the boundary condition is given by:

$$p_1(0,t)=\mu P_2(t) \tag{17}$$

The initial condition given by Eq. (15) is fundamental for solving the equations. It accounts for uncertainties in the component age. The function appearing on the right hand side is exactly the probability density given by Eq. (1). The probability that the component is in state 1 at $t = 0$ is given by Eq. (7).

It remains to show that the solutions $P_1(t)$ and $P_2(t)$ satisfy the probability condition, that is:

$$P_1(t)+P_2(t)=1 \tag{18}$$

To see this, one takes the Laplace transform of Eq. (13), so that:

$$s\tilde{p}_1(x,s)-f_X(x)+\frac{\partial \tilde{p}_1(x,s)}{\partial x}=-h(x)\tilde{p}_1(x,s) \tag{19}$$

By integrating Eq. (19) with respect to x and by using the Laplace transform in Eq. (14) together with the condition given by Eq. (17), one obtains Eq. (18).

It is not difficult to note that the system of Eqs. (13)-(17) reproduces the well-known solution when the failure rate is constant; that is, when one has the exponential failure mode. To see this, one solves Eq. (19):

$$\tilde{p}_1(x,s)=exp[-u(s,x)]\int_0^{x} f(r)exp[u(s,r)]dr+\mu\tilde{p}_2(s)exp[-u(s,x)] \tag{20}$$

in which:

$$u(s,r)=sr+\int_0^{r} h(u)du \tag{21}$$

Thus, by using the Laplace transform of (14) and Eq. (21), one has:

$$\tilde{p}_2(s) = \frac{\int_0^\infty h(x)\exp[-u(s,x)]\int_0^x f(r)\exp[u(s,r)]dr\,dx}{s+\mu-\mu\int_0^x h(x)\exp[-u(s,x)]dx} \tag{22}$$

which results in [when one uses $h(t) = \lambda$ = constant]:

$$P_1(t) = \frac{\mu}{\lambda+\mu} + \frac{\lambda}{\lambda+\mu}\exp[-(\lambda+\mu)t] \tag{23}$$

The steady-state solution for this model is obtained by setting the chronological time derivatives in Eqs. (13)-(14) equal to zero and solving the resulting system. One obtains:

$$p_1(x,\infty) = c\ \exp\left[-\int_0^x h(x')dx'\right] \tag{24}$$

and

$$P_2(\infty) = \frac{c}{\mu}\int_0^\infty h(x)\exp\left[-\int_0^x h(x')dx'\right]dx \tag{25}$$

The normalization constant c is obtained by substituting Eqs. (24)-(25) for Eq. (18) where $P_1(t)$ is given by Eq. (7).

The same problem will be solved by means of the device of stages, so as to allow for checking the behavior of the solution obtained by the method of supplementary variables.

As already discussed, the convolution of two identical and independent exponential distributions with parameter λ gives rise to an Erlangian distribution [as may be seen from Eq. (4)]. On the grounds of the device of stages, this feature allows solving this same problem by means of two stages.

The functioning state (state 1) is replaced by the two aforementioned stages (Figure 4) whose transition rates are constant. The system of differential equations to be solved here is given by:

$$\frac{dP(t)}{dt} = MP(t) \tag{26}$$

for which $P(t) = [P_1(t), P_2(t), P_3(t)]^T$ and

$$M = \begin{bmatrix} -\lambda & 0 & \mu \\ \lambda & -\lambda & 0 \\ 0 & \lambda & -\mu \end{bmatrix} \tag{27}$$

The steady-state solution for this system is given by:

$$P_i(\infty) = \frac{\mu}{\lambda+2\mu},\ i = 1,2 \tag{28}$$

$$P_3(\infty) = \frac{\lambda}{\lambda + 2\mu} \tag{29}$$

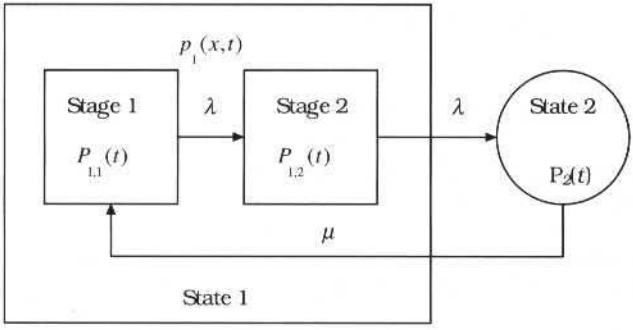

Fig. 4 State Transition Diagram for Casel (ρ= 1) by the Device

It should be mentioned that the solution of this problem by the device of stages implies that an initial condition involving a stage must be considered, meaning that, for $t = 0$, the component will be in a fictitious state. Specifically, for this case, state 1 has been split into stages 1 and 2 (see Figure 4). State 2 remains as the failure state. The initial condition will be given by $P_{1,1}(0) = 1$. In order to evaluate the influence of the stage modeling, the case for which $P_{1,2}(0) = 1$ will also be analyzed.

The second case to be analyzed is the one for which the failure times follow an Erlangian distribution obtained by placing $\rho = 4$ in Eq. (1) (see Fig. 1). The corresponding failure rate is obtained by setting $\rho = 4$ in Eq. (2) (see Fig. 2).

We now have four independent and identically distributed exponential distributions with parameter λ. To solve this problem by the supplementary variables method, one has to consider the same group of equations which was used for solving case 1; that is, Eqs. (13)-(17). The steady-state solution is once again given by Eqs. (24)-(25).

On the other hand, the solution by the device of stages implies splitting the functioning state into four stages. In this sense, the state transition diagram is recast into one with 5 states (see Fig. 5). The system of equations to be solved is equal, Eq. (26), but the transition matrix is given by:

$$M = \begin{bmatrix} -\lambda & 0 & 0 & 0 & \mu \\ \lambda & -\lambda & 0 & 0 & 0 \\ 0 & \lambda & -\lambda & 0 & 0 \\ 0 & 0 & \lambda & -\lambda & 0 \\ 0 & 0 & 0 & \lambda & -\mu \end{bmatrix} \tag{30}$$

The steady-state solutions for this case are given by:

$$P_i(\infty) = \frac{\mu}{\lambda + 4\mu}, \quad i = 1,\ldots,4 \tag{31}$$

and

$$P_5(\infty) = \frac{\lambda}{\lambda + 4\mu} \tag{32}$$

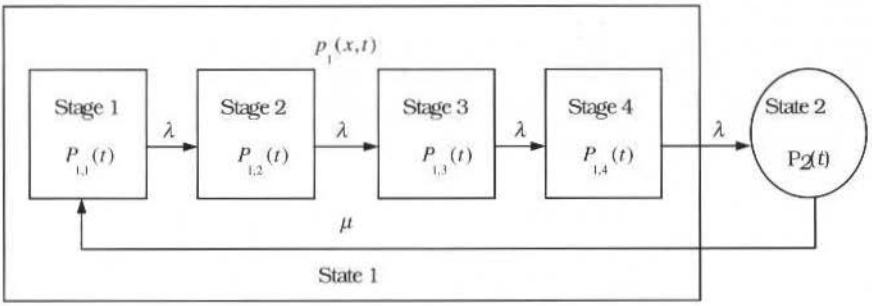

Fig. 5 State Transition Diagram for Case 2 (ρ = 4) by the Device of Stages

One should observe that the number of equations to be solved in this case is much greater; on the other hand, if one considers the supplementary variables method, the same number of equations is to be solved, which is clearly advantageous.

The solution of the equations obtained by the supplementary variables method is performed by means of finite differences. Particularly, those equations which involve partial derivatives are much more tedious and difficult to solve because stability problems may arise. The solution method of Lax (Anderson *et alii* , 1984, Press *et alii* ,1992) was chosen, due to its stability property. One has:

$$\frac{\partial p}{\partial t} \cong \frac{p_{i,j+1} - \dfrac{p_{i+1,j} + p_{i-1,j}}{2}}{\Delta t} \tag{33}$$

and

$$\frac{\partial p}{\partial x} \cong \frac{p_{i+1,j} - p_{i-1,j}}{2\Delta x} \tag{34}$$

Stability of the solutions will be obtained whenever

$$\frac{\Delta t}{\Delta x} \leq 1 \tag{35}$$

The solution of the equations for the device of stages was obtained by means of the Bulirsh-Stoer method, Press *et alii* (1992). The Runge-Kutta method was not employed because it is known that the solutions for these equations are always combinations of negative exponential functions, which, in general, present a smooth behavior. In this regard, the method employed gave more precise results.

Numerical Results Obtained

Both cases were analyzed considering λ = .876/yr (10^{-4}/hr) and μ = 87.6/yr (10^{-2}/hr), which are typical parameters of exponential distributions found in the practice of failure and repair times modeling. The failure and repair data have been chosen considering that: a) the constant failure rate of 10^{-4}/hr is typical for general mechanical components, as may be seen in Appendix 14 of Lees (1996); b) constant repair rates are typically greater than failure rates. Thus, a repair rate equal to 10^{-2}/hr is quite reasonable, Lewis (1996), McCormick (1981).

In order to evaluate the influence of the initial condition in the context of the device of stages, three possibilities were analyzed for case 1. The first one considered that the component was in the first stage for $t = 0$. As a second possibility, it was considered that the component had a .5 probability of being in

the first stage, and the same probability of being in the second one. The final possibility was that the component was in the second stage for $t = 0$.

Figure 6 presents the results obtained for case 1 by the device of stages. It should be observed that varying the initial condition means that the behavior of the component, in terms of its availability, is such that an initial depression is present (transient behavior), very similar to the one found by using the supplementary variables method. The steady-state availability obtained by the two methods was almost the same. The small differences observed were due to the fact that both solutions were obtained by numerical methods.

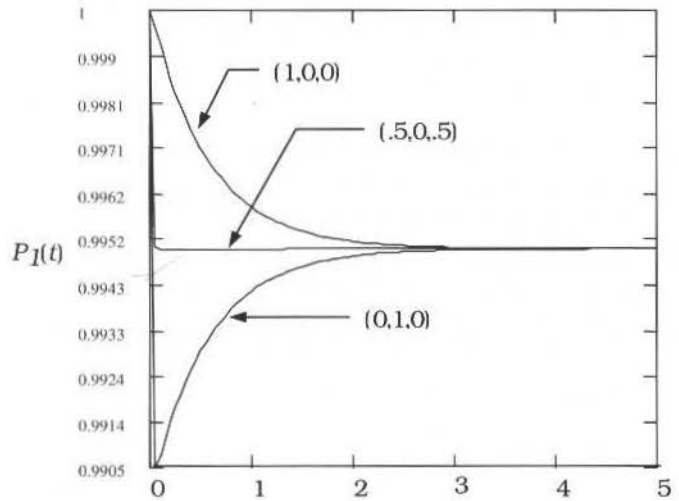

Fig. 6 Results for Case 1 by the Device of Stages (Different initial Conditions Displayed)

Figure 7 presents the results of both methods for case 1. The results obtained from the device of stages consider that the component was initially at the first stage.

Figure 8 displays the surface of $p_1(x,t)$ for the case at hand.

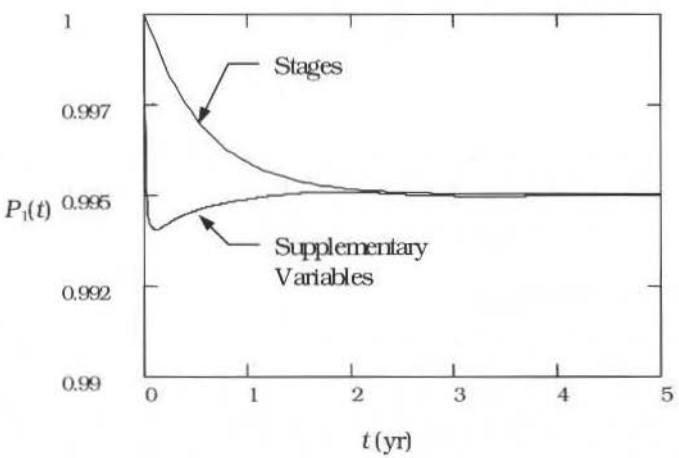

Fig. 7 Results for Case 1 by Suplementary Variables (Also Displayed are Results by the Device os Stages)

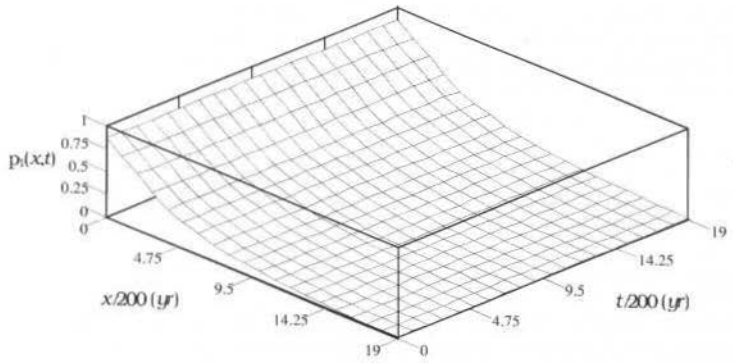

Fig. 8 Probability Density $\rho 1(x,t)$ for the Erlangian with $\rho = 2$

Figure 9 presents the results for case 2 by the device of stages with the different initial conditions taken into account.

Figure 10 presents the results for both methods. The curve generated by means of the device of stages displayed in this figure considers that the component was at stage 1 for $t = 0$. Again, a reasonable agreement has been observed between the steady-state availabilities; also, a less conservative behavior of the transient solution obtained by the method of supplementary variables was obtained, mainly for the transient solution.

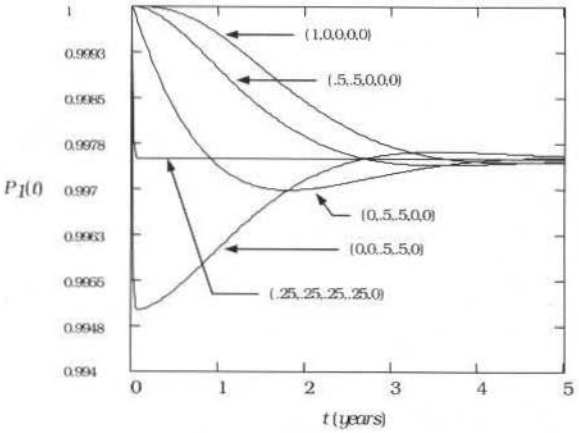

Fig. 9 Results for Case 2 by the Devices of Stages

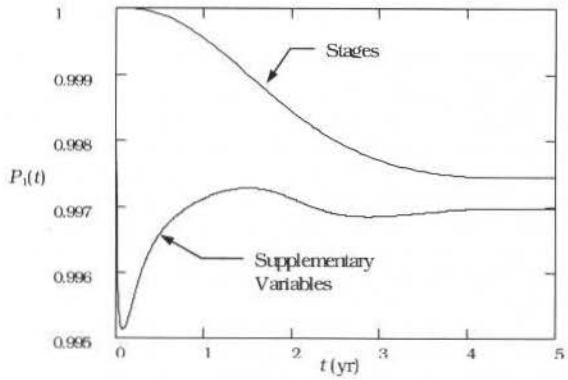

Fig. 10 Results for Case 2 by Supplementary Variables (Also Displayed are Results by the Device of Stage)

It may be seen from Figure 10 that by applying the supplementary variables method for case 2, the resulting curve is steeper for the first two years. This feature may be explained by the behavior of the failure rate $h(x)$ in this same period, as opposed to what occurs for case 1 (see Figure 7).

Table 1 summarizes the results for the steady-state unavailabilities.

Table 1 Asymptotic Unavailabilities

Case	Supplementary Variables			
	Device of Stages		Supplementary Variables	
	Theoretical	Numerical	Theoretical	Numerical
1 (ρ=2)	4.98×10^{-3}	5.0×10^{-3}	4.3×10^{-3}	5.0×10^{-3}
2 (ρ=4)	2.49×10^{-3}	2.6×10^{-3}	2.34×10^{-3}	2.4×10^{-3}

A final comment concerns the comparison between the analytical and numerical solutions for one stage; that is, comparison between the analytical result furnished by Eq. (23) and the numerical solution furnished by Eqs. (13)-(17), by putting $\rho = 1$ in Eq. (1) and then inserting it into Eq. (15). The results are displayed in Figure 11. It can be seen that the agreement between both results was excellent.

Conclusions and Recommendations

This paper presented the solution of an availability problem considering wearout by applying two traditional methods, the device of stages and the method of supplementary variables. Although the problem seems to be quite simple, the consideration of wearout results in a more complex solution. Wearout, in practice, is a very serious problem if one considers real plant environments where many factors contribute to it.

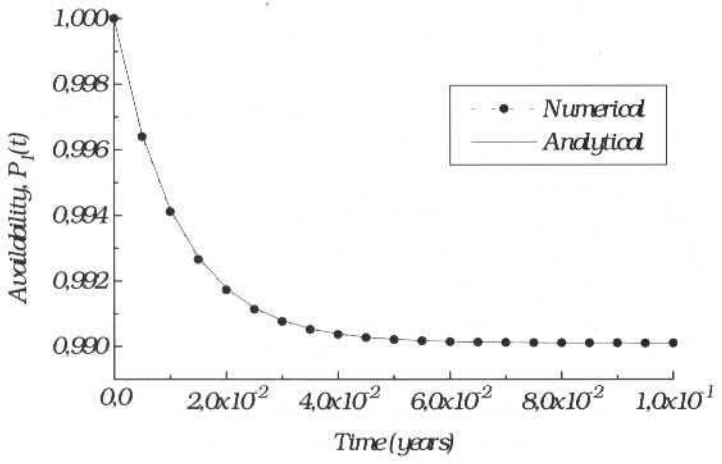

Fig. 11 Comparison between analytical and numerical solutions for one stage

Of course, consideration of a simple failure time distribution, as the Erlangian, cannot solve many of the practical problems found, for which a Weibull or a lognormal distribution is much more adequate to fit the failure data, but the purpose was to show the solution, both from the point of view of transient behavior and steady-state solution when even a simple wearout model is adopted. The Erlangian distribution can always be recast into the sum of independent identical exponential distributions and, thus, from the point of view of the device of stages, theoretical exact solutions can be obtained. This is an important feature for comparison purposes. Stability problems in this context do not exist. Numerical solutions must be used for the number of equations to be solved growing with the number of stages considered, as the two analyzed cases showed.

On the other hand, when the method of supplementary variables is employed, even though the number of equations always remains the same, new features must be taken into account. One should always employ numerical methods, even for simple distributions, like Erlangian's. A new feature to be considered is the one related to stability difficulties.

From the theoretical point of view, it can be shown that for a system like the one in Eqs. (13)-(17) for the existence and unicity conditions, the solution is stable, Burton (1983). However, on the grounds of numerical solutions, stability problems arise when calculating partial derivatives.

One could be tempted to employ a direct method, such as:

$$\frac{\partial p}{\partial t} = \frac{p_{i,j+1} - \dfrac{p_{i+1,j} + p_{i,j}}{2}}{\Delta t} \quad and \quad \frac{\partial p}{\partial x} = \frac{p_{i+1,j} - p_{i,j}}{\Delta x}, \tag{36}$$

for solving Eq. (13). However, this method is not stable. In this regard, alternatives had to be sought. A conditionally stable method found is that in Eqs. (33)-(34) with the condition given by Eq. (35), the so-called Lax indirect method, Anderson *et alii* (1984).

A final comment concerning the solution of Eqs. (13)-(17) is related to the solution of the integrals. Used was the Gauss-Laguerre formula, which showed it to be sufficiently accurate for our purposes.

We recommend that the solution presented be expanded to consider possible redundancies, a situation of great practical importance. Also, we suggest failure times modeling by alternative distributions, such as Weibull and lognormal.

A point worth mentioning in this context is that it has not been our intent to discuss the advantages or limitations of the employed methodologies in this paper; that is, supplementary variables and/or the device of stages. An alternative approach to consider when repair is taken into account is that of Poisson point processes, Ascher & Feingold, 1984.

Acknowledgements

We would like to acknowledge appreciation of financial support from the National Council of Scientific and Technological Development (CNPq) for developing the work presented in this paper [Project Number 520224/94-9(NV)].

References

Anderson, D. A., Tannehill, J. C. and Pletcher, R. H., 1984, "Computational Fluid Mechanics and Heat Transfer", Hemisphere Publishing Corporation, New York.

Ascher, H., and Feingold, H., 1984, "Repairable Systems Reliability, Modeling, Inference, Misconceptions and their Causes", Marcel Dekker, Inc., New York.

Billinton, R. and Allan, R. N., 1983, "Reliability Evaluation of Engineering Systems: Concepts and Techniques", Plenum Press, New York.

Burton, T. A., 1983, "Volterra Integral and Differential Equations", Academic Press, New York.

Cox, D. R., 1955, "The Analysis of Non-Markovian Stochastic Processes by the Inclusion of Supplementary Variables", Proc. Camb. Phil. Soc., vol. 61, pp. 433-441.

Cox, D. R. and Miller, H. D., 1965, "The Theory of Stochastic Processes", Chapman and Hall, London.

Dhillon, B.S., 1992, "Stochastic Modelling of *k*-out-of-*n* Unity Family of Systems", International Journal of Systems Sciences, vol. 23(8), pp. 1277-1287.

Dhillon, B. S. and Anude, O. C., 1993, "Common-Cause Failure Analysis of a Non-Identical Unit Parallel System with Arbitrarily Distributed Repair Times", Microelectronics and Reliability, vol. 33(1), pp. 87-103.

Dhillon, B. S. and Yang, N. ,1993a, "Human Error Analysis of a Standby Redundant System with Arbitrarily Distributed Repair Times", Microelectronics and Reliability, vol. 33(3), pp. 431-444.

Dhillon, B. S. and Yang, N., 1993b, "Availability of a Man-Machine System with Critical and Non-Critical Human Error", Microelectronics and Reliability, vol. 33(10), pp. 1511-1521.

Dhillon, B. S. and Anude, O. C., 1994, "Income Optimization of a Repairable and Redundant System", Microelectronics and Reliability, vol. 34(11), pp. 1709-1720.

Kececioglu, D. C., 1991, "Reliability Engineering Handbook", Prentice-Hall, Englewood Cliffs, New Jersey.

Kumar, D., Singh, J. and Singh, I. P., 1988, "Availability of the Feeding System in the Sugar Industry", Microelectronics and Reliability, vol. 28(6), pp. 867-871.

Lees, F., 1996, "Loss Prevention in the Process Industries, Hazard Identification, Assessment and Control", 2nd edition, Butterworth-Heinemann, Oxford, UK.

Lewis, E. E., 1996, "Introduction to Reliability Engineering", 2nd edition, John Wiley and Sons, New York.

McCormick, N. J., 1981, "Reliability and Risk Analysis, Methods and Nuclear Power Applications", Academic Press, New York.

Nunes, M. E. C , 1995, "Application of the Device of Stages to the Unavailability Analysis of a Single Protective Channel" (in Portuguese), M. S. Thesis, COPPE/UFRJ, Rio de Janeiro.

Press, W. H., Flannery, B. P., Teukolsky, S. A. and Vetterling, W. T., 1992, "Numerical Recipes in Fortran, The Art of Scientific Computing", Cambridge University Press, Cambridge, UK.

Ross, S. M., 1993, "Introduction to Probability Models", Academic Press, New York.

Singh, J., 1989, "A Warm Standby Redundant System with Common Cause Failures", Reliability Engineering and System Safety, vol. 26, pp. 135-141.

Singh, C. and Billinton, R., 1977, "System Reliability Modelling and Evaluation", Hutchinson, London.

Singh, J. and Murati, K. ,1984, "Reliability of a Fertilizer Production Supply Problem", Proceedings of the 3rd Annual Conference of Indian Society for Theory of Probability and its Applications, Wiley Eastern Ltd., New Delhi, pp. 92-94.

Soong, T. T., 1981, "Probabilistic Modeling and Analysis in Engineering and Science", John Wiley & Sons, New York.

RBCM - J. of the Braz. Soc. Mechanical Sciences
Vol. XXI - No.1 - 1999 - pp. 123-132

ISSN 0100-7386
Printed in Brazil

A Study of Parameter Monitoring in Stationary Mechanical Systems

André Garcia Chiarello
Escola Federal de Engenharia de Itajubá
Departamento de Mecânica
37500-000, Itajubá, MG Brazil
andregc@iem.efei.br

Robson Pederiva
Universidade Estadual de Campinas
Faculdade de Engenharia Mecânica
Departamento de Projeto Mecânico
13083-970, Campinas, SP Brazil
robson@fem.unicamp.br

Abstract

This work describes a method of parameter monitoring in stationary mechanical systems for fault detection and location purposes. Using a state space model of the system and an auxiliary one, called filter, analytical redundancy equations are defined. The redundancy equations are based on correlation functions involving systems parameters. It is demonstrated that these correlation functions can be used to generate residual functions for fault monitoring. All residual functions estimated for the healthy system are ideally zero but when a fault occurs, some estimated residuals differ from zero. Using a parametric residual analysis, one can locate the physical parameter that is directly related to the system fault. The proposed approach is demonstrated using a numerical example.
Keywords: *Fault Detection, Diagnosis, Model Based.*

Introduction

Model based fault detection in dynamic systems (MBFD) has been the subject of extensive research (Gertler, 1991; Patton at all, 1989). Unlike conventional monitoring techniques, which are based on hardware redundancy, the techniques based on MBFD rely on the concept of analytical redundancy. There is a great number of MBFD methods, among them one can distinguish the observers approach (Frank, 1990 and 1992), physical parameter estimation (Isermann 1993), parity space approach (Medvedev, 1995, Chow, 1984) and residual generation (Gertler, 1995).

There is a growing interest in recent years for on-line fault diagnosis to increase the reliability of complex systems. Robust methods that are insensitive to noise and disturbances are particularly interesting for real situations, where noise and disturbances are always present (Patton and Chen, 1992). The design of residual generation always involves two steps: the specification of residual properties and the analysis based on these residuals. The residual sets are usually specified to enhance fault isolation properties.

This paper describes a residual generation for stationary mechanical systems. As a first step, an auxiliary system is used to generate signals, which will be correlated to inputs and outputs of the system through appropriated correlation functions. These correlation functions are then transformed in a residual generator that is nominally nearly zero, if no faults are present in the system. As a second step, the residuals are examined using a parametric analysis to identify the physical parameter that is related to the fault. The fault in the system affects all correlation functions; however, not all residual functions are affected after a fault occurrence. It is demonstrated that only the residual functions that are associated with the fault parameters differ from zero after the fault occurrence.

The main advantage of the proposed technique is the possibility of locating the fault into the system, i.e., the identification of the physical parameter which is related to the fault. The location of the fault parameter has not been the aim of the methods based on the observer approach, parity space approach and the residual generation approach. The emphasis in these methods lies only on fault detection (the time identification of fault occurrence). Otherwise, the methods based on physical parameter estimation have been used for fault location purpose, but the estimation process is, in general, very sensitive to additive random noise. To overcome this drawback, this paper used the correlation technique in the residual estimation process. The simulation of a numerical example showed that the location of fault parameter is also possible even when additive random noise is present in the system signals.

Manuscript received: August 1998, Technical Editor: Hans Ingo Weber.

Residual Functions

A widely used model for mechanical systems with lumped parameters is given by

$$\boldsymbol{M}\ddot{\boldsymbol{d}}(t)+\boldsymbol{D}\dot{\boldsymbol{d}}(t)+\boldsymbol{K}\boldsymbol{d}(t)=\boldsymbol{U}\boldsymbol{u}(t) \tag{1}$$

where $\boldsymbol{d}(t)$ is the n dimensional vector of displacements and the dots indicate differentiation with respect to time. The vector $\boldsymbol{u}(t)$ represents the p dimensional vector of input forces, $\boldsymbol{M}$, $\boldsymbol{D}$, $\boldsymbol{K}$ and $\boldsymbol{U}$ are respectively, the mass, damping, stiffness and input matrices of appropriate dimensions. It is easy to transform the above n dimensional equation into a $2n$ dimensional state space model,

$$\begin{aligned}\dot{\boldsymbol{x}}(t)&=\boldsymbol{A}\boldsymbol{x}(t)+\boldsymbol{B}\boldsymbol{u}(t)\\ y(t)&=\boldsymbol{C}\boldsymbol{x}(t)\end{aligned} \tag{2}$$

with the following definitions:

$$\boldsymbol{x}(t)=\begin{Bmatrix}\boldsymbol{d}(t)\\ \dot{\boldsymbol{d}}(t)\end{Bmatrix} \quad , \quad \boldsymbol{A}=\begin{bmatrix}\boldsymbol{O} & \boldsymbol{I}\\ -\boldsymbol{M}^{-1}\boldsymbol{K} & -\boldsymbol{M}^{-1}\boldsymbol{D}\end{bmatrix} \quad , \quad \boldsymbol{B}=\begin{bmatrix}\boldsymbol{O}\\ \boldsymbol{M}^{-1}\boldsymbol{U}\end{bmatrix} \tag{3}$$

where $\boldsymbol{x}(t)$ is the $2n$, dimensional state vector and $\boldsymbol{y}(t)$ is the m dimensional output sensor vector. The dimensionless matrix $\boldsymbol{C}$ is assumed to be in a generalized form with full column rank. The dimensionless transformation matrix $\boldsymbol{T}$, with full rank and appropriate dimensions can be defined, satisfying

$$\boldsymbol{C}\boldsymbol{T}=[\boldsymbol{I}_{(m,\,m)} \vdots \boldsymbol{O}_{(m,\,2n-m)}] \tag{4}$$

Using the transformation matrix $\boldsymbol{T}$, the system in Eq.(2) can be transformed to the following form,

$$\begin{aligned}\dot{\bar{\boldsymbol{x}}}(t)&=\bar{\boldsymbol{A}}\bar{\boldsymbol{x}}(t)+\bar{\boldsymbol{B}}\boldsymbol{u}(t)\\ y(t)&=\bar{\boldsymbol{C}}\bar{\boldsymbol{x}}(t)\end{aligned} \tag{5}$$

where,

$$\bar{\boldsymbol{x}}(t)=\boldsymbol{T}^{-1}x(t)=\begin{Bmatrix}\boldsymbol{y}(t)\\ \boldsymbol{v}(t)\end{Bmatrix} \quad , \quad \bar{\boldsymbol{A}}=\boldsymbol{T}^{-1}\boldsymbol{A}\boldsymbol{T} \quad , \quad \bar{\boldsymbol{B}}=\boldsymbol{T}^{-1}\boldsymbol{B} \quad , \quad \bar{\boldsymbol{C}}=[\boldsymbol{I} \vdots \boldsymbol{O}] \tag{6}$$

The $(2n - m)$ dimensional vector $\boldsymbol{v}(t)$ represents the state variables that can not be directly measured by the sensors. However, an unitary-dimension auxiliary system can be used to filter the vector of measurements in the following form,

$$\dot{\boldsymbol{w}}(t)=N\boldsymbol{w}(t)+\boldsymbol{p}^{T}\boldsymbol{y}(t) \tag{7}$$

The N and $\boldsymbol{p}^{T}$ filter parameters need to be set in order to assign asymptotically stability and appropriated cut frequency. The transformed system and the filter can be rewritten in a single state equation as

$$\dot{\boldsymbol{z}}(t)=\boldsymbol{F}\boldsymbol{z}(t)+\boldsymbol{G}\boldsymbol{u}(t) \tag{8}$$

with the following definitions:

$$z(t)=\begin{Bmatrix}\overline{x}(t)\\ w(t)\end{Bmatrix} \quad , \quad \boldsymbol{F}=\begin{bmatrix}\overline{\boldsymbol{A}} & o\\ \boldsymbol{p}^T\overline{\boldsymbol{C}} & N\end{bmatrix} \quad , \quad \boldsymbol{G}=\begin{bmatrix}\overline{\boldsymbol{B}}\\ \boldsymbol{o}^T\end{bmatrix} \tag{9}$$

It is now assumed that the input vector, $\boldsymbol{u}(t)$, is an ergotic, stationary process, in a wide sense. The correlation matrix, $\boldsymbol{R}_{zz}(\tau)$, can be defined by

$$\boldsymbol{R}_{zz}(\tau)=\lim_{T\to\infty}\frac{1}{T}\int_0^T z(t)z^T(t+\tau)dt \tag{10}$$

and it is well known that this matrix is numerically constant and only function of time delay τ (Yaglom, 1962). Applying the differentiation rules in Eq. (10) using Eq. (8), the following matricial relation holds true (Melsa, 1973):

$$\boldsymbol{F}\boldsymbol{R}_{zz}(\tau)+\boldsymbol{R}_{zz}(\tau)\boldsymbol{F}^T+\boldsymbol{G}\boldsymbol{R}_{uz}(\tau)+\boldsymbol{R}_{zu}(\tau)\boldsymbol{G}^T=\boldsymbol{O} \tag{11}$$

After some ordinary mathematical manipulation, the following relation can be written

$$[\boldsymbol{A}_1 \vdots \boldsymbol{B}_1]\begin{bmatrix}\boldsymbol{r}_{yw}(\tau)\\ \boldsymbol{r}_{uw}(\tau)\end{bmatrix}=-\boldsymbol{A}_2\boldsymbol{r}_{vw}(\tau)-\boldsymbol{R}_{yy}(\tau)\boldsymbol{p}-\boldsymbol{r}_{yw}(\tau)N \tag{12}$$

where the partitioned matrices are defined by,

$$\overline{\boldsymbol{A}}=\boldsymbol{T}^{-1}\boldsymbol{A}\boldsymbol{T}=\begin{bmatrix}\boldsymbol{A}_{1(m,\,m)} & \boldsymbol{A}_{2(m,\,2n-m)}\\ \boldsymbol{A}_{3(2n-m,\,m)} & \boldsymbol{A}_{4(2n-m,\,2n-m)}\end{bmatrix} \quad , \quad \overline{\boldsymbol{B}}=\boldsymbol{T}^{-1}\boldsymbol{B}=\begin{bmatrix}\boldsymbol{B}_{1(m,p)}\\ \boldsymbol{B}_{2(2n-m,\,p)}\end{bmatrix} \tag{13}$$

The correlation vector $\boldsymbol{r}_{vw}(\tau)$ can not be directly estimated, however, it is possible to define linearly independent vectors $\boldsymbol{s}_i^T$, with dimension $(1, m)$, orthogonal to all columns of matrix $\boldsymbol{A}_2$, satisfying,

$$\boldsymbol{s}_i^T\boldsymbol{A}_2=\boldsymbol{o}^T_{(1,\,2n-m)} \quad , \quad i=1,\cdots,j \tag{14}$$

and the number j of linearly independent vectors $\boldsymbol{s}_i^T$ is given by

$$j=m-rank[\boldsymbol{A}_2] \tag{15}$$

i.e., the vectors $\boldsymbol{s}_i^T$ lie in the null space of matrix $\boldsymbol{A}_2$. The condition (14) is satisfied when $\boldsymbol{A}_2$ has incomplete column rank, however, this rank condition can be achieved by selecting an appropriated transformation matrix $\boldsymbol{T}$. Left multiplying both sides of Eq.(12) by $\boldsymbol{s}_i^T$ gives,

$$\boldsymbol{s}_i^T[\boldsymbol{A}_1 \;\vdots\; \boldsymbol{B}_1]\begin{bmatrix}\boldsymbol{r}_{yw}(\tau)\\ \boldsymbol{r}_{uw}(\tau)\end{bmatrix}+\boldsymbol{s}_i^T[\boldsymbol{R}_{yy}(\tau) \;\vdots\; \boldsymbol{r}_{yw}(\tau)]\begin{bmatrix}\boldsymbol{p}\\ N\end{bmatrix}=0 \quad , \quad i=1,\cdots,j \tag{16}$$

The Equation (16) can be used as a residual function for monitoring system faults. The residual function $e_i(\tau)$ will be defined in the following form,

$$e_i(\tau)=s_i^T\left[A_1 \;\vdots\; B_1\right]\begin{bmatrix} r_{yw}(\tau) \\ r_{uw}(\tau)\end{bmatrix}+s_i^T\left[R_{yy}(\tau) \;\vdots\; r_{yw}(\tau)\right]\begin{bmatrix} p \\ N\end{bmatrix}=0 \quad , \quad i=1,\cdots,j \tag{17}$$

It can be seen that it is possible to construct only j linearly independent residual functions and each residual function is an analytical combination of known system parameters and correlation functions. It is important to note that all correlation functions in Eq.(17) can be estimated using the measured vectors $\boldsymbol{u}(t)$ and $\boldsymbol{y}(t)$.

Fault Detection and Location

When there is no fault in the system and after response transients, the estimation of residuals satisfy

$$e_i(\tau)=0 \quad , \quad i=1,\cdots,j \tag{18}$$

It is now assumed that a fault in the system is represented by an unknown and permanent parameter variation. Each residual function $e_i(\tau)$ has an known analytic combination of system parameters. Assuming that the unknown fault parameter is only related to the residual function $e_k(\tau)$, the estimation of residuals for a fault system gives,

$$\begin{cases} e_i(\tau)=0 \quad , \quad i\neq k \\ \\ e_i(\tau)\neq 0 \quad , \quad i=k \end{cases} \tag{19}$$

The analysis of discrepancies in the estimated residuals shows the location of the fault in the system, i.e., the group of parameters, which are directly related to the fault. In this case, the residual function $e_k(\tau)$ contains the fault parameter because after the fault occurrence $e_k(\tau)$ differs from zero. The condition (14) must be observed also in a fault system, and this restriction can be satisfied selecting an appropriate transformation matrix $\boldsymbol{T}$. This can be achieved introducing zeros into matrix $\boldsymbol{T}$ and analyzing the resulted analytical structure of matrix $\boldsymbol{A}_1$ and $\boldsymbol{B}_1$.

The fault location is now investigated when the measured system signals have additive noise, in the following form,

$$\begin{aligned} \boldsymbol{y}_r(t)&=\boldsymbol{y}(t)+\boldsymbol{g}(t) \\ \\ \boldsymbol{u}_r(t)&=\boldsymbol{u}(t)+\boldsymbol{q}(t) \end{aligned} \tag{20}$$

where $\boldsymbol{g}(t)$ and $\boldsymbol{q}(t)$ are stationary random noise signals. The estimated residual functions in the presence of noise, can be written in the following form

$$e_i(\tau)=e_{ri}(\tau)+s_i^T\left[A_1 \;\vdots\; B_1\right]\begin{bmatrix} r_{gw}(\tau) \\ r_{qw}(\tau)\end{bmatrix}+s_i^T\left[R_{gy_r}(\tau)+R_{y_rg}(\tau)-R_{gg}(\tau) \;\vdots\; r_{gw}(\tau)\right]\begin{bmatrix} p \\ N\end{bmatrix} \tag{21}$$

where, $e_{ri}(\tau)$ are residual functions directly estimated with noise signals, i.e.,

$$e_{ri}(\tau)=s_i^T\left[A_1 \;\vdots\; B_1\right]\begin{bmatrix} r_{y_rw}(\tau) \\ r_{u_rw}(\tau)\end{bmatrix}+s_i^T\left[R_{y_ry_r}(\tau) \;\vdots\; r_{y_rw}(\tau)\right]\begin{bmatrix} p \\ N\end{bmatrix} \tag{22}$$

If the additive noise is a white process, i.e., it is not correlated for $\tau\neq 0$, the second part of the Eq.(21) becomes null, that is

$$s_i^T [A_1 \vdots B_1] \begin{bmatrix} r_{gw}(\tau) \\ r_{qw}(\tau) \end{bmatrix} + s_i^T \left[R_{gy_r}(\tau) + R_{y_r g}(\tau) - R_{gg}(\tau) \vdots r_{gw}(\tau) \right] \begin{bmatrix} p \\ N \end{bmatrix} = 0 \qquad (23)$$

and

$$e_{ri}(\tau) = 0 \quad , \quad i = 1, \cdots, j \qquad (24)$$

Hence, the estimated residuals in the presence of additive white noise, using direct estimation in Eq.(22) leads to the same results of the ideal case in Eq.(17).

Numerical Example

The proposed approach was applied in a six DOF vertical rotating system shown in Fig. 1. The vertical rotor is supported by hydrodynamic bearing and driven by an electric motor. Figure 1 also list some system parameters (but not all) used in the modeling process. The complete description of this model is given by Pederiva (1992). The objective of this example is to demonstrate how to detect a bearing fault and to identify the physical parameters that are related to the fault. The bearing fault will be characterized by an abrupt and permanent variation of bearing stiffness and damping coefficients

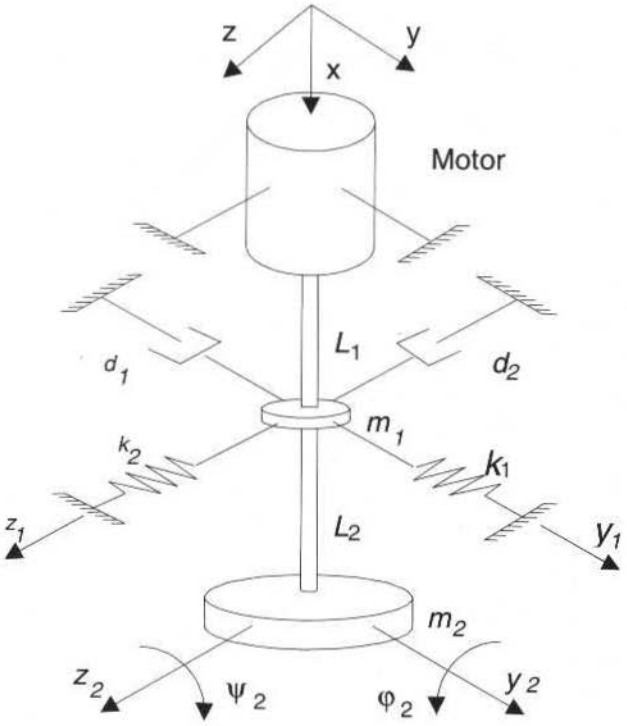

Model Parameters:

$m_1=15$, $m_2=10$: Bearing and rotor masses [*kg*].

$k_1=90{,}000$, $k_2=120{,}000$: Bearing stiffness [*N/m*].

$d_1=30{,}000$, $d_2=37{,}500$: Bearing damping [*kg/s*].

$L_1=L_2=0.4$: Lengths of the rotor [*m*].

y_1 , y_2 , z_1 , z_2 : Linear displacements [*m*].

φ_2 , ψ_2 : Angular displacements [*rad*].

Fig. 1 Model of vertical rotor

The numeric values of measuring matrix $\boldsymbol{C}$ and transformation matrix $\boldsymbol{T}$ for this model is,

$$C=\begin{bmatrix} 1 & 0 & 0 & 0 & 0 & 0 & 0 & 0 & 0 & 0 & 0 & 0 \\ 0 & 1 & 0 & 0 & 0 & 0 & 0 & 0 & 0 & 0 & 0 & 0 \\ 0 & 0 & 0 & 1 & 0 & 0 & 0 & 0 & 0 & 0 & 0 & 0 \\ 0 & 0 & 0 & 0 & 1 & 0 & 0 & 0 & 0 & 0 & 0 & 0 \\ 0 & 0 & 0 & 0 & 0 & 0 & 1 & 0 & 0 & 0 & 0 & 0 \\ 0 & 0 & 0 & 0 & 0 & 0 & 0 & 1 & 0 & 0 & 0 & 0 \\ 0 & 0 & 0 & 0 & 0 & 0 & 0 & 0 & 1 & 0 & 0 & 0 \\ 0 & 0 & 0 & 0 & 0 & 0 & 0 & 0 & 0 & 1 & 0 & 0 \end{bmatrix}, \quad T=\begin{bmatrix} 1 & 0 & 0 & 0 & 0 & 0 & 0 & 0 & 0 & 0 & 0 & 0 \\ 0 & 1 & 0 & 0 & 0 & 0 & 0 & 0 & 0 & 0 & 0 & 0 \\ 1 & 1 & 1 & 1 & 1 & 1 & 1 & 1 & 1 & 0 & 0 & 0 \\ 0 & 0 & 1 & 0 & 0 & 0 & 0 & 0 & 0 & 0 & 0 & 0 \\ 0 & 0 & 0 & 1 & 0 & 0 & 0 & 0 & 0 & 0 & 0 & 0 \\ 1 & 1 & 1 & 1 & 1 & 1 & 1 & 1 & 0 & 1 & 0 & 0 \\ 0 & 0 & 0 & 0 & 1 & 0 & 0 & 0 & 0 & 0 & 0 & 0 \\ 0 & 0 & 0 & 0 & 0 & 1 & 0 & 0 & 0 & 0 & 0 & 0 \\ 1 & 1 & 1 & 1 & 1 & 1 & 1 & 1 & 0 & 0 & 1 & 0 \\ 0 & 0 & 0 & 0 & 0 & 0 & 1 & 0 & 0 & 0 & 0 & 0 \\ 0 & 0 & 0 & 0 & 0 & 0 & 0 & 1 & 0 & 0 & 0 & 0 \\ 1 & 1 & 1 & 1 & 1 & 1 & 1 & 1 & 0 & 0 & 0 & 1 \end{bmatrix} \tag{25}$$

This transformation matrix leads to the desired special form,

$$\overline{C}=CT=\left[I_{(8,8)} \;\vdots\; O_{(8,4)}\right] \tag{26}$$

and, additionally, matrix A_2 satisfies the condition in Eq.(14) using the following vectors s_i^T, $i=1,\cdots,4$,

$$\begin{bmatrix} s_1^T \\ s_2^T \\ s_3^T \\ s_4^T \end{bmatrix}=\begin{bmatrix} 1 & 1 & 1 & 0 & 1.5 & 1 & 0 & 0 \\ 1 & 1 & 0 & 1 & 0 & 0 & 1.5 & 1 \\ 1 & 0 & 1 & 1 & 1.5 & 1 & 1.5 & 1 \\ 1 & 1 & 1 & 1 & 0 & 0 & 0 & 0 \end{bmatrix} \tag{27}$$

The resulted residual functions $e_i(\tau)$, $i=1,\cdots,4$ have the following analytical form:

$$e_1(\tau)=\left[\frac{-1.5}{m_1}\left[k_1+6(a+b)\right] \quad \frac{-6a}{m_2} \quad 0 \quad 0 \quad \frac{-1.5d_1}{m_1} \quad 1 \quad -1-\frac{0.5d_2}{m_1} \quad 0 \right.$$
$$\left. e\Omega^2 \quad 0 \quad \frac{1.5}{m_1}\right]\begin{Bmatrix} r_{yw}(\tau) \\ r_{uw}(\tau) \end{Bmatrix}+r_1(\tau) \tag{28}$$

$$e_2(\tau)=\left[0 \quad 0 \quad \frac{-1.5}{m_1}\left[k_2+6(a+b)\right] \quad \frac{-6a}{m_2} \quad 1 \quad 0 \quad 1-\frac{d_2}{m_1} \quad 1 \right.$$
$$\left. 0 \quad e\Omega^2 \quad \frac{1.5}{m_1}+\frac{2}{m_2}\right]\begin{Bmatrix} r_{yw}(\tau) \\ r_{uw}(\tau) \end{Bmatrix}+r_2(\tau) \tag{29}$$

$$e_3(\tau)=\left[\frac{-1.5}{m_1}[k_1+6(a+b)]\quad\frac{-6a}{m_2}\quad\frac{-1.5}{m_1}[k_2+6(a+b)]\quad\frac{-6a}{m_2}\quad 1-\frac{1.5d_1}{m_1}\quad 1\right.$$
$$\left.\frac{-15d_2}{m_1}\quad 1\quad e\Omega^2\quad e\Omega^2\quad\frac{3}{m_1}+\frac{2}{m_2}\right]\begin{Bmatrix}r_{yw}(\tau)\\ r_{uw}(\tau)\end{Bmatrix}+r_3(\tau) \tag{30}$$

$$e_4(\tau)=\begin{bmatrix}0 & 0 & 0 & 0 & 1 & 1 & 1 & 1 & 0 & 0 & 0\end{bmatrix}\begin{Bmatrix}r_{yw}(\tau)\\ r_{uw}(\tau)\end{Bmatrix}+r_4(\tau) \tag{31}$$

where the following definition was used:

$$r_i(\tau)=s_i^T\left[\boldsymbol{R}_{yy}(\tau)\ \vdots\ \boldsymbol{r}_{yw}(\tau)\right]\begin{Bmatrix}\boldsymbol{p}\\ N\end{Bmatrix}\quad,\quad i=1,\cdots,4 \tag{32}$$

The parameters a , b and e are known system constants. The parameter Ω is the rotor rotation ($\Omega = 60$ *rad/s*) and corresponds to the excitation frequencies of the system. All critical speeds of this model are higher than *100* rad/s. The residuals are in an adequate form for monitoring linearised system parameters related to the hydrodynamic bearing, i.e., stiffness parameters k_1 and $k2$, and damping parameters d_1 and d_2. The residual $e_1(\tau)$ is a function of k_1 and d_1, the residual $e_2(\tau)$ is a function of k_2 and d_2, the residual $e_3(\tau)$ is a function of all bearing parameters, and the residual $e_4(\tau)$ is not function of bearing parameters. A stationary sinusoidal input force was used to generate response data. The system response was simulated using the *Matlab®* software and a sampling interval of *0.01* seconds. The following filter parameters were used:

$$N=-100,\quad \boldsymbol{p}=10^3\begin{bmatrix}1 & 1 & 1 & 1 & 1 & 1 & 1 & 1\end{bmatrix} \tag{33}$$

The filter cut frequency $(100\ rad/s)$ is higher than the input system frequency. This is a necessary condition once the filter can not attenuate the excitation frequency of the system. The residual functions were estimated in an iterative form using *4,000* discrete system response values. Table 1 shows the simulated fault conditions.

Figure 2 shows the percentage variation of estimated residuals with no system faults. It can be seen that the percentage variation of each estimated residual tends to vanish when more data are used in the estimation process (longer record of system data). After *100* estimated values ($n = 100$) the faults described in Table 1 are introduced into the system and the results are plotted in Figs. *3*, *4*, *5*, *6* and *7*. All faults represent an abrupt and permanent system parameter variation.

Table 1 Simulated fault conditions

Condition	Fault Description	Noise (% rms)
1	System with no faults	0
2	k_1 increases 20%	0
3	d_1 and d_2 increase 5%	0
4	d_2 increases 5%	0
5	d_2 increases 30%	10
6	k_1 and k_2 increase 50%	10

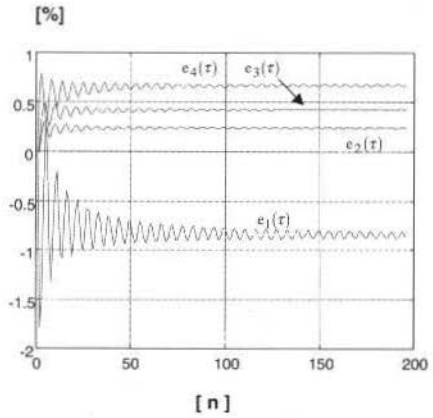

Fig. 2 Variation of estimated residuals in condition 1

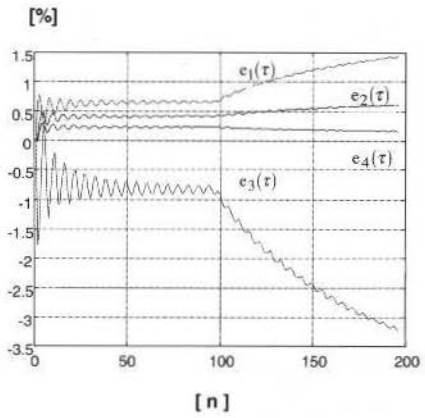

Fig. 3 Variation of estimated residuals in condition 2

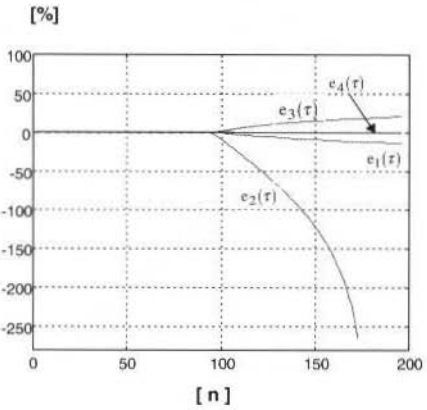

Fig. 4 Variation of estimated residuals in condition 3

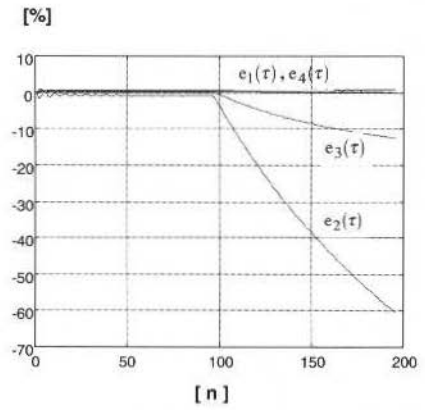

Fig. 5 Variation of estimated residuals in condition 4

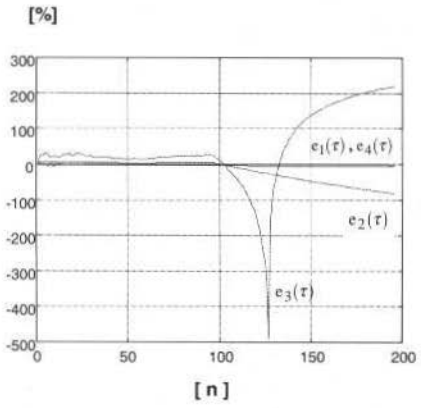

Fig. 6 Variation of estimated residuals in condition 5

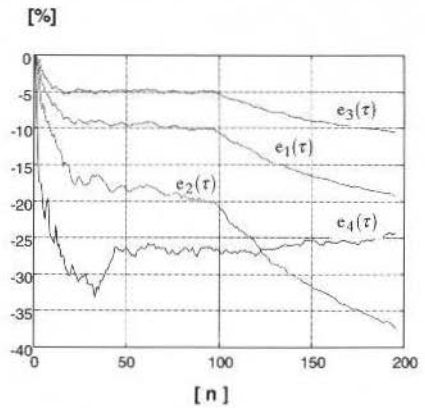

Fig. 7 Variation of estimated residuals in condition 6

It can be seen that after the fault occurrence, the residuals related to fault parameters have higher percentage variation than the residuals not related to fault parameters (Figs. 3, 4 and 5). These

discrepancies on residuals are also observed when an additive random noise is presented in the system signals (Figs. 6 and 7). However, when the noise is present, the identification of the fault residual is not easy as the ideal case (without noise).

The estimated residuals showed more sensibility to damping variation than stiffness variation. These residuals characteristics are correlated to system parameters sensibility, once the simulated model has more sensibility to damping variation than stiffness variation. Fault location is achieved by identifying the physical parameters that are related to the residuals with higher percentage variation after the fault occurrence.

Conclusions

A new method of model based fault detection and location for stationary mechanical systems was presented and verified with a numeric example. In this approach, fault isolation is achieved by analyzing discrepancies in estimated residuals using an appropriated parametric residual analysis. The system parameters that can be monitored are directly related to the number of linearly independent residual functions. The transformation matrix $\boldsymbol{T}$ and the decoupling vectors $\boldsymbol{s}_i$ must be assigned to provide an adequate selection of the system parameters for monitoring purposes.

To maximize residual fault sensibility, the filter cut frequencies must be higher than the excitation frequencies, however, the numerical simulation showed that higher cut frequencies produces smaller residual sensibility and only severe faults can be located by monitoring residual functions.

To simulate practical situations, additive noise was introduced into the system signals. The numerical results showed that the identification of the fault residual is also possible when the noise intensity is less than 10% .

Symbol List

Matrices: Capital letter and **bold**, example: $\boldsymbol{A}, \boldsymbol{B}, \boldsymbol{C}, \boldsymbol{T}$.

Vectors: **Bold** letter, example: $\boldsymbol{x(t)}, \boldsymbol{y(t)}, \boldsymbol{s}, \boldsymbol{p}$.

$\boldsymbol{I}$, $\boldsymbol{O}$, $\boldsymbol{o}$: Identity matrix, null matrix and null vector, respectively.

$\boldsymbol{r}_{xx}(\tau)$, $\boldsymbol{R}_{xx}(\tau)$: Correlation vector and correlation matrix for time delay τ , respectively.

Superscript $(\cdots)^T$: Matrix transpose or vector transpose.

Superscript $(\cdots)^{-1}$: Matrix inverse.

Subscript $(\cdots)_{(n,p)}$: Matrix dimension, example: $A_{(n\,,\,n)}$.

$\begin{Bmatrix} a \\ \cdots \\ b \end{Bmatrix}$, $\begin{bmatrix} A & \vdots & B \\ & \cdots & \\ C & \vdots & D \end{bmatrix}$: Vector partition and matrix partition, respectively.

References

Chow, E.Y and Willsky, A., 1984, "Analytical Redundancy and Design of Robust Failure Detection Systems", IEEE Transactions on Automatic Control, Vol. 29, No.7, pp. 603-614.

Frank, P.M, 1992, "Principles of Model Based Fault Detection", Proceedings of the IFAC Artificial Intelligence in real-time Control, pp. 213-220.

Frank, P.M., 1990, "Fault Diagnosis in Dynamic Systems Using Analytical and Knowledge-Based Redundancy - A Survey and Some New Results", Automatica, Vol. 26, No. 3, pp. 459-474.

Gertler, J., 1991, "Analytical Redundancy Methods in Fault Detection and Isolation - A Survey and Synthesis", IFAC Safeprocess Symposium, Baden-Baden, Germany, plenary paper.

Gertler, J. and Kunwer, M.M., 1995, "Optimal Residual Decoupling for Robust Fault Diagnosis", International Journal of Control, Vol. 61, No.2, pp. 395-421.

Isermann, R., 1993," Fault Diagnosis of Machines via Parameter Estimation and Knowledge Processing- Tutorial Paper", Automatica, Vol. 29, No.4, pp. 815-835.

Medvedev, A., 1995, "Fault Detection and Isolation by a Continuous Parity Space Method", Automatica, Vol. 31, No.7, pp.1039-1044.

Melsa, J. L. and Sage, A.P, 1973 "An Introduction to Probability and Stochastic Process", Prentice Hall, pp. 245-270.

Pederiva, R., 1992, "Identificação Paramétrica de Sistemas Mecânicos Excitados Estocasticamente", Ph.D. Thesis, State University of Campinas, SP, Brasil.

Patton, R.J., Chen, J., 1992, "Robustness in model based fault diagnosis", Concise Encyclopedia of Modeling & Simulation, Pergamon Press, UK, pp. 379-392.

Patton, R.J., Frank, P. and Clark, R., 1989, "Fault Diagnosis in Dynamic Systems", Prentice Hall, UK.

Eagle, A.M., 1962, "An Introduction to the Theory of Stationary Random Functions", Englewood Cliffs, Prentice Hall, UK, pp. 9-28.

RBCM - J. of the Braz. Soc. Mechanical Sciences
Vol. XXI - No.1 - 1999 - pp. 133-143

ISSN 0100-7386
Printed in Brazil

Heat Diffusion in Two-Dimensional Fractals

Fernando Manuel Ramos
Instituto Nacional de Pesquisas Espaciais
Laboratório Associado de Computação e Matemática Aplicada
12201-970 São José dos Campos, SP Brazil
fernando@lac.inpe.br

Abstracts

A simple and versatile methodology for the solution of the diffusion equation in two-dimensional fractals is presented. The numerical model is based on an explicit finite-difference scheme, and handles any geometry which can be represented on a rectangular grid, including problems with an internal complex morphology, such as a Sierpinski carpet, or an intricate external shape, like a quadratic Koch plate. For validation purposes, the model is also applied to a spatially periodic porous medium for which numerical and experimental data can be found in the literature. The proposed methodology is general and can be extended to three-dimensional heterogeneous solids, made up of two or more media.
Keywords: *Heat Diffusion, Fractals, Finite-differences, Porous Media, Effective Thermal Conductivity.*

Introduction

The emergence of fractals, originally introduced by Mandelbrot (1967), was a significant breakthrough in rendering complex geometries tractable. Fractals are made of parts similar to the whole in some way (Feder, 1988). This definition contains the essential feature in fractal geometry: *self-similarity*. Exact fractals like Koch curves or Sierpinski gaskets exhibit this property over an infinite range of length of scales. The fact that many natural objects - cracked interfaces, turbulence, coastlines, and others - can be described as fractals, at least over a certain range of scales, explains the wide applicability of fractal geometry in science and engineering.

Formally, fractals are best characterized by their Hausdorf-Besicovitch or fractal dimension, D. This exponent allows to establish a scaling relationship $M(\delta) \sim \delta^D$ between a characteristic linear length scale, δ, and a measure (i.e., a length, area or volume), $M(\delta)$, of the fractal object. Other exponents and characterization are needed in order to emphasize different aspects and properties of fractals. A comprehensive treatment of fractal geometry, its mathematical foundations and applications, can be found in Feder (1998) and Falconer (1990).

The recent literature on fractals cover a broad range of applications, which are of both scientific and technological interest. In the context of geophysics, Turcotte (1992) applied the notion of scale invariance to various geological phenomena. The scattering of electromagnetic waves from rough surfaces was modeled by Jaggard and Sun (1990) using a roughness fractal function. Panagiotopoulos et al. (1992) used a fractal approximation to analyze the unilateral contact and friction problem in a cracked elastic body. Sapoval and collaborators (1991) numerically and experimentally addressed the vibrational properties of two-dimensional fractal drums.

In the field of transport phenomena, the advent of fractals represented an important advance with the realization that they are a very good model for the geometrical structure of rough surfaces and of most disordered materials (Havlin and Ben-Avraham, 1987). However, there are still relatively few works that apply the concept of fractal to heat transfer problems. Yao and Pitchumani (1990) and Pitchumani and Yao (1991) adopted a local fractal dimension technique to characterize the effective thermal conductivity of unidirectional fibrous composites. Majumdar and Tien (1989) analyzed the heat conduction between two contacting rough surfaces using a fractal network model. Thovert et al. (1990) numerically determined the effective thermal conductivity of porous random media and regular fractals.

The goal of this article is to present a simple and versatile methodology for the solution of the diffusion equation in two-dimensional fractals. The present approach, based on an explicit finite-difference scheme, handles any geometry which can be represented on a rectangular grid. It goes one step beyond previous research of Thovert (1990) by treating, with the same numerical model, geometries displaying whether an *internal* complex morphology, such as a Sierpinski carpet, or an intricate *external* shape, like a quadratic Koch plate. Although we restrict our focus to two-dimensional fractals made up of one or two phases, the method of solution is general and can be extended to three-dimensional heterogeneous solids composed of several media.

Manuscript received: November 1996; revised: August 1998. Technical Editor: Angela Ourívio Nieckele.

Mathematical Model

The problem is governed by the diffusion equation

$$k\nabla^2 T(\mathbf{r},t)+g(\mathbf{r},t)=\rho c_p \frac{\partial T(\mathbf{r},t)}{\partial t}, \tag{1}$$

in a two-dimensional domain Ω, composed of one or two isotropic and homogeneous media, subjected to an initial condition

$$T(\mathbf{r},0) = F(\mathbf{r}), \tag{2}$$

and, for $t > 0$, to boundary conditions of third kind on $\partial\Omega$,

$$k\frac{\partial T}{\partial n}\bigg|_{\mathbf{r}'\in\partial\Omega} + hT(\mathbf{r}',t) = f(\mathbf{r}',t), \tag{3}$$

where $\partial/\partial n$ denotes the normal derivative at the boundary, $T(\mathbf{r}, t)$ is the temperature, $g(\mathbf{r}, t)$ is a volumetric power source term, h is the convection coefficient, $f(\mathbf{r}, t)$ is a specified boundary condition function, and k, ρ, and c_p are the thermal conductivity, the density and the specific heat, respectively. Across the interfaces of different materials, there is continuity of temperature and heat flux. The thermophysical properties are assumed to be temperature-independent.

A uniform square Cartesian mesh consisting of $N \times N$ grid points is used to discretize the computational domain. For the sake of brevity, we restrict our analysis to the two configurations shown in Fig. 1. In order to easily map onto the numerical model the morphological complexities of the problem geometry, we define a matrix $\mathbf{A} = \{a(i, j); i, j = 1, 2, ..., N\}$ as follows:

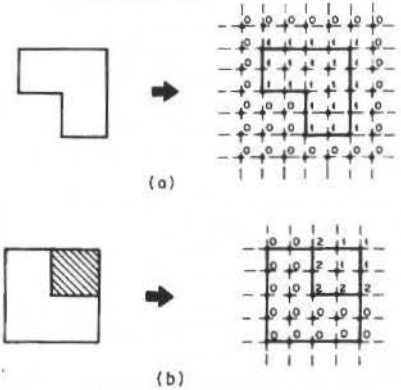

Fig. 1 Configurations in study and associated A matrices: (a) homogeneous body with irregular shape, and (b) square heterogeneous body composed of two media.

Nomenclature

a, c, l	=	geometric parameters in Fig. 4
a(i, j)	=	element of matrix **A** in Eqs. (4) and (5)
c_c, c_w, c_s c_s, c_n	=	coefficients of Eq. (6)
c_p	=	specific heat
d	=	diffusion number
D	=	Hausdorf-Besicovitch or fractal dimension
g	=	volumetric power source
h	=	convection coefficient
k	=	thermal conductivity
k_e	=	effective thermal conductivity
m	=	Archie's exponent
n	=	fractal construction stage
r	=	position vector
t	=	time
p(k, l)	=	element of matrix **P** in Eq. (8)
q(k, l)	=	element of matrix **Q** in Eq. (9)
r(k, l, m)	=	element of matrix **R** in Eqs. (11) to (13)
s(k, l, m)	=	element of matrix **S** in Eqs. (14) to (16)
T	=	temperature
δ	=	characteristic linear length scale
Δt	=	time step
Δx	=	grid size
ρ	=	density
ϕ	=	porosity

- Homogeneous body with irregular shape (Fig. 1a):

$$a(i,j)=\begin{cases}1 \text{ if } node(i,j)\in \Omega\cup\partial\Omega\\ 0 \text{ else,}\end{cases} \tag{4}$$

- Square heterogeneous body with two media Ω_1 and Ω_2 (Fig. 1b):

$$a(i,j)=\begin{cases}0 \text{ if } node(i,j)\in \Omega_1\cup\partial\Omega_1\\ 1 \text{ if } node(i,j)\in \Omega_2\cup\partial\Omega_2\\ 2 \text{ if } node(i,j)\in \partial\Omega_{1,2}.\end{cases} \tag{5}$$

Discretization of Eq. (1) in the space grid by a forward-time centered-space (FTCS) finite-difference scheme yields

$$T_{i,j}^{n+1}=(1+c_c)T_{i,j}^{n}+c_wT_{i,j-1}^{n}+c_eT_{i,j+1}^{n}+c_sT_{i-1,j}^{n}+c_nT_{i+1,j}^{n}. \tag{6}$$

For the homogeneous configuration, the coefficients of Eq. (6) are given by the elements of matrices $\boldsymbol{P} = \{p(k, l); k, l = 0,1\}$ and $\boldsymbol{Q} = \{q(k, l); k, l = 0,1\}$:

$$\begin{aligned}
c_c &= p(a(i, j-1), a(i, j+1)) \\
&\quad + p(a(i-1, j), a(i+1, j)) \\
c_w &= q(a(i, j-1), a(i, j+1)) \\
c_e &= q(a(i, j+1), a(i, j-1)) \\
c_s &= q(a(i-1, j), a(i+1, j)) \\
c_n &= q(a(i+1, j), a(i-1, j)),
\end{aligned} \tag{7}$$

where

$$\boldsymbol{P}=\begin{bmatrix} 0 & -2d(1+\Delta x h/k) \\ -2d(1+\Delta x h/k) & -2d \end{bmatrix} \tag{8}$$

and

$$\boldsymbol{Q}=\begin{bmatrix} 0 & 0 \\ 2d & d \end{bmatrix}, \tag{9}$$

with $d = \alpha\Delta t / \Delta x^2$, $\alpha = k / \rho c_p$ being the thermal diffusivity, Δt the time step, and Δx the grid size.

In the case of the heterogeneous configuration, the solution coefficients for the internal grid points are the elements of the three-dimensional matrices $\mathbf{R} = \{r(k, l, m); k, l, m = 0, 1, 2\}$ and $\mathbf{S} = \{s(k, l, m); k, l, m = 0, 1, 2\}$:

$$
\begin{aligned}
c_c &= r(a(i, j-1), a(i, j+1), a(i, j)) \\
&\quad + r(a(i-1, j), a(i+1, j), a(i, j)) \\
c_w &= s(a(i, j-1), a(i, j+1), a(i, j)) \\
c_e &= s(a(i, j+1), a(i, j-1), a(i, j)) \\
c_s &= s(a(i-1, j), a(i+1, j), a(i, j)) \\
c_n &= s(a(i+1, j), a(i-1, j), a(i, j)),
\end{aligned} \tag{10}
$$

where

$$
\boldsymbol{R}_{m=0} = \begin{bmatrix} -2d_1 & 0 & -2d_1 \\ 0 & 0 & 0 \\ -2d_1 & 0 & 0 \end{bmatrix}, \tag{11}
$$

$$
\boldsymbol{R}_{m=1} = \begin{bmatrix} 0 & 0 & 0 \\ 0 & -2d_2 & -2d_2 \\ 0 & -2d_2 & 0 \end{bmatrix}, \tag{12}
$$

$$
\boldsymbol{R}_{m=2} = \begin{bmatrix} -2d_1 & -2\dfrac{(k_1+k_2)}{(k_1/d_1)+(k_2/d_2)} & -2\dfrac{(k_1+k_3)}{(k_1/d_1)+(k_3/d_3)} \\ -2\dfrac{(k_2+k_1)}{(k_2/d_2)+(k_1/d_1)} & -2d_2 & -2\dfrac{(k_2+k_3)}{(k_2/d_2)+(k_3/d_3)} \\ -2\dfrac{(k_3+k_1)}{(k_3/d_3)+(k_1/d_1)} & -2\dfrac{(k_3+k_2)}{(k_3/d_3)+(k_2/d_2)} & -2d_3 \end{bmatrix}, \tag{13}
$$

and

$$
\boldsymbol{S}_{m=0} = \begin{bmatrix} d_1 & 0 & d_1 \\ 0 & 0 & 0 \\ d_1 & 0 & 0 \end{bmatrix}, \tag{14}
$$

$$
\boldsymbol{S}_{m=1} = \begin{bmatrix} 0 & 0 & 0 \\ 0 & d_2 & d_2 \\ 0 & d_2 & 0 \end{bmatrix}, \tag{15}
$$

$$
\boldsymbol{S}_{m=2} = \begin{bmatrix} d_1 & 2\dfrac{k_1}{(k_1/d_1)+(k_2/d_2)} & 2\dfrac{k_1}{(k_1/d_1)+(k_3/d_3)} \\ 2\dfrac{k_2}{(k_2/d_2)+(k_1/d_1)} & d_2 & 2\dfrac{k_2}{(k_2/d_2)+(k_3/d_3)} \\ 2\dfrac{k_3}{(k_3/d_3)+(k_1/d_1)} & 2\dfrac{k_3}{(k_3/d_3)+(k_2/d_2)} & d_3 \end{bmatrix}, \tag{16}
$$

with $k_3 = (k_1 + k_2)/2$, $\alpha_3 = (\alpha_1 + \alpha_2)/(k_1/\alpha_1 + k_2/\alpha_2)$, and $d_q = \alpha_q \Delta t/\Delta x^2$ for $q = 1, 2, 3$. Similar relations can be derived for the nodes located on the external boundary $\partial\Omega = \partial\Omega_1 \cup \partial\Omega_2$. Continuity of temperature and heat flux across simple interfaces, edges and corners is incorporated into the numerical model through the elements of matrices $R_{n=2}$ and $S_{n=2}$. The numerical scheme given by Eq. (6) has a truncation error of $O(\Delta x^2)$ and $O(\Delta t)$, and is conditionally stable for values of $d_{max} = \alpha_{max} \Delta t/\Delta x^2 \leq 0.25$, with $\alpha_{max} = max\{\alpha_1, \alpha_2\}$.

Some applications require the computation of asymptotic steady state solutions. Consequently, the restriction imposed on Δt by the stability condition may lead to a prohibitive computational effort. A better approach in this case is to replace Eq. (1) by the respective Poisson equation, and Eq. (6) by a SOR (Successive Overrelaxation) numerical scheme. This modification can be easily implemented with only minor adaptations on the procedure described above.

Numerical Examples

To illustrate the methodology presented in the previous section, three representative examples were considered, including two deterministic fractals and a spatially periodic porous medium. Although this last example may not be considered an exact fractal, constructed by a rigorous deterministic recursive law, it will be useful to validate the numerical model in comparison with experimental data published in the literature. Since the number of grid points grows roughly one order of magnitude at each fractal construction stage n, for a fixed resolution at lower scales, only low values of n were used in the simulations because of the enormous computational time required.

Effective Thermal Conductivity of Sierpinski Carpets

The first example concerns the problem of determining the effective thermal conductivity of a Sierpinski carpet (SC). Denoted by k_e, the effective thermal conductivity is defined as the conductivity of an equivalent homogeneous medium, which exhibits the same steady-state characteristics as the heterogeneous body.

The value of k_e is minimum if the different media are disposed in layers normal to the direction of the heat flow. On the other hand, the maximum value is attained when all materials are arranged in parallel to the heat flux. Expressing the spatial average flux in terms of the gradient of the average temperature and the effective thermal conductivity tensor $\boldsymbol{K}_e$, we have (Nozad et al., 1985):

$$\langle \boldsymbol{q} \rangle = -\boldsymbol{K}_e \cdot \nabla \langle T \rangle \tag{17}$$

Sierpinski carpets are constructed according to the procedure depicted in Fig. 2. At order n =1, the initial filled square is divided into 9 equal-sized smaller pieces, the central square being removed. At subsequent orders, this procedure is repeatedly applied to the remaining squares. After each iteration, the area (and hence the mass) of the carpet is reduced by a factor of 8/9, while the total perimeter increases. In the limit of $n \to \infty$, the carpet area vanishes, while the perimeter is infinite. The fractal dimension of a SC generated by this procedure is $D = \log 8/\log 3 \approx 1.893$.

The effective thermal conductivity of the SC was numerically computed up to the forth construction stage. Applying a uniform heat flux along the longitudinal direction ($\pm q_f$, at y = 0 and 1, respectively), and assuming adiabatic conditions at the lateral carpet sides, the effective thermal conductivity k_e can be extracted from Eq. (17) by spatial averaging the temperature gradient over N_l parallel layers of width Δx and unit length. Summing up over all layers the resulting conductances, the average flux in the i-th layer can be approximated as follows:

$$q_f = -k_e^i \frac{d\langle T_i \rangle}{dy} \approx k_e^i \left(\langle T_i \rangle_{y=0} - \langle T_i \rangle_{y=1} \right) \tag{18}$$

Thus, the value of k_e is given by

$$k_e = \sum_{i=1}^{N_l} k_e^i \, \Delta x = \sum_{i=1}^{N_l} \frac{q_f \, \Delta x}{\langle T_i \rangle_{y=0} - \langle T_i \rangle_{y=1}}, \tag{19}$$

where

$$\langle T_i \rangle = \frac{(T_i + T_{i+1})}{2}. \tag{20}$$

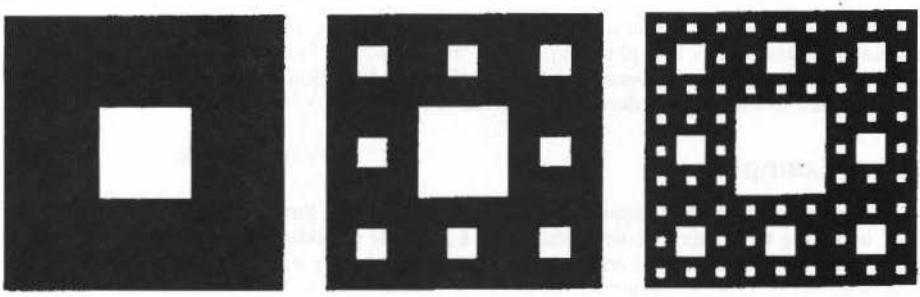

Fig. 2 Construction of the Sierpinski carpet

In all simulations, convergence was assumed to be reached when the difference of the computed values at two consecutive iterations was less then 1×10^{-5}. Meshes of 82×82 nodes (for n =4, 244×244 nodes) were used in the simulations.

Figure 3a presents, for a SC composed of voids ($k_f \approx 0$) and a matrix of unit conductivity ($k_s = 1$), the effective thermal conductivity as a function of the complementary porosity $\phi^* = 1 - \phi$ where ϕ is the porosity. The porosity depends on the construction stage n, and is given by $\phi = \sum_{l=1}^{n} 8^{l-1}/9^l$. A contour plot is also shown in Fig. 3b to illustrate the temperature distribution in a SC made up of a resistive matrix and conductive inclusions, with $k/k_f = 0.1$. These results are in accordance with Archie's law, relating conductivity and porosity in rocks fully saturated by a conducting fluid. Empirically it is found that (Nigmatullin et al., 1992)

$$k_e = \phi^{*m}, \tag{21}$$

where m is the Archie's exponent, usually ranging from 1.3 to 2.5. Particularly, we obtained $m = 1.863$, which is in good agreement with the result computed by Thovert and collaborators (1990), $m = 1.89$.

Extensive simulations with Sierpinski carpets generated through different construction procedures (for instance, the initial filled square is divided into 16 equal-sized smaller pieces and the 4 central squares are the removed, with $D = \log 12/\log 4 \approx 1.792$), for various conductivity rations, have shown that the effective conductivity of a SC is given by a generalization of Archie's law, so that Eq. (21) takes the from:

$$k_e^{\gamma} = (1 - \phi) k_s^{\gamma} + \phi k_f^{\gamma}, \tag{22}$$

where $\gamma = 1/m$, with $-1 \le \gamma \le 1$. The exponent γ expresses how parallel is the internal morphology relatively to the heat flux. Is does not depend on the fractal dimension D. For $n \to \infty$, $\phi \to 1$ and $k_e = k_f$. From Eq. (22) it is possible to retrieve the well known correlations for maximum and minimum value of the effective thermal conductivity of an arrangement of two media. Indeed, whether the two media are disposed in layers arranged in parallel or in series in the direction of the temperature gradient, γ equals 1 or -1. Simulations with random media suggest that this correlation may hold for other types of heterogeneous materials and, thus, have a broader applicability. This last point is currently in study and will be discussed in a coming paper.

Effective Thermal Conductivity of a Spatially Periodic Porous Medium

The determination of the effective thermal conductivity of porous media is a problem of great interest to engineers and geophysicists. Two recent studies reveal the existence of several empirical correlations and theoretical models (Hsu et al., 1995; Tavman, 1996). These models predict the effective thermal conductivity as a function of the porosity, the thermal conductivity of each phase, the shape, orientation and distribution of the solid particles, the thermal contact resistance between particles, and other parameters. In the porous medium, heat is transported mainly by conduction through the solid and fluid phases, although radiation between the solid particles and convection in the fluid phase may play a significant role, depending on the size of the pores and the temperature of the body.

Because of the symmetry of the thermal paths, a common approach when dealing with spatially periodic porous media is to estimate the average properties from the thermal behavior of a unit cell, assuming adiabatic conditions at the local boundaries parallel to the macroscopic heat flux. In this second numerical example, we estimate the effective thermal conductivity of a two-dimensional

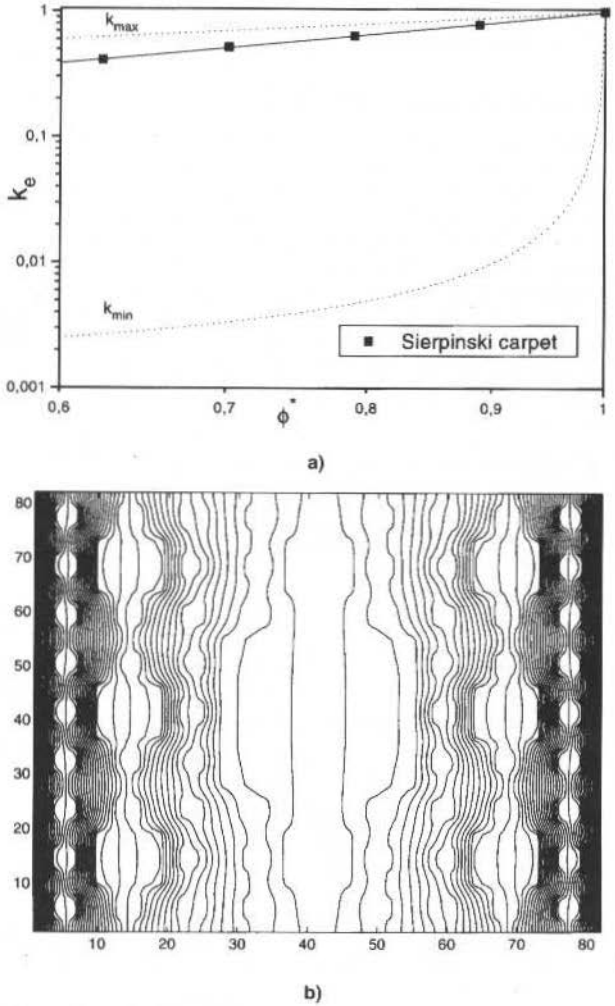

Fig. 3 (a) Effective thermal conductivity of the Sierpinski carpet as a function of $\phi^* = 1 - \phi$, where k_{max} and k_{min} are, respectively, the upper and lower bounds on the value of k_e; (b) Contour plot of the temperature distribution in the Sierpinski carpet.

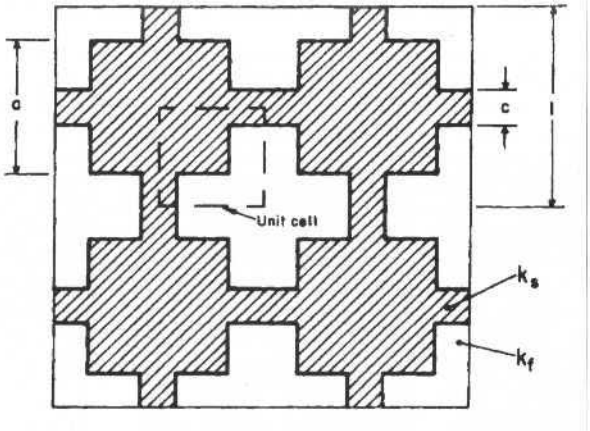

Fig. 4 Array of touching square cylinders and its corresponding unit cell (dotted square).

array of touching square cylinders, whose cross-section morphology and respective unit cell is shown schematically in Fig. 4, with c/a = 0.02, a/l = 0.80 and $\phi = 0.36$. A mesh of 126 × 126 nodes was used in all computations. Radiation and convection effects are neglected. The results are presented in Fig. 5 for a wide range of conductivity ratios k/k_f, where k_s and k_f are the conductivity of the solid and fluid phases, respectively. Globally, the results obtained by our model are in excellent agreement with experimental and numerical data of Nozad et al. (1985) and Hsu et al. (1995). For $k/k_f < 1$ and $k/k_f > 1000$, the present model underpredicts the effective thermal conductivity when compared with the experimental data. For very high values of k/k_f, discrepancy occurs because, in this case, it is crucial to have a good estimate of c/a, which remains as an empirical parameter of the model. On the other hand, when the conductivity ratio is lower than one, the solid phase starts to behave like a heat barrier, and the appearance of three-dimensional heat conduction effects becomes relevant and must be taken into account by the model.

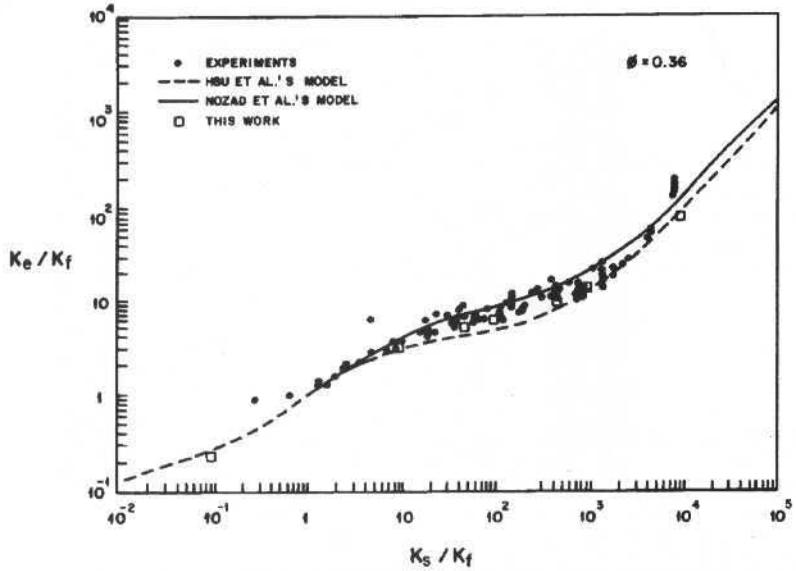

Fig. 5 Comparison of effective thermal conductivity of a two-dimensional array of touching square cylinders with experimental data and numerical results of Nozad et al. (1984) and Hsu et al. (1995); Hsu et al.'s results were obtained for a touching parameter of c/a = 0.01.

Transient Heat Diffusion in a Quadratic Koch Plate

In this last example, we consider a two-dimensional quadratic Koch plate, maintained at a uniform initial temperature of 0°C. For $t > 0$, the temperature at point A or O (test cases (a) and (b), respectively; see Fig. 6) is suddenly raised and maintained at 1.0°C, while heat is transfered by convection from the external boundary to a fluid at 0°C, with $h = 100$ W/m²K.

Temperature distributions in the quadratic Koch plate, at $t = 24$ s, are shown in Figs. 7a and 7b. Numerical results are also presented in Table 1 in the form of ratios T^n/T^0, for different times and $n = 1$, 2, 3, between the temperature at construction stage n and the corresponding temperature in the square that originated the fractal ($n = 0$). We note that, as the value of n increases, the energy introduced at one of the edges of the Koch plate (point A in test case (a)) tends to be almost completely dissipated by convection at the local level, little affecting the other branches of the fractal object (point B). As $n \to \infty$, the plate perimeter approaches infinity and all the heat is dissipated locally. In comparison, the thermal coupling between the center (point O) and the periphery (points A and B) remains relatively unchanged with the growing irregularity on the plate shape. These results illustrate the well known damping properties of fractal boundaries (Sapoval et al., 1990), and may explain why objects displaying fractal properties appear so often in nature.

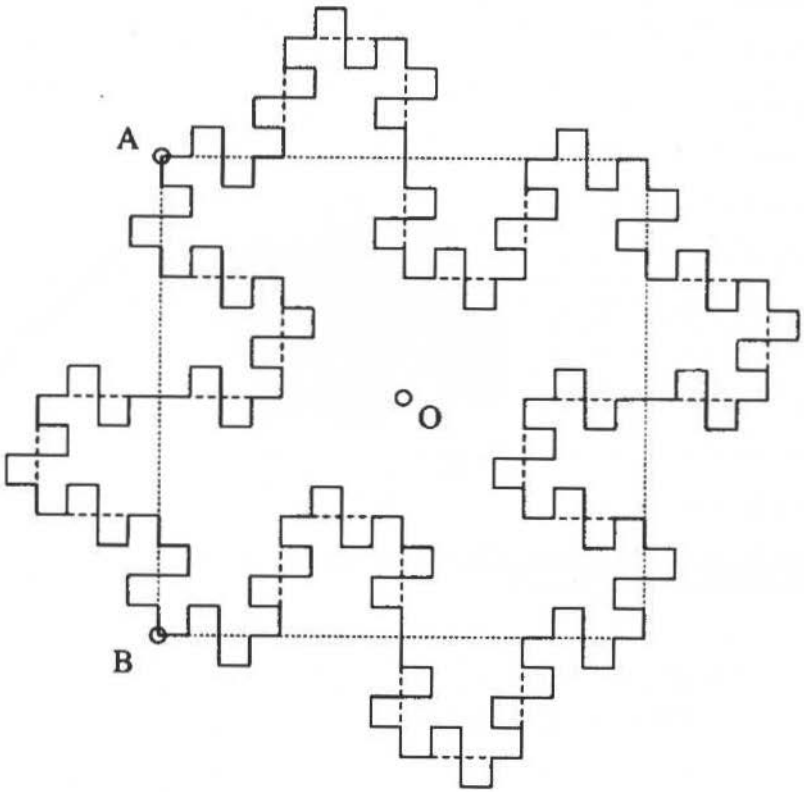

Fig. 6 Geometry of the quadratic Koch plate.

Conclusion

In the field of transport phenomena, the advent of fractals represented an important advance with the realization that they are a very good model for the geometrical structure of rough surfaces and of most disordered materials. In this paper, we presented a simple and versatile methodology for

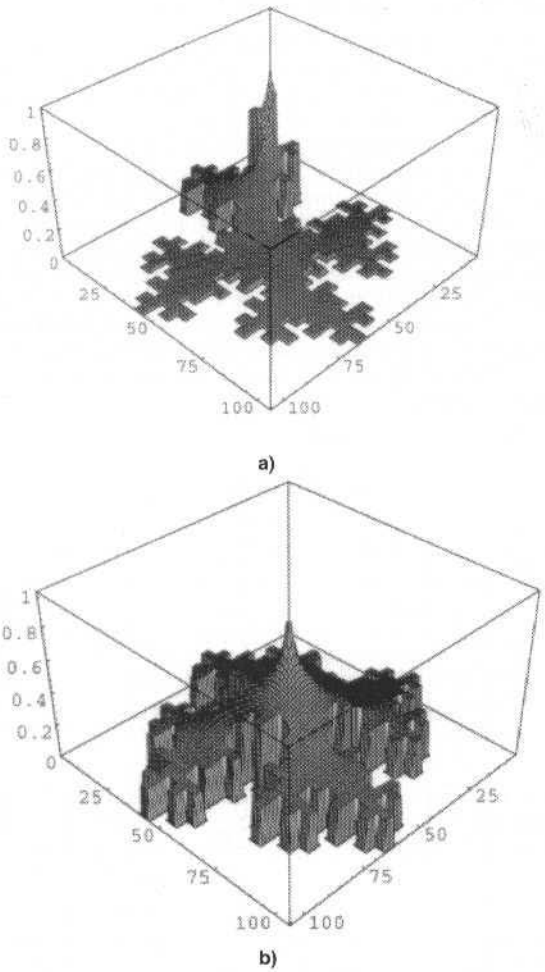

Fig. 7 Temperature distribution in the quadratic Koch plate for t = 24 s, n = 2, h = 100 W/m^{2}K, and (a) T_A fixed at 1ºC, and (b) T_O fixed at 1ºC.

Table 1 Numerical results for the quadratic Koch plate.

Temperature Ratio	Test Case	Time (s)	Construction Stage n = 1	n = 2	n = 3
T_B^n / T_B^0	(a)	6	6.61×10^{-6}	1.49×10^{-7}	1.88×10^{-8}
		12	1.36×10^{-3}	1.10×10^{-4}	2.27×10^{-5}
		24	2.18×10^{-2}	3.45×10^{-3}	1.16×10^{-3}
T_O^n / T_O^0	(a)	6	6.93×10^{-1}	4.11×10^{-1}	2.11×10^{-1}
		12	7.43×10^{-1}	4.09×10^{-1}	2.36×10^{-1}
		24	7.84×10^{-1}	4.37×10^{-1}	2.82×10^{-1}
T_A^n / T_A^0	(b)	6	6.93×10^{-1}	4.06×10^{-1}	2.05×10^{-1}
		12	7.42×10^{-1}	4.08×10^{-1}	2.53×10^{-1}
		24	7.82×10^{-1}	4.52×10^{-1}	3.31×10^{-1}

the solution of the diffusion equation in two-dimensional fractals. The numerical model is based on an explicit finite-difference scheme, and handles any geometry which can be represented on a rectangular grid. This work goes one step beyond previous research of Thovert (1990) by treating, with the same numerical model, geometries displaying whether an *internal* complex morphology, such as a Sierpinski carpet, or an intricate *external* shape, like quadratic Koch plate.

The performance of the proposed model is illustrated with the help of three representative examples, which include a Sierpinski carpet, a quadratic Koch plate and a spatially periodic porous medium. Particularly in this last example, the results were found to be in excellent agreement with experimental and numerical data published in the literature. Although we restricted our focus to these two-dimensional examples, the method of solution is general and can be extended to three-dimensional heterogeneous solids made up of two or more media.

References

Falconer, K., 1990, Fractal Geometry: Mathematical Foundations and Applications, John Wiley & Sons, New York.

Feder, J., 1998, Fractals, Plenum Press, New York.

Havlin, S., and Ben-Avraham, D., 1987, "Disordered Media", Advances in Physics, Vol. 36, N° 6, pp. 695-798.

Hsu, C. T., Cheng, P., and Wong, K. W., 1995, "A Lumped-Parameter Model for Stagnant Thermal Conductivity of Spatially Periodic Porous Media", ASME Journal of Heat Transfer, Vol. 117, pp. 264-269.

Jaggard, D. L., and Sun, X., 1990, "Fractal Surface Scattering: A Generalized Rayleigh Solution", Journal of Applied Physics, Vol. 68, pp. 5456-5462.

Majumdar, A., and Tien, C. L., 1991, "Fractal Network Model for Contact Conductance", ASME Journal of Heat Transfer, Vol. 113, pp. 516-525.

Mandelbrot, B. B., 1967, "How Long is the Coast of Britain? Statistical Self-Similarity and Fractional Dimension", Science, Vol. 155, pp. 636-638.

Nigmatullin, R. R., Dissado, L. A., and Soutougin, N., N., 1992 "A Fractal Pore Model for Archie's Law in Sedimentary Rocks", Journal of Physics D: Applied Physics, Vol. 25, pp. 32-37.

Nozad, L., Carbonnel, R. G., and Whitaker, S., 1985, "Heat Conduction in Multiphase Systems, Theory and Experiment for Two-Phase Systems", Chemical Engineering Science, Vol. 40, pp. 843-955.

Panagiotopoulos, P. D., Mistakidis, E. S., and Panagouli, O. K., 1992, "Fractal Interfaces with Unilateral Contact and Friction Conditions", Computer Methods in Applied Mechanics and Engineering, Vol. 99, pp. 395-412.

Pitchumani, R., and Yao, S. C., 1991, "Correlation of Thermal Conductivities of Unidirectional Fibrous Composites Using Local Fractal Techniques", ASME Journal of Heat Transfer, Vol. 113, pp. 788-796.

Sapoval, B., Gobron, T., and Margolina, A., 1991, "Vibrations of Fractal Drums", Physical Review Letters, Vol. 67, N° 21, pp. 2974-2977.

Tavman, I, H., 1996, "Effective Thermal Conductivity of Granular Porous Materials", International Communications in Heat and Mass Transfer, Vol. 23, N° 2, pp. 169-176.

Thovert, J. F., Wary, F., and Adler, P. M., 1990, "Thermal Conductivity of Random Media and Regular Fractals", Journal of Applied Physics, Vol. 68, pp. 3872-3883.

Turcotte, D. L., 1992, Fractals and Chaos in Geology and Geophysics, Cambridge University Press, Cambridge.

RBCM - J. of the Braz. Soc. Mechanical Sciences
Vol. XXI - No.1 - 1999 - pp. 144-153

ISSN 0100-7386
Printed in Brazil

On a Thermodynamically Consistent Modeling of Viscoelastic Fluid Behavior

Heraldo S. Costa Mattos
Universidade Federal Fluminense
Departamento de Engenharia Mecânica
24210 - 240, Niterói, RJ Brazil
heraldo@caa.vff.br

Abstract

This work presents a general procedure, developed within the framework of thermodynamics of irreversible processes, to obtain constitutive relations for fluids that verify automatically the principle of material objectivity and a local version of the second law of thermodynamics. In this constitutive theory the free energy is suposed to be a differentiable function of a finite set of variables, some of them introduced to account for the interference of the microstructure with the macrostructure. This phenomenological theory may allow a simplified macroscopic description of the microstructural physical mechanisms, relevant for certain classes of fluids. The choice of a particular objective time derivative and of two thermodynamic potentials is sufficient to define a complete set of constitutive equations. Some basic features and possibilities of the theory are presented through examples concerning viscoelastic fluids.

Keywords: *Viscoelastic Fluids, Thermodynamics of Irreversible Processes, Rate Type Constitutive Theories*

Introduction

To set up a general constitutive theory for fluids it is necessary to consider aspects of the second law of thermodynamics since dissipative phenomena must be taken into account. In addition, the constitutive equations must satisfy the principle of material objectivity. The constitutive theories in which the free energy is supposed to be a function of a set of independent variables (Germain et al., 1983), widely used in solid mechanics (Halphen and Quoc Son, 1975; Cleja-Tigoiu and Soós, 1990), may provide practical tools for the modeling of non-newtonian fluids especially when it is necessary to account for the interference of the microstructure with the macrostructure. That is the case, for instance, of certain kinds of polymeric liquids in which the breakdown of connections between the structural units that characterize the internal, i.e., the submacroscopic structure, may induce a decrease in the resistance to flow (Byrd et al., 1987; Billington and Tate, 1981). In these theories, some variables are introduced to account for dissipative mechanisms. In a phenomenological approach, such additional variables are supposed to contain microstructural information, relevant for certain classes of materials. To each of these variables is associated one constitutive equation in such a way that a local version of the second law of thermodynamics must be satisfied.

This paper is concerned with a systematic procedure to obtain constitutive equations for fluids within this framework. Whatever is the choice and interpretation of the aditional variables introduced to account for dissipative mechanisms, the resulting constitutive equations are objective and satisfy a local version of the second law of thermodynamics no matter the external actions and the initial and boundary conditions. The choice of two potentials and of a particular objective time derivative is sufficient to define a complete set of constitutive equations. Although a large number of alternative objective time derivatives found in literature can be considered in rate-type constitutive theories (Jaumann, Truesdell, Cotter-Rivling, etc.), some of them may lead to physically unrealistic oscillatory behaviors even if the resulting constitutive equations are thermodinamically admissible and satisfy the principle of material objectivity. Hence, in order to assure material objectivity without undesirable oscillations, special kinds of objective time derivatives for tensorial quantities are considered. Since the choice of a particular objective time derivative can be interpreted as a constitutive assumption, it is presented a discussion about the physical interpretation of these derivatives and their possible relation with micromotions.

The main features and possibilities of the theory are presented through examples concerning viscoelastic fluids. The study of fluids that may store elastic energy is interesting because some important phenomena, such as the the variability of viscosity with rate of shear and normal stress effects such as the die - swell and centripetal (or rod climbing) motion may be connected with the ability of the fluid to store elastic energy temporarily. To better understand the role of the objective time derivative in the theory, a simple shear flow of (generalized) Maxwell fluids is studied. The analysis of

Manuscript received: March 1997; revised: November 1998. Technical Editor: Angela Ourívio Nieckele.

this particular example allows to verify that, due to the dissipative behavior, in some non-newtonian fluids a flow may strongly depend on the initial conditions adopted for some of the independent variables.

The Second Law of Thermodynamics

Under suitable regularity assumptions, it is possible to consider the following local version of the second law of thermodynamics:

$$d = \mathbf{T}.\mathbf{D} - \varrho(\dot{e} - \theta\,\dot{s}) + \mathbf{q}.\mathbf{g} \geq 0 \qquad (1)$$

where $(\dot{})$ denotes the material time derivative of $(\,)$; ρ is the mass density; $\mathbf{T}$ the Cauchy stress tensor; $\mathbf{D} = 1/2\,[grad\mathbf{v} + grad\mathbf{v})^T]$ the deformation rate tensor; e the internal energy per unit mass; θ the absolute temperature; s the total entropy per unit mass; $\mathbf{q}$ the heat flux vector and $\mathbf{g} = -\,grad\,(log\theta)$, $log\theta$ standing for the logarithm of the absolute temperature. d is the rate of energy dissipation per unit volume. The second law of thermodynamics makes a distintion between possible processes ($d \geq 0$) and impossible processes ($d < 0$). The possible processes may be reversible (the rate of energy dissipation d is always equal to zero) or not. The Clausius-Dühem inequality, an alternative local version of the second law of thermodynamics, is obtained introducing the definition of the Helmholtz free energy per unit mass $\Psi\,(\Psi = e - \theta s)$ in Eq. (1):

$$d = \mathbf{T}.\mathbf{D} - \rho(\dot{\Psi} - s\dot{\theta}) + \mathbf{q}.\mathbf{g} \geq 0 \qquad (2)$$

Constitutive Theory

A general procedure to obtain a set of thermodynamically admissible constitutive equations for fluids that verify automatically the principle of objectivity can be described by the following steps:

Free energy potential

To set up a constitutive theory within the framework of the thermo-dynamics of irreversible processes, the present work consider fluids for which the Helmhotz free energy Ψ can be expressed as an isotropic and differentiable function of the absolute temperature θ, of the density ρ, of a measure of strain ε (to be defined in the next section) and of wathever may be relevant independent variables, which must be objective quantities. Generally, these variables are used to model the interference of the microstructure with the macrostructure. For instance: a tensorial variable related to the irreversible part of the fluid deformation caused by different possible submacroscopic mechanisms in molten metals and polymers; a tensorial variable that takes into account the incompatibility between different slip systems in crystalline fluids; a scalar variable related to the size and volume fraction of particles in suspensions; a scalar variable related with the proportion of broken connections between structural units in a macromolecule; etc.

A further discussion about the definition, choice and interpretation of these variables is performed in the next sections. Since, in this theory, most of the difficulties with material objectivity appear when these additional variables are tensorial quantities, only one abstract additional second order symmetric tensorial variable $\mathbf{A}$ is considered from now on in order to simplify the presentation:

$$\psi = \psi(\rho, \boldsymbol{\varepsilon}, \boldsymbol{A}, \theta) \qquad (3)$$

Objective time derivatives

The concepts underlying these constitutive equations cannot be presented without regard to the question of whether they satisfy the principle of material objectivity.

Since the material time derivative of an objective tensorial quantity is not necessarily objective, it is interesting to use some special kind of time derivative in rate type constitutive equations in order to assure the objectivity (for a further discussion see, for instance, Billington and Tate, 1981 and Truesdell and Noll, 1965.

A large number of definitions of objective time derivatives can be found in the literature (Jaumann, Truesdell, Cotter-Rivling, etc.). The choice of a particular derivative is very important and can be interpreted as a constitutive assumption. The present study is restricted to a particular family of derivatives:

$$\begin{aligned}\breve{T} &= \dot{T} + T(W - W^R) - (W - W^R)T \\ \breve{A} &= \dot{A} + A(W - W^R) - (W - W^R)A \\ \breve{\varepsilon} &= \dot{\varepsilon} + \varepsilon(W - W^R) - (W - W^R)\varepsilon\end{aligned} \tag{4}$$

where $\breve{T}, \breve{A}, \breve{\varepsilon}$, are objective time derivatives of the objective quantities T, A, ε. $W = 1/2\,[grad\ v\ grad\ v)^T]$ is the spin tensor and W^R is a skew-symmetric second order tensor. The objective derivatives $\breve{T}, \breve{A}$ and $\breve{\varepsilon}$ are equal to the material derivatives of T, A and ε as they would appear to an observer in a frame of reference attached to the particle and rotating with it at an angular velocity equal to the instantaneous value of the spin (W - W^R). The spin W^R can be associated to micromotions of the material structure or substructure. Neverteless, it is not a simple task to give a complete interpretation of this additional spin based on microstructural consideration. The term (W W^R) can be associated to the independent movement of a unit vector n attached to the material point: $\dot{n} = (W - W^R)$ may be interpreted as relative rotation of the material structure or substructure with respect to the continuum. In this case, W^R coincides with the concept of relative spin proposed by Zbib and Aifantis, 1987, in the context of solid mechanics which is a generalization of the plastic spin utilized by Dafalias, 1985 and Van Der Giessen, 1991.

The determination of the additional spin W^R can be based on the analysis of the interference of the microstructure (micromovements) with the macrostructure or on a phenomenological approach (which is the way adopted in this paper), presenting directly macroscopic constitutive relations for W^R. If $W^R = 0$ the derivatives $\breve{T}, \breve{A}, \breve{\varepsilon}$ coincide, respectively, with the definition of the Jaumann derivative of T, A and ε. From a phenomenological point of view, the spin W^R should be introduced in the theory to eliminate physically unrealistic oscillations of the variables T, A and ε that may appear if the Jaumann derivative is considered. In this phenomenological approach, the relative spin is assumed to be an objective function of the deformation rate tensor D, of the cauchy stress T and also of A such that $W^R = 0$ if $D = 0$. Hence, very general expressions can be adopted for the skew-symmetric tensor $W^R(T, D, A)$. In general, for an adequate phenomenological description of fluid behavior, in order to eliminate the undesirable oscillations induced by the Jaumann derivative, it is sufficient to consider:

$$W^R = \eta(AD - DA) \tag{5}$$

with η being a constant. For the sake of simplicity, this expression for W^R is adopted in the examples presented.

The definition of the objective derivative $\breve{\varepsilon}$ allows to propose a definition for the measure of deformation ε considered in this paper - ε is the second order tensor such that:

$$\breve{\varepsilon} = D, \forall t \tag{6}$$

As it is shown elsewhere, such definition of ε is very useful in the modeling of elastic effects in some fluid flows.

Fourier Law

The main idea in this theory is to characterize a fluid behavior through the free energy Ψ and the rate of energy dissipation d. Consequently, constitutive informations about the parcel q . g of the rate of energy dissipation d must be given. In this theory these information are obtained through the following constitutive relation between q and g:

$$q = k(\theta)\ g \tag{7}$$

where k is a positive scalar function of θ. From the definition of **g** it comes that:

$$\boldsymbol{q} = \mathrm{k}(\theta)\ \ grad(log\theta) = -\frac{k(\theta)}{\theta} grad\theta = -K(\theta)\, grad\theta \tag{8}$$

Equation (8) is a generalized version of the Fourier law with K being the thermal conductivity. It can be reduced to the usual Fourier law (K = *constant*) if small deviations of temperature from a fixed θ_0 is assumed.

Rate of energy dissipation

The choice and interpretation of the auxiliary variable **A** may vary from one problem to another. Nevertheless, in the present theory, such kind of variable is supposed to be related with irreversible changes on the microstructure and, consequently, with dissipative mechanisms. This relation with dissipative mechanisms is introduced through the constitutive assumption that the parcel $(\boldsymbol{T}\,.\,\boldsymbol{D} - \rho(\dot{\Psi} + s\dot{\theta}))$ of the rate of energy dissipation d can be expressed as a function d_m of $\boldsymbol{D}$ and $\breve{\boldsymbol{A}}$ such that $d_m(\boldsymbol{0},\boldsymbol{0}) = 0$.

$$\boldsymbol{T}\,.\,\boldsymbol{D} - \rho(\dot{\Psi} + s\dot{\theta}) = d_m(\boldsymbol{D}, \breve{\boldsymbol{A}}) \quad ; \quad d_m(\boldsymbol{0},\boldsymbol{0}) = 0 \tag{9}$$

Hence, $\left(\boldsymbol{T}\,.\,\boldsymbol{D} - \rho(\dot{\Psi} + s\dot{\theta})\right) = \left(d - \boldsymbol{q}\,.\,\boldsymbol{g}\right) = d_m(\boldsymbol{D}, \breve{\boldsymbol{A}})$ is a parcel of the rate of energy dissipation related only to mechanical effects since d_m is supposed to be only a function of $\boldsymbol{D}$ and $\breve{\boldsymbol{A}}$. This assumption has an important role in the theory. For instance, in any homothermal rigid body motion, the rate of energy dissipation d may be positive $(d > 0)$ only if $\breve{\boldsymbol{A}} \neq \boldsymbol{0}$, otherwise, $d = 0$. As a consequence, in this kind of motion, the only possible dissipative mechanism would be the microscopic changes related to the variable $\boldsymbol{A}$. Besides, if the potential ψ is a function only of ρ and $\boldsymbol{\varepsilon}$, all possible processes must be reversible.

d_m is supposed to have the following form for the fluids considered in this theory:

$$d_m = \frac{\partial \phi}{\partial \boldsymbol{D}}\,.\,\boldsymbol{D} + \frac{\partial \phi}{\partial \breve{\boldsymbol{A}}}\,.\,\breve{\boldsymbol{A}} \tag{10}$$

where ϕ is a differentiable function of $\boldsymbol{D}$ and $\breve{\boldsymbol{A}}$ such that $\phi\,(\boldsymbol{0},\boldsymbol{0}) = 0$. Equation (10) implies that the parcel of the rate of energy dissipation due to mechanical effects is the sum of two parts, the first one $\left((\partial\phi/\partial D).\boldsymbol{D}\right)$ related to the rate of energy dissipation due to viscous phenomena and the second one $\left((\partial\phi/\partial\breve{\boldsymbol{A}}).\breve{\boldsymbol{A}}\right)$ related to the dissipation due to internal changes of the material.

To understand the implications of the choice of expression (10), it is interesting to use the following local form for the rate of energy dissipation, obtained from Eqs. (2) and (3):

$$d = \boldsymbol{T}\,.\,\boldsymbol{D} - \rho\left(\frac{\partial \psi}{\partial \rho}\dot{\rho} + \frac{\partial \psi}{\partial \boldsymbol{\varepsilon}}\,.\,\dot{\boldsymbol{\varepsilon}} + \frac{\partial \psi}{\partial\, \boldsymbol{A}}\,.\,\dot{\boldsymbol{A}} + \frac{\partial \psi}{\partial \theta}\dot{\theta} + s\dot{\theta}\right) + \boldsymbol{q}\,.\,\boldsymbol{g} \tag{11}$$

Using the symmetry of ε and **A** it is possible to verify that:

$$\frac{\partial \psi}{\partial \boldsymbol{\varepsilon}}\,.\,\dot{\boldsymbol{\varepsilon}} = \frac{\partial \psi}{\partial \boldsymbol{\varepsilon}}\,.\,\breve{\boldsymbol{\varepsilon}} = \frac{\partial \psi}{\partial \boldsymbol{\varepsilon}}\,.\,\boldsymbol{D} \quad ; \quad \frac{\partial \psi}{\partial \boldsymbol{A}}\,.\,\dot{\boldsymbol{A}} = \frac{\partial \psi}{\partial \boldsymbol{A}}\,.\,\breve{\boldsymbol{A}} \tag{12}$$

Introducing the balance of mass equation and Eqs. (12) in (11), it then comes that:

$$d = \left(\boldsymbol{T} - \rho \frac{\partial \psi}{\partial \varepsilon} + \rho^2 \frac{\partial \psi}{\partial \rho} \boldsymbol{I} \right) . \boldsymbol{D} - \rho \frac{\partial \psi}{\partial \boldsymbol{A}} . \overset{\nabla}{\boldsymbol{A}} - \rho \frac{\partial \psi}{\partial \theta} \dot{\theta} - \rho s \dot{\theta} + \boldsymbol{q} . \boldsymbol{g} \tag{13}$$

Since a_m is given by (10), then:

$$d_m(\boldsymbol{D}, \overset{\nabla}{\boldsymbol{A}}) = d - \boldsymbol{q} . \boldsymbol{g} = \left(\boldsymbol{T} - \rho \frac{\partial \psi}{\partial \varepsilon} + \rho^2 \frac{\partial \psi}{\partial \rho} \boldsymbol{I} \right) \boldsymbol{D} - \rho \frac{\partial \psi}{\partial \boldsymbol{A}} . \overset{\nabla}{\boldsymbol{A}} - \left(\frac{\partial \psi}{\partial \theta} + \rho s \right) \dot{\theta} = \frac{\partial \phi}{\partial \boldsymbol{D}} . \boldsymbol{D} + \frac{\partial \phi}{\partial \overset{\nabla}{\boldsymbol{A}}} . \overset{\nabla}{\boldsymbol{A}} \tag{14}$$

And, consequently:

$$\left(\boldsymbol{T} + \rho^2 \frac{\partial \psi}{\partial \rho} \boldsymbol{I} - \rho \frac{\partial \psi}{\partial \varepsilon} - \frac{\partial \phi}{\partial \boldsymbol{D}} \right) . \boldsymbol{D} - \left(\rho \frac{\partial \psi}{\partial \boldsymbol{A}} + \frac{\partial \phi}{\partial \overset{\nabla}{\boldsymbol{A}}} \right) . \overset{\nabla}{\boldsymbol{A}} - \left(\rho \frac{\partial \psi}{\partial \theta} + \rho s \right) \dot{\theta} = 0 \tag{15}$$

Equation (15) must hold in any possible process.Thus, it is possible to conclude that the following relations must always hold:

$$s = - \frac{\partial \psi}{\partial \theta} \tag{16.1}$$

$$\rho \frac{\partial \psi}{\partial \boldsymbol{A}} + \frac{\partial \phi}{\partial \overset{\nabla}{\boldsymbol{A}}} = 0 \tag{16.2}$$

$$\boldsymbol{T} = -\rho^2 \frac{\partial \psi}{\partial \rho} \boldsymbol{I} + \rho \frac{\partial \psi}{\partial \varepsilon} + \frac{\partial \phi}{\partial \boldsymbol{D}} \quad if \quad tr\, \boldsymbol{D} \neq \boldsymbol{0} \tag{16.3a}$$

$$\boldsymbol{T} = -P \boldsymbol{I} + \rho \frac{\partial \psi}{\partial \varepsilon} + \frac{\partial \phi}{\partial \boldsymbol{D}} \quad if \quad tr\, \boldsymbol{D} = \boldsymbol{0} \tag{16.3b}$$

Equations (16) are constitutive relations that result from the hypothesis adopted for the free energy Ψ and the rate of energy dissipation d. The choice of the expression for the relative spin $\boldsymbol{W}^R$ and also for the potentials ψ and ϕ characterize completely a given fluid in this theory. Equations (16) together with the Fourier law (8), then form a complete set of objective constitutive equations.

Equation (16.1) is a classical expression found in many works, which is very good, at least, in the case of small variations of temperature from a fixed θ_0.

Equation (16.2) relates the objective time derivative of $\boldsymbol{A}$ with the other independent variables. Similar expressions appear in some works concerned with solid mechanics (Halphen and Quoc Son, 1975) and are generally called complementary equations. Nevertheless, these complementary equations are directly postulated and they are not obtained, like in the present work, as consequences of hypothesis concerning the free energy and the rate of energy dissipation.

The stress tensor $\boldsymbol{T}$ and the others variables are related through Eq. (16.3a) (compressible fluids) or equation (16.3b) (incompressible fluids). The term $(\rho(\partial\psi/\partial\varepsilon))$ is the elastic or reversible part of $\boldsymbol{T}$ and $(\partial\phi/\partial\boldsymbol{D})$ the irreversible part of $\boldsymbol{T}$ which is related to viscous phenomena. The term $(\rho^2(\partial\psi/\partial\rho))$ is the thermodynamic pressure. P is a multiplier of the incompressibility constraint $tr\, \boldsymbol{D} = \boldsymbol{0}$. P is an unknown quantity to be determined from the problem formed by the balance equations, the constitutive equations and a suitable set of boundary and initial conditions.

Equation (14) shows that, in order to have $d \geq 0$, the following condition is necessary:

$$\frac{\partial \phi}{\partial \boldsymbol{D}} . \boldsymbol{D} + \frac{\partial \phi}{\partial \breve{\boldsymbol{A}}} . \breve{\boldsymbol{A}} \geq -\boldsymbol{q} . \boldsymbol{g}$$

Since the Fourier law is assumed to be valid for this class of materials, the parcel of the dissipation rate due to thermal effects is always non-negative ($\boldsymbol{q} . \boldsymbol{g} = \boldsymbol{K}\boldsymbol{g} . \boldsymbol{g} \geq 0$). This fact leads to the classical heat conduction inequality ($-\boldsymbol{q} . grad\theta \geq 0$) since the absolute temperature θ is a positive quantity. Hence, the parcel of the dissipation rate due to mechanical effects is not necessarily non-negative, exept for homothermal processes ($grad\theta = \boldsymbol{0}$). However, in the present theory, the following constitutive assumption for the potential ϕ is taken into account:

$$\frac{\partial \phi}{\partial \boldsymbol{D}} . \boldsymbol{D} + \frac{\partial \phi}{\partial \breve{\boldsymbol{A}}} . \breve{\boldsymbol{A}} \geq 0 \quad \forall (\boldsymbol{D}, \breve{\boldsymbol{A}}) \tag{17}$$

For any particular set of constitutive equations obtained within this context, if condition (17) is verified, the second law inequality is automatically satisfied in any process, regardless the external actions, the boundary conditions and also the initial conditions. It is important to remark that the potentials ψ and ϕ do not need to be convex fuctions. The convexity of ϕ is only a sufficient condition in order to verify (17).

Viscoelastic Fluids

In this theory, the so-called viscoelastic fluids have the following basic features:

(i) ψ is, at least, a function of ρ, $\boldsymbol{\varepsilon}$, θ and the free energy potential has the following particular form:

$$\psi(\rho, \boldsymbol{\varepsilon}, \boldsymbol{A}, \theta) = \psi_m(\rho, \boldsymbol{\varepsilon}, \boldsymbol{A}) + \psi_t(\theta)$$

$$\psi_m(\rho, \boldsymbol{\varepsilon}, \boldsymbol{A}) = \frac{1}{\rho}\hat{\psi}_m(\boldsymbol{\varepsilon}, \boldsymbol{A}) \tag{18}$$

where $\boldsymbol{\psi}_m$ is a differentiable function of (ε, **A**).

(ii) The potencial ϕ is a differentiable isotropic function of $\boldsymbol{D}$ and $\breve{\boldsymbol{A}}$; This potential cannot be identically equal to zero: $\phi \not\equiv 0$.

From Equation (16) it comes that:

$$\boldsymbol{T} = -P\boldsymbol{1} + \frac{\partial \hat{\psi}_m}{\partial \boldsymbol{\varepsilon}} + \frac{\partial \phi}{\partial \boldsymbol{D}} ; \frac{\partial \hat{\psi}_m}{\partial \boldsymbol{A}} + \frac{\partial \phi}{\partial \breve{\boldsymbol{A}}} = 0 \tag{19}$$

$\left(\partial \hat{\psi}_m / \partial \varepsilon\right)$ is the elastic or reversible parcel of the stress tensor $\boldsymbol{T}$. ($\partial\phi/\partial\boldsymbol{D}$) is the viscous part of $\boldsymbol{T}$. This general class of constitutive equations may be used to model the macroscopic behavior of macromolecular fluids (molten plastics, some lubricating oil and paints, etc.).

An example of a viscoelastic fluids is the so-called Generalized Maxwell's fluid which is defined as follows:

Generalized Maxwell fluid

Besides the variable $\boldsymbol{\varepsilon}$, the potential $\hat{\psi}_m$ for such kind of fluid kind is a function of a symmetric second order internal variable **A** called the anelastic or irreversible strain tensor.

$$\hat{\psi}_m(\boldsymbol{\varepsilon}, \boldsymbol{A}) = \frac{1}{2}\lambda(\boldsymbol{\varepsilon}-\boldsymbol{A}).(\boldsymbol{\varepsilon}-\boldsymbol{A}) \; ; \; \phi(\overset{\nabla}{\boldsymbol{A}}) = \frac{1}{2}\kappa \overset{\nabla}{\boldsymbol{A}}.\overset{\nabla}{\boldsymbol{A}} \tag{20}$$

with $\kappa > 0$ and $\lambda > 0$.

From (19) and (20) it follows that:

$$\boldsymbol{T} = -P\boldsymbol{I} + \lambda(\boldsymbol{\varepsilon} - \boldsymbol{A}) \; ; \; \lambda(\boldsymbol{\varepsilon} - \boldsymbol{A}) = \kappa\overset{\nabla}{\boldsymbol{A}} \tag{21}$$

And, defining $\boldsymbol{T}^P = \boldsymbol{T} + P\boldsymbol{I}$, it is possible to conclude that:

$$\boldsymbol{T}^P = \lambda(\boldsymbol{\varepsilon} - \boldsymbol{A}) \Rightarrow \boldsymbol{T}^P = \kappa\overset{\nabla}{\boldsymbol{A}} \tag{22}$$

Hence, deriving the first identity in (22) and combining with the second one it is possible to obtain the following relation:

$$\boldsymbol{D} = \overset{\nabla}{\boldsymbol{\varepsilon}} = \lambda^{-1}\overset{\nabla}{\boldsymbol{T}}^P + \kappa^{-1}\boldsymbol{T}^P \tag{23}$$

Equation (23) is one possible generalized version of the classical Maxwell viscoelastic model in small strains. The importance of the choice of the objective derivative, the role of the initial conditions for the variable **A** and other features of this model can be seen through a very simple example - a shear flow - which is usually defined by:

$$v_1 = \dot{\gamma}\, x_2 \quad v_2 = v_3 = 0 \tag{24}$$

with v_1, v_2, v_3 being the cartesian coordinates of the velocity **v** and $\dot{\gamma}$ the shear strain.

In this case, taking $\boldsymbol{W}^R$ given by (5), it can be shown that relations $\boldsymbol{T}^R = \kappa\dot{\boldsymbol{A}}$, and $\overset{\nabla}{\boldsymbol{\varepsilon}} = \boldsymbol{D}$ are equivalent to:

$$\dot{A}_{11} - 2\dot{\gamma}[1 - 2\eta A_{11}]A_{12} = \left(\frac{1}{\kappa}\right)T_{11}^P = 0 \tag{25.1}$$

$$\dot{A}_{12} + 2\dot{\gamma}[1 - 2\eta A_{11}] = \left(\frac{1}{\kappa}\right)T_{12}^P \tag{25.2}$$

$$A_{22} = -A_{11} \; ; \; A_{13} = A_{23} = A_{33} = 0 \tag{25.3}$$

$$\dot{\varepsilon}_{11} - 2\dot{\gamma}[1 - 2\eta A_{11}]\varepsilon_{12} = 0 \tag{26.1}$$

$$\dot{\varepsilon}_{12} + 2\dot{\gamma}[1 - 2\eta A_{11}]\varepsilon_{11} = \dot{\gamma} \tag{26.2}$$

$$\varepsilon_{22} = -\varepsilon_{11} \; ; \; \varepsilon_{13} = \varepsilon_{23} = \varepsilon_{33} = 0 \tag{26.3}$$

and (42) is equivalent to:

$$\dot{T}_{11}^{P} - 2\dot{\gamma}[1 - 2\eta A_{11}]T_{12}^{P} + \left(\frac{\lambda}{\kappa}\right)T_{11}^{P} = 0 \tag{27.1}$$

$$\dot{T}_{12}^{P} + 2\dot{\gamma}[1 - 2\eta A_{11}]T_{11}^{P} + \left(\frac{\lambda}{\kappa}\right)T_{12}^{P} = \dot{\gamma}\lambda \tag{27.2}$$

$$T_{22}^{P} = -T_{11}^{P} \; ; \; \dot{T}_{13}^{P} = \dot{T}_{23}^{P} = \dot{T}_{33}^{P} = 0 \tag{27.3}$$

If $\eta = 0$ then $\boldsymbol{W}^{R} = 0$ (the Jaumann derivative). In this case the components of $\boldsymbol{T}$, $\boldsymbol{A}$ and $\boldsymbol{\varepsilon}$ can be computed analytically. For instance, taking the initial conditions $\boldsymbol{A}(t = 0) = \boldsymbol{\varepsilon}(t = 0) = \boldsymbol{T}(t = 0) = \boldsymbol{0}$ the following expressions are obtained:

$$\varepsilon_{12}(t) = \frac{1}{2}sen(2\dot{\gamma}t) \; ; \; \varepsilon_{11}(t) = \frac{1}{2}(1 - cos(2\dot{\gamma}t))$$

$$T_{12}(t) = C\left[e^{-\left(\frac{\lambda}{\kappa}\right)t}\left(\left(-\frac{\lambda}{\kappa}\right)cos(2\dot{\gamma}t) + 2\dot{\gamma}\,sin(2\dot{\gamma}t)\right) + \left(\frac{\lambda}{\kappa}\right)\right]$$

$$C = \frac{\dot{\gamma}\lambda}{4\dot{\gamma}^{2} + (\lambda/\kappa)^{2}}$$

Similarly as in the case of a rigid-viscoplastic fluid, the choice of the Jaumann derivative can lead to undesirable oscillations. The use of positive values for η can atenuate and even eliminate such kind of oscillations. To illustrate the implications of the use of the relative spin ($\eta \neq 0$), the system of non-linear ordinary differential equations formed by (25), (26) and (27) is solved numerically for $\eta = 1$. The initial value problem can be put into a dimensionless form. In the process, only one dimensionless parameter $\alpha = [\lambda/(\dot{\gamma}\kappa)]$ accounts for the material properties. Figure 1 shows the evolution of the stress components $T_{12}^{P} = T_{12}$ and T_{11}^{P} taking $\eta = 1$ and $\alpha = 1$.

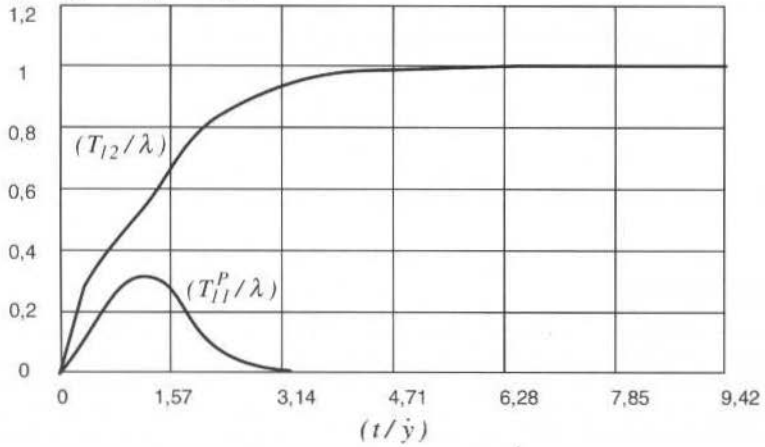

Fig. 1 Evolution of the stress components $T_{12}^{P} = T_{12}$ and T_{11}^{P} in a shear flow. η=1 and α=1.

It can be verified that λ is a limit value for the shear component T_{12}. After $t = \dot{\gamma}\pi$, the normal stress difference $(T_{11} - T_{22}) = 2T_{11}^{P}$ is zero because the elastic part of strain $(\varepsilon_{11} - A_{11})$ is zero. The evolution of the components of A and ε is depicted in Figs. 2 and 3. It is important to remark that even in this simple problem, due to the dissipative behavior of such kind of fluid, the study of the flow depends strongly on the initial conditions adopted for A.

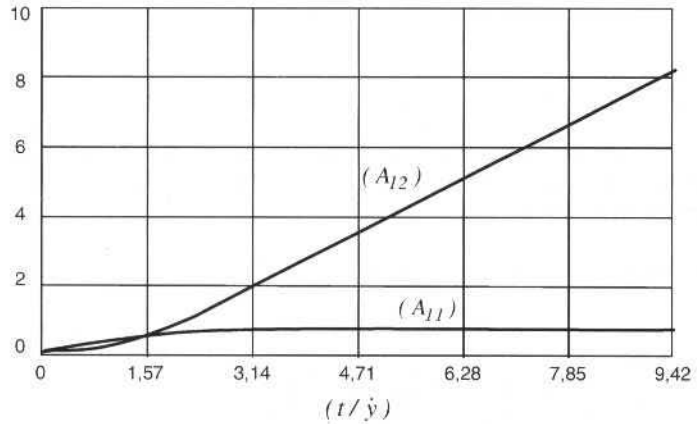

Fig. 2 Evolution of the anelastic strain components A_{12} and A_{11} in a shear flow. $\eta = 1$ and $\alpha = 1$.

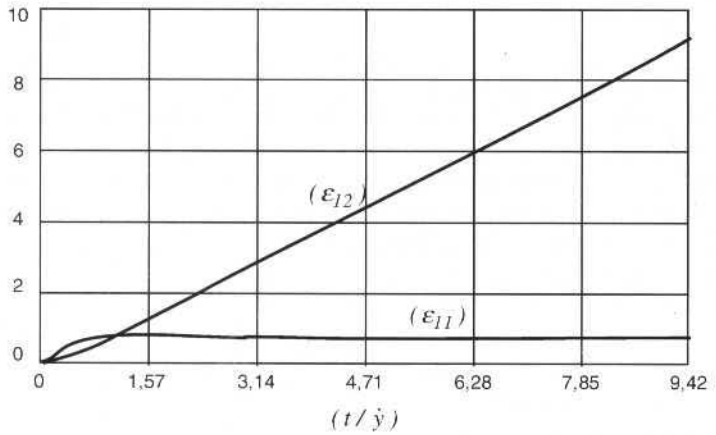

Fig. 3 Evolution of the strain components ε_{12} and ε_{11} in a shear flow. $\eta = 1$ and $\alpha = 1$.

Concluding Remarks

The procedure to obtain constitutive relations that verify automatically the principle of material objectivity and the second law of thermodynamics proposed in this paper can be an useful tool in the modeling of non-newtonian fluids. It allows a generalization of classical rheological models (Jeffreys, Maxwell, Oldroyd, etc. Byrd et al., 1987; Astarita and Marucci, 1986; Doi and Eduards, 1986, by including microstructural effects. The interference of the microstructure with the macrostructure can be achieved not only by the choice of the potentials ψ, ϕ and its arguments but also by the choice of the relative spin W^{R}.

It is important to enfasize the phenomenological approach of the present work. It is not its goal to give an interpretation completely based on microstructural consideration of the auxiliary variable **A** and of the relative spin tensor. Such kind of definition is a very complex task not yet fully developed even in solid mechanics, where such kind of approach has been used for many years.

Additional couplings between non-linear physical mechanisms (such as between the strain-hardening or the strain-softening and the anelastic strain rate), can be described through the introduction of other auxiliary variables in the problem. Such kind of procedure has been used in solid mechanics and mixture theories with very good results (Costa Mattos et al., 1992, 1995).

Temperature plays an important role in complex flows of non-newtonian fluids in many industrial applications, such as injection molding of polymers. The proposed theory allows an adequate modeling and a simple interpretation of thermomechanical couplings when dissipative mechanisms related to changes on the material structure or substructure must also be taken into account. Interesting works can be made by analyzing the dependence of the potentials ψ and ϕ on the temperature and the resulting thermomechanical couplings simmilarly as it was done in Pacheco, 1994 for solid materials.

References

Astarita, E. and Marucci, G, 1974, "Principle of Non-Newtonian Fluid Mechanics". McGraw-Hill, London.

Billington, E. W. and Tate, A., 198 I, "The Physics of Deformation and Flow", Mc Graw Hill Byrd, R. B., Armstrong, R. C. and Hassager, O., 1987, "Dynamics of Polymeric Liquids". Vols. I and II John Willey, New York.

Cleja-Tigoiu S. and Soós, E., 1990, "Elastoviscoplastic Models with Relaxed Configurations and Internal State Variables". Appl. Mech. Rev., vol. 43, pp. 131 - 15 1.

Costa-Mattos, H. S., Martins Costa, M. L. and Saldanha da Gama, R. M., 1995, "On The Modelling of Momentum and Energy Transfer in Incompressible Mixtures". Int. J. Non-linear Mech., vol. 30, pp. 419 - 431.

Costa-Mattos, H. S., Fremond, M. and. Mamyia, E. N., 1992, "A Simple Model of the Mechanical Behavior of Ceramic-Like Materials", Int. J. Solids and Structures, vol. 20, pp. 3185 - 3200.

Dafalias, Y. F., 1985, "The Plastic Spin", Trans ASME, J. Appl. Mech, vol. 52, pp. 865 - 871.

Doi, M. and Eduards, S., 1986, "The Theory of Polymer Dynamics". Claredon Press, Oxford.

Germain, P., Quoc Son, N. and Suquet, P., 1983, "Continuum Thermodynamics". J. Appl. Mech. ASME, vol. 50, pp. 10 I O- I 020.

Halphen, B. and Quoc Son, N., 1975, "Sur les Materiaux Standarts Generalisés". J. Mécanique, vol. 14, pp. 33 - 63.

Pacheco, P. C. L., 1994, "Analysis of the Thermomechanical Couplings in Elasto-Viscoplastic Materials", Doctor Thesis (in Portuguese). Department of Mechanical Engineering, Pontificia Universidade Católica do Rio de Janeiro.

Truesdell, C. and W. Noll, W., 1965, "The Nonlinear Fields Theories of Mechanics". Enc. Phys. vol. 111/3. Springer, Berlin.

Van der Giessen, E., 199 I, ."Micromechanical and Thermodynamic Aspects of the Plastic Spin". Int. J. Plasticity, vol. 7, pp. 365 - 386.

Zbib, H. M. and Aifantis, E. C., 1987, "Constitutive Equations for Large Material Rotations, in Constitutive Laws for Eng. Materials: Theory and Applications", Elsevier, U. K., pp. 1411 1418.

RBCM - J. of the Braz. Soc. Mechanical Sciences
Vol. XXI - No.1 - 1999 - pp. 154-157

ISSN 0100-7386
Printed in Brazil

Abstracts

Abrão, A. M. and Aspinwall, D. K., 1999, " Tool Wear of Polycrystalline Cubic Boron Nitride and Ceramic Materials When Hard Turning Bearing Steel", J. of the Braz. Soc. Mechanical Sciences, Vol. 21, No. 1, pp. 1-9.

This work aims to investigate the principal wear mechanisms involved when turning AISI E53100 bearing steel hardened to 60-62HRC using two grades of polycrystalline cubic boron nitride (PCBN) and three grades of ceramic tool materials (mixed alumina, whisker reinforced alumina and silicon nitride-based). In addition to the tool life data, scanning electronic micrographs of the cutting edge and the profile of the rake and clearance faces are presented. The results suggest that the mixed alumina tool presented highest flank wear resistance when cutting under finishing conditions, whereas the low content PCBN compact was superior when rough cutting. Diffusion, abrasion and plastic deformation were the main cause of tool failure.
Keywords: *Hard Turning, Bearing Steel, PCBN and Ceramic Tools.*

Rosa, D.dos S., Volponi, J. E. and Júnior, S. S., 1999, " Analysis of Polyethylenes Used to Coat Telephone Wires and Cables Submitted to Severe Wether-Ometer Conditions", J. of the Braz. Soc. Mechanical Sciences, Vol. 21, No. 1, pp. 10-16.

Polyethylenes, used to coat telephone cables and wires, are the materials that have shown the best behavior when submitted to the action of the environment; in many cases they last over twenty years. Among them, we highlight low-density polyethylene (LDPE), that, however, has low resistance to abrasion: this makes impossible its use in networks that undergo a great incidence of kites and cutting materials. An alternative for this material is the high-density polyethylene (HDPE). Detailed studies have shown that both, in the laboratory as in the field, have similar behavior as to resistance to severe weather conditions, with the additional advantage that HDPE has a much higher mechanical resistance. This work presents aa assessment of the behavior of these materials and demonstrate why they have an excellent resistance to severe weather conditions.
Keywords: *Wire and Cable Coating, Polyethylenes, Aging*

Bazzo, E., Colle, S. and Groll, M., 1999 ," Theoretical and Experimental Study of a CPL Using Freon 11 as the Working Fluid", J. of the Braz. Soc. Mechanical Sciences, Vol. 21, No. 1, pp. 17-28.
Sergio Colle

Theoretical and experimental analysis are presented for a Capillary Pumped Loop (CPL), using Freon 11 as the working fluid. A mathematical model to predict the hydrodynamic behavior and the heat transport capability on the basis of capillary limitation is presented. Circumferentially grooved heat pipes are considered to be used as the capillary pumps. The capillary pumps consist of 19 mm O.D. aluminum tubes, with fine circumferential grooves machined along their inner surfaces. Start-up, heat transport limits and repriming after dryout were investigated. Experimental results up to 1.7 W/cm^2 were found. A good agreement between measured values and those computed by using the theoretical model has been observed.
Keywords*: CPL, Capillary Pumped Loop, Heat Pipe, Two-Phase Heat Transfer Loop.*

Frey, S., Araujo, J. H. C. and Ramos, M. A. M. S., 1999, " Finite Element Approximation for the Heat Transfer in Incompressible Oldroyd-B Flows", J. of the Braz. Soc. Mechanical Sciences, Vol. 21, No. 1, pp. 29-40.

The main purpose of this article is the numerical simulation of the heat transfer in an incompressible viscoelastic flow via a stable finite element method. The chosen nonlinear model was the differential Oldroyd-B *liquid with constant viscoelastic properties. The proposed numerical scheme is based upon a four-field finite element formulation whose main features are the optimal representation of the stress tensor in the Stokes context and the use of upwind strategies in order to stabilize both stress and temperature fields in advective-dominated situations. Some two-dimensional simulations illustrate the stable and accurate performance of the finite element method employed.*
Keywords: *Viscoelastic Flows, Heat Convection, Finite Elements, Bubble Functions, Stabilized Methods.*

Gama, R. M. S., 1999, "A Finite Element Approximation for the Heat Transfer Process in a Plate with a Nonuniform Temperature-Dependent Source", J. of the Braz. Soc. Mechanical Sciences, Vol. 21, No. 1, pp. 41-50.

In this work the steady-state heat transfer process in an opaque plate with a nonuniform temperature-dependent source is modelled assuming that there exists a heat transfer from/to the plate following Newton's law of cooling. It is presented a quadratic functional whose minimization corresponds to the solution of the heat transfer problem. A finite element approximation is proposed for carrying out numerical simulations through the minimization of the functional. Some particular problems are simulated.

Keywords: *Conduction Heat Transfer, Minimum Principle, Plate Approximation, Finite Elements.*

Sodré, J. R. and Parise, J. A. R., 1999, " Friction Factor in Annular Conduits with Tubular Fins", J. of the Braz. Soc. Mechanical Sciences, Vol. 21, No. 1, pp. 51-60.

The friction factor for turbulent fully developed flow of air at steady state conditions through an annular conduit with tubular fins has been determined. The tubular fins consisted of tubes inserted in the annular gap to increment heat transfer. The finned annular section was built to simulate the heat exchangers (cooler and heater) of a Stirling engine. Tests were carried out in an annular section with a radius ratio of 1.083, covering Reynolds numbers between 1000 and 6000. The results have shown that the utilization of annular fins increased the pressure loss by friction by a factor of 7 to 12, within the range studied.

Keywords: *Annular Pipe, Stirling Engines, Friction Factor.*

Mesquita, A. L. A., Serra, C. M. V., Cruz, D. O. A. and Filho, N. M., 1999, "A Simplified Method for Axial-Flow Turbomachinery Design", J. of the Braz. Soc. Mechanical Sciences, Vol. 21, No. 1, pp. 61-70.

This paper presents a methodology for design of axial-flow turbomachinery using the cascade flow model and the boundary-layer theory. The inviscid cascade flow is treated by means of a panel method with an empirical correction to take in account the viscous effects. By applying the momentum equation the drag coefficient of the cascade airfoils is related to the loss coefficient, the deflection coefficient, the inflow angle, and all the cascade geometric parameters. The applicability of the design criterion and the validity of the prediction method are analyzed by using experimental data from axial-flow fan rig tests.

Keywords: *Axial-Flow Turbomachinery, Cascade, Boundary-Layer, Fan.*

Hofer, E. P., Rembe, C. and Beuten, M., 1999, " High Speed Cinematography of Dynamical Processes in Microdevices", J. of the Braz. Soc. Mechanical Sciences, Vol. 21, No. 1, pp. 71-81.

Testing of micro devices, especially micro mechanical systems with movable parts, seems to be an essential step prior to introduction into the market. The acceptance of the micro device and its market share strongly depend on reliability which requires advanced testing methods.

In this paper, a testing equipment for visualizing and recording of highly dynamical phenomena of very short time durations in micro structures is presented. The cinematographic image sequences allow the extraction of position, velocity and acceleration of moving parts in micro devices.

In a first application, results for thermal ink jet print heads with emphasis on the fluid dynamical processes in the ink chamber were presented at DINAME 95 by Hofer, Patzer and Beurer (1995). For this microactuator - most sold world wide - the whole life cycle of droplet generation can be shown as it appears in real time. In addition to experimental testing, analytical and numerical studies have been carried out for a better understanding of the governing physical phenomena in thermal ink jet printing. As a consequence, valuable information about the design of ink jet print heads, wear of its heating element, printing at very high frequencies and the existence of satellite droplets during printing could be extracted.

The second application, which is presented in this paper, studies the dynamics of an electromagnetic micro relay in detail. The dynamical behavior of the free and bounded oscillations of the switching of the relay has been visualized in order to identify material parameters which are included in a state space model. This example clearly demonstrates the capability of a combined approach using cinematographic visualization together with systems theoretic methods for the development of high performance micro devices.

An outlook towards future research within the framework of high speed cinematography of dynamical processes in micro devices with emphasis on gaining more insight in transient behaviors concludes this research work

Keywords: *High-Speed-Photomicrography, Cinematography, Highly Dynamical Phenomena, Parameter Identification, Microactuators*

Rade, D. A. and Silva, L. A., 1999, "On the Usefulness of Antiresonances in Structural Dynamics", J. of the Braz. Soc. Mechanical Sciences, Vol. 21, No. 1, pp. 82-90.

In this paper a study focusing the zeros of frequency response functions (FRFs) of linear mechanical systems is presented. Two major aspects are focused: the underlying theory, including a physical interpretation of the zeros of both transfer and driving point FRFs in terms of structural modifications, and the possibility of practical exploration of the FRF in some structural dynamics applications, namely: finite element updating, structural damage identification and vibration attenuation using dynamic vibration absorbers. After presentation of the theory, some results of applications performed on both numerically simulated and experimental mechanical systems are presented o illustrate the practical use of the zeros.

Keywords: *Antiresonances, System Identification, Modal Analysis, Structural Modifications, Damage Localization*

Santisteban, J. A., Ripper, A, Stephan, R. M., David, D. and Noronha, R., 1999, "Controller Design for a Bearingless Electric Motor", J. of the Braz. Soc. Mechanical Sciences, Vol. 21, No. 1, pp. 91-98.

An electromagnetic and a mechanical model for a bearingless electric motor are presented. Based on these models, a controller structure is proposed and simulations presented. A laboratory prototype of this motor was constructed and experimental results validated the model. The proposed approach can also be used for the design of better controllers.

Keywords: *Magnetic Bearing, Bearingless Motor, Modeling.*

Pereira, J. A., Lopes, V. Jr. and Weber, H. I., 1999, "Automation In Fault Detection Using Neural Network and Model Updating", J. of the Braz. Soc. Mechanical Sciences, Vol. 21, No. 1, pp. 99-108.

In this article, an implementation of structural health monitoring process automation based on vibration measurements is proposed. The work presents an alternative approach which intent is to exploit the capability of model updating techniques associated to neural networks to be used in a process of automation of fault detection. The updating procedure supplies a reliable model which permits to simulate any damage condition in order to establish direct correlation between faults and deviation in the response of the model. The ability of the neural networks to recognise, at known signature, changes in the actual data of a model in real time are explored to investigate changes of the actual operation conditions of the system. The learning of the network is performed using a compressed spectrum signal created for each specific type of fault. Different fault conditions for a frame structure are evaluated using simulated data as well as measured experimental data.

Keywords: *Neural Network, Fault Detection, Model Updating, Predictive Maintenance*

Pinho, M. O., Fernandez, H. C. N., Alvim, A. C. M. and Melo, P. F. F. F., 1999, "Availability of a Component Subject to an Erlangian Failure Model Under Wearout by Supplementary Variables", J. of the Braz. Soc. Mechanical Sciences, Vol. 21, No. 1, pp. 109-122.

This paper presents the availability analysis of a component by means of supplementary variables taking wearout into account. An Erlangian failure model is adopted, so as to allow comparison of the results with those obtained from the device of stages, which, for this failure model, theoretically gives exact results. The component availabilities obtained from both methods are well in agreement, although the results obtained from the supplementary variables method are less conservative. A point worth mentioning is that the solutions have been obtained for the transient period, a feature not commonly approached in the literature. The supplementary variables method is more general, although it may present numerical instability problems if proper care is not taken when discretization of the system is made. In this paper, the indirect method of Lax is shown to be stable for the problem modeled.

Keywords: *Availability Analysis, Wearout, Non-Markovian Models, Device of Stages, Supplementary Variables*

Chiarello, A. G. and Pederiva, R., 1999, " A Study of Parameter Monitoring in Stationary Mechanical Systems", J. of the Braz. Soc. Mechanical Sciences, Vol. 21, No. 1, pp. 123-132.

This work describes a method of parameter monitoring in stationary mechanical systems for fault detection and location purposes. Using a state space model of the system and an auxiliary one, called filter, analytical redundancy equations are defined. The redundancy equations are based on correlation functions involving systems parameters. It is demonstrated that these correlation functions can be used to generate residual functions for fault monitoring. All residual functions estimated for the healthy system are ideally zero but when a fault occurs, some estimated

residuals differ from zero. Using a parametric residual analysis, one can locate the physical parameter that is directly related to the system fault. The proposed approach is demonstrated using a numerical example.
Keywords: *Fault Detection, Diagnosis, Model Based.*

Ramos, F. M., 1999, " Heat Diffusion in Two-Dimensional Fractals", J. of the Braz. Soc. Mechanical Sciences, Vol. 21, No. 1, pp. 133-143.

A simple and versatile methodology for the solution of the diffusion equation in two-dimensional fractals is presented. The numerical model is based on an explicit finite-difference scheme, and handles any geometry which can be represented on a rectangular grid, including problems with an internal complex morphology, such as a Sierpinski carpet, or an intricate external shape, like a quadratic Koch plate. For validation purposes, the model is also applied to a spatially periodic porous medium for which numerical and experimental data can be found in the literature. The proposed methodology is general and can be extended to three-dimensional heterogeneous solids, made up of two or more media.
Keywords: *Heat Diffusion, Fractals, Finite-differences, Porous Media, Effective Thermal Conductivity.*

Mattos, H. S. C., 1999, " On a Thermodynamically Consistent Modeling of Viscoelastic Fluid Behavior", J. of the Braz. Soc. Mechanical Sciences, Vol. 21, No. 1, pp. 144-153.

This work presents a general procedure, developed within the framework of thermodynamics of irreversible processes, to obtain constitutive relations for fluids that verify automatically the principle of material objectivity and a local version of the second law of thermodynamics. In this constitutive theory the free energy is suposed to be a differentiable function of a finite set of variables, some of them introduced to account for the interference of the microstructure with the macrostructure. This phenomenological theory may allow a simplified macroscopic description of the microstructural physical mechanisms, relevant for certain classes of fluids. The choice of a particular objective time derivative and of two thermodynamic potentials is sufficient to define a complete set of constitutive equations. Some basic features and possibilities of the theory are presented through examples concerning viscoelastic fluids.
Keywords: *Viscoelastic Fluids, Thermodynamics of Irreversible Processes, Rate Type Constitutive Theories*

Journal of the Brazilian Society of Mechanical Sciences
Referees - 1998

Revista Brasileira de Ciências Mecânicas
Revisores - 1998

A

Abimael Loula	LNCC
Adriana S. França	UFMG
Alcir de Faro Orlando	PUC-Rio
Alexandre Bracarense Queiróz	UFMG
Alexandre Mendes Abrão	UFMG
Alisson Rocha Machado	UFU
Álvaro Costa Neto	USP/EESC
Álvaro Luiz Gayoso de Azevedo Coutinho	UFRJ-COPPE
Álvaro Toubes Prata	UFSC
Américo Scotti	UFU
Amilcar Porto Pimenta	CTA-ITA
Angela Ourivio Nieckele	PUC-Rio
Anselmo Eduardo Diniz	UNICAMP
Antonio Carlos Bannwart	UNICAMP
Antonio Carlos Ribeiro Nogueira	UFSC
Antonio Fernando Bertachini de Almeida Prado	INPE
Antonio Francisco P. Fortes	UnB
Antonio Moreira dos Santos	USP-EESC
Aron José Pazin de Andrade	Fundação Adib Jatene
Átila Pantaleão Silva Freira	UFRJ-COPPE
Aura Conci	UFF
Aureo Campos Ferreira	UFSC

B

Benedito de Moraes Purquério	USP/EESC

C

Caio Glauco Sánchez	UNICAMP
Carlos Alberto de Almeida	PUC-Rio
Carlos Alberto Ferrari	UNICAMP
Carlos Alberto Martins	UFSC
Carlos Alberto Nunes Dias	USP/EP
Carlos Augusto Silva de Oliveira	UFSC
Carlos Kaminski	USP-EP
Carlos Roberto Ribeiro	UFU
Celso Pupo Pesce	USP-EP
Cesar Vitório Franco	UFSC
Cézar O. R. Negrão	UFSC
Claudio Melo	UFSC
Claudio Moisés Ribeiro	CEPEL
Clóvis de Arruda Martins	USP/EP

D

Dirceu Spinelli	USP-EESC
Durval Duarte	USP/EESC
Décio Crisol Donha	USP-EP

E

Edson Del Rio	UNESP - FEIS
Eduardo Balster Martins	UNICAMP
Eduardo Fancello	UFSC
Eitaro Yamane	USP/EP

F

Felipe Rachid	UFF
Fernando Alves Rochinha	UFRJ-COPPE
Fernando Eduardo Milioli	USP/EESC
Francesco Scofano Neto	IME
Francisco Domingues Alves de Souza	IPT-DME

G

George Stanescu	FURG
Geraldo Spinelli Ribeiro	PETROBRAS/CENPES
Gustavo C. R. Bodstein	UFRJ-COPPE

H

Hans Ingo Weber	PUC-Rio
Henrique Rozenfeld	USP-EESC
Heraldo da Silva Couto	INPE
Heraldo S. da Costa Mattos	UFF
Horácio Helman	UFMG
Hugo Borelli Resende	EMBRAER

J

Jair Carlos Dutra	UFSC
Janardan Rohatgi	UFPE
Jerônimo S. Travelho	INPE
João Andrade de Carvalho Júnior	INPE
João Fernando Gomes Oliveira	USP-EESC
João Luiz Filgueiras de Azevedo	CTA - IAE
João Maurício Rosário	UNICAMP
João Nildo de Souza Vianna	UnB
Jorge Isaias Llagostera Beltran	UNICAMP
Jorge Ledo Larangeira	UFRGS
José Alberto Cuminato	USP-EESC
José Alberto dos Reis Parise	PUC-Rio
José Antonio Bellini da Cunha Neto	UFSC
José Arana Varela	UNESP
José Arnaldo Barra Montevecchi	EFEI
José Augusto Penteado Aranha	USP/EP
José Guilherme Silva Menezes Senna	USP-EESC
José L. Lage	Southern Methodist University
José Manoel Balthazar	UNESP
José Maria Saiz Jabardo	USP-EESC
José Maurício Gurgel	UFPB
J.R. Sodré	PUC-MG
José Reinaldo Silva	USP-EP
José Ricardo Figueiredo	UNICAMP
José Roberto Moraes d'Almeida	PUC-Rio
José Roberto Simões Moreira	USP-EP
José Sotelo Júnior	USP-EP
José Teixeira Freire	UFSCar
José Viriato Coelho Vargas	UFPR
Júlio Romano Meneghini	USP-EP
Júlio Wilson Ribeiro	UFCE

L

Linilson R. Padovese	USP-EP
Luis Carlos de Castro Santos	USP
Luis Carlos Martins	UFRJ/COPPE
Luis Felipe Mendes de Moura	UNICAMP
Luis Fernando Gonçalves Pires	IPE – CTEx
Luiz Augusto Horta Nogueira	EFEI
Luiz Carlos Sandoval Góes	CTA-ITA
Luiz Fernando Milanez	UNICAMP
Luiz Gonzaga Trabasso	CTA - ITA

M

Maher Nasr Bismark-Nasr	CTA -ITA
Marcelo G. Simões	USP-EP
Marcelo J. Santos Lemos	CTA-ITA
Márcio Carvalho	PUC-Rio
Marco Stipkovik Filho	USP-EP
Marcos Aurélio Ortega	CTA-ITA
Marcos de Mattos Pimenta	USP-EP
Marcos de Sales Guerra Tsuzuki	USP-EP
Marcos Ribeiro Pereira Barretto	USP-EP
Marcos Sebastião de Paula Gomes	PUC-Rio
Marcos Vinicius Bortolus	UFMG
Mardson Queiroz McQuay	Brigham Young University
Maria Laura Martins Costa	UFF
Maria Regina da Silva Galetti	CODERE
Mauri Fortes	UFMG
Mauro Speranza	PUC-Rio
Max Suell Dutra	UNESP-FEIS
Michael George Maunsell	USP-EESC
Miguel H. Hirata	EFEI
Mônica Feijó Naccache	PUC-Rio

N

Narciso A. Ramos Arroyo	UFSC
Newton Maruyama	USP-EP
Norberto Mangiavacchi	UFRJ-COPPE
Nilson Dias Vieira Júnior	IPEN-CNEN
Nivaldo Lemos Coppini	UNICAMP
Noemi Rodriguez	PUC-Rio

O

Oswaldo Horikawa	USP/EP

P

Paulo Ballin	PETROBRAS
Paulo Carlos Kaminski	USP-EP
Paulo José Modenesi	UFMG
Paulo Roberto de Souza Mendes	PUC-Rio
Paulo Sergio Pereira da Silva	USP-EP
Pedro Carajilescov	UFF
Pedro Leite da Silva Dias	USP
Peter Hagedorn	T.U. Darmstadt
Phillemon da Cunha Melo	PUC-Rio

R

Ramon Molina Valle	UFMG
Raul Gonzales Lima	USP-EP
Rogério Martins Saldanha da Gama	LNCC
Regina Célia Cerqueira de Almeida	LNCC
Reinhard Radermacher	University of Maryland
Renato Simões Silva	LNCC
Roberval Rymer da Silva Carvalho	EFEI
Rodnei Bertazzolli	UNICAMP
Roseana da Exaltação Trevisan	UNICAMP

S

Sergio Bogado Leite	CNEN
Sérgio Colle	UFSC
Sérgio Frey	UFRGS
Sergio Möller	PROMEC-UFRGS
Sérgio N. Bordalo	UNICAMP
Sérgio Roberto Robles Vertiola	IPT-DME
Sérgio Tonini Button	UNICAMP
Sidney Stuckembruck	Olympus Software
Stephan Wolynec	USP-EP

V

Valter A. Alves	USP-EP
Vilson Carlos da Silva Ferreira	UFRGS
Vitor Ferreira Romano	UFRJ-COPPE

W

Waldir Antonio Bizzo	UNICAMP
Waldir Luiz Ribeiro Gallo	UNICAMP
Washington Braga	PUC-Rio
Willie A. Bueno	USP

Z

Zebhour Panossian	IPT

Journal of the Brazilian Society of Mechanical Sciences

Information for Authors

SCOPE AND POLICY

- The purpose of the Journal of the Brazilian Society of Mechanical Sciences is to publish papers of permanent interest dealing with research, development and design related to science and technology in Mechanical Engineering, encompassing interfaces with Civil, Electrical, Chemical, Naval, Nuclear, Materials, Aerospace, Petroleum, System Engineering, Food, Agriculture, etc., as well as with Physics and Applied Mathematics.
- The Journal publishes Full Length Papers, Review Papers, Book Reviews and Letters to the Editor. Authors must agree not to publish elsewhere a paper submitted and accepted by the Journal. Papers previously published in proceedings of conferences can also be considered for publication; this event should be cited as a footnote on the title page. Copies of the conference referees' reviews should be included. Review articles should constitute a critical appraisal of the published information.
- The decision of acceptance for publication lies with the Editors and is based on the recommendations of at least two ad hoc reviewers, and of the Editorial Board, if necessary.

SUBMISSION

- Manuscripts and correspondence should be sent to the Editor or, alternatively, to the nearest Associate Editor.
- Five (5) copies of the paper are required. The Author should retain the manuscript disk until the end of the review process.
- Manuscripts should be submitted only in **English**.
- A manuscript submitted for publication should be accompanied by a cover page containing the full name of the Author(s), the Author for contact, institution address, phone number, e-mail address and, if the Authors so wish, the names of up to five (5) possible referees, with respective addresses.

FORMAT

- Manuscripts should begin with the title, followed by an Abstract and from three to five Keywords. The manuscript should not contain the Authors' names. The Abstract should state the objectives, methodology used and main conclusions, in no more than 200 words.
- In research papers sufficient information should be provided in the text, or by referring to papers in generally available Journals, to permit the work to be repeated.
- The paper must begin with an Introduction that is written for the general reader of the Journal, not for the specialist. This section should describe the problem statement, its relevance, significant results and conclusions from prior work, and objectives of the present work.
- Uncertainties should be specified for experimental and numerical results.
- Manuscripts should be typed double-spaced, on one side of the page, using A4 sized paper, with 2 cm margins. The pages should be numbered and not to excess 24, including tables and figures. Avoid footnotes.
- All symbols should be defined in the text. A separate nomenclature section should list, in alphabetical order, the symbols used and their definitions. The Greek symbols follow the English symbols, and are followed by the subscripts and superscripts. Each dimensional symbol must have SI (metric) units mentioned; in addition, English units may be included parenthetically. Dimensionless groups and coefficients must be so defined and indicated.

MATHEMATICAL EQUATIONS

- All mathematical expressions should be typewritten using only letters and symbols available on the keyboard.
- Equations that extend beyond the text width should be restated to go in two or more lines, as necessary to fit within the page width.
- Fractional powers should be used instead of root signs.
- A solidus (/) should be used instead of an horizontal line for fractions, whenever possible; for example, use 2/3 for two-thirds.

- Mathematical expressions should not be introduced along the text itself, as part of a sentence line, but typed on individual lines.
- Numbers that identify mathematical expressions should be enclosed in parenthesis. Refer to equations in the text as " Eq.(1)" or, if at the beginning of a sentence, as " Equation (1)".
- Vectors should be typed **boldface**. Do not use arrows, wavy-line underscoring,etc.

FIGURES AND TABLES

- Figures and Tables should be referred in consecutive Arabic numerals. They should have a caption and be placed as close as possible to their first reference in the text. Refer to figures in the text with the abbreviation "Fig. 1", except at the beginning of a sentence, where " Figure 1" should be used.
- The figures presenting technical data/results should have a boundary on all four sides, with scale indicators (tick marks) on all sides.
- The legend for the data symbols should be put inside the figure, as well as the labels for each curve. Lettering should be large enough to be clearly legible (1.5-2.0 mm).
- Laser print output line drawings are preferred. Drawings prepared on tracing paper or vellum, using black india ink, are acceptable.
- Photographs must be glossy prints.

REFERENCES

- References should be cited in the text by giving the last name of the author(s) and the year of publication. Either use "Recent work (Smith and Farias, 1997) or " Recently Smith and Farias (1997). With four (4) or more names, use the form " Smith et al. (1997)". If two or more references would have the same identification, distinguish them by appending "a","b", etc., to the year of publication.
- Acceptable references include journal articles, numbered papers, dissertations, thesis, published conference proceedings, preprints from conferences, books, submitted articles, if the journal is identified, and private communications.
- References should be listed in alphabetical order, according to the last name of the first author, at the end of the paper. Some sample references follow:
- Soviero, P.A.O. and Lavagna, L.G.M.,1997, "A Numerical Model for Thin Airfoils in Unsteady Motion", RBCM- J. of the Brazilian Soc. Mechanical Sciences, Vol.19, No. 3, pp. 332-340.
- Bordalo, S.N., Ferziger,J.H. and Kline, S.J.,1989, "The Development of Zonal Models for Turbulence", Proceedings of the 10th Brazilian Congress of Mechanical Engineering, Vol.1, Rio de Janeiro, Brazil, pp. 41-44.
- Sparrow, E.M., 1980a, "Forced Convection Heat Transfer in a Duct Having Spanwise-Periodic Rectangular Protuberances", Numerical Heat Transfer, Vol.3, pp. 149-167.
- Sparrow, E.M., 1980b, "Fluid-to-Fluid Conjugate Heat Transfer for a Vertical Pipe-Internal and External Natural Convection", ASME Journal of Heat Transfer, Vol.102, pp. 402-407.
- Silva, L.H.M.,1988, "New Integral Formulation for Problems in Mechanics" (In Portuguese), Ph.D. Thesis, Federal University of Santa Catarina, Florianópolis, S.C., Brazil, 223 p.
- Coimbra, A.L., 1978, "Lessons of Continuum Mechanics", Ed. Edgard Blücher, S.Paulo, Brazil, 428 p.
- Clark, J.A.,1986, Private Communication, University of Michigan, Ann Harbor.

FINAL VERSION OF THE MANUSCRIPT

- Upon notification of acceptance, Authors should submit two copies of the final version and the manuscript disk, in Windows or Macintosh, Word or WordPerfect , thus avoiding retyping, with subsequent reduction of errors.

(Contents Continued)

ISSN 0100 - 7386

JOURNAL OF THE BRAZILIAN SOCIETY OF MECHANICAL SCIENCES
REVISTA BRASILEIRA DE CIÊNCIAS MECÂNICAS

VOL. XXI - No. 1 - MARCH 1999

(Continued on Inside Back Cover)